A STUDY OF NEUTRAL STRANGE PARTICLE PRODUCTION AT $\sqrt{s} = 38.8$ GeV IN p-Si INTERACTIONS

by

CASEY MICHELLE DURANDET

A dissertation submitted in partial fulfillment

of the requirements for the degree of

Doctor of Philosophy

(Physics)

at the

UNIVERSITY OF WISCONSIN - MADISON

1995

Abstract

A STUDY OF NEUTRAL STRANGE PARTICLE PRODUCTION AT $\sqrt{s} = 38.8$ GeV IN p-Si INTERACTIONS

Under the supervision of Professor Albert R. Erwin

At the University of Wisconsin-Madison

This dissertation studies K°, Λ°, and $\overline{\Lambda^\circ}$ production (neutral V° particle production) in a beauty enhanced trigger mode run of an 800 GeV/c proton beam on a silicon fixed target. Average multiplicities and p_t spectra are determined for the V° production via minimum bias triggered events, single muon triggered events, and double muon triggered events. The estimated total K°, Λ°, and $\overline{\Lambda^\circ}$ production cross sections are 13.31±0.65 mb, 6.06±1.09 mb, and 3.15±0.45 mb, respectively, and their differential cross sections at zero rapidity are 1.46±0.06 mb, 0.40±0.08 mb, and 0.32±0.09 mb, respectively. A comparison is made between V° production for minimum bias triggered events, for single and double muon triggered events, and for "charm" and "beauty" enhanced events. It is shown that the specially triggered events enrich V° production, with increased $< p_t >$.

ACKNOWLEDGEMENTS

Many people deserve my gratitude for the completion of this manuscript. They were there to keep me going to obtain this goal. To them I am most grateful.

To **Albert R. Erwin, Jr.:** My thesis adviser, you had faith in me right from the start, even when I doubted myself. Thank you, Albert, for everything you have done for me.

To **Vasso, Theo, and Elias:** You all have become quite special to me over the years I have known you. I would especially like to thank you, Theo, for **all** the help you have given me. It has been a real joy watching you all grow as a family.

To **Adam M. Bincer:** Thank you, Adam, for your friendship. All your courses were the best, and I especially enjoyed the opportunity to help you out with your computer "glitches".

To **Megan and Murray Thompson:** Thank you both for your hospitality and kindness. Yes, Murray, out of 9 lives, 6 left?

To **Jesse, George, and Bob:** Thanks guys for everything. Remember the first year I worked as an undergraduate hourly? It only seems like yesterday. Wherever you are, Jess, I thank you for your inspiration to keep me going.

To my **E771 Colleagues:** I thank everyone involved in this experiment. It was fun working with all of you, and I appreciate all the help everyone gave me.

To **"Crew 9":** Thanks especially to Tom, Tom, and Howard. You were loads of fun during the wee hours of the morning, and you all gave me a better perspective on life.

And finally, many thanks to all the friends I made here at Wisconsin during my undergraduate and graduate years.

JTAA

Surtout que je n'oublierai jamais tout ce que tu as fait pour moi.

Contents

Abstract **i**

1 Introduction **1**

1.1 Theory 1

1.1.1 Standard Model 2

1.1.2 Mesons and Baryons From Quarks 4

1.1.3 Decay of Charm and Beauty 4

1.2 History of Neutral Strange Particle Production 9

2 Experimental Setup **12**

2.1 E771 Main Objective 12

2.2 Fermilab Layout 12

2.3 E771 Spectrometer Layout 17

2.3.1 The Beam and Halo Veto Counters 17

2.3.2 The Main Target and Beam Silicon 20

2.3.3 The Silicon Microstrip Vertex Detector 22

2.3.4 The Front Tracking Chambers 25

2.3.5 The Analysis Magnet 28

2.3.6 The Rear Tracking Chambers 30

2.3.7 The Charged Particle Hodoscope 33
2.3.8 The Electromagnetic Calorimeter 36
2.3.9 The RPC Muon Detectors 37
2.4 "F6" Pad Chamber Readout 40
2.4.1 Mechanical Layout and Voltage Conditions 42
2.4.2 Readout Electronics 43

3 Triggers and Data Acquisition **46**
3.1 The E771 Triggers 46
3.1.1 The Beam Trigger 47
3.1.2 The Interaction Trigger 49
3.1.3 The 1A Trigger 51
3.1.4 The 1B Trigger 53
3.2 Data Acquisition 55

4 LTELE **58**
4.1 Physical Description 58
4.2 LTELE Triggering 59
4.3 Physics Goals - Differential Cross Section 61
4.3.1 The (dN/N) Ratio 67
4.4 $(d\sigma/d\eta)$ for Silicon as a Function of Tapeset Number 70

5 Monte Carlo **75**
5.1 PYTHIA and JETSET 75
5.2 Fast Monte Carlo 76

5.2.1 Predictions of (dN/dy) and (dN/dp_t) 77

5.2.2 Geometrical Acceptances 87

5.3 GEANT Monte Carlo 87

5.3.1 K° and Λ° Simulation 88

5.3.2 Event Reconstruction Efficiencies 90

6 Neutral Particle Selection Criteria **92**

6.1 E771 Main Tracking Program 92

6.2 Neutral Strange Particle Analysis Routine 96

6.3 K° Invariant Mass Plots 100

6.4 $\Lambda^\circ/\overline{\Lambda^\circ}$ Invariant Mass Plots 105

6.5 K°, Λ°, and $\overline{\Lambda^\circ}$ Particle Mis-Identification 111

7 Minimum Bias Events **116**

7.1 The LED Trigger 116

7.2 Overlay and Data (dN/dy) and (dN/dp_t) 117

7.3 K° 122

7.3.1 P_t Distribution 122

7.3.2 Multiplicity, Rapidity, and x_f Distributions 126

7.3.3 Minimum Bias PYTHIA 127

7.3.4 Comparison of Data to PYTHIA 129

7.3.5 Mass Fitting Algorithm 131

7.3.6 K° Cross Section 134

7.3.7 $(d\sigma/dy)|_{y=0}$ 146

7.4 Λ° 149

7.4.1 P_t Distribution 149

7.4.2 Multiplicity, Rapidity, and x_f Distributions 152

7.4.3 Minimum Bias PYTHIA 153

7.4.4 Comparison of Data to PYTHIA 155

7.4.5 Mass Fitting Algorithm 156

7.4.6 Λ° Cross Section 159

7.4.7 $(d\sigma/dy)|_{y=0}$ 171

7.5 $\overline{\Lambda^\circ}$ 172

7.5.1 P_t Distribution 174

7.5.2 Multiplicity, Rapidity, and x_f Distributions 177

7.5.3 Minimum Bias PYTHIA 179

7.5.4 Comparison of Data to PYTHIA 181

7.5.5 Mass Fitting Algorithm 182

7.5.6 $\overline{\Lambda^\circ}$ Cross Section 183

7.5.7 $(d\sigma/dy)|_{y=0}$ 192

7.6 Signal/Background Ratios 195

7.7 Data Sets Analyzed for Minimum Bias Events 197

8 Single-μ Triggered Events **201**

8.1 Raw K° Events, Overlay Efficiency, Corrected K° Acceptance . . . 201

8.2 K° p_t, Multiplicity, Rapidity, and x_f Distributions 209

8.2.1 Data 209

8.2.2 Minimum Bias PYTHIA 213

8.2.3 Comparison of Data to PYTHIA 215

8.3 Raw Λ° Events, Overlay Efficiency, Corrected Λ° Acceptance 217

8.4 Λ° p_t, Multiplicity, Rapidity, and x_f Distributions 222

8.4.1 Data 222

8.4.2 Minimum Bias PYTHIA 230

8.4.3 Comparison of Data to PYTHIA 230

8.5 Raw $\overline{\Lambda^\circ}$ Events, Overlay Efficiency, Corrected $\overline{\Lambda^\circ}$ Acceptance 232

8.6 $\overline{\Lambda^\circ}$ p_t, Multiplicity, Rapidity, and x_f Distributions 237

8.6.1 Data 237

8.6.2 Minimum Bias PYTHIA 244

8.6.3 Comparison of Data to PYTHIA 246

8.7 Signal/Background Ratios 247

8.8 Data Sets Analyzed for Single Muon Triggered Events 248

9 Double-μ Triggered Events 250

9.1 Raw K° Events, Overlay Efficiency, Corrected K° Acceptance . . . 250

9.2 K° p_t, Multiplicity, Rapidity, and x_f Distributions 254

9.2.1 Data 258

9.2.2 Minimum Bias PYTHIA 262

9.2.3 Comparison of Data to PYTHIA 264

9.3 Raw Λ° Events, Overlay Efficiency, Corrected Λ° Acceptance 265

9.4 Λ° p_t, Multiplicity, Rapidity, and x_f Distributions 272

9.4.1 Data 272

9.4.2 Minimum Bias PYTHIA 277

9.4.3 Comparison of Data to PYTHIA 279

9.5 Raw $\overline{\Lambda^\circ}$ Events, Overlay Efficiency, Corrected $\overline{\Lambda^\circ}$ Acceptance 281

9.6 $\overline{\Lambda^\circ}$ p_t, Multiplicity, Rapidity, and x_f Distributions 287

9.6.1 Data 287

9.6.2 Minimum Bias PYTHIA 294

9.6.3 Comparison of Data to PYTHIA 295

9.7 Signal/Background Ratios 296

9.8 Data Sets Analyzed for Double Muon Triggered Events 297

10 Charm and Beauty **299**

10.1 Charm Enhanced Events 299

10.1.1 K°, Λ°, and $\overline{\Lambda^\circ}$ Results 300

10.1.2 Charm PYTHIA 311

10.1.3 Comparison of Data to PYTHIA 312

10.2 Beauty Enhanced Events 313

10.2.1 K°, Λ°, and $\overline{\Lambda^\circ}$ Results 314

10.2.2 Beauty PYTHIA 324

10.2.3 Comparison of Data to PYTHIA 325

11 Results and Conclusions **327**

11.1 Cross Sections 327

11.2 Enriched V° Production 331

Bibliography **337**

List of Tables

2.1 E771 run conditions. 19

2.2 E771 silicon plane tracker parameters. 23

2.3 E771 front chamber tracking parameters for the PCB chambers. (Note: The z-positions are with respect to the center of the analysis magnet.) 27

2.4 E771 front chamber tracking parameters for the PC chambers. (Note: The z-positions are with respect to the center of the analysis magnet.) 28

2.5 E771 front chamber tracking parameters for the Drift Chambers. (Note: The z-positions are with respect to the center of the analysis magnet.) 29

2.6 E771 rear chamber tracking parameters for the drift chambers. (Note: The z-positions are with respect to the center of the analysis magnet.) 31

2.7 E771 rear chamber tracking parameters for the central chambers. (Note: The z-positions are with respect to the center of the analysis magnet.) 33

2.8 E771 rear chamber tracking parameters for the wing chambers. (Note: The z-positions are with respect to the center of the analysis magnet.) 35

2.9 E771 muon shielding absorber characteristics. 39

4.1 Data and cross sections for LTELE as a function of target material. 69

4.2 Data and cross sections using LTELE as a function of tapeset number for the silicon target. 74

5.1 E771 Monte Carlo geometrical acceptances with variations on chamber efficiencies and number of planes required to be hit. 88

7.1 Comparison of minimum bias PYTHIA generated events and data events for K° produced particles with no muon trigger imposed. . . 131

7.2 Comparison of minimum bias PYTHIA generated events and data events for Λ° produced particles with no muon trigger imposed. . . 156

7.3 Comparison of minimum bias PYTHIA generated events and data events for $\overline{\Lambda^\circ}$ produced particles with no muon trigger imposed. . . 182

7.4 Run statistics for minimum bias triggered events. 199

7.5 Run statistics for minimum bias triggered events. (Continuation of Table 7.4.) 200

8.1 Comparison of minimum bias single muon triggered PYTHIA generated events and data events for K° produced particles. 216

8.2 Comparison of minimum bias single muon triggered PYTHIA generated events and data events for Λ° produced particles. 231

8.3 Comparison of minimum bias single muon triggered PYTHIA generated events and data events for $\overline{\Lambda^\circ}$ produced particles. 247

8.4 Run statistics for tracked single muon triggered events and double muon triggered events. 249

9.1 Comparison of minimum bias double muon triggered PYTHIA generated events and data events for K° produced particles. 265

9.2 Comparison of minimum bias double muon triggered PYTHIA generated events and data events for Λ° produced particles. 280

9.3 Comparison of minimum bias double muon triggered PYTHIA generated events and data events for $\overline{\Lambda^\circ}$ produced particles. 296

9.4 Run statistics for tracked single muon triggered events and double muon triggered events. 298

10.1 Comparison of charm enhanced PYTHIA generated events and data events for K° produced particles. 313

10.2 Comparison of beauty enhanced PYTHIA generated events and data events for K° production. 325

11.1 σ_{tot} and $(d\sigma/dy)_{y=0}$ for K°, Λ°, and $\overline{\Lambda^\circ}$ production from minimum bias triggered events. 329

11.2 Various data measurements for $K^\circ \rightarrow \pi^+\pi^-$ from minimum bias events, single muon and double muon triggered events, and $c\bar{c}$ and $b\bar{b}$ enhanced events. 333

11.3 Various data measurements for $\Lambda^\circ \rightarrow p\pi^-$ from minimum bias events, single muon triggered events, and double muon triggered events. 333

11.4 Various data measurements for $\overline{\Lambda^{\circ}} \rightarrow \overline{p}\pi^{+}$ from minimum bias events, single muon triggered events, and double muon triggered events. 335

List of Figures

1.1 The Standard Model. 3

1.2 The Feynman Diagram decay of the $K_s^\circ \rightarrow \pi^+\pi^-$. The K_s°, composed of a $d\bar{s}$ quark pair decays to the $d\bar{u}$ pair and a $u\bar{d}$ pair by the emission of a W^+ boson. 6

1.3 Decay of $\Lambda^\circ \rightarrow p + \pi^-$. 7

1.4 Decay of $J/\psi \rightarrow \mu^+ + \mu^-$. 8

1.5 Decay of $B_d^\circ \rightarrow J/\psi + K_s^\circ$. 9

1.6 Decay of $\Lambda_b^\circ \rightarrow J/\psi + \Lambda^\circ$. 10

2.1 FNAL layout. 13

2.2 An aerial view of Fermilab. The main injector is seen in the foreground, and the main ring is seen in the background. The High Rise is located to the left of the main ring, and the fixed target lines are located further in the background relative to the High Rise. 15

2.3 Proton West beamline septa. 16

2.4 E771 spectrometer. 18

2.5 E771 beam halo set up. (A) shows a beam's eye view of the scintillators, and (b) shows a top view of the location of the counters with respect to the main target. 21

2.6 E771 precision beam planes, silicon target, and silicon tracker. . . . 24
2.7 E771 pad chamber layout. (a) Wire plane view. (B) Top view of the chambers. (C) Map of pad sizes and positions. 34
2.8 Top view of the E771 electromagnetic calorimeter. 38
2.9 E771 resistive plate counters layout. 41
2.10 "F6" pad chamber trigger logic. 44

3.1 E771 beam trigger logic. 48
3.2 E771 interaction trigger logic. 50
3.3 E771 topological definition of the 1A trigger. 52
3.4 E771 1A2μ trigger logic. 54
3.5 The E771 data acquisition system. 57

4.1 LTELE trigger logic. 60
4.2 Maximum RF timing for LTELE as a function of tapeset number. . 62
4.3 Mean RF timing for LTELE as a function of tapeset number. 63
4.4 LTELE/PW6IC as a function of tapeset number. 64
4.5 Sketch of LTELE's position with respect to the beam line. This shows the strip of view where the scintillator was able to detect the passage of particles. 66
4.6 LTELE inclusive cross section as a function of target material. . . . 71
4.7 LTELE inclusive cross section as a function of tapeset number for a silicon target. 73

5.1 Monte Carlo simulated event through E771's spectrometer (not including the CPH, the EMC, or the RPCs). 78

5.2 Monte Carlo rapidity distribution for K_s° particles showing the generated and accepted distributions. 80

5.3 Monte Carlo rapidity distribution for Λ° particles showing the generated and accepted distributions. 82

5.4 Monte Carlo p_t distribution for K_s° particles showing the generated and accepted distributions. 85

5.5 Monte Carlo p_t distribution for Λ° particles showing the generated and accepted distributions. 86

6.1 Sample display of a tracked LED (minimum bias) event. The solid lines indicate those tracks that were matched in the front and rear, where the dashed lines indicate no front-rear matched combinations. 95

6.2 Δz distribution for two charged tracks. 99

6.3 $cos(\theta)$ distribution for decay of the K_s° into its two constituents. . . 101

6.4 Invariant mass distributions for $K_s^\circ, \overline{K_s^\circ} \rightarrow \pi^\pm\pi^\mp$ for unlike sign charged tracks. 102

6.5 Invariant mass distributions for $K_s^\circ, \overline{K_s^\circ} \rightarrow \pi^\pm\pi^\pm$ for like sign charged tracks. 104

6.6 Monte Carlo distribution of p_p vs. p_{π^-} for Λ° decays. 106

6.7 Invariant mass distributions for $\Lambda^\circ, \overline{\Lambda^\circ} \rightarrow p^\pm\pi^\mp$ for unlike sign charged tracks. 108

6.8 Decay mode for $\Xi^- \rightarrow \Lambda^\circ + \pi^-$. Shown is how the wrong π mass may be assigned to the Λ° mass to yield a wide peak distribution at 1.15 GeV/c^2. 109

6.9 Invariant mass distributions for $\Lambda^\circ, \overline{\Lambda^\circ} \rightarrow p^\pm\pi^\pm$ for like sign charged tracks. 110

6.10 Decay distribution of the $K_s^\circ \rightarrow \pi^+ + \pi^-$, using the Podolanski-Armenteros variables, p_t and α. 112

6.11 Podolanski-Armenteros theoretical plot of p_t vs. α for the $K_s^\circ \rightarrow \pi^+\pi^-$, $\Lambda^\circ \rightarrow p\pi^-$, and $\overline{\Lambda^\circ} \rightarrow \overline{p}\pi^+$ decays. 113

6.12 Podolanski-Armenteros data plot of p_t vs. α for the $K_s^\circ \rightarrow \pi^+\pi^-$, $\Lambda^\circ \rightarrow p\pi^-$, and $\overline{\Lambda^\circ} \rightarrow \overline{p}\pi^+$ decays. 114

7.1 Overlay and data rapidity distribution plots for the K°'s using the LED triggered events. (a) is the input Monte Carlo rapidity distribution (dashed curve) superimposed on the overlay accepted distribution (solid curve), both with the same area normalization. (b) is the overlay efficiency, ϵ. (c) is the superposition of the uncorrected real data (solid) and the overlay data (dashed), both normalized to the same area. (d) is the final efficiency corrected rapidity distribution. 119

7.2 Overlay and data p_t distribution for the K°'s using the LED triggered events. (a) is the input Monte Carlo p_t distribution (dashed curve) superimposed on the overlay accepted curve (solid curve), both normalized to the same area. (b) is the overlay efficiency, ϵ. (c) is the superposition of the real data (solid) and the overlay data (dashed), both normalized to the same area. (d) is the final efficiency corrected p_t distribution. 121

7.3 The K° p_t distribution from LED triggered events. The same plot is shown three times for each of three different fitting functions. (a) uses Equation (7.2) as the fit, (b) uses Equation (7.3) as the fit, and (c) uses Equation (7.4) as the fit. 125

7.4 (a) N_c, (b) y_{cm}, and (c) center of mass x_f distributions for the K° LED triggered events. These distributions are not corrected for full spectrometer acceptance. 128

7.5 Sample K° mass fitting algorithm. (a) is the mass distribution with a Gaussian fit to the signal. (b) is the same as (a) but with the signal peak subtracted in order to fit the background. (c) is the polynomial curve drawn out as a result of the fit to the background. (d) is the final distribution showing the Gaussian fit to the signal and the polynomial fit to the background. 133

7.6 Fitted Gaussian distribution to the $K_s^\circ \rightarrow \pi^+\pi^-$ mass peak. 135

7.7 K° mass distributions from minimum bias triggered events for various z-decay and $|\Delta z|$ cuts, with no coplanarity criterion imposed. Each horizontal scale is the mass value in GeV/c^2, and each vertical scale is the number of pairs per 10 MeV/c^2. 137

7.8 K° mass distributions from minimum bias triggered events for various z-decay and $|\Delta z|$ cuts, with a coplanarity criterion imposed. Each horizontal scale is the mass value in GeV/c^2, and each vertical scale is the number of pairs per 10 MeV/c^2. 139

7.9 Total number of K°'s, N_{K°, as a function of $|\Delta z|$ and z-decay cuts. Shown are curves for coplanar tracks and curves for non-coplanar tracks. 140

7.10 Overlay efficiency, ϵ, for tracking a K° as a function of $|\Delta z|$ and z-decay cuts. Shown are curves for coplanar tracks and curves for non-coplanar tracks. 141

7.11 Corrected number of K° events, N_{K°/ϵ, as a function of $|\Delta z|$ and z-decay cuts. Shown are curves for coplanar tracks and curves for non-coplanar tracks. 143

7.12 E771 estimated σ_{tot} for K° production versus P_{lab} compared to world data. 145

7.13 K° $(d\sigma/dy)_{y=0}$ versus $\sqrt{s}$ compared to world data with a $ln(s)$ curve drawn through E771's data point. 148

7.14 The Λ° p_t distribution from LED triggered events. The same plot is shown three times for each of three different fitting functions. (a) uses Equation (7.19) as the fit, (b) uses Equation (7.20) as the fit, and (c) uses Equation (7.21) as the fit. 151

7.15 (a) N_c, (b) y_{cm}, and (c) center of mass x_f distributions for the Λ° LED triggered events. These distributions are not corrected for full spectrometer acceptance. 154

7.16 Sample Λ° mass fitting algorithm. (a) is the mass distribution with a Gaussian fit to the signal. (b) is the same as (a) but with the signal peak subtracted in order to fit the background. (c) is the polynomial curve drawn out as a result of the fit to the background. (d) is the final distribution showing the Gaussian fit to the signal and the polynomial fit to the background. 158

7.17 Fitted Gaussian distribution to the $\Lambda^\circ \rightarrow p + \pi^-$ mass peak. 160

7.18 Λ° mass distributions from minimum bias triggered events for various z-decay and $|\Delta z|$ cuts, with no coplanarity criterion imposed. Each horizontal scale is the mass value in GeV/c^2, and each vertical scale is the number of pairs per 2.5 MeV/c^2. 162

7.19 Λ° mass distributions from minimum bias triggered events for various z-decay and $|\Delta z|$ cuts, with a coplanarity criterion imposed. Each horizontal scale is the mass value in GeV/c^2, and each vertical scale is the number of pairs per 2.5 MeV/c^2. 164

7.20 Total number of Λ°'s, N_{Λ°, as a function of $|\Delta z|$ and z-decay cuts, with the curved lines representing different z-decay cuts. Shown are curves for coplanar tracks and curves for non-coplanar tracks. . . . 165

7.21 Overlay efficiency, ϵ, for tracking a Λ° as a function of $|\Delta z|$ and z-decay cuts, with the curved lines representing different z-decay cuts. Shown are curves for coplanar tracks and curves for non-coplanar tracks. 166

7.22 Corrected number of Λ°, $N_{\Lambda^\circ}/\epsilon$, as a function of $|\Delta z|$ and z-decay cuts, with the curved lines representing different z-decay cuts. Shown are curves for coplanar tracks and curves for non-coplanar tracks. . 168

7.23 Λ° σ_{tot} versus P_{lab} compared to world data. 170

7.24 Λ° $(d\sigma/dy)_{y=0}$ versus $\sqrt{s}$ compared to world data. 173

7.25 The $\overline{\Lambda^\circ}$ p_t distribution from LED triggered events. The same plot is shown three times for each of three different fitting functions. (a) uses Equation (7.27) as the fit, (b) uses Equation (7.28) as the fit, and (c) uses Equation (7.29) as the fit. 176

7.26 (a) N_c, (b) y_{cm}, and (c) center of mass x_f distributions for the $\overline{\Lambda^\circ}$ LED triggered events. These distributions are not corrected for full spectrometer acceptance. 180

7.27 $\overline{\Lambda^\circ}$ mass distributions from minimum bias triggered events for various z-decay and $|\Delta z|$ cuts, with no coplanarity criterion imposed. Each horizontal scale is the mass value in GeV/c^2, and each vertical scale is the number of pairs per 2.5 MeV/c^2. 186

7.28 $\overline{\Lambda^\circ}$ mass distributions from minimum bias triggered events for various z-decay and $|\Delta z|$ cuts, with a coplanarity criterion imposed. Each horizontal scale is the mass value in GeV/c^2, and each vertical scale is the number of pairs per 2.5 MeV/c^2. 187

7.29 Total number of $\overline{\Lambda^\circ}$'s, $N_{\overline{\Lambda^\circ}}$, as a function of $|\Delta z|$ and z-decay cuts, with the curved lines representing different z-decay cuts. 188

7.30 Overlay efficiency, ϵ, for tracking a $\overline{\Lambda^\circ}$ as a function of $|\Delta z|$ and z-decay cuts, with the curved lines representing different z-decay cuts. 189

7.31 Corrected number of $\overline{\Lambda^\circ}$, $N_{\overline{\Lambda^\circ}}/\epsilon$, as a function of $|\Delta z|$ and z-decay cuts, with the curved lines representing different z-decay cuts. . . . 191

7.32 $\overline{\Lambda^\circ}$ σ_{tot} versus P_{lab} compared to world data. 193

7.33 $\overline{\Lambda^\circ}$ $(d\sigma/dy)_{y=0}$ versus $\sqrt{s}$ compared to world data. 196

8.1 K° mass distributions from single muon triggered events for different z-decay and $|\Delta z|$ cuts, with no coplanarity cut imposed. Each horizontal scale is the mass value in GeV/c^2, and each vertical scale is the number of pairs per 10 MeV/c^2. 203

8.2 K° mass distributions from single muon triggered events for different z-decay and $|\Delta z|$ cuts, with a coplanarity criterion imposed. Each horizontal scale is the mass value in GeV/c^2, and each vertical scale is the number of pairs per 10 MeV/c^2. 204

8.3 Total number of K°'s, N_{K°, as a function of $|\Delta z|$ and z-decay cuts. Shown are curves for coplanar tracks and curves for non-coplanar tracks. 206

8.4 Overlay efficiency, ϵ, for tracking a K° as a function of $|\Delta z|$ and z-decay cuts. Shown are curves for coplanar tracks and curves for non-coplanar tracks. 207

8.5 Corrected number of K°'s, N_{K°/ϵ, as a function of $|\Delta z|$ and z-decay cuts. Shown are curves for coplanar tracks and curves for non-coplanar tracks. 208

8.6 The K° p_t distribution from single muon triggered events. The same plot is shown three times for each of three different fitting functions. (a) uses Equation (8.2) as the fit, (b) uses Equation (8.3) as the fit, and (c) uses Equation (8.4) as the fit. 211

8.7 (a) N_c, (b) y_{cm}, and (c) center of mass x_f distributions for K°'s from single muon triggered events. These distributions are not corrected for full spectrometer acceptance. 214

8.8 Λ° mass distributions from single muon triggered events using different z-decay and $|\Delta z|$ cuts, with no coplanarity cut imposed. Each horizontal scale is the mass value in GeV/c^2, and each vertical scale is the number of pairs per 2.5 MeV/c^2. 219

8.9 Λ° mass distributions from single muon triggered events using different z-decay and $|\Delta z|$ cuts, with a coplanarity cut imposed. Each horizontal scale is the mass value in GeV/c^2, and each vertical scale is the number of pairs per 2.5 MeV/c^2. 220

8.10 Total number of Λ°'s, N_{Λ°, as a function of $|\Delta z|$ and z-decay cuts. Shown are curves for coplanar tracks and curves for non-coplanar tracks. 221

8.11 Overlay efficiency, ϵ, for tracking a Λ° as a function of $|\Delta z|$ and z-decay cuts. Shown are curves for coplanar tracks and curves for non-coplanar tracks. 223

8.12 Corrected number of Λ°'s, $N_{\Lambda^\circ}/\epsilon$, as a function of $|\Delta z|$ and z-decay cuts. Shown are curves for coplanar tracks and curves for non-coplanar tracks. 224

8.13 The Λ° p_t distribution from single muon triggered events. The same plot is shown three times for each of three different fitting functions. (a) uses Equation (8.10) as the fit, (b) uses Equation (8.11) as the fit, and (c) uses Equation (8.12) as the fit. 226

8.14 (a) N_c, (b) y_{cm}, and (c) center of mass x_f distributions for Λ°'s from single muon triggered events. These distributions are not corrected for full spectrometer acceptance. 229

8.15 $\overline{\Lambda^\circ}$ mass distributions from single muon triggered events for different z-decay and $|\Delta z|$ cuts, with no coplanarity cut imposed. Each horizontal scale is the mass value in GeV/c^2, and each vertical scale is the number of pairs per 2.5 MeV/c^2. 233

8.16 $\overline{\Lambda^\circ}$ mass distributions from single muon triggered events for different z-decay and $|\Delta z|$ cuts, with a coplanarity cut imposed. Each horizontal scale is the mass value in GeV/c^2, and each vertical scale is the number of pairs per 2.5 MeV/c^2. 235

8.17 Total number of $\overline{\Lambda^\circ}$, $N_{\overline{\Lambda^\circ}}$, as a function of $|\Delta z|$ and z-decay cuts. Shown are curves for coplanar tracks and curves for non-coplanar tracks. 236

8.18 Overlay efficiency, ϵ, for tracking a Λ° as a function of $|\Delta z|$ and z-decay cuts. Shown are curves for coplanar tracks and curves for non-coplanar tracks. 238

8.19 Corrected number of $\overline{\Lambda^\circ}$'s, $N_{\overline{\Lambda^\circ}}/\epsilon$, as a function of $|\Delta z|$ and z-decay cuts. Shown are curves for coplanar tracks and curves for non-coplanar tracks. 239

8.20 The $\overline{\Lambda^\circ}$ p_t distribution from single muon triggered events. The same plot is shown three times for each of three different fitting functions. (a) uses Equation (8.18) as the fit, (b) uses Equation (8.19) as the fit, and (c) uses Equation (8.20) as the fit. 242

8.21 (a) N_c, (b) y_{cm}, and (c) center of mass x_f distributions for the $\overline{\Lambda^\circ}$ single muon triggered events. These distributions are not corrected for full spectrometer acceptance. 245

9.1 K° mass distributions from double muon triggered events for different z-decay and $|\Delta z|$ cuts, with no coplanarity criterion imposed. Each horizontal scale is the mass value in GeV/c^2, and each vertical scale is the number of pairs per 10 MeV/c^2. 252

9.2 K° mass distributions from double muon triggered events for different z-decay and $|\Delta z|$ cuts, with a coplanarity criterion imposed. Each horizontal scale is the mass value in GeV/c^2, and each vertical scale is the number of pairs per 10 MeV/c^2. 253

9.3 Total number of K°'s, N_{K°, as a function of $|\Delta z|$ and z-decay cuts. Shown are curves for coplanar tracks and curves for non-coplanar tracks. 255

9.4 Overlay efficiency, ϵ, for tracking a K° as a function of $|\Delta z|$ and z-decay cuts. Shown are curves for coplanar tracks and curves for non-coplanar tracks. 256

9.5 Corrected number of K°'s, N_{K°/ϵ, as a function of $|\Delta z|$ and z-decay cuts. Shown are curves for coplanar tracks and curves for non-coplanar tracks. 257

9.6 K° p_t distribution from double muon triggered events shown three times for each of three different fitting functions. (a) uses Equation (9.2) as the fit, (b) uses Equation (9.3) as the fit, and (c) uses Equation (9.4) as the fit. 260

9.7 (a) N_c, (b) y_{cm}, and (c) center of mass x_f distributions for the K° from double muon triggered events. The distributions are not corrected for full spectrometer acceptance. 263

9.8 Λ° mass distributions from double muon triggered events for different z-decay and $|\Delta z|$ cuts, with no coplanarity cut imposed. Each horizontal scale is the mass value in GeV/c^2, and each vertical scale is the number of pairs per 2.5 MeV/c^2. 267

9.9 Λ° mass distributions from double muon triggered events for different z-decay and $|\Delta z|$ cuts, with a coplanarity cut imposed. Each horizontal scale is the mass value in GeV/c^2, and each vertical scale is the number of pairs per 2.5 MeV/c^2. 268

9.10 Total number of Λ°'s, N_{Λ°, as a function of $|\Delta z|$ and z-decay cuts. Shown are curves for coplanar tracks and curves for non-coplanar tracks. 270

9.11 Overlay efficiency, ϵ, for tracking a Λ° as a function of $|\Delta z|$ and z-decay cuts. Shown are curves for coplanar tracks and curves for non-coplanar tracks. 271

9.12 Corrected number of Λ°'s, $N_{\Lambda^\circ}/\epsilon$, as a function of $|\Delta z|$ and z-decay cuts. Shown are curves for coplanar tracks and curves for non-coplanar tracks. 273

9.13 Λ° p_t distribution from double muon triggered events, same plot shown three times for each of three different fitting functions. (a) uses Equation (9.10) as the fit, (b) uses Equation (9.11) as the fit, and (c) uses Equation (9.12) as the fit. 275

9.14 (a) N_c, (b) y_{cm}, and (c) center of mass x_f distributions for the Λ° double muon triggered events. These distributions are not corrected for full spectrometer acceptance. 278

9.15 $\overline{\Lambda^\circ}$ mass distributions from double muon triggered events for different z-decay and $|\Delta z|$ cuts, with no coplanarity criterion imposed. Each horizontal scale is the mass value in GeV/c^2, and each vertical scale is the number of pairs per 2.5 MeV/c^2. 282

9.16 $\overline{\Lambda^\circ}$ mass distributions from double muon triggered events for different z-decay and $|\Delta z|$ cuts, with a coplanarity criterion imposed. Each horizontal scale is the mass value in GeV/c^2, and each vertical scale is the number of pairs per 2.5 MeV/c^2. 284

9.17 Total number of $\overline{\Lambda^\circ}$, $N_{\overline{\Lambda^\circ}}$, as a function of $|\Delta z|$ and z-decay cuts. Shown are curves for coplanar tracks and curves for non-coplanar tracks. 285

9.18 Overlay efficiency, ϵ, for tracking a $\overline{\Lambda^\circ}$ as a function of $|\Delta z|$ and z-decay cuts. Shown are curves for coplanar tracks and curves for non-coplanar tracks. 286

9.19 Corrected number of $\overline{\Lambda^\circ}$'s, $N_{\overline{\Lambda^\circ}}/\epsilon$, as a function of $|\Delta z|$ and z-decay cuts. Shown are curves for coplanar tracks and curves for non-coplanar tracks. 288

9.20 The $\overline{\Lambda^\circ}$ p_t distribution from double muon triggered events, same distribution shown three times for each of three different fitting functions. (a) uses Equation (9.18) as the fit, (b) uses Equation (9.19) as the fit, and (c) uses Equation (9.20) as the fit. 290

9.21 (a) N_c, (b) y_{cm}, and (c) center of mass x_f distributions for the $\overline{\Lambda^\circ}$ from double muon triggered events. These distributions are not corrected for full spectrometer acceptance. 293

10.1 K° mass distributions from a charm enhanced sample for various z-decay and $|\Delta z|$ cuts, with no coplanarity criterion imposed. Each horizontal scale is the mass value in GeV/c^2, and each vertical scale is the number of pairs per 10 MeV/c^2. 302

10.2 K° mass distributions from a charm enhanced sample for various z-decay and $|\Delta z|$ cuts, with a coplanarity criterion imposed. Each horizontal scale is the mass value in GeV/c^2, and each vertical scale is the number of pairs per 10 MeV/c^2. 304

10.3 Λ° mass distributions from a charm enhanced sample for various z-decay and $|\Delta z|$ cuts, with no coplanarity criterion imposed. Each horizontal scale is the mass value in GeV/c^2, and each vertical scale is the number of pairs per 2.5 MeV/c^2. 306

10.4 Λ° mass distributions from a charm enhanced sample for various z-decay and $|\Delta z|$ cuts, with a coplanarity criterion imposed. Each horizontal scale is the mass value in GeV/c^2, and each vertical scale is the number of pairs per 2.5 MeV/c^2. 307

10.5 $\overline{\Lambda^\circ}$ mass distributions from a charm enhanced sample for various z-decay and $|\Delta z|$ cuts, with no coplanarity criterion imposed. Each horizontal scale is the mass value in GeV/c^2, and each vertical scale is the number of pairs per 2.5 MeV/c^2. 308

10.6 $\overline{\Lambda^\circ}$ mass distributions from a charm enhanced sample for various z-decay and $|\Delta z|$ cuts, with a coplanarity criterion imposed. Each horizontal scale is the mass value in GeV/c^2, and each vertical scale is the number of pairs per 2.5 MeV/c^2. 310

10.7 K° mass distributions from a beauty enhanced sample for various z-decay and $|\Delta z|$ cuts, with no coplanarity criterion imposed. Each horizontal scale is the mass value in GeV/c^2, and each vertical scale is the number of pairs per 10 MeV/c^2. 316

10.8 K° mass distributions from a beauty enhanced sample for various z-decay and $|\Delta z|$ cuts, with a coplanarity criterion imposed. Each horizontal scale is the mass value in GeV/c^2, and each vertical scale is the number of pairs per 10 MeV/c^2. 318

10.9 Λ° mass distributions from a beauty enhanced sample for various z-decay and $|\Delta z|$ cuts, with no coplanarity criterion imposed. Each horizontal scale is the mass value in GeV/c^2, and each vertical scale is the number of pairs per 2.5 MeV/c^2. 320

10.10 Λ° mass distributions from a beauty enhanced sample for various z-decay and $|\Delta z|$ cuts, with a coplanarity criterion imposed. Each horizontal scale is the mass value in GeV/c^2, and each vertical scale is the number of pairs per 2.5 MeV/c^2. 321

10.11 $\overline{\Lambda^\circ}$ mass distributions from a beauty enhanced sample for various z-decay and $|\Delta z|$ cuts, with no coplanarity criterion imposed. Each horizontal scale is the mass value in GeV/c^2, and each vertical scale is the number of pairs per 2.5 MeV/c^2. 322

10.12 $\overline{\Lambda^\circ}$ mass distributions from a beauty enhanced sample for various z-decay and $|\Delta z|$ cuts, with a coplanarity criterion imposed. Each horizontal scale is the mass value in GeV/c^2, and each vertical scale is the number of pairs per 2.5 MeV/c^2. 323

11.1 Estimated total cross section values for K°, Λ°, and $\overline{\Lambda^\circ}$ production for E771 data and compared to world data. 328

11.2 Differential cross section plots at zero rapidity for K°, Λ°, and $\overline{\Lambda^\circ}$ production for E771 data and compared to world data. 330

11.3 Plots of the various quantities measured for K° production as a function of increasing trigger complexity. 332

11.4 Plots of the various quantities measured for Λ° production as a function of increasing trigger complexity. 334

11.5 Plots of the various quantities measured for $\overline{\Lambda^\circ}$ production as a function of increasing trigger complexity. 336

Chapter 1

Introduction

This dissertation will study the characteristics observed in the decays of the $K_s^\circ \rightarrow \pi^+\pi^-$ and $\Lambda^\circ \rightarrow p\pi^-$ ($\overline{\Lambda^\circ} \rightarrow \overline{p}\pi^+$) at 800 GeV/c fixed target beam momentum. Such studies have not been performed at a beam energy this high. The thesis will compare what is observed at this energy to that from a previous era (bubble chamber era), it will compare cross section results, and it will look at the enhanced production of neutral strange particles when $c\overline{c}$ and $b\overline{b}$ enhanced events are studied. The intent of the study of K° and Λ° production is to incorporate it into E771's main focus, the pursuit of B physics and CP violating modes.

1.1 Theory

The following sections will cover the theoretical aspects of the study of B physics and CP violation. The relevant decay processes via quark exchanges will be discussed.

1.1.1 Standard Model

According to the well known Standard Model of elementary particles (summarized in Figure 1.1), all matter falls into three classification schemes: the quarks, the leptons, and the gauge bosons. The quarks contain charges of +2/3 and -1/3. For example, the flavored quarks, the up (u), charm (c), and top (t) quarks are of positive charge, whereas the down (d), strange (s), and bottom (b) quarks are of the negative charge. The anti-quarks have opposite sign. Most everyday matter is made up of protons and neutrons, which are in turn made up of the up and down quarks. Our study will involve the use of the less frequently occurring quarks. The six leptons are the e and the ν_e, the μ and the ν_μ, and the τ and ν_τ. Similarly, there exist six anti-leptons.

There are four forces found in nature governing the interactions, and they include the strong, the electromagnetic, the weak, and the gravitational. Sometimes they are referred to the three forces with the electromagnetic and weak combined into the electroweak force. Each of these forces has its own mediator, the gluon belonging to the strong force, the photon to the electromagnetic force, the $W^{\pm}$ and Z to the weak force, and the graviton to the gravitational force. These mediators are the ones that transmit a force between a quark or lepton to another quark or lepton. The strong force has the most "strength", decreasing in strength in order to the weakest one of gravity.

The strong interaction is described by *Quantum Chromodynamics* and is one of the components of the SU(3) $\times$ SU(2) $\times$ U(1) of the Standard Model. It is the force that holds atomic nuclei together. A single quark of a specific flavor

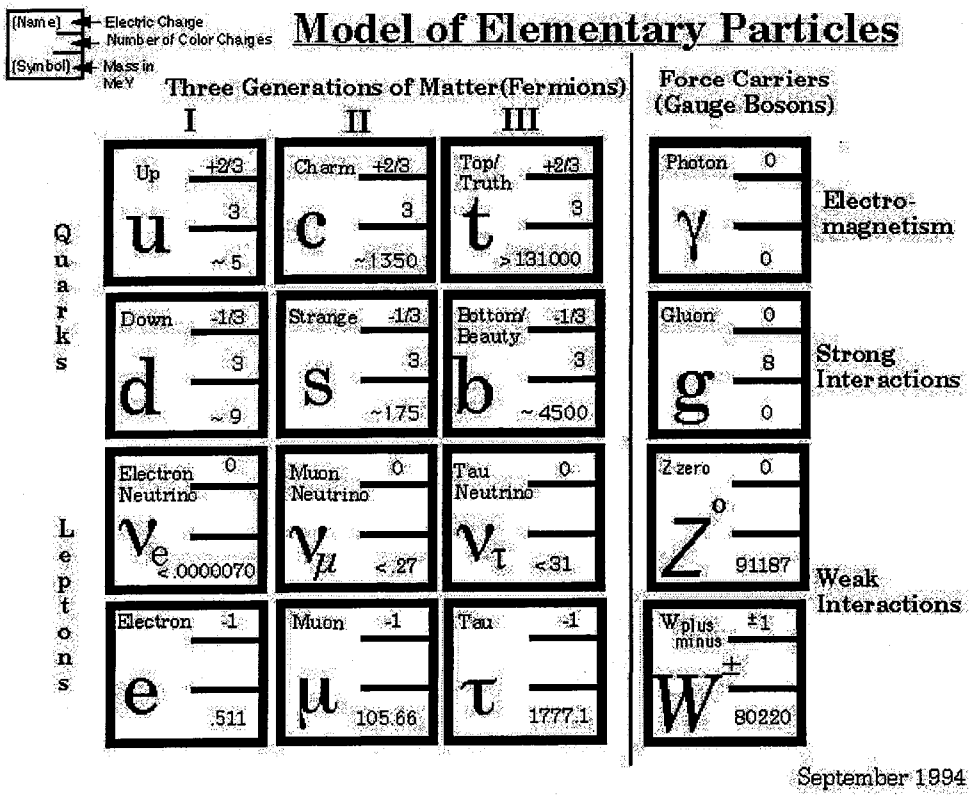

Figure 1.1: The Standard Model.

may come in three colors. The SU(3) symmetry group has 8 gluons (massless mediators). This force allows for the transition of quarks into hadrons.

The electromagnetic interaction is described by *Quantum Electrodynamics* and its force is carried by the mediating massless photon and is represented by the U(1) symmetry group. The weak interaction is described by the SU(2) symmetry group and is responsible for nuclear β decays. Its force is mediated by the $W^{\pm}$ and Z°, massive intermediate vector bosons. A gauge theory unifying the electromagnetic and weak interactions was proposed in 1967 by Salam, Weinberg, and Glashow [1]. In this theory, named the *Electroweak* theory, the forces obey the SU(2) $\times$ U(1) gauge symmetry, the spontaneously broken symmetry group.

1.1.2 Mesons and Baryons From Quarks

Quarks have spin 1/2 and may be used to form mesons or baryons. A meson is a bound state of a quark (q) and an antiquark ($\overline{q}$) (their flavors do not necessarily have to be the same). A baryon is a three quark state, and each state is a SU(3) color singlet. Mesons are classified as bosons (integral spin particles), and baryons are classified as fermions (1/2 integral spin particles).

1.1.3 Decay of Charm and Beauty

The K° and Λ° are classified as *strange* particles. This is due to the fact that strange particles are produced in abundance on a time scale of order 10^{-23} sec which implies the strong interaction process, yet these particles themselves decay by the weak interaction process of order 10^{-10} sec. Pais [2] noted this phenomenon and also noted that strange particles should be produced in pairs, e. g. ,

$$p + \pi^- \rightarrow K^\circ + \Lambda^\circ,$$

but not individually. The K° has strangeness S=1, and the Λ° has strangeness S=-1. Since these particles decay by the weak interaction, strangeness is not conserved.

To get an idea of how these decays occur, the Feynman diagram of $K_s^\circ \rightarrow \pi^+\pi^-$ is depicted in Figure 1.2. The K_s° is composed of a d quark and $\overline{s}$ quark. It decays by the electroweak mechanism through the change of the $\overline{s}$ quark to the $\overline{u}$ quark with the emission of a W^+ that decays to a (u$\overline{d}$) pair. The d quark of the K° decay plays the part of the "spectator" quark. Its role is simply to go along for the ride since, although the Cabibbo mechanism (to be discussed below) favors the transition from the d quark to a u quark, Fermi's Golden Rule [3] takes into account not only the matrix element (which is a constant), but the phase space as well. The $\overline{s}$ quark, being more massive than the d quark has a greater phase space, therefore the d quark is more likely to remain the spectator.

The Cabibbo-Kobayashi-Maskawa (CKM) [4] mixing matrix is part of a theory which relates the quark mass eigenstates to the weak eigenstates for the six quarks. This theory generalized that of Cabibbo's [5] four quark states. It states that via conventional methods the u, c, and t quarks (all +2/3 charge) are unmixed. The mixing may then be expressed by a 3×3 unitary matrix V operating on the d, s, and b quarks (all -1/3 charge). It is expressed in the following form:

$$\begin{pmatrix} d' \\ s' \\ b' \end{pmatrix} = \begin{pmatrix} V_{ud} & V_{us} & V_{ub} \\ V_{cd} & V_{cs} & V_{cb} \\ V_{td} & V_{ts} & V_{tb} \end{pmatrix} \begin{pmatrix} d \\ s \\ b \end{pmatrix}. \tag{1.1}$$

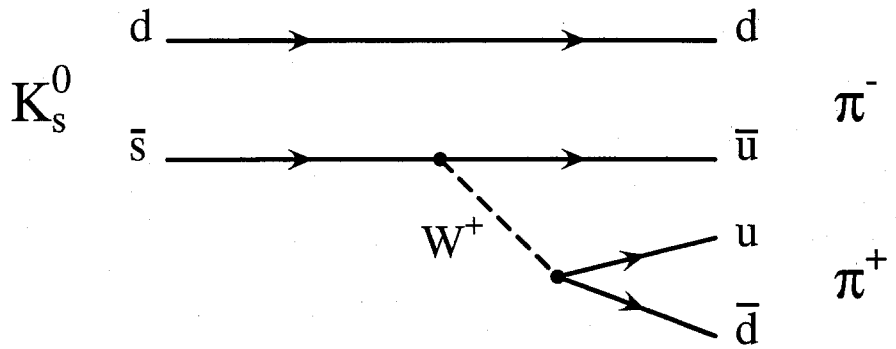

Figure 1.2: The Feynman Diagram decay of the $K_s^\circ \rightarrow \pi^+\pi^-$. The K_s°, composed of a $d\bar{s}$ quark pair decays to the $d\bar{u}$ pair and a $u\bar{d}$ pair by the emission of a W^+ boson.

The values of the V_{xx} elements may be determined by weak decays of the relevant quarks. With the assumption that we are working with only three quark generations, and assuming a confidence level of 90%, we obtain limits on the matrix elements to be [6]:

$$\begin{pmatrix} 0.9747 - 0.9759 & 0.218 - 0.224 & 0.002 - 0.005 \\ 0.218 - 0.224 & 0.9738 - 0.9752 & 0.032 - 0.048 \\ 0.004 - 0.015 & 0.030 - 0.048 & 0.9988 - 0.9995 \end{pmatrix}. \tag{1.2}$$

The non-leptonic decay of the Λ-hyperon (uds) quark content to a p and π^- (shown in Figure 1.3) involves the change of the s quark to a u quark and, by the mediating W^- boson, the ($d\bar{u}$) quarks. The original u and d quarks remain the spectator quarks in the Λ° decay. Following the same argument outlined in the decay mode for the K_s°, the s quark's decay activity supersedes those of the less massive u and d quarks.

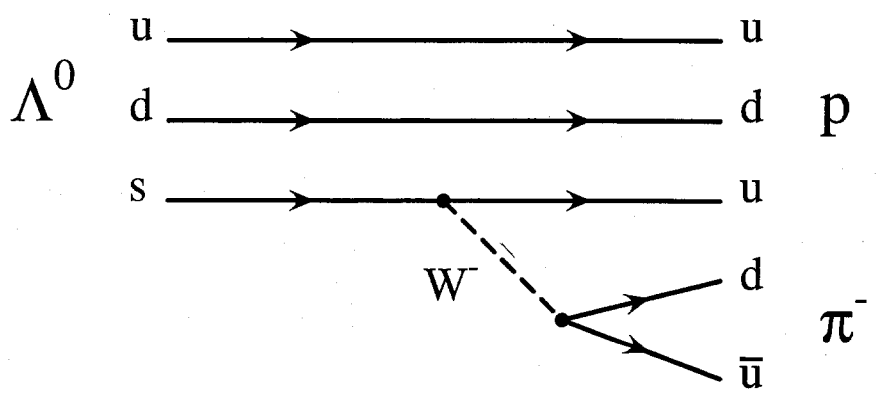

Figure 1.3: Decay of $\Lambda^\circ \rightarrow p + \pi^-$.

The J/ψ was discovered in November 1974 by two independent experiments, one at the Stanford Linear Accelerator Collider [7] and the other at the Brookhaven National Laboratory [8]. Because two groups simultaneously discovered this particle, two names were applied to it, the J by the Brookhaven group and the ψ by the SLAC group. Hence, it is commonly referred to as the J/ψ. One of the main features of E771's objective was to study B physics through the decay mechanism of the $J/\psi \rightarrow \mu^+\mu^-$. Due to its narrow mass width, the J/ψ was known to be the lowest bound state of a newly discovered quark and antiquark, $c\bar{c}$. This type of quark had previously been postulated by Glashow, Iliopoulos, and Maiani [9] in 1970. This charmed quark, like the strange quark, had assigned to it a quantum number C (Charm) which obeyed conservation in strong and electromagnetic interactions. Since $M_{J/\psi} < 2M_D$, where D is a charmed meson, the decay channel of the J/ψ into $D\overline{D}$ would not be allowed since it would violate energy conservation. The other decay channel it could follow would be from a strong decay to two mesons by three gluons. This too is not observed since it is suppressed by the OZI

Rule [3]. Therefore, as depicted in Figure 1.4, the J/ψ proceeds to decay by the electromagnetic interaction.

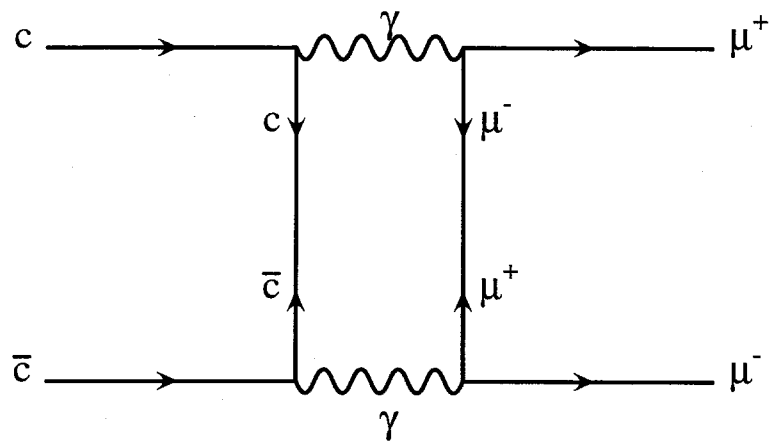

Figure 1.4: Decay of $J/\psi \rightarrow \mu^+ + \mu^-$.

Kaons play an important role in the decay of the B meson since the most frequent production mechanism is the quark decay chain $b \rightarrow c \rightarrow s$. As E771 was designed to study the decay of beauty mesons, one of the decay mechanisms would have been the exclusive decay mode of $B_d^\circ \rightarrow J/\psi + K_s^\circ$, shown in Figure 1.5. The branching ratio for observing this decay mode is 3.2×10^{-4} with 0.686 for the exclusive decay of $K_s^\circ \rightarrow \pi^+\pi^-$ to yield a composite branching ratio of 1.3×10^{-5} for the sequence $B_d^\circ \rightarrow J/\psi + K_s^\circ \rightarrow \mu^+\mu^- + \pi^+\pi^-$. Several examples of b mesons decaying into J/ψ's were found in E771 using a di-muon trigger.

Another likely decay of a b quark would be the observation of $\Lambda_b \rightarrow J/\psi + \Lambda^\circ \rightarrow \mu^+\mu^- + p\pi^-$, as shown in Figure 1.6. In this process, the J/ψ would provide a relatively clean mass spectrum when the di-muon trigger is imposed, and the decay of the $\Lambda^\circ \rightarrow p\pi^-$, with its high branching ratio of 64.1% and relatively

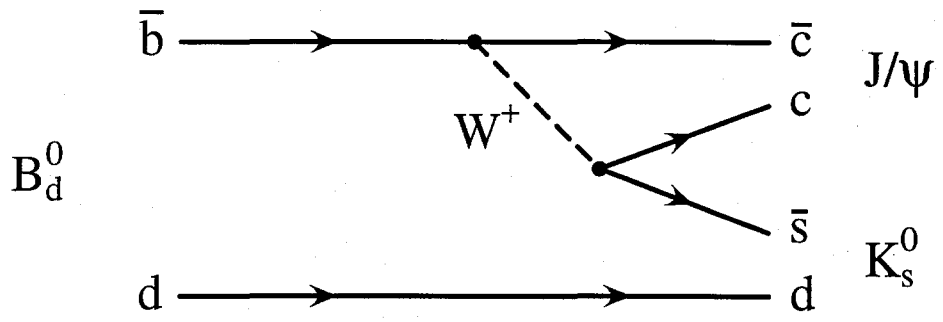

Figure 1.5: Decay of $B_d^\circ \rightarrow J/\psi + K_s^\circ$.

long lifetime, would provide a good signal. In practice one would reconstruct J/ψ events, and from this set search for the Λ° decays. A final search for Λ_b° would be made in events containing both J/ψ and Λ° decays. Given the fact that a clean J/ψ spectrum was obtained and that the Λ° decay was observed, a limit on the cross section times the branching ratio for the Λ_b could have been obtained. The Λ_b has been observed at UA1 [10] with a product of the production fraction and branching ratio determined to be

$$f_{\Lambda_b} BR(\Lambda_b \rightarrow J/\psi + \Lambda^\circ) = (1.8 \pm 1.0) \times 10^{-3}.$$

1.2 History of Neutral Strange Particle Production

The inclusive neutral strange particle production in high energy pp collisions was exhaustively studied during the bubble chamber era at Fermilab with the predominant use of the 30 inch liquid hydrogen bubble chamber as well as the Fermilab 15 foot bubble chamber for the energy region of 12.4 to 405 GeV/c [11]. Concrete trends in the energy dependence of these cross sections have been established,

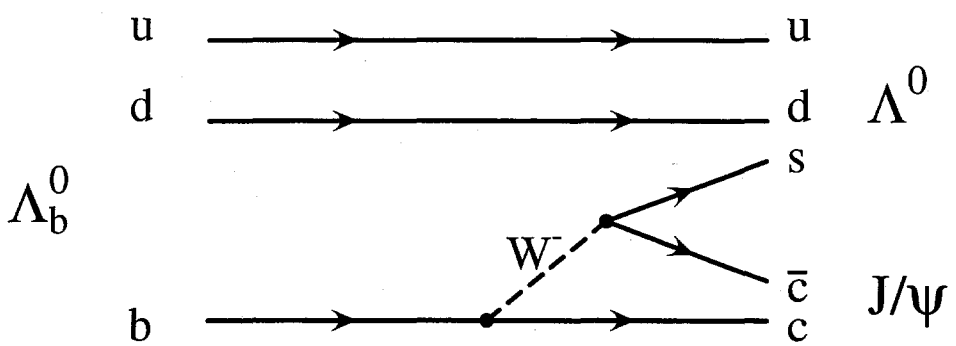

Figure 1.6: Decay of $\Lambda_b^\circ \rightarrow J/\psi + \Lambda^\circ$.

namely, the K° and $\overline{\Lambda^\circ}$ production increased rapidly with increasing beam momentum and occurred predominantly in the central region. The Λ° production was observed to have been a constant when the beam momentum was below 69 GeV/c, and increased slowly with beam momentum above 69 GeV/c, and its main contribution came from fragmentation processes. Because most of these observations occurred with the 30 inch bubble chamber, most production processes were only observable in the backward hemisphere of the center-of-mass system.

Neutral strange particles are produced from the sea of $s\bar{s}$ quarks, according to models for a non-strange initial state [12]. Particles with non-zero strangeness can be formed only as a result of the sea $s\bar{s}$ quark pair production and their subsequent hadronization into states with open strangeness. With a proton beam hitting different nuclear targets, these targets may serve as a form of observing the space-time evolution of hadronic interactions on a small distance scale. With a silicon target having been used in E771, cross sections and relevant characteristics of neutral V's may be observed and studied, and an attempt may be made to

determine whether the interaction of protons with nuclei yield large cross sections for strange particle production.

This thesis will devote a considerable amount of attention to these past studies and will be used to ask correlating questions such as, do the cross sections remain constant for increasing beam energy, or do new characteristic behaviors appear? An attempt will be made to answer these kinds of questions and others like it. No literature has been produced on the study of neutral strange particle production at beam momenta of 800 GeV/c for fixed target runs, so this will be an attempt to continue the study of neutral strange particle production at higher beam momenta.

Chapter 2

Experimental Setup

2.1 E771 Main Objective

Experiment 771 (E771) was a fixed target experiment dedicated to the search of B - mesons through the double muonic decays of

$$B \rightarrow J/\psi + X \rightarrow \mu^+\mu^- + X$$

or through the semi-leptonic decays of

$$B \rightarrow \mu^\pm + X.$$

E771's stated main objectives were to measure the total cross section for B-meson production, to determine charged and neutral B-meson lifetimes, to observe $B\overline{B}$ mixing, and, ultimately, to observe CP violation. This experiment accumulated physics data during the 1991-1992 fixed target run for an approximate five week period from the first week of December 1991 to the end of the first week in January 1992.

2.2 Fermilab Layout

E771 was run at the Fermi National Accelerator Laboratory (FNAL). Fermilab, located about 35 miles west of Chicago, is situated on a natural prairie. Figure 2.1

is a graphic depiction of the lab's physical layout, and Figure 2.2 is an aerial view of the lab.

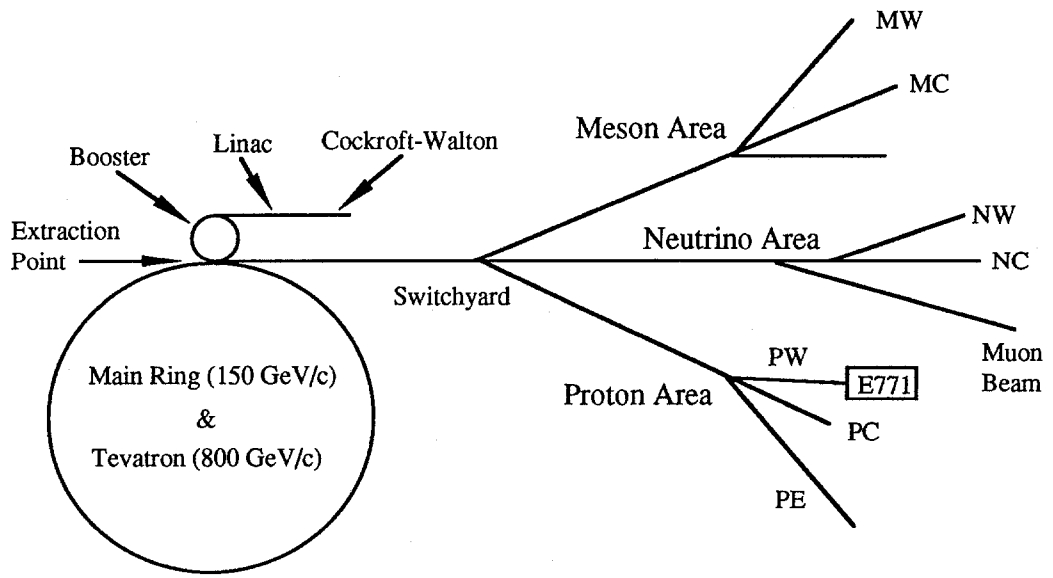

Figure 2.1: FNAL layout.

Before considering a proton beam in the fixed target line, one should observe how the proton beam is made. The journey begins with a device called the Cockroft-Walton accelerator. This device adds electrons to pre-existing hydrogen gas atoms giving them two electrons and one proton (forming negative ions). These are attracted to a positive voltage and accelerated to 750 keV. After exiting the Cockroft-Walton accelerator, the negatively charged ions head down the linear accelerator, the Linac (500 feet in length), increasing in energy to 200 MeV and passing through a carbon foil which strips the electrons. Only the protons remain. The protons continue their journey into the Booster, a rapid cycling synchrotron 500 feet in diameter. Here the protons travel around the Booster about 20,000

times in order to increase their energy to 8 GeV. During this repeated circular motion the protons feel the repeated action of the accelerating electric fields which raise their energy. Once the protons have reached their 8 GeV energy level, they are then sent to the Main Ring, another circular synchrotron 4 miles in circumference, which accelerates the protons to 150 Gev. They are then sent "down" to the Tevatron, housed in the same area beneath the Main Ring. The Tevatron can then accelerate the protons to their final energy of 800 GeV. Unlike the conventional magnets used in the Main Ring, the Tevatron is comprised of superconducting magnets which operate in the temperature range of liquid helium (-450° F).

For our fixed target experimental run mode, the proton beam was extracted from the main ring and sent to its respective beamlines. E771 was located at the High Intensity Laboratory (HIL - PW8) along the Proton West (PW) beamline. Before the beam arrived at PW8, it was steered along the beam pipe by dipole magnets, and quadrupole magnets were used to keep the beam in focus. The beam position and spot size were monitored with Segmented Wire Ionization Chambers (SWICs), and the beam intensity was monitored with secondary emission monitors (SEMs). The proton west beamline leading up to PW8 is depicted in Figure 2.3. The main accelerator delivered the beam particles in packets of 2 ns "buckets" each spaced at equal time intervals. Each bucket period was about 18.9 ns which corresponded to the accelerator RF of 53.1 MHz.

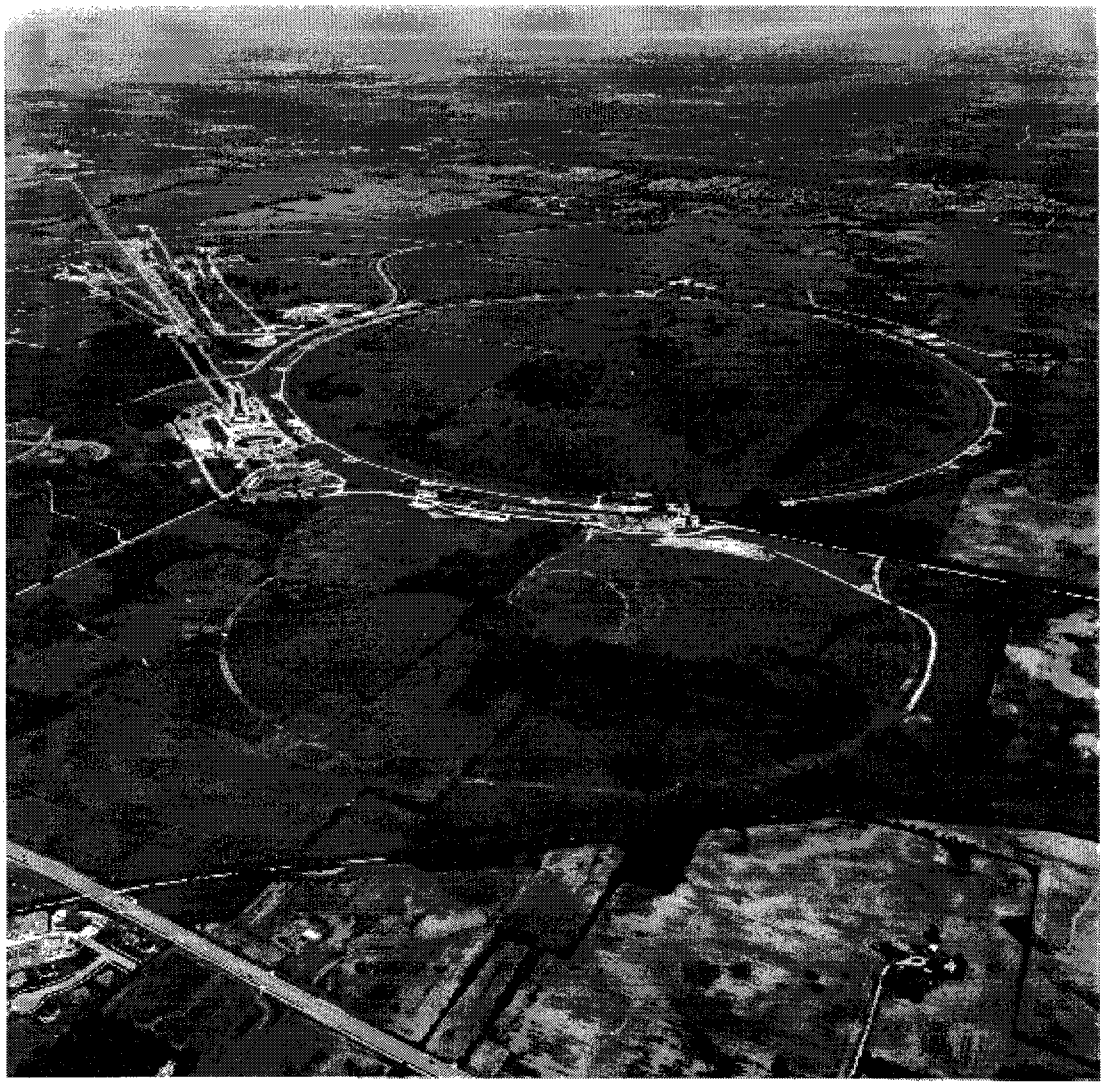

Figure 2.2: An aerial view of Fermilab. The main injector is seen in the foreground, and the main ring is seen in the background. The High Rise is located to the left of the main ring, and the fixed target lines are located further in the background relative to the High Rise.

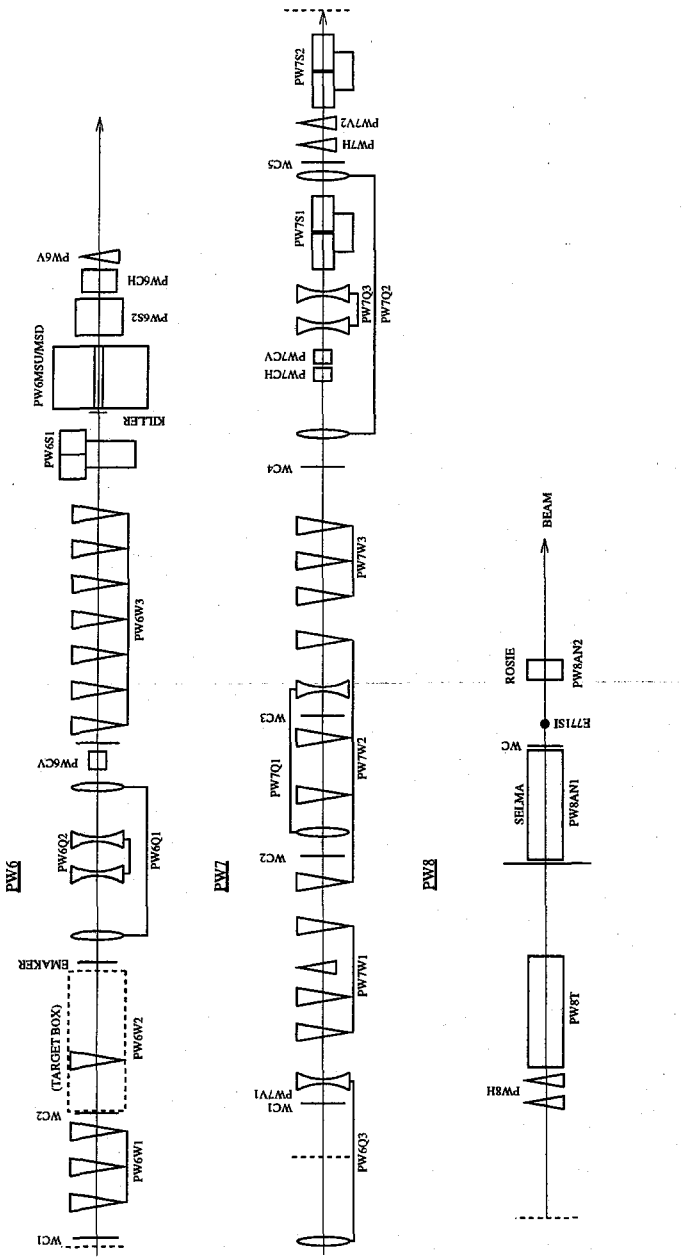

Figure 2.3: Proton West beamline septa.

2.3 E771 Spectrometer Layout

This section will cover the specifics of E771's operational mode. Before getting into the details, a coordinate system needs to be set up. For our purposes, the + z-axis will be along the beam direction (pointing north - downstream). The y-axis runs in the "upward" direction, which means the x-axis runs along the horizontal, in the west direction. The origin of this coordinate system is in the middle of the analyzing magnet, ROSIE. The spectrometer itself covered a total distance of approximately 27 meters and is shown in Figure 2.4.

E771 was an upgrade to the previous experiments, E537 and E705, which were devoted to charmonium. The main added features were the silicon target and silicon microvertex detector, extra wire chambers with pad readout capabilities, and the Resistive Plate Counters (RPCs). Table 2.1 summarizes E771's run conditions.

The description of E771 will be broken down into 9 specific categories, which follow.

2.3.1 The Beam and Halo Veto Counters

As described earlier, the beam being sent to PW8 was kept in focus and attempts were made to retain an ideal spot size. Even in the most ideal situation with the beam traversing through the vacuum, the protons would sometimes interact with some impurities in the vacuum, and this in turn would cause the creation of unwanted particles. In order to prevent these unwanted particles (referred to as halo particles) from being introduced in E771's detector, beam and halo veto

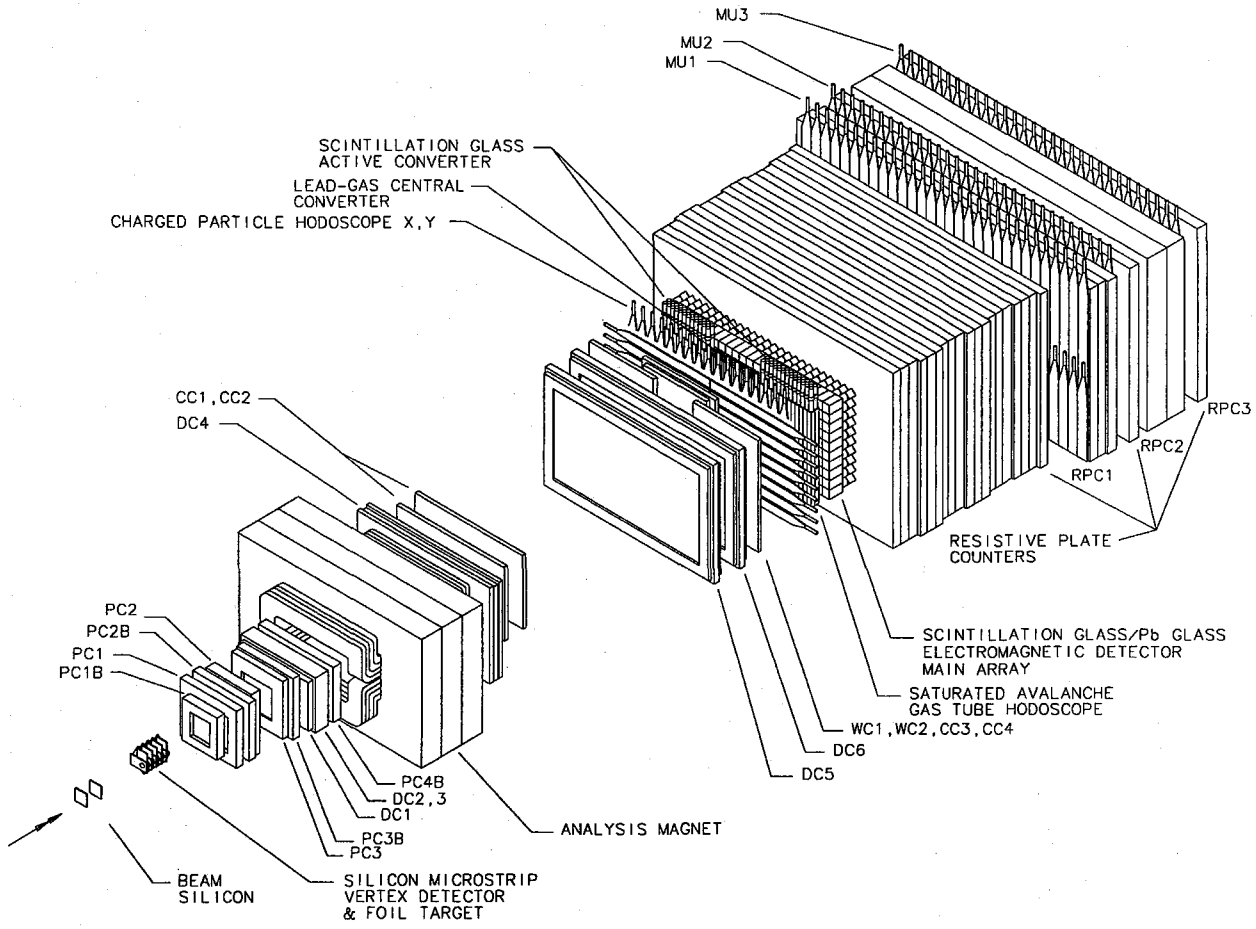

Figure 2.4: E771 spectrometer.

Run Conditions	1991 Run
Proton Beam Momentum	800 GeV/c
Spill Length	$\sim$ 22 sec. every 57 sec.
Target	2 mm Si foils (12)
Target Radiation Length	25.66%
Target Interaction Length	5.28%
Average Interactions/Second in Target	1.9 $\times 10^6$
Beam protons/Second	3.6 $\times 10^7$
Beam size σ_x, σ_y	2.3 mm, 1.8 mm

Table 2.1: E771 run conditions.

counters were needed. In order to reject these halo particles, scintillator counters were placed at specific intervals upstream of the main target. The veto system [13] consisted of multiple sets of scintillator counters.

The furthest set of veto counters was located 11.8 meters upstream of the main target. This set of veto counters was termed the VX-I veto counter and encompassed an area of 203 $\times$ 80 in^2, with an 11 inch gap for the beam pipe. Looking downstream, in the northerly direction, 6 scintillator counters, each 10$\times$58 in^2, were to the east of the beam pipe, another identical six scintillator counters, were located to the west of the beam pipe, with an additional 10 (72 $\times$ 80 in^2) scintillator counters mounted on a movable hinge. The added counters to the west of the beam pipe were due to the curvature of the PW beamline.

The next set of veto counters was located 2.75 m upstream of the main target. These were termed the VY counters and contained a total of 16 horizontally positioned counters. Eight of these were located to the east of the beam pipe and the other eight were located to the west of the beam pipe. The inner eight counters were each of dimension $41 \times 5\ in^2$ and the outer eight counters (four on top and four on bottom) were each of $41 \times 10\ in^2$. The innermost 4 counters of the 8 inner counters were offset horizontally by $3.5 \times 10\ in^2$ in order to accommodate the beam pipe dimensions.

The last set of veto counters, measuring a total area of $40 \times 62\ in^2$, was located 2.65 m upstream of the main target. This set of VX-II counters consisted of 10 scintillator counters, the outer 2 of which measured $10 \times 62\ in^2$. The other eight counters each measured $5 \times 31\ in^2$, with the innermost four counters displaced in the vertical direction to allow for a $10 \times 3.5\ in^2$ hole opening for the beam pipe.

Right next to this last set of veto counters, positioned closest to the main target, was a single counter V1/V2 with a hole 2 in in diameter for passage of the beam. The veto counter had two independent photomultiplier tubes attached at either end in order to produce increased efficiency. The physical layout of the beam halo veto counters is shown in Figure 2.5.

2.3.2 The Main Target and Beam Silicon

A few centimeters upstream of the main target lay the silicon beam chambers and the precision beam planes. These were used to observe the exact location of the beam relative to its interaction in the target and to measure the beam flux.

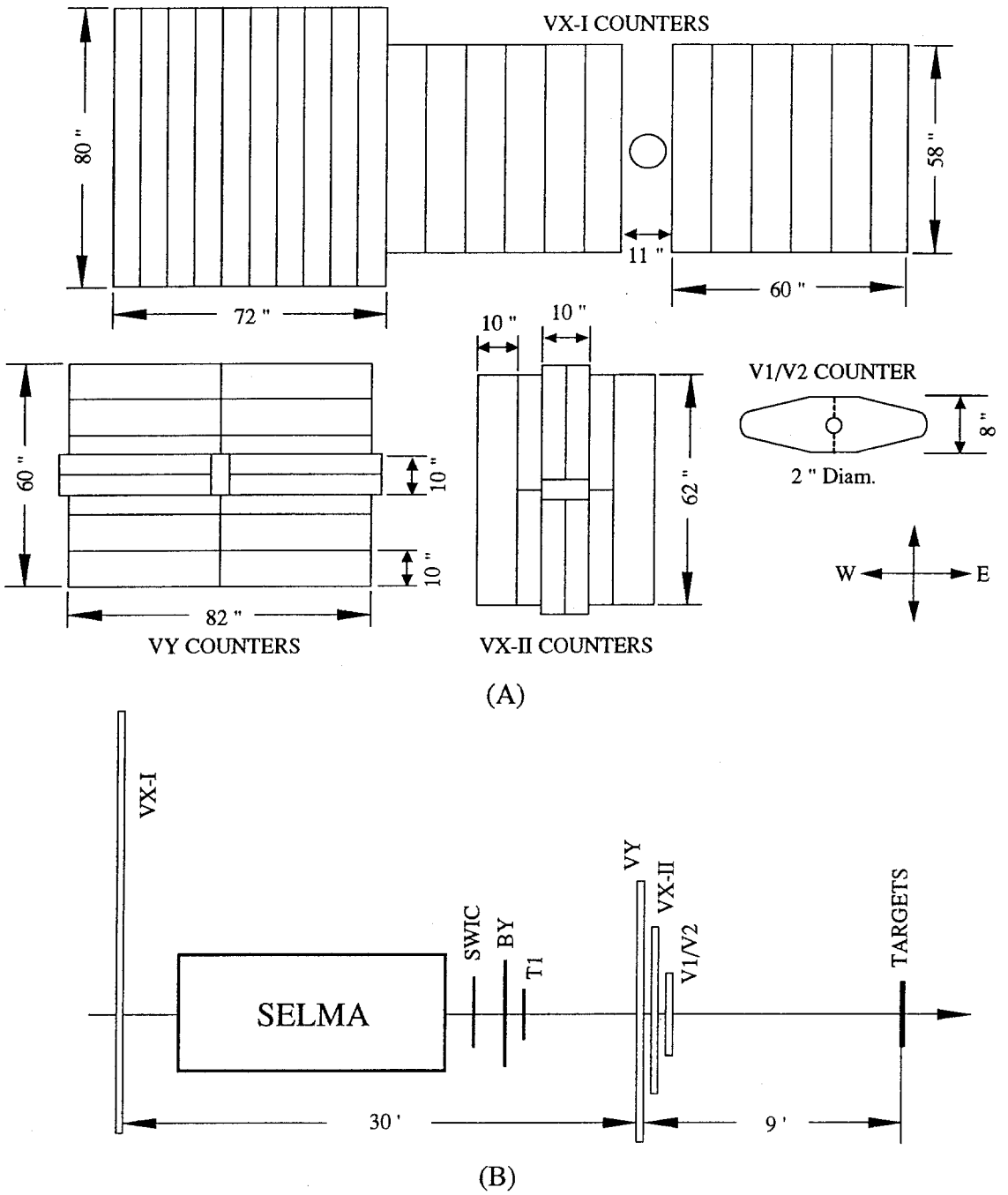

Figure 2.5: E771 beam halo set up. (A) shows a beam's eye view of the scintillators, and (b) shows a top view of the location of the counters with respect to the main target.

The main target system used in E771 consisted of 12 silicon foil disks each 2 mm thick and 5.08 cm in diameter with an air gap spacing of 4 mm between each foil. The air gap spacing allowed for the observation of particle decays. With a total target volume of 47.1 cm^3 and total target mass of 109.74 g, the silicon target had a length, λ_I, of 5.6 g/cm^2. With the nuclear interaction length for Si of 106.0 g/cm^2 and a radiation length of 21.82 g/cm^2 [14], this represented 5.28% of a nuclear interaction length and 25.66% of a radiation length.

Silicon was chosen as the main target for this B-meson fixed target experiment due to its relatively large radiation length which reduced the chances of observing unwanted photon conversions and its short interaction length to allow for the observation of decays in the air gaps between each foil. It was also desirable in the sense of using the linear A dependence of B production cross sections, which would yield a higher B-meson rate in a heavier nucleus.

2.3.3 The Silicon Microstrip Vertex Detector

The silicon microstrip vertex detector (SMVD) [15] consisted of 14 tracker planes, with the first tracker plane located 5 mm downstream of the last silicon target foil. The total dimensions of the SMVD measured $5 \times 5 \times 10$ cm^3. Each tracker station had 2 or 3 planes that had a spacing of 4 mm between planes and 2 cm between stations. Micron Semiconductor Ltd. designed the L and K planes and Hamamatsu designed the B planes for E771's purposes. The B-type planes encompassed an area of 2.8×2.8 cm^2 and were segmented into 112 strips, each strip 2.8 cm long and having a 250 μm pitch. The L-type planes had 384 15 μm

strips situated on a 25 μm pitch in the center with 304 25 μm strips on 50 μm centers located at the edges, and this comprised a total of 688 channels per plane. The K-type plane had 25 μm strips with a 50 μm pitch at the center and 75 μm wide strips on 100 μm centers located on the edges, and this comprised a total of 688 channels per plane.

Some planes (x-planes) had strips parallel to the y-axis, others (y-planes) had strips parallel to the x-axis. There also existed U and V planes that were located $\pm$ 45° with respect to the x or y planes and were of K-type silicon wafers. The thickness for all detector planes was 300 $\pm$ 5 μm. The following table (Table 2.2) summarizes the SMVD properties.

Plane Type	Thickness (μm)	Number Strips	Strip Pitch (μm)	Strip Active Length (cm)	Plane Active Width (cm)
B	200	112	250	2.8	2.8
L	300	688	25/50	3.5	2.48
K	300	688	50/100	4.96	4.96

Table 2.2: E771 silicon plane tracker parameters.

An intricate, detailed layout of the silicon targets and the silicon tracker is shown in Figure 2.6.

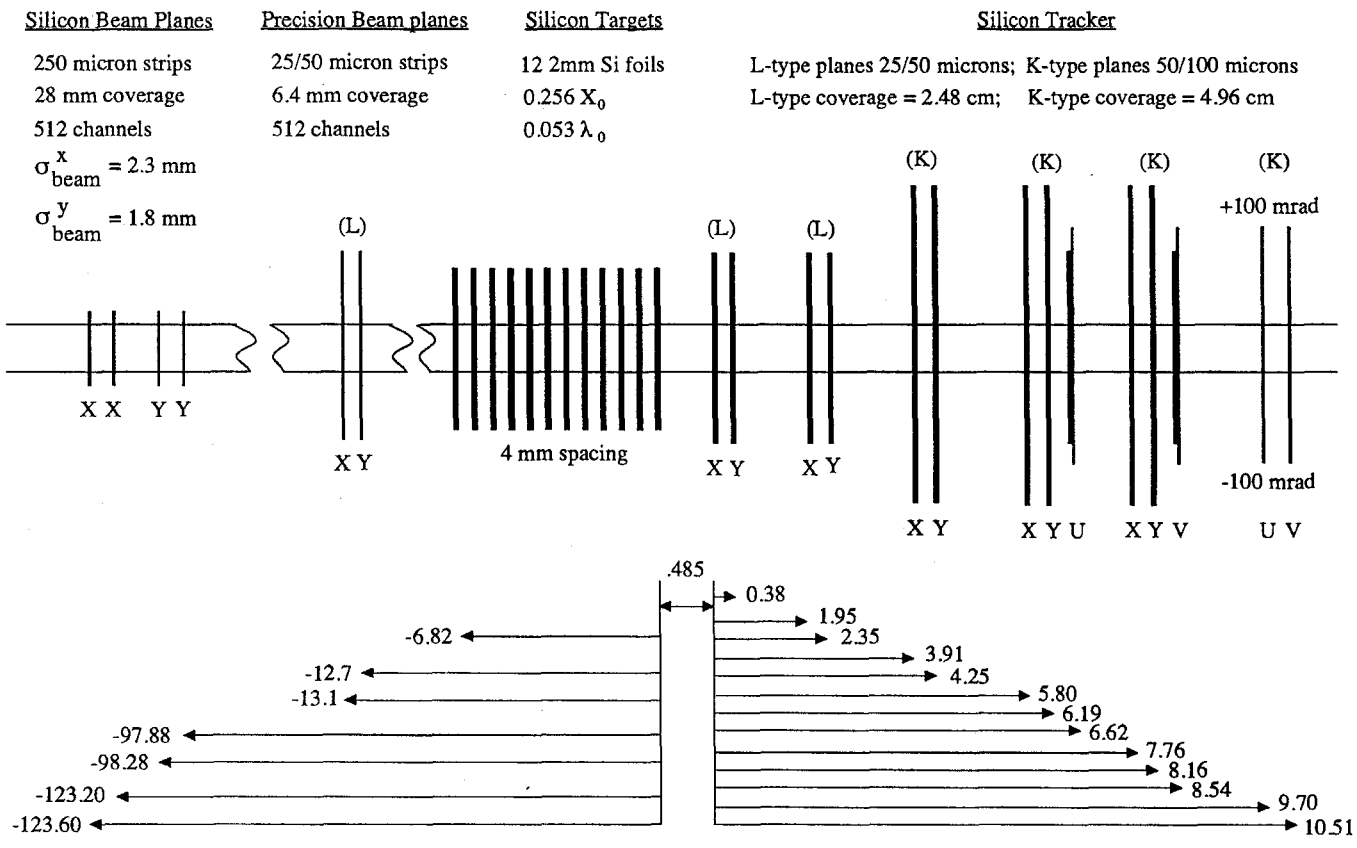

Figure 2.6: E771 precision beam planes, silicon target, and silicon tracker.

2.3.4 The Front Tracking Chambers

For our intents and purposes, the *front tracking chambers* are defined as those chambers upstream of the analysis magnet, ROSIE. The *rear tracking chambers* are defined as those chambers downstream of the analysis magnet.

The front tracking chambers can be segregated into three groups for purposes of explicit descriptions:

- The 4 PCB chambers.
- The 3 PC chambers.
- The 3 drift chambers.

There were 4 Beam Proportional Counter chambers (termed PCB1 through PCB4) that encompassed the smallest angular region of the 3 sets of front chambers and were designed to track those interactions that traversed at a near parallel direction to the beam hole region. These chambers had a small deadened central region in order to protect them from a high flux of non-interacting beam tracks. The deadened region was achieved by silver flash-coating the wires with a 98% Cu/1.85% Be mixture which reduced the electric field due to an increased wire diameter. The anode sense wires consisted of gold plated tungsten/rhenium wires held at a positive high voltage spaced midway between the ground cathode planes that were made from an evaporated gold film of thickness 1200 $\AA$ on 25.4 μm capton. The gas mixture used in the PCBs consisted of a "magic gas" ratio of 72.5% argon, 23% isobutane, 4% methylal, and 0.5% freon 13B1. This mixture was bubbled through ethanol at a constant temperature of 0° C. The active region

of PCB1 encompassed an area of $13.2 \times 30\ cm^2$, that of PCB2 encompassed an area of $16.0 \times 40.0\ cm^2$, that of PCB3 encompassed an area of $16.0 \times 50.0\ cm^2$, and that of PCB4 encompassed an area of $16.0 \times 50.0\ cm^2$. The physical characteristics of these chambers consisted of plane views in the X, U, and V directions. The X view was projected along the bend projection for the analysis magnet with vertical sense wires. The U and V views were the "stereo" views at angles of $\pm$ 28.1°, respectively, with respect to the positive y axis. These 3 plane views allowed for track reconstruction in 3-dimensional space. The signals from these chambers were amplified by Nanometric N-277D amplifiers and were "Sippach" latched by custom made latches for E771's purposes. The physical parameters of the PCBs are laid out in detail in Table 2.3.

There were three sets of large Proportional Chambers used in the front tracking part of E771's run. These chambers encompassed a much greater area than did the beam chambers for their purpose was to aid in the tracking of larger opening angle particles. The active areas covered by PC1, PC2, and PC3 were $53.29 \times 20.0\ cm^2$, $72.34 \times 39.0\ cm^2$, and $102.4 \times 50.0\ cm^2$, respectively. Accordingly, they had a greater dead central beam region. The U and V stereo views were situated at angles of $\pm$ 16.7°, respectively, with respect to the positive y axis. The gas mixture used in the PC chambers consisted of 72.5% argon, 23% isobutane, 4% methylal, and 0.5% freon. This gas mixture was bubbled through ethanol at a constant temperature of 5° C. Gold plated tungsten wires were used for the sense wires which were positioned midway between the cathode wire planes. The upstream and downstream planes of the sense wires were grounded. The signals

Plane	View	Angle from Y-Axis (deg)	Number of Wires	Z Position (cm)	Wire Spacing (cm)	Wire Length (cm)	Deadened Region (cm^2)	Resolution (μm)	Efficiency
PCB1	V	-28.1	176	-466.15	0.0750	30.0	1.50×1.50	217.0	0.93
PCB1	X	0.0	176	-465.55	0.0750	30.0	1.50×1.50	217.0	0.95
PCB1	U	28.1	176	-464.95	0.0750	30.0	1.50×1.50	217.0	0.94
PCB2	V	-28.1	160	-425.06	0.1000	40.0	1.50×1.50	289.0	0.93
PCB2	X	0.0	160	-424.46	0.1000	40.0	1.50×1.50	289.0	0.88
PCB2	U	28.1	160	-423.86	0.1000	40.0	1.50×1.50	289.0	0.93
PCB3	V	-28.1	160	-284.25	0.1000	50.0	1.50×1.50	289.0	0.87
PCB3	X	0.0	160	-283.65	0.1000	50.0	1.50×1.50	289.0	0.92
PCB3	U	28.1	160	-283.05	0.1000	50.0	1.50×1.50	289.0	0.91
PCB4	V	-28.1	160	-196.91	0.1000	50.0	1.50×1.50	289.0	0.92
PCB4	X	0.0	160	-196.31	0.1000	50.0	1.50×1.50	289.0	0.89
PCB4	U	28.1	160	-195.71	0.1000	50.0	1.50×1.50	289.0	0.91

Table 2.3: E771 front chamber tracking parameters for the PCB chambers. (Note: The z-positions are with respect to the center of the analysis magnet.)

from these chambers were amplified by Nanometric N-277D amplifiers and were latched by Nanometric N-278 latch units. The physical characteristics of the PCBs are detailed in Table 2.4.

The last set of chambers consisted of the 3 Drift Chambers. Like the PC chambers, these too encompassed a greater area than the PCB chambers. DC1 was mounted on its own frame, while DC2 and DC3 shared the same mount. The planes of these chambers encompassed an active area of 115.20×50.80 cm^2 for DC1, 118.10×50.80 cm^2 for DC2, and 116.84×50.80 cm^2 for DC3. Each drift chamber had 3 planes which consisted of alternating anode wires and cathode field

Plane	View	Angle from Y-Axis (deg)	Number of Wires	Z Position (cm)	Wire Spacing (cm)	Wire Length (cm)	Deadened Region (cm^2)	Resolution (μm)	Efficiency
PC1	X	0.0	352	-447.18	0.1514	29.0	2.54×2.54	437.0	0.41
PC1	V	-16.7	348	-445.91	0.1514	29.0	2.54×2.54	437.0	0.43
PC1	X	0.0	352	-444.64	0.1514	29.0	2.54×2.54	437.0	0.40
PC1	U	16.7	349	-443.37	0.1514	29.0	2.54×2.54	437.0	0.55
PC2	U	16.7	480	-375.76	0.1507	39.4	5.08×5.08	435.0	0.84
PC2	X	0.0	480	-374.49	0.1507	39.4	5.08×5.08	435.0	0.88
PC2	V	-16.7	480	-373.22	0.1507	39.4	5.08×5.08	435.0	0.83
PC3	V	-16.7	512	-307.13	0.2000	50.0	6.35×6.35	577.0	0.69
PC3	X	0.0	512	-305.86	0.2000	50.0	6.35×6.35	577.0	0.86
PC3	U	16.7	512	-304.59	0.2000	50.0	6.35×6.35	577.0	0.73

Table 2.4: E771 front chamber tracking parameters for the PC chambers. (Note: The z-positions are with respect to the center of the analysis magnet.)

wires. These wires were in turn sandwiched between two grounded cathode planes. While DC1 was instrumented with wire planes, DC2 and DC3 were instrumented with 25.4 μm aluminized mylar. The U and V stereo planes were placed at angles of $\pm$ 16.7° with respect to the positive y axis. The gas mixture used to run these chambers was a 50% ratio of argon gas to 50% ethane gas bubbled through ethyl alcohol at 0° C. A more detailed depiction of the DCs is given in Table 2.5.

2.3.5 The Analysis Magnet

ROSIE (formally know as PW8AN2), the analysis magnet, was a 150-ton DC dipole magnet of dimensions 185.54 × 91.38 × 152.40 cm^3. It was nominally run

Plane	View	Angle from Y-Axis (deg)	Number of Wires	Z Position (cm)	Wire Spacing (cm)	Wire Length (cm)	Deadened Region (cm^2)	Resolution (μm)	Efficiency
DC1	U	16.7	192	-257.01	0.6000	50.8	6.35×6.35	444±13	0.73
DC1	X	0.0	192	-256.38	0.6000	50.8	6.35×6.35	376±78	0.82
DC1	V	-16.7	192	-255.74	0.6000	50.8	6.35×6.35	466±10	0.88
DC2	V	-16.7	92	-235.47	1.2700	49.8	6.35×6.35	467±11	0.66
DC2	X	0.0	93	-234.20	1.2700	49.8	6.35×6.35	343±83	0.66
DC2	U	16.7	93	-232.93	1.2700	49.8	6.35×6.35	452±11	0.59
DC3	U	16.7	93	-221.50	1.2700	50.8	6.35×6.35	462±11	0.65
DC3	X	0.0	92	-220.23	1.2700	50.8	6.35×6.35	385±93	0.65
DC3	V	-16.7	92	-218.96	1.2700	50.8	6.35×6.35	445±9	0.72

Table 2.5: E771 front chamber tracking parameters for the Drift Chambers. (Note: The z-positions are with respect to the center of the analysis magnet.)

at a current value of 2400 A, which produced a 1.43 Tesla field. In order to reduce the fringe field effects, 22 cm thick iron mirror plates were mounted at the upstream end of the magnet and the downstream end of the magnet. The magnetic field was determined by two independent measurements: (1) by a Hall probe attached to the bottom center of the magnet which monitored the central field, and (2) by measuring the induced current flowing through a device as this device was computer manipulated stepwise through the magnetic field. These two independent B-field testing devices in general yielded the same results.

According to relativistic kinematics, the Lorentz force law states that a particle traveling perpendicular to a uniform magnetic field will experience a force of the

form

$$\vec{F} = q\frac{\vec{v}}{c} \times \vec{B} \tag{2.1}$$

and move in a circular trajectory with a radius given by

$$r = \frac{pc}{qB}. \tag{2.2}$$

Since the $\vec{B}$ field was in the y direction, particles passing through the magnet experienced forces that bent them only in the x-plane. The p_t kick was found by

$$\Delta p_t = \frac{q}{c}\int \vec{B} \times d\vec{l}, \tag{2.3}$$

thus with the field in the y direction,

$$\Delta p_t = \frac{q}{c}\int B_y dz. \tag{2.4}$$

With a 1.43 Tesla field, this resulted in a 0.821 GeV/c "p_t kick" for tracks parallel to the z-axis.

2.3.6 The Rear Tracking Chambers

As outlined for the front tracking chambers, the rear tracking chambers may be categorized in the following groups:

- 3 Drift Chambers (DC's).
- 4 Central Tracking/Pad Chambers (CC's).
- 2 Wing/Pad Chambers (WC's).

The rear drift chambers (DC4, DC5, and DC6) were comparable to the front drift chambers. DC4 encompassed an active region of 236.22 × 99.06 cm^2, DC5 encompassed an active region of 335.28 × 167.64 cm^2, and DC6 encompassed an active region of 335.28 × 167.64 cm^2. DC4 had identical internal properties as DC2 and DC3, mainly its cathode plane consisted of 25.4 μm aluminized mylar. DC5 and DC6, on the other hand, were instrumented in a way similar to DC1, mainly they were instrumented with wire planes. The U and V stereo planes were at angles of ± 16.7° with respect to the y axis. The physical parameters for the rear Drift Chambers are outlined in Table 2.6.

Plane	View	Angle from Y-Axis (deg)	Number of Wires	Z Position (cm)	Wire Spacing (cm)	Wire Length (cm)	Deadened Region (cm^2)	Resolution (μm)	Efficiency
DC4	V	-16.7	124	170.84	1.9050	99.06	25.72×11.43	1000±16	0.81
DC4	X	0.0	124	172.75	1.9050	99.06	25.72×11.43	528±19	0.75
DC4	U	16.7	123	174.65	1.9050	99.06	25.72×11.43	1000±14	0.78
DC4	X	0.0	123	176.56	1.9050	99.06	25.72×11.43	541±71	0.70
DC5	X	0.0	176	620.73	1.9050	167.64	26.67×7.62	428±33	0.71
DC5	V	-16.7	192	622.63	1.9050	167.64	26.67×7.62	753±11	0.81
DC5	X	0.0	176	624.54	1.9050	167.64	26.67×7.62	396±10	0.77
DC5	U	16.7	192	626.44	1.9050	167.64	26.67×7.62	761±13	0.74
DC6	X	0.0	176	725.68	1.9050	167.64	26.67×7.62	436±43	0.57
DC6	V	-16.7	192	727.58	1.9050	167.64	26.67×7.62	833±16	0.59
DC6	X	0.0	176	729.49	1.9050	167.64	26.67×7.62	503±10	0.53
DC6	U	16.7	192	731.39	1.9050	167.64	26.67×7.62	815±15	0.60

Table 2.6: E771 rear chamber tracking parameters for the drift chambers. (Note: The z-positions are with respect to the center of the analysis magnet.)

The last sets of chambers, the CC set of chambers and the WC set of chambers, were added for the E771 run in order to improve pattern recognition [16]. They also were expected to provide charged particle tracking coverage over $\pm$ 120 mr in the horizontal plane and $\pm$ 60 mr in the vertical plane at distances of 8 and 13 meters downstream of the main target. They were expected to provide pad signal inputs to an on-line trigger processor for the selection of high p_t muons, and they were expected to sustain high interaction rates of the order 10 MHz.

The "CC" in the nomenclature of these particular pad chambers stood for centrally located chambers relative to the beam axis. The "WC" in the nomenclature of these particular pad chambers stood for the "wing" chambers that were off the beam axis. The active regions for the CC chambers were 179.2×102.4 cm^2 for CC1 and CC2, 115.2×179.2 cm^2 for CC3, CC4, WC1, and WC2. The beam hole dimensions for the CC chambers were 19.2×9.6 cm^2 for CC1 and CC2, and 19.2×16.8 cm^2 for CC3 and CC4. The WCs, being off axis, had no deadened hole regions. Many of the chamber dimensions were quantized in units of 8.001 mm. The drift cells were all one unit square, and so the pads were one, two, or four units in width. The physical parameters for the rear Central Tracking Chambers are outlined in Table 2.7 and those for the rear Wing Chambers are outlined in Table 2.8.

Each chamber module represented a pair of identical planes, two sets of anode wires, two sets of stripes, and two sets of pads. A charged particle's x-coordinate was measured by the wire planes, its y-coordinate was measured by the stripes, and its "stereo" x-y coordinates were measured by the pads. The wire signals were

Plane	View	Angle from Y-Axis (deg)	Number of Wires	Z Position (cm)	Wire Spacing (cm)	Wire Length (cm)	Deadened Region (cm^2)	Resolution (μm)	Efficiency
CC1U	X	0.0	224	228.70	0.8001	102.41	9.60×4.80	400±15	0.88
CC1D	X	0.0	224	230.40	0.8001	102.41	9.60×4.80	434±9	0.87
CC2U	X	0.0	224	269.90	0.8001	102.41	9.60×4.80	363±16	0.87
CC2D	X	0.0	224	271.60	0.8001	102.41	9.60×4.80	396±13	0.87
CC3U	X	0.0	144	804.30	0.8001	179.22	9.60×8.40	479±28	0.85
CC3D	X	0.0	144	806.00	0.8001	179.22	9.60×8.40	501±18	0.89
CC4U	X	0.0	144	824.60	0.8001	179.22	9.60×8.40	514±14	0.89

Table 2.7: E771 rear chamber tracking parameters for the central chambers. (Note: The z-positions are with respect to the center of the analysis magnet.)

amplified, discriminated in a postamp comparator [17], and directed to LeCroy 4291 10-bit TDC modules. The stripe signals and pad signals were also sent to the same fastbus system, but these signals were processed entirely within the fastbus system. A diagrammatical representation of the pad chambers is shown in Figure 2.7.

All Drift Chambers operated with the gas mixture of 50/50 Argon-Ethane bubbled through ethanol at 0° C.

2.3.7 The Charged Particle Hodoscope

The charged particle hodoscope (CPH) was located immediately downstream of the last of the CC pad chambers. It consisted of 1 cm thick NE110 plastic scintillator counters arranged horizontally and vertically. The horizontally arranged counters

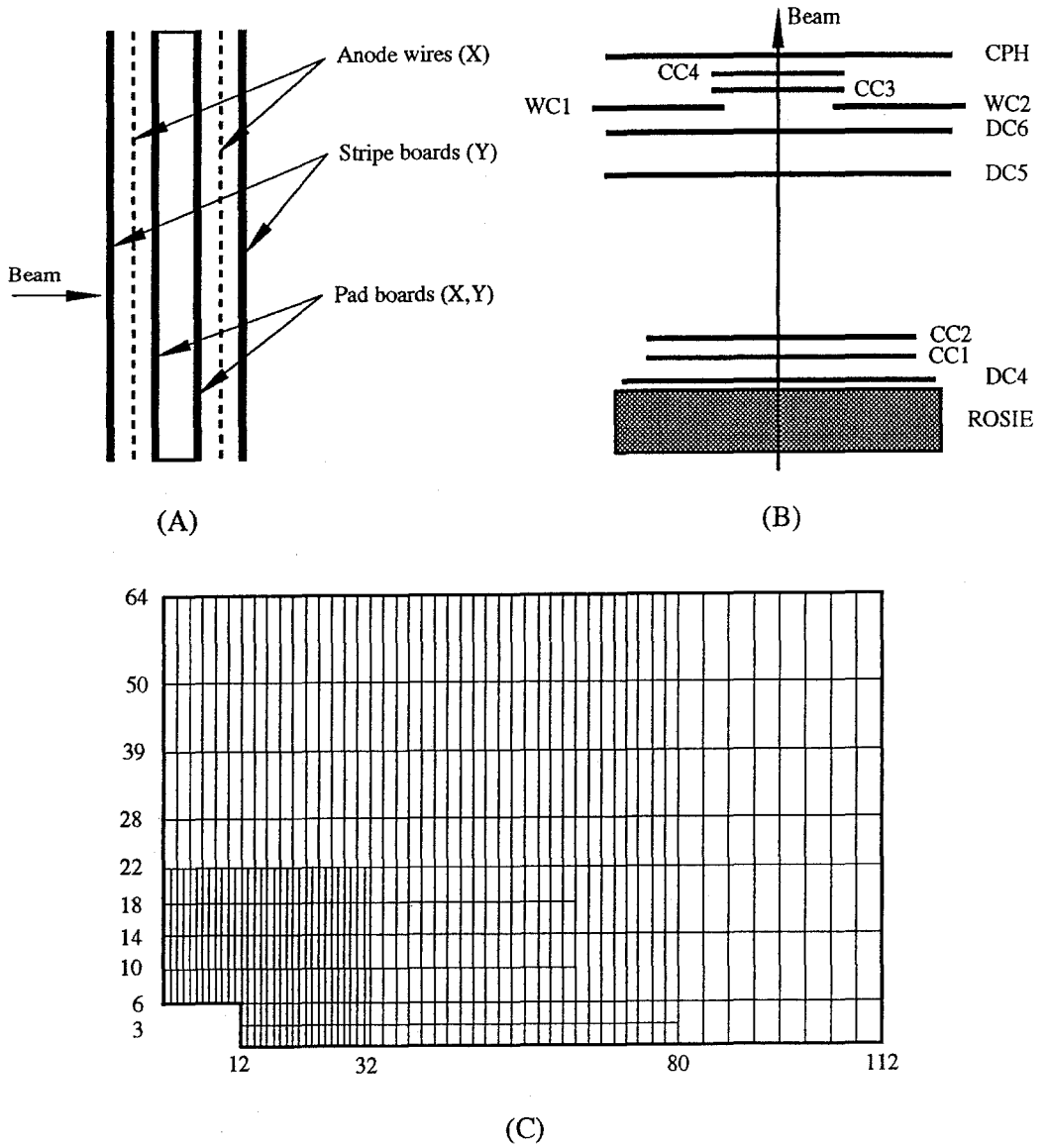

Figure 2.7: E771 pad chamber layout. (a) Wire plane view. (B) Top view of the chambers. (C) Map of pad sizes and positions.

Plane	View	Angle from Y-Axis (deg)	Number of Wires	Z Position (cm)	Wire Spacing (cm)	Wire Length (cm)	Deadened Region (cm^2)	Resolution (μm)	Efficiency
WC1U	X	0.0	144	783.80	0.8001	179.22	-	410±14	0.85
WC1D	X	0.0	144	785.50	0.8001	179.22	-	510±14	0.87
WC2U	X	0.0	144	783.80	0.8001	179.22	-	410±14	0.90
WC2D	X	0.0	144	785.50	0.8001	179.22	-	510±14	0.93

Table 2.8: E771 rear chamber tracking parameters for the wing chambers. (Note: The z-positions are with respect to the center of the analysis magnet.)

were labeled CPX, and the vertically arranged counters were labeled CPY. The CPX counters contained two rows of 92 counters each, and the CPY counters contained two columns of 24 counters each. With each CPX counter being 1 cm thick, 3.8 cm wide, and 100 cm long, they covered a total area of 350×200 cm^2 with a deadened central beam hole region encompassing 30×15 cm^2. With each CPY counter being 1 cm thick, 7.5 cm wide, and 200 cm long, they covered a total area of 400×180 cm^2 with a deadened beam hole region encompassing 30×15 cm^2.

The CPH was used initially as an interaction trigger, and in order for an interaction to have occurred, at least two hit CPX counters would have to have been in coincidence with the beam particle trigger. Once the main silicon interaction trigger came on-line, the CPH counters were no longer used as the interaction trigger.

2.3.8 The Electromagnetic Calorimeter

Electromagnetic showers [18] are those which detect an incident e^+, e^-, or γ. Since the π° decays into γ's, and since on average 1/3 of the pionic energy is in π°'s, electromagnetic calorimeters are of importance when studying hadronic interactions. Electromagnetic showering implies the further production of electromagnetic particles from the internal reactions in the calorimeter. The showering usually begins within a small fraction of a radiation length, and it usually begins on a somewhat faster time scale for electrons than for photons. The showering multiplies until eventually all the track energies become too small and then ionization and Compton scattering start to take over in the absorption of the low-energy shower. As the shower proceeds along, it experiences a (dE/dx) loss taking the shape of an exponentially increasing form. Some of the common electromagnetic interactions in electron-induced or photon-induced showers are:

- Bremsstrahlung (photon emission in acceleration),
- Electron-positron pair creation ($\gamma \rightarrow e^+e^-$),
- Compton scattering (photon-electron scattering),
- Coulomb scattering (electron-positron scattering),
- Bhabha scattering (electron-positron scattering),
- Photoeffect (electron emission from γ-irradiated nuclei),
- Møller scattering (electron-electron scattering), and

- Annihilation ($e^+e^- \rightarrow \mu^+\mu^-$, or $\rightarrow \gamma\gamma$).

The electromagnetic calorimeter (EMC) (see Figure 2.8) used in E771 was located immediately downstream of the CPH at a position where the front face was 935.5 cm from the center of the analysis magnet. Its main component was the Main Array which consisted of 406 scintillating glass and lead glass blocks encompassing an area of 1.95×3.75 m^2. The innermost portion of the EMC was made of 92 SCG1-C scintillation glass blocks covering an area of 7.5×7.5 cm^2. The outer portion of the EMC was made of 228 SF5 lead glass blocks covering an area of 15×15 cm^2. Sandwiched between the innermost portion and the outer portion of the EMC was a region consisting of 86 scintillation glass blocks enveloping an area of 15×15 cm^2. The deadened beam hole region covered an area of 30×15 cm^2.

As the EMC was helpful in studying B-mesons and charm physics, it was not utilized for this dissertation. More explicit details may be found elsewhere [19].

2.3.9 The RPC Muon Detectors

E771 had two muon detectors. The first detector was made of three planes of scintillator counters, each specifically arranged in an upper row and a lower row. The second detector consisted of three planes of Resistive Plate Counters (RPCs) [20]. Each plane of detector was imbedded in thick layers of concrete, lead, and steel absorbers, mainly to prevent the passage of all particles except the most energetic muons. The first shielding consisted of 40 cm of copper, and following this was a 3.1 m thick iron wall. At 3.1 m, this iron wall corresponded to 18.2 interaction

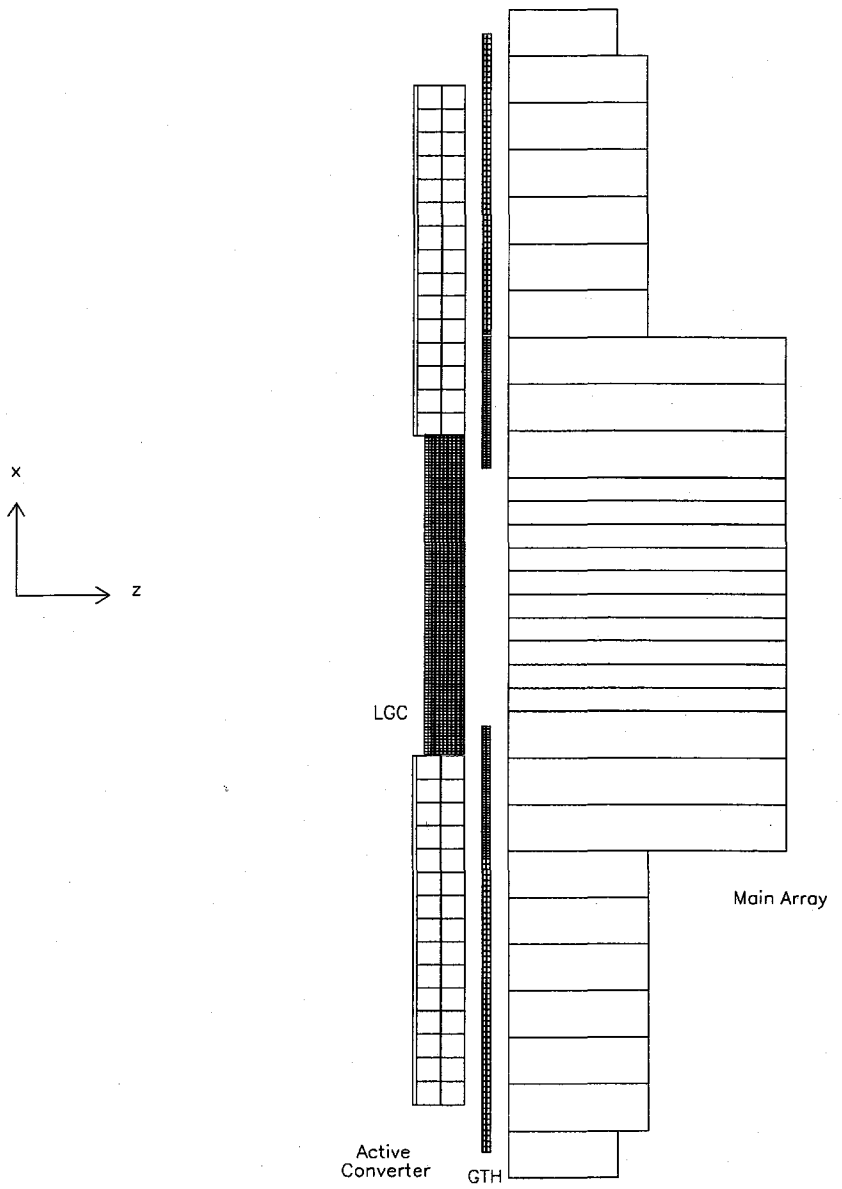

Figure 2.8: Top view of the E771 electromagnetic calorimeter.

lengths. This was deemed sufficient to stop all hadrons from penetrating through. The second iron wall shielding measured 60 *cm* in thickness, and the last concrete shielding measured 91 *cm* in thickness. A summary of the muon shielding absorbers is detailed in Table 2.9.

Material Layer/ Type	Thickness (cm)	Thickness (Interaction Lengths)	Cumulative Interaction Lengths
Copper	40.6	2.7	2.7
Iron	305	18.2	20.9
Gap 1 ($\mu 1$)	91.4	-	-
Iron	61.0	3.6	24.5
Gap 2 ($\mu 2$)	76.2	-	-
Concrete	91.4	2.3	26.8
Lead	142	8.3	35.1
Gap 3 ($\mu 3$)	-	-	-

Table 2.9: E771 muon shielding absorber characteristics.

Although there were two types of muon detectors, the scintillator counters and the RPCs, the RPCs were ultimately the ones used for triggering processes. The scintillator counters were used mainly as a check on the RPCs.

The RPCs were gas particle detectors that operated under a gas mixture of 54% Argon, 42% Butane, and 4% Freon at atmospheric pressure. A uniform electric

field was applied and allowed them to be operated in local streamer mode in the 4 to 4.5 kV/mm range. This field was generated by the application of high voltage across two parallel plates of high resistivity ($\rho = 10^{11}\Omega cm$) phenolic polymers. The phenolic polymers were coated with a layer of graphite paint on their outer extremities.

Each plane of the RPC's measured a total volume of $6 \times 3 \times 0.002\ m^3$, and there were 2048 copper pads per plane. The copper pads ranged in size, with the smaller sized pads closest to the beam region and increasing in area as one subtends a larger angle. The pad sizes were different due to the uncertainty of the muon trajectories from multiple scattering. The smallest pads ranged in size of $6 \times 6\ cm^2$ and increased up to $12 \times 12\ cm^2$ for those outer regions representing the lower momentum tracks, see Figure 2.9.

In the RPC triggering mode, the logic time allowed to determine muon identification was on the order of 600 ns. In order for a particle to be recognized as a muon, a triple coincidence must have occurred within the three RPC planes within specific locations per plane.

2.4 "F6" Pad Chamber Readout

Wisconsin was involved in the instrumentation of approximately 4000 readout channels for the CC1 and CC4 pad chambers. Four read-out multiplexers were used. Each multiplexer was capable of reading out a set of 32 F6 boards. A surplus of EFCIS high-flux MWPC fast read-out systems based on two custom-designed monolithic integrated circuits [21] was used for this task, donated by the E771

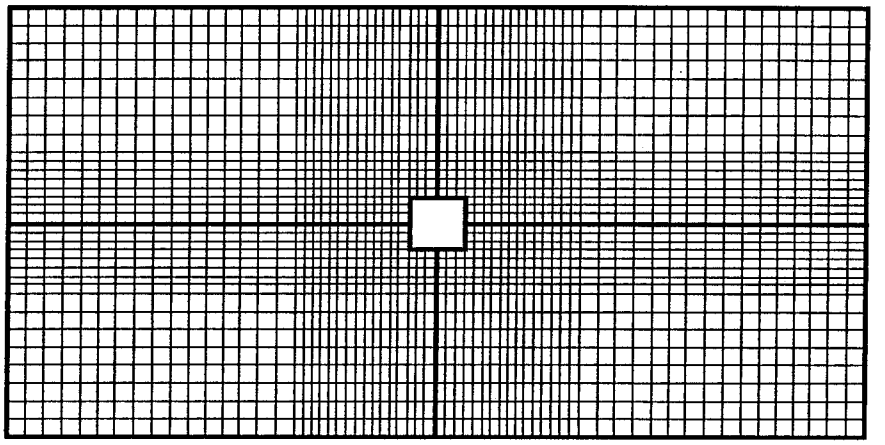

(A)

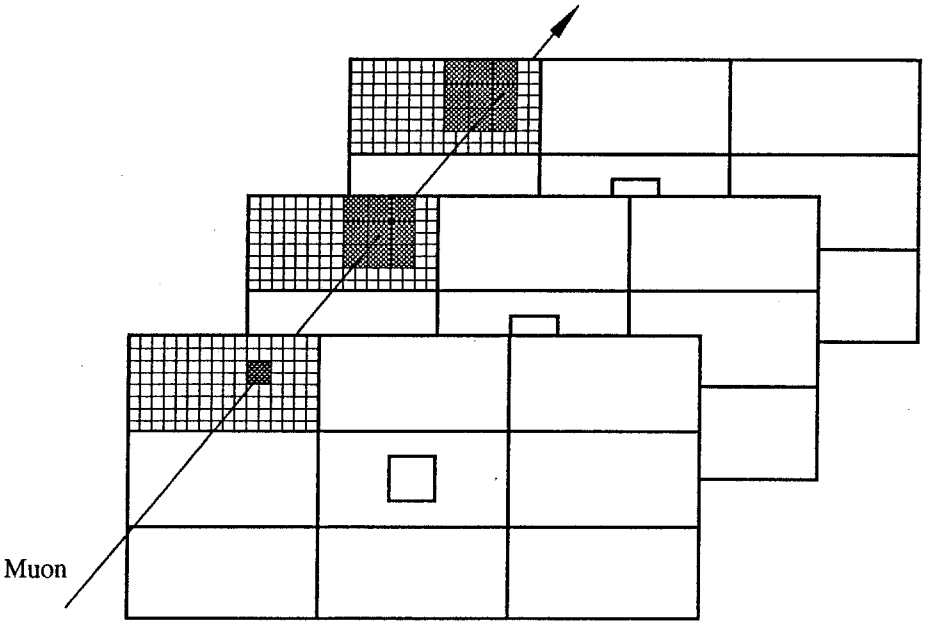

(B)

Figure 2.9: E771 resistive plate counters layout.

Russian collaborators. These integrated circuits had been developed as the heart of an electronic read-out system for equipping lower flux multi-wire proportional chambers placed in the muon beam of the CERN 400 GeV/c SPS accelerator. Wisconsin adapted these to a higher flux read out condition. As a note, the *F6* denoted the name applied to the boards and chips as standing for the EFCIS company that built the electronics.

In order to eliminate the ambiguities in the tracking and to speed the tracking process itself, the CC1 and CC4 pad chambers had to be instrumented. Once instrumented, ambiguities in the tracking were eliminated by allowing the determination of a track in both the x and y positions, whereas the regular wire instrumented chambers could only give a good location in one view, the x-view.

2.4.1 Mechanical Layout and Voltage Conditions

The pad electronics were constructed for the two drift chambers, CC1 and CC4, both located in the rear part of the spectrometer region. Each chamber was served by its own nest of low voltage power and a single CAMAC crate. The nest for CC1 was located in a unistrut tower immediately adjacent to the east side of CC1 halfway between the top and bottom of the chamber. The nest for CC4 was located on a unistrut platform directly under the beam line about 1.5 m upstream of CC4.

The electronics for the chambers were mounted in light, rectangular aluminum frames measuring $20 \times 46 \times 183\ cm^3$, and these frames rode piggy-back style on previously installed preamplifier boxes. The frames for CC1 were mounted on the top and bottom of the chamber, and the frames for CC4 were mounted on the

sides of the chamber. Cooling of the electronics was achieved via convection in the open framework, although the muffin fans for the preamplifier boxes contributed considerably to the air flux.

Each power nest delivered 5V at 55 Amperes, -5V at 45 Amperes, and -12V at 3 Amperes. The 5 Volt and 12 Volt supplies each used #6 AWG wire pairs for the hot and return leads that went between the supplies and the amplifier frames. At the frame, the #6 AWG wires joined a harness of #18 AWG wires which fanned out to the individual amplifier/latches. Each #18 AWG wire carried a maximum of 1 Ampere.

In addition to the low voltage power supplies described above, there were six supplies that delivered low control voltages at "zero" current. The voltages controlled the discriminator thresholds and the time delay of the pulses. Four supplies ran at 0.88 Volt and two ran at 7 Volts. These supplies were all located upstairs in a counting room where they could easily be accessible and were connected downstairs through ground-isolated RG-58 coax cables. At the amplifier/latch frames, these voltages fanned out into the wire harness on the #18 AWG wire to reach the individual circuit boards. Each of these control supplies was capable of delivering a few hundred milliamps at most.

2.4.2 Readout Electronics

Figure 2.10 shows the CC1 and CC4 "F6" trigger electronics. The readout scheme for the F6 electronics appeared somewhat complicated due to the fact that the CAMAC was able to read out only 16 subaddresses in a crate slot. If each subad-

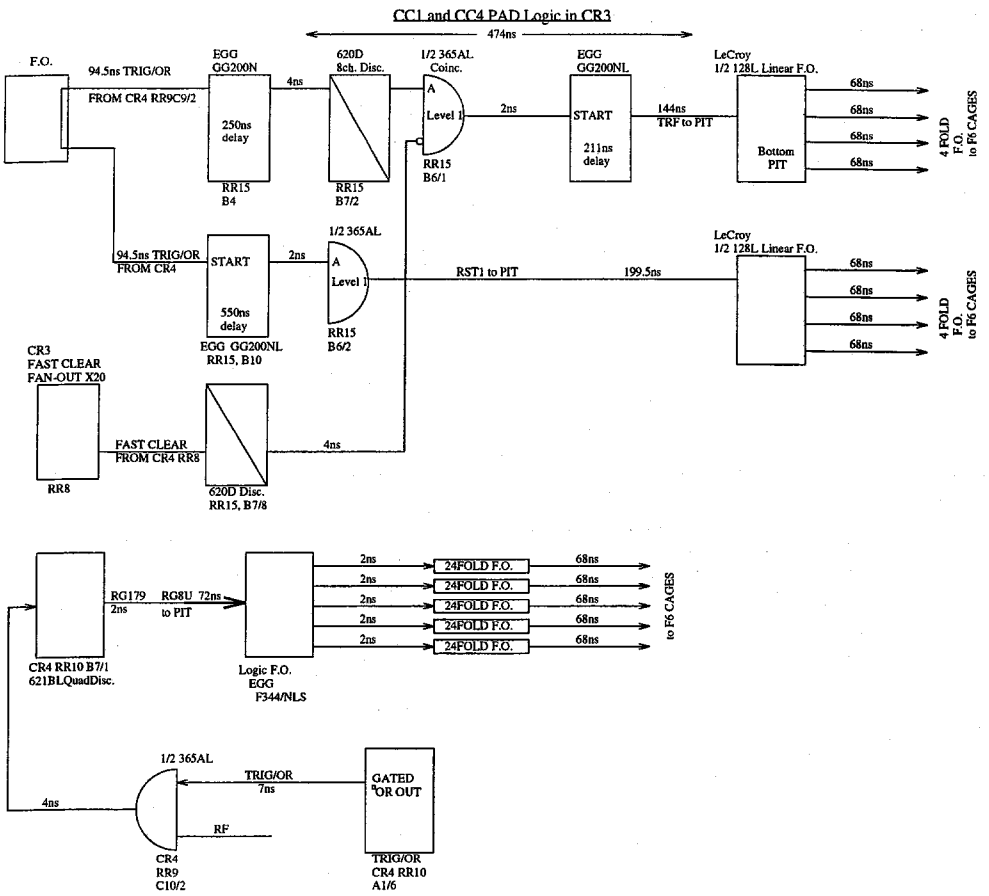

Figure 2.10: "F6" pad chamber trigger logic.

dress had a 16 bit word, this limited the number of bits to 256. A single readout board on the chamber had 32 bits. A single toggle bit, called the A bit, allowed a second reading of the same subaddress to fetch the second half of a readout board. Use of two different readout commands, F0 and F1, allowed one to access another 16 subaddresses the same way. Altogether one was able to read 1024 bits through a single slot by combining the toggle and the two read commands.

Chapter 3

Triggers and Data Acquisition

3.1 The E771 Triggers

E771 began accumulating real physics data in the first week of December 1991 and ended its data taking mode at the end of the first week in January 1992. During this short time interval, the experiment accumulated approximately 130 million dimuon triggers written to data tapes and approximately 60 million single muon triggers written to data tapes. The experiment ran at an average interaction rate of approximately 3 MHz and the data acquisition system (DAQ) was able to handle about 600 Hz with a 40% dead time.

In order to accumulate the "interesting" events, certain triggers were implemented for this experiment. Mainly, they consisted of the beam trigger, the interaction trigger, the single muon trigger (the 1A1μ), the double muon trigger (the 1A2μ), and a combination of the latter two with the high-p_t trigger (the 1B). The two triggers that were most frequently used in this experiment were the 1A1μ1B and the 1A2μ.

3.1.1 The Beam Trigger

The beam trigger [22] was the most fundamental of the triggers and was devoted primarily to the determination of the existence of a beam particle. During the run, most of the time the beam frequency was much lower than the machine bucket frequency. This meant that most of the RF buckets did not contain a beam particle. If a beam particle existed, it was defined by the triple coincidence of an accelerator RF signal, and the signals from the silicon beam planes. The logic definition of a beam trigger was known as

$$BeamV \equiv RF \bullet T1 \bullet (\Sigma Si > n) \bullet \overline{Halo}. \tag{3.1}$$

$BeamV$ was defined by an RF signal coming in from the accelerator in coincidence with a beam particle having no muon halos, $\overline{Halo}$. The beam particle was determined by the scintillator counter $T1$, located amongst the beam and halo veto counters upstream of the main target, being activated by its passage. An OR signal from two beam silicon X planes was used to aid in the determination of the existence of a beam particle. The amplified signals from each of the two silicon X planes were then discriminated after they had been sent up to the main counting room. The two X planes overlapped each other by half a pitch, so this allowed the overlapping of one strip in one X plane to two strips in the other X plane. A signal from one X plane strip was ANDed with the OR signal from the other X plane with the two overlapping strips. All of these were then ORed together to give the final $\Sigma Si > n$. The logic diagram of the beam trigger is shown in Figure 3.1.

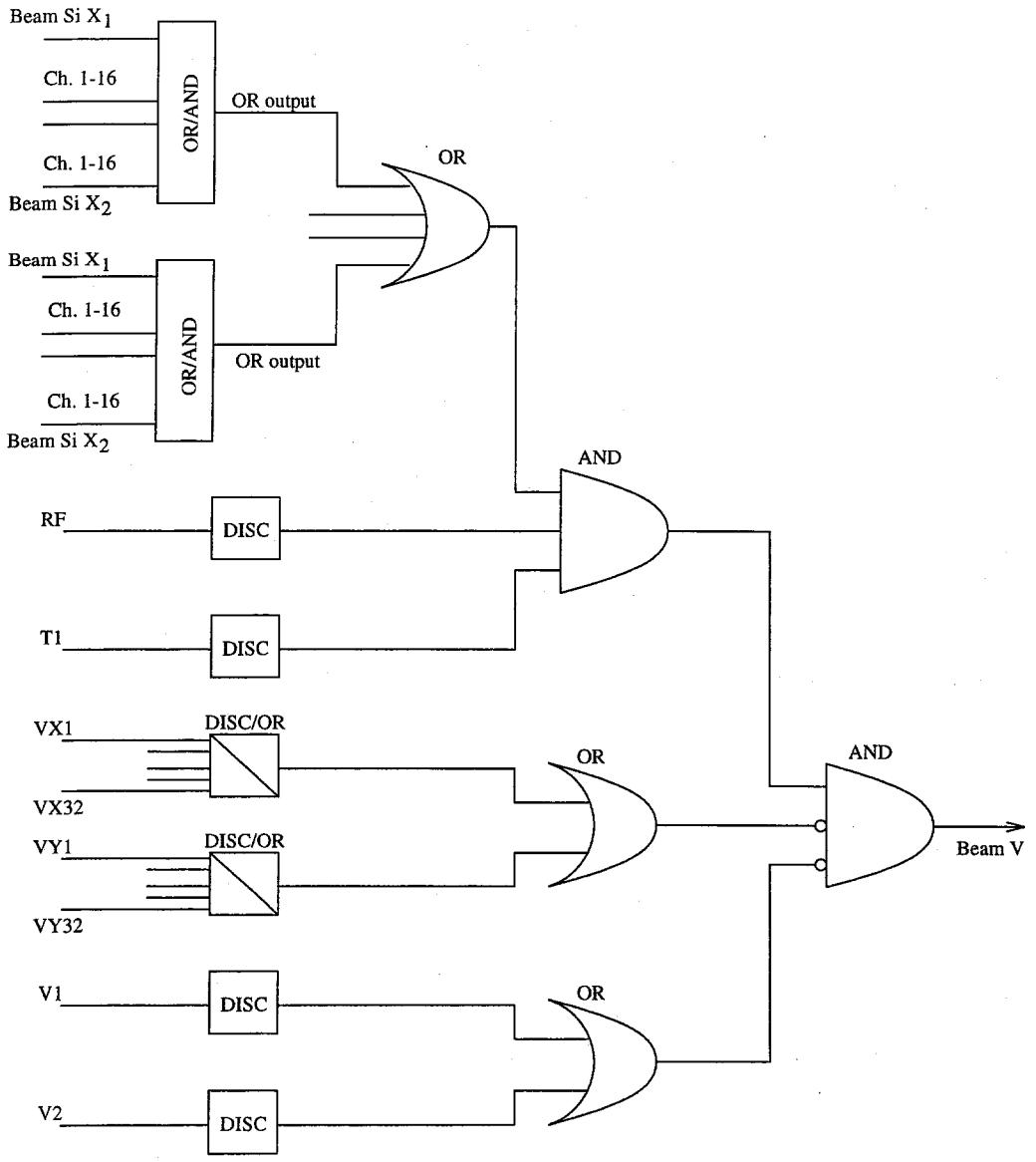

Figure 3.1: E771 beam trigger logic.

3.1.2 The Interaction Trigger

Once the beam trigger was satisfied, the next stage for trigger acceptance was the interaction trigger mode. This trigger was meant to accept only those beam triggered events that had an interaction in the silicon target. This was an infrequent process since the silicon target had about 5% of an interaction length which meant 1 of every 20 beam protons produced an interaction.

The silicon interaction trigger [23] used a hit multiplicity in the silicon tracker X3 plane. The strip signals from silicon plane 3 (X3) were amplified, discriminated, and summed to give an output signal whose size was proportional to the number of input signals. This output was discriminated to form a trigger if there were more than n_1 hits and less than n_2 hits. An additional requirement of more than n_3 hits in a beam silicon plane (X1) was imposed. The minimum number of hits was preselected by an adjustment of the threshold level. The output was then ANDed with the $BeamV$ trigger to produce the INT trigger, defined as

$$INT = BeamV \bullet (\Sigma Si > n_1) \bullet (\overline{\Sigma Si > n_2}) \bullet (\overline{\Sigma BeamSi > n_3}), \tag{3.2}$$

and its corresponding logic diagram is shown in Figure 3.2.

Multiplicity cuts in the silicon tracker planes were imposed by use of the X1 beam silicon plane and the X3 silicon tracker plane. If the silicon X3 plane had a hit multiplicity greater than n_3, then an OR output was generated and sent to an AND module in order to inhibit the interaction signal. A similar procedure occurred for the beam silicon X1 plane if its multiplicity was greater than n_3. E771 imposed multiplicity cuts of 4 to 8 hits for n_1, 80 hits for n_2, and 5 to 10 hits for n_3.

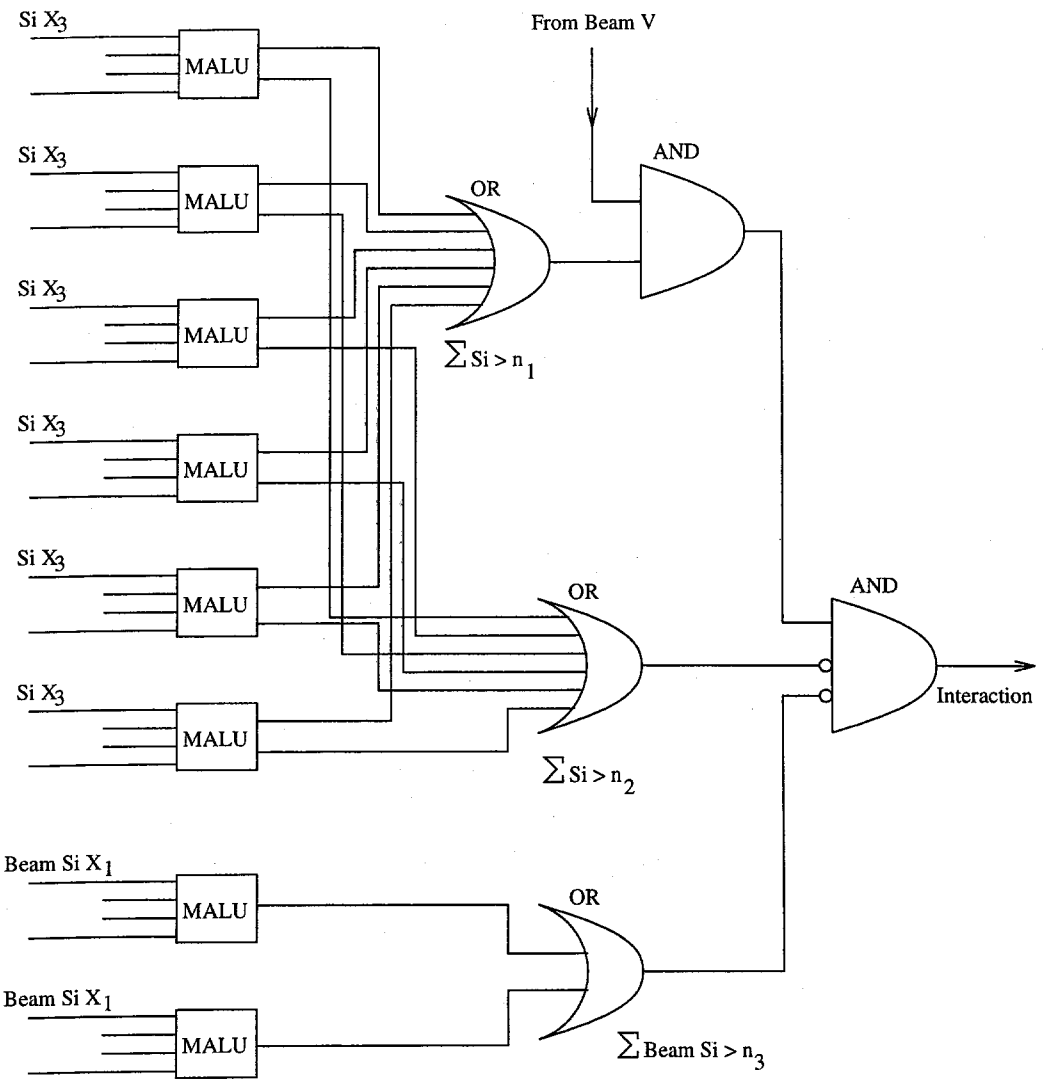

Figure 3.2: E771 interaction trigger logic.

3.1.3 The 1A Trigger

The 1A Trigger [24] was designed to select dimuons and single muons from the decays of

$$B \rightarrow J/\psi + X \rightarrow \mu^+\mu^- + X$$

and

$$B \rightarrow \mu^\pm\nu + X.$$

This trigger used the muon Resistive Plate Counters (RPCs), and in the most simplistic terms, a muon was defined as a triple coincidence among the three layers of RPCs. The OR of 4 (2×2) adjacent pads (OR4) in a RPC constituted the unit of a 1A trigger. Superpads were defined in the second and third planes as 9 (3×3) OR's. See Figure 3.3. The 1A logic required a triple coincidence between an OR4 in the first plane and superpads in the second and third planes. This logic was performed by Programmable Gate Arrays (PGAs) Xilink XC2064 microchips. There were 512 possible triple coincidences originating from the OR4's of the RPC1 plane. They were ORed together in adjacent groups of 16 ORs by LeCroy 4564 OR logic units. The 32 resulting signals were called *superORs*, and the single muon trigger was obtained by ORing the 32 *superOR*'s and ANDing it with the interaction trigger. Hence, the *single muon* trigger was defined as

$$1A1\mu = superOR(=1) \bullet INT. \tag{3.3}$$

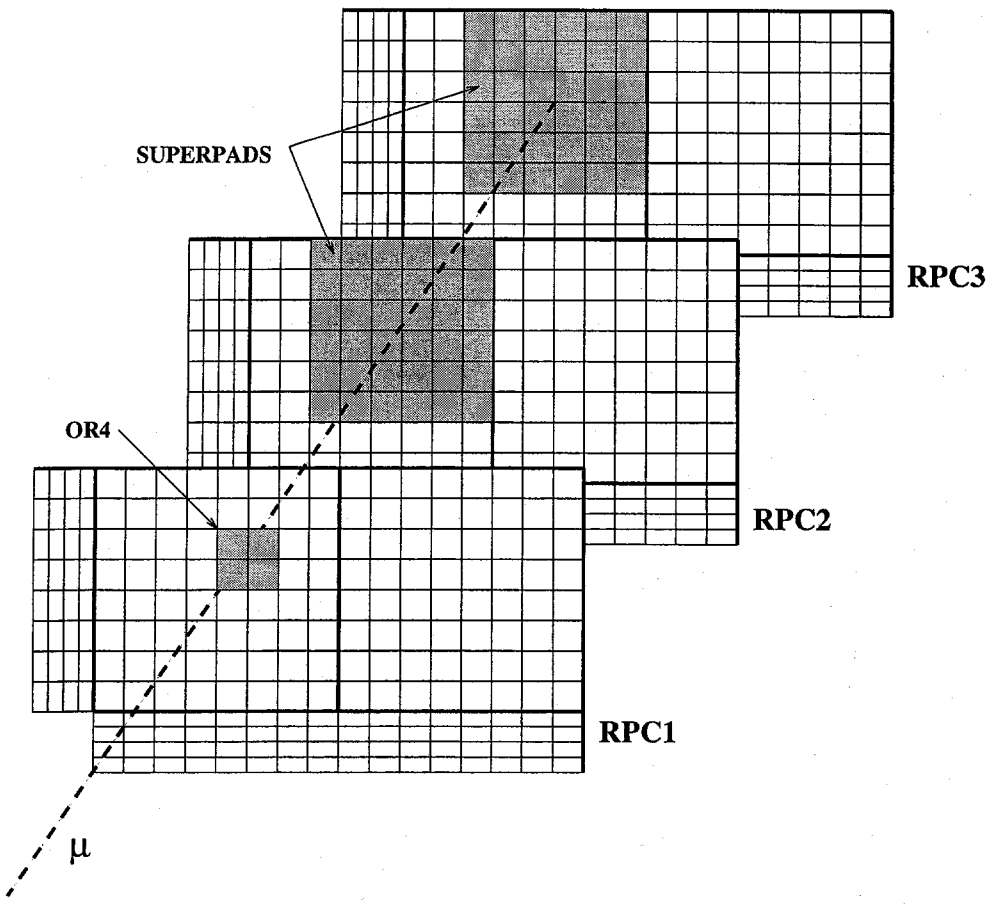

Figure 3.3: E771 topological definition of the 1A trigger.

It frequently occurred that fake dimuon signals would be produced with a single muon trigger accompanied by a hadronic shower of a δ-ray hitting an adjacent *superOR*. In order to eliminate this problem, two MALU modules were used as on-line rejectors of horizontal ($\overline{ADJ_H}$) and vertical adjacent ($\overline{ADJ_V}$) *superORs*. The double muon trigger was therefore defined as

$$1A2\mu = (superOR(\geq 2) \bullet \overline{ADJ_H}) \bullet (superOR(\geq 2) \bullet \overline{ADJ_V}) \bullet INT, \qquad (3.4)$$

and its logic diagram is shown in Figure 3.4.

3.1.4 The 1B Trigger

One method used to obtain clean events from heavy quark physics, such as B-mesons, is a condition on the p_t of a track that is a result of the large B mass (5.3 GeV/c^2). The large energy release of a low multiplicity B decay can give a transverse kick greater than that found in normal pion production. By selecting a threshold above a particular p_t value, a large fraction of minimum bias events may be rejected.

Muons that were of high enough momentum would experience a smaller B-field kick and therefore would not be deflected as much by the analysis magnet. The resultant trajectories of these muons would have a relatively small number of aligned pads in the CC2 and CC3 chambers and the RPC1 superpads. Horizontal bands of pads in the CC chambers and the RPC chambers were searched for coincidences, called *y-bands* pointing back to the target. There were $\sim$ 40,000 pad combinations, and they were divided up into 5 trigger classes called (1) *OBHI* - Outbender with high p_t (p_t > 1.0 GeV/c), (2) *IBHI* - Inbender with high p_t

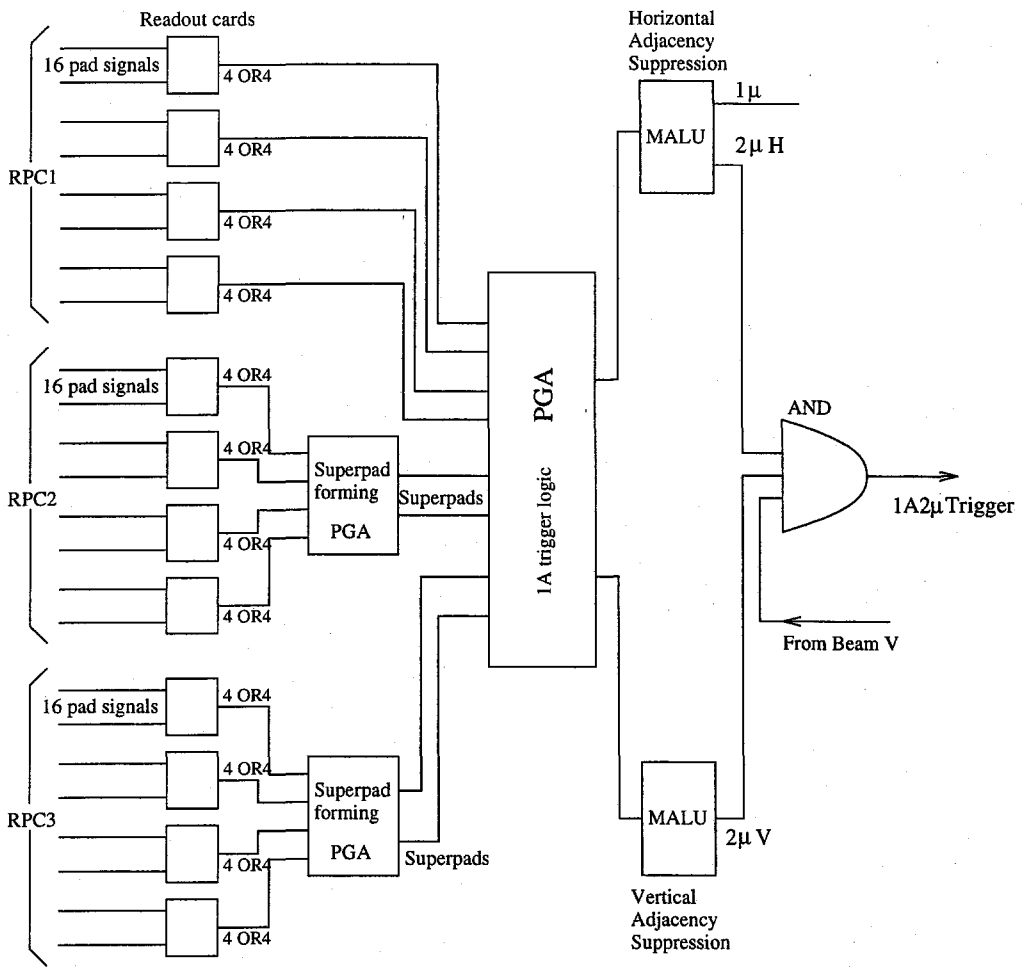

Figure 3.4: E771 1A2μ trigger logic.

($p_t > 1.0$ GeV/c), (3) *OBLO* - Outbender with low p_t ($0.8 < p_t < 1.0$ GeV/c), (4) *IBLO* - Inbender with low p_t ($0.8 < p_t < 1.0$ GeV/c), and (5) *PDMT* - "Dimuon only" trigger (outbenders with p_t as low as 0.6 GeV/c). This high-p_t trigger was designed to operate at a certain p_t cut-off with the ability to switch from 0.8 GeV/c to 1.0 GeV/c. This 1B trigger was eventually used as the primary *single muon trigger* and was defined as $1A1\mu \bullet 1B$.

3.2 Data Acquisition

The E771 data acquisition [25] consisted of a trigger distribution system which was responsible for initiating the readout of an event using smart crate controllers into six data readout chains. The readout from each chain was stored in six VDAS buffers until it was retrieved by an ACP (computer) node which recorded the data onto 8 *mm* exabyte tapes. The DA was able to write about 600 events per second to 12 tapes with a 40% dead time.

All the triggered signals were sent to the Trigger-OR module where they were selected and prescaled. The Trigger-OR output was fanned to multiple readout electronics for initiating a readout cycle. The triggered signals were also sent to the trigger box so that a trigger pattern was created to indicate which trigger initiated a particular event. This trigger pattern was then sent to the readout controllers in order to activate the readout of that trigger pattern. The data transfer occurred from the Camac Smart Crate Controllers (CSCC's) and the Fastbus Smart Crate Controllers (FSCC's) to the VDAS buffers.

As shown in Figure 3.5, the DA had six data chains that were read out in

parallel, where four of them were CAMAC and the other two were FASTBUS. The devices in each of the six data chains were read out in succession until the last chain sent its data packet and its termination message. In order to construct the event, there were ACP processors in three VME crates which were used to retrieve the data from the VDAS buffers. Six event buffer interfaces (EBI), four event handlers (EH), one ACP Boss, one tape drive interface, and other modules were included in the ACP nodes of each VME crate. All VME crates operated in parallel in order to access simultaneously different VDAS buffers. The constructed events were then written to twelve tapes in a parallel fashion to compensate for the mechanical time loss in writing an event to a single tape.

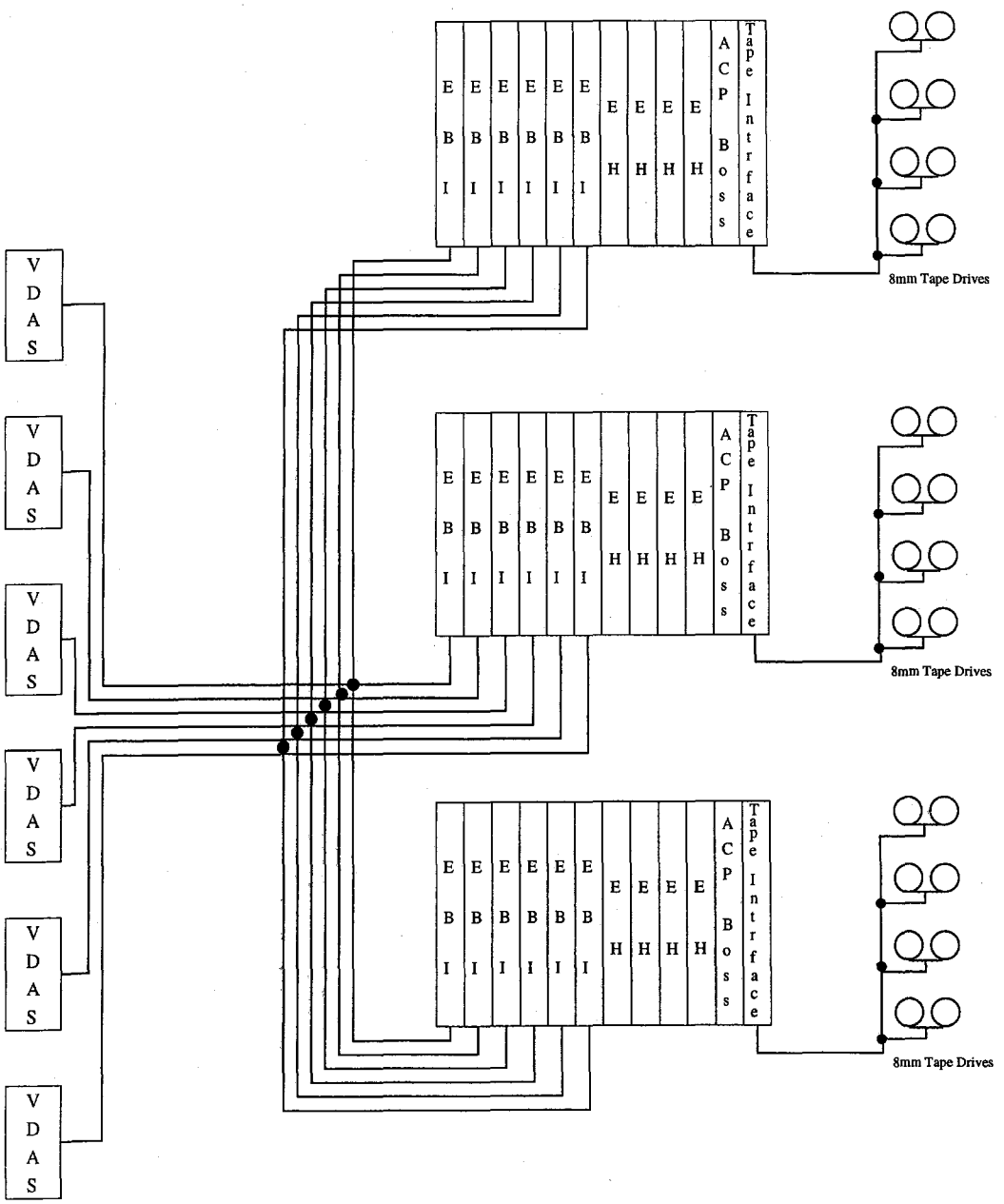

Figure 3.5: The E771 data acquisition system.

Chapter 4

LTELE

The luminosity interaction telescope, most frequently referred to as LTELE, was built and maintained by Wisconsin. It was used in E771 to monitor the 53.1 MHz radio frequency time (corresponding to beam buckets spaced in equal intervals of 18.9 ns) with respect to beam-on-target time, and it was also used to obtain cross sections for inclusive charged particle production for different fixed targets of beryllium, silicon, copper, and tungsten.

4.1 Physical Description

The luminosity interaction telescope was made of three RCA 6342A photomultiplier tubes, each tube having a hexagonal scintillator attached to it where the scintillating material was 0.5 in thick and $\sim$ 2 in in diameter. The first photomultiplier tube of the telescope was situated 142.0 cm from the interaction target, the second photomultiplier 172.0 cm from the target, and the third photomultiplier 201.33 cm from the target. The mount the telescope rested on was at beam height. Each tube was separated from its closest neighbor by 13.5 cm, and the telescope formed an angle with respect to the beam line of 24.25°. The particular angle

LTELE made with respect to the beam axis was simply a matter of convenience, i.e., it was at the smallest angle not interfering with the tracking chambers. It had originally been planned to put LTELE right in the beam line in the Glass House in order to monitor the full beam particles, but later it was deemed more appropriate to situate the device at a larger angle with respect to the beam axis in order to define better only those particles from interactions with the target. A closer angle would have accepted more false interactions, such as those from halo particles, interactions with air, etc.

4.2 LTELE Triggering

A triple coincidence from LTELE was used as a START for a TDC and was used simultaneously to gate a particular BEAMV (RF) pulse into a delay line. The delayed BEAMV pulse was used as a STOP pulse for the TDC (see Figure 4.1). Since a particle from the target into LTELE did not necessarily belong to a triggered event, the digitized time remained in the TDC until a trigger initiated a read-out. This method of recording data was necessary to enhance LTELE live-time because LTELE counts rarely coincided with triggered events.

The range of timing shifts that could be covered by this arrangement was about $\pm$ 8 ns, the spacing between RF buckets. Variations of $\pm$ 2 ns in time of the RF versus the target were acceptable for our triggering. The timing changes that did occur mostly dealt with time delays being added to the BEAMV cables or subtracting time delays from the BEAMV cables. Figures 4.2 and 4.3 show the maximum and mean RF timing for the luminosity interaction telescope as a

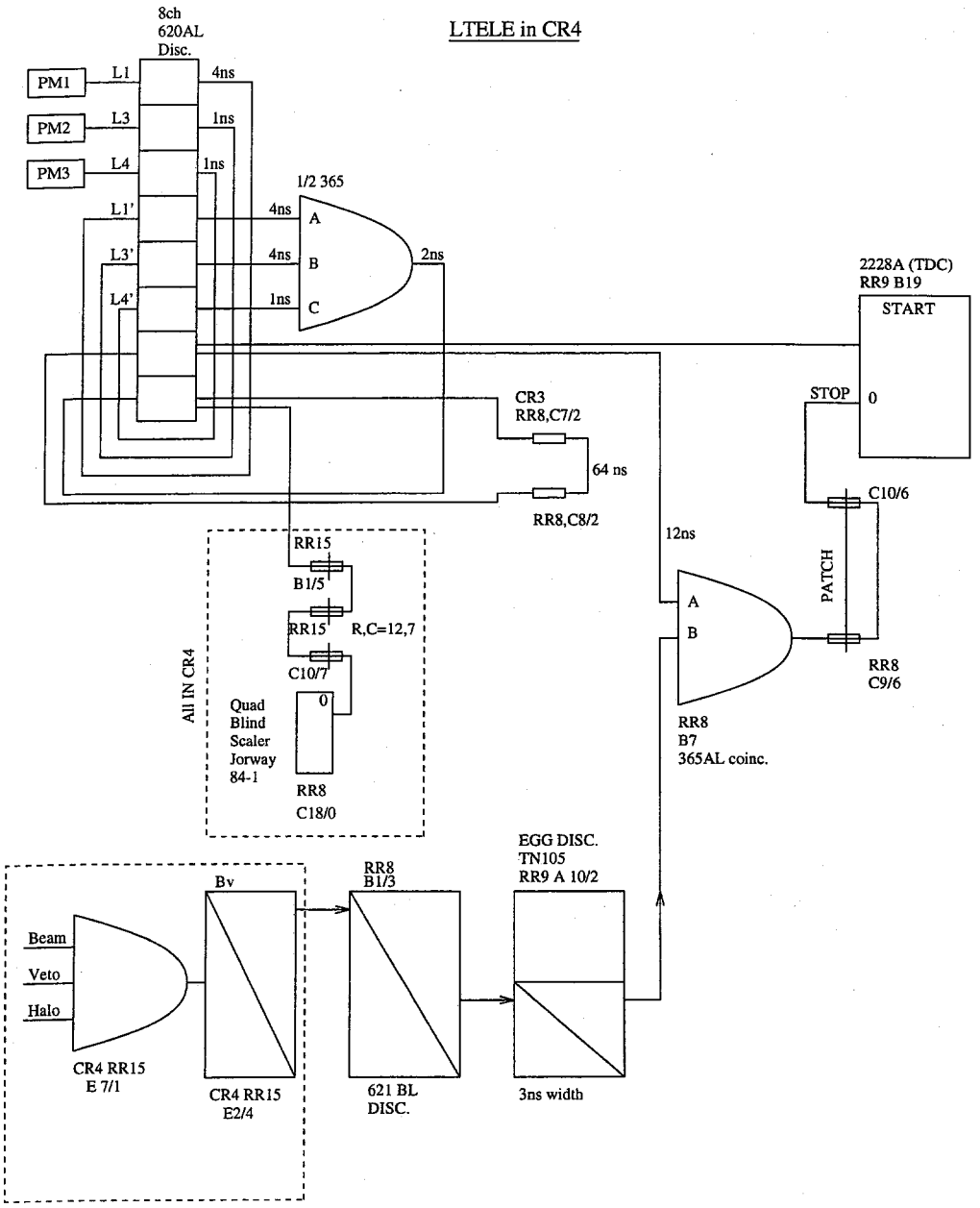

Figure 4.1: LTELE trigger logic.

function of the tapeset number, respectively. No disastrous or unexplained timing shifts were observed such as reported by other Fermilab experimental groups.

LTELE was also used as a luminosity monitor. Figure 4.4 shows a plot of the ratio of LTELE to PW6IC versus TAPESET NUMBER, where PW6IC was the Ion Chamber located in PW6 counting the raw beam particles, and a TAPESET NUMBER corresponded to a particular number being assigned to twelve 8 mm 2.39 GByte magnetic tapes. Ideally, the ratio would have remained constant, but bad data points were obtained where, e.g., accidental disconnection of cables occurred, high voltage supplies were turned off, etc. Smaller variations of ± 10% were probably related to changes in beam optics during the experiment.

4.3 Physics Goals - Differential Cross Section

One of the physics results one may extract from the use of LTELE was the measurement of the total differential cross section for producing a particle at 24.25° with respect to the beam axis when a proton beam hit a target, such as beryllium, copper, silicon, or tungsten (see Figure 4.5). This angle with respect to the beam axis corresponded to a pseudorapidity value of η_{cm}=-2.182, with η_{cm} being defined as

$$\eta_{cm} = -ln \ \ tan(\frac{\theta_{cm}}{2}), \tag{4.1}$$

where

$$tan(\theta_{cm}) = \frac{sin(\theta_{lab})}{\gamma_{cm}(cos(\theta_{lab}) - \beta_{cm})}, \tag{4.2}$$

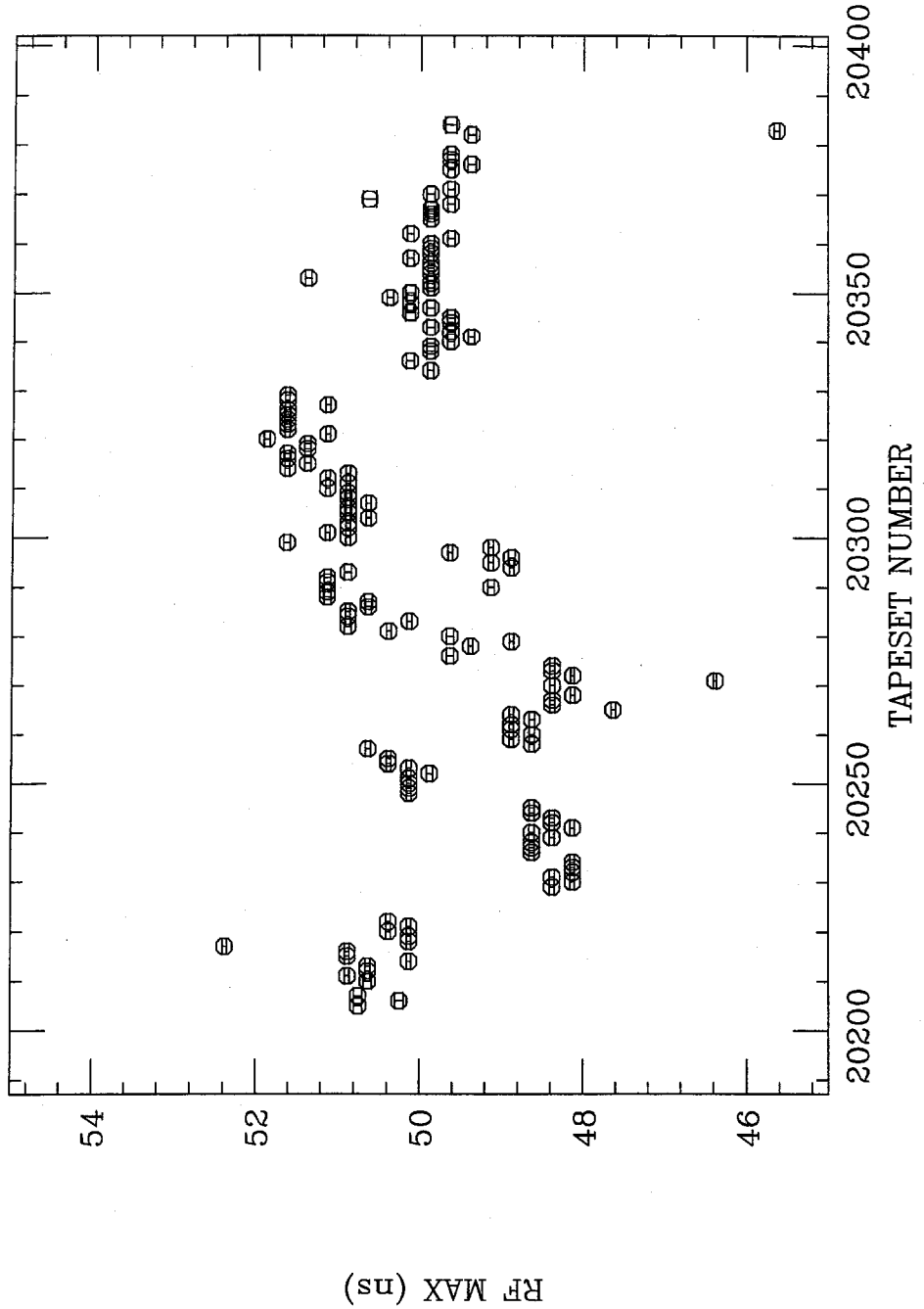

Figure 4.2: Maximum RF timing for LTELE as a function of tapeset number.

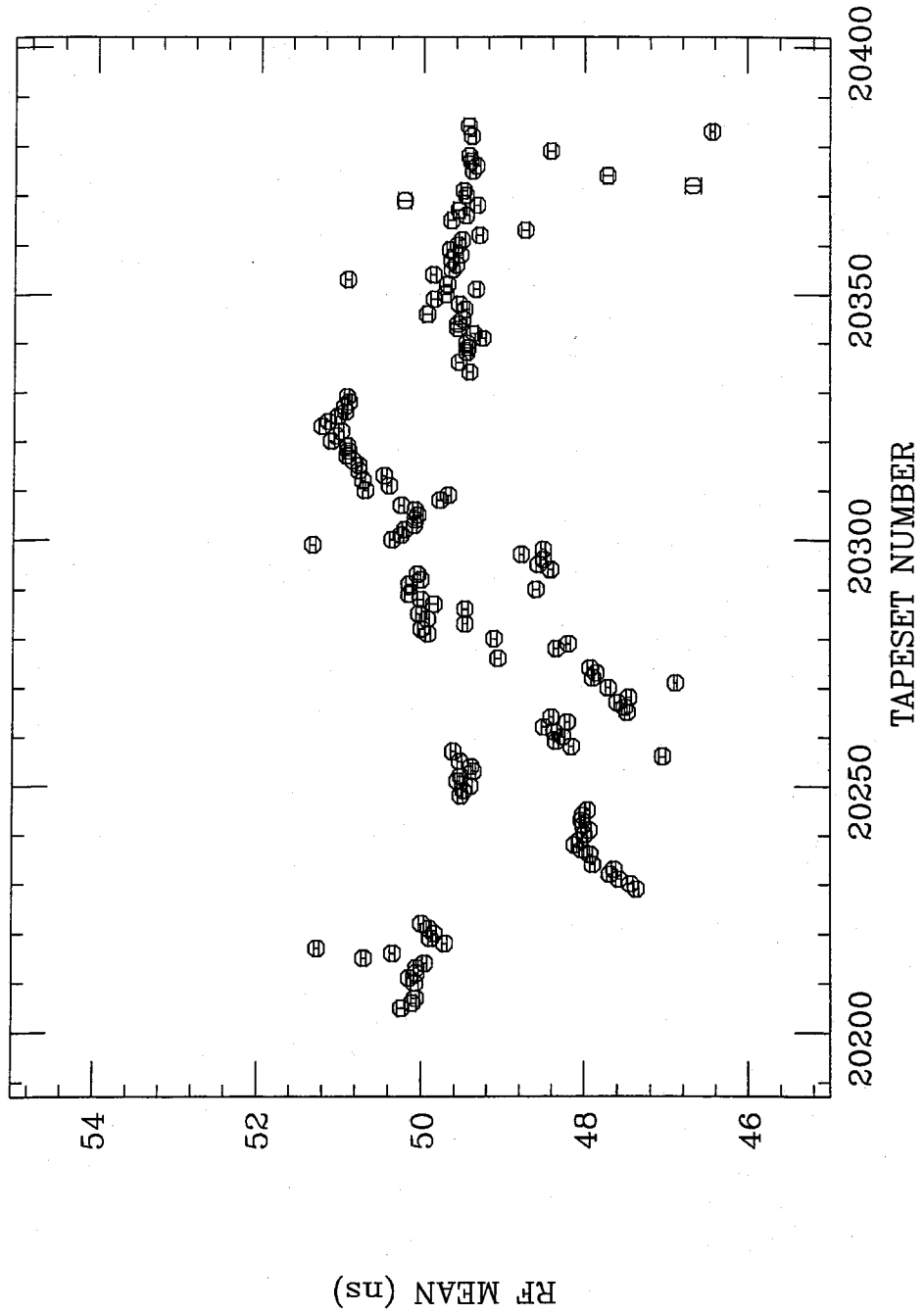

Figure 4.3: Mean RF timing for LTELE as a function of tapeset number.

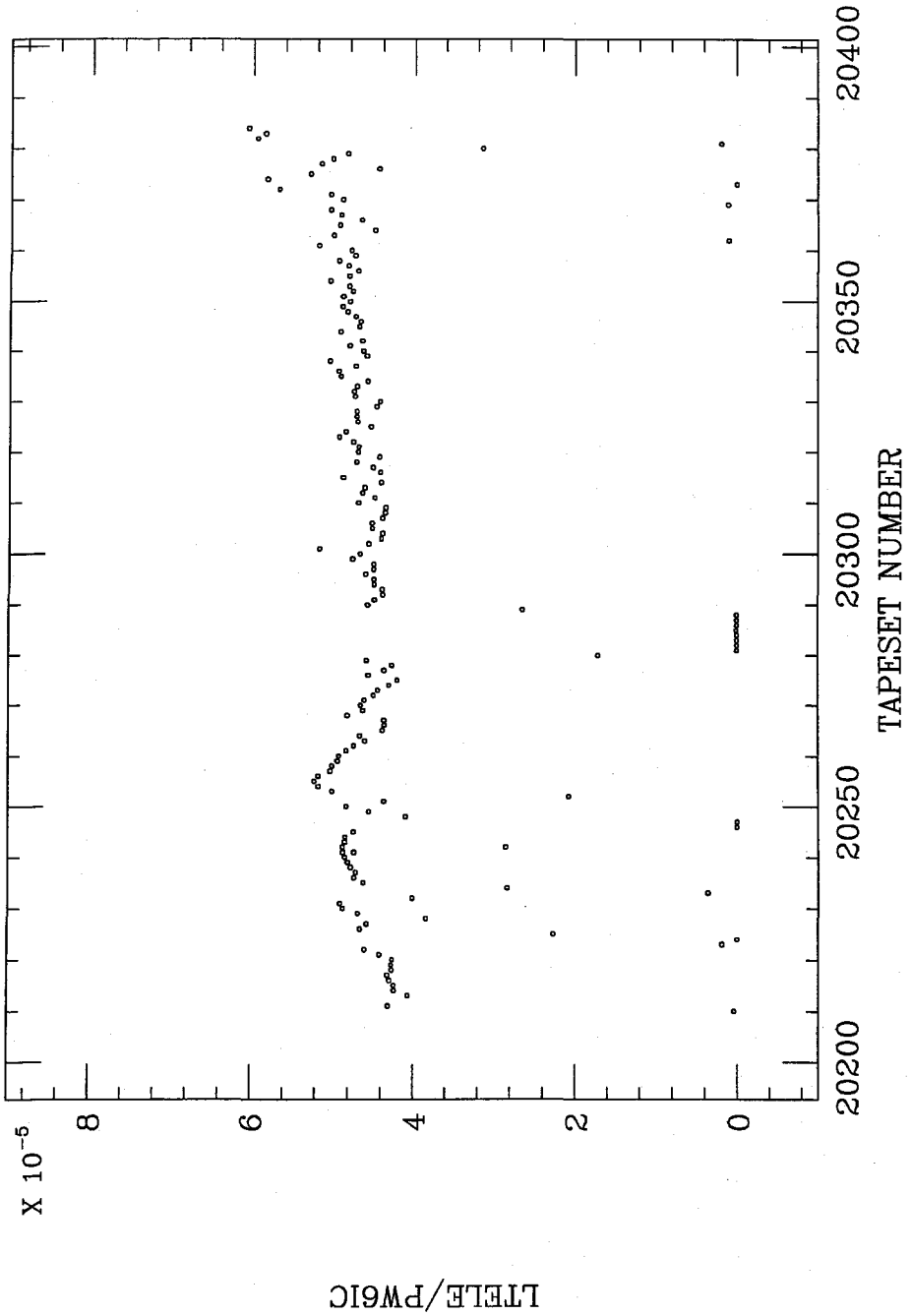

Figure 4.4: LTELE/PW6IC as a function of tapeset number.

and

$$\beta_{cm} = \frac{p_{lab}}{(E_{lab} + m_p)}, \qquad \gamma_{cm} = \frac{1}{\sqrt{1 - \beta_{cm}^2}}. \tag{4.3}$$

The assumption made here is that the particle has velocity $v = c$.

LTELE was able only to sample a fraction of the particles produced at the angle θ=24.25°. This is the fraction of the full 2π azimuthal angle subtended by LTELE. From Figure 4.5, the fraction f that LTELE could see of the decay products was computed as

$$f = \frac{\pi(\frac{D}{2})^2}{D2\pi r'} = (\frac{1}{8})\frac{D}{r'}, \tag{4.4}$$

where the diameter of LTELE's scintillator was $D = 4.62\ cm$, and the perpendicular distance from the beam line to LTELE's photomultiplier tube was $r' = 82.69\ cm$. The fractional value was $1/f$=143.19. With $d\eta = (d\theta/sin(\theta))$, $1/d\eta$=17.92. The total differential cross section at η_{cm}=-2.182 was computed by

$$\frac{d\sigma}{d\eta}|_{\eta cm} = \sigma(\frac{1}{f})(\frac{1}{d\eta}), \tag{4.5}$$

where the cross section value was defined by

$$\sigma = \frac{A_{wt}}{\rho N_A x}(\frac{dN}{N}). \tag{4.6}$$

The atomic weight of the material is defined as A_{wt}. ρ is the density of the material. N_A is Avogadro's number. x is the material thickness, and (dN/N) is the number of LTELE particles per beam particle. LTELE particles were counted in the scalers if a particle traversing the three photomultipliers formed a triple coincidence. The individual σ values for the four targets were

$$\text{Be} \Rightarrow \sigma = 1.189 \times 10^{-24}\ cm^2 \times\ (dN/N),$$

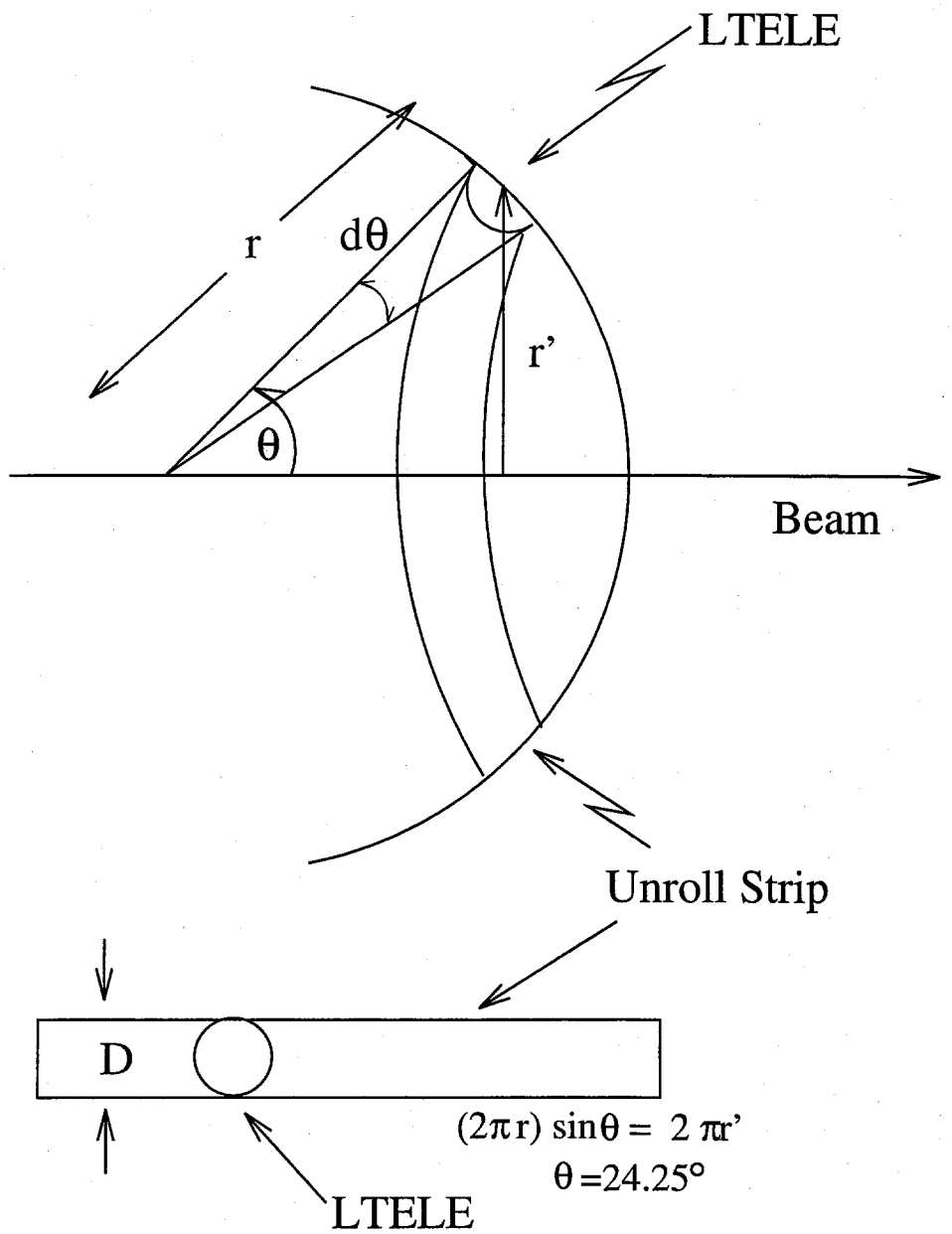

Figure 4.5: Sketch of LTELE's position with respect to the beam line. This shows the strip of view where the scintillator was able to detect the passage of particles.

$$\text{Si} \Rightarrow \sigma = 8.343 \times 10^{-24}\ cm^2 \times\ (dN/N),$$
$$\text{Cu} \Rightarrow \sigma = 4.712 \times 10^{-24}\ cm^2 \times\ (dN/N),$$
$$\text{W} \Rightarrow \sigma = 9.658 \times 10^{-24}\ cm^2 \times\ (dN/N).$$

4.3.1 The (dN/N) Ratio

Two methods were used to obtain the dN/N ratio. During the early part of the run the ratio of (dN/N) was defined as $(LTELE/BEAM)$, where $LTELE$ was the number of counts within a 20 second beam spill occurring every 57 seconds, and $BEAM$ was defined as $T1 \bullet SumBy$, the coincidence of the $T1$ counter and the $SumBy$ counter. The $T1$ counter was located approximately 3 meters upstream of the main target, encompassed an area of 20 $\times$ 10 cm^2, had a thickness of 1 mm, and was used to define the traversing of beam particles and supplied a timing reference for all detector components. The $SumBy$ counter was located immediately upstream of the $T1$ counter and provided the same characteristics as the $T1$ counter, although it encompassed a slightly greater area. It was eventually discovered that a big contributing factor to the beam halo came from the $T1$ counter (therefore, it had to be removed from the beam). It was for this reason that a different ratio of dN/N during the latter part of the run was utilized, and this was defined as $LTELE/PW6IC$, with $LTELE$ defined as above, and $PW6IC$ the proportional wire ion chamber located in the proton west 6 area. The (dN/N) ratio of $LTELE/BEAM$ was employed for the copper and tungsten targets, while the ratio $LTELE/PW6IC$ was used for the beryllium and silicon targets.

Efficiency parameters needed to be taken into account when dealing with the

beam counters. It was determined that the $T1$ counter was 0.739 efficient at low counting rates. As the efficiency of the $SumBy$ counter was not readily available, the following was assumed:

$$\frac{T1}{\epsilon(T1)} = \frac{SumBy}{\epsilon(SumBy)} = \frac{T1 \bullet SumBy}{\epsilon(T1)\epsilon(SumBy)}, \tag{4.7}$$

and with the assumption that the $T1$ and $SumBy$ counters had approximately the same number of particles passing through them, then

$$\frac{T1}{\epsilon(T1)} = \frac{T1 \bullet SumBy}{\epsilon(T1)\epsilon(SumBy)}, \tag{4.8}$$

$$\Rightarrow \epsilon(SumBy) = \frac{T1 \bullet SumBy}{T1}. \tag{4.9}$$

From this an efficiency of the $SumBy$ counter was obtained where $\epsilon(SumBy)$=0.833. This above assumption was made using the known facts that the T1 counter and the SumBy counter were located right next to each other, and that the beam size was smaller than either. The efficiencies of the two were in relative agreement.

The cross section values for Cu and W were thus obtained. Using the parameters defined earlier, the cross section equations for Cu and W were

$$\text{Cu} \Rightarrow \sigma = 4.712 \times 10^{-24}\ cm^2 \times \ (\tfrac{LTELE}{(BEAM/0.613)}),$$
$$\text{W} \Rightarrow \sigma = 9.658 \times 10^{-24}\ cm^2 \times \ (\tfrac{LTELE}{(BEAM/0.613)}),$$

where the beam counter was corrected by the product of the efficiency for the $T1$ and $SumBy$ counters.

For the latter part of the run, the (dN/N) ratio was defined as $LTELE/PW6IC$, where $PW6IC$ was the ion chamber located in the proton west 6 area counting the beam particles. Due to the ion chamber's location, its counts had to be calibrated to those of the $T1$ counter located only $\simeq 3\ m$ upstream of the main target. The

calibration value was calculated to be 1.4, and the cross section equations for the Be and Si targets were

$$\text{Be} \Rightarrow \sigma = 1.189 \times 10^{-24}\ cm^2 \times \ (\frac{LTELE}{(PW6IC/1.4)}),$$
$$\text{Si} \Rightarrow \sigma = 8.343 \times 10^{-24}\ cm^2 \times \ (\frac{LTELE}{(PW6IC/1.4)}).$$

Target (tgt)	Atomic Weight	Density (g/cm^3)	Thickness (cm)	$(d\sigma_{tgt}/d\eta)$ $(barns)$	$(d\sigma_{pN}/d\eta)$ (mb)
Be	9.0122	1.848	6.8150	0.1821 ± 0.0004	42.020 ± 0.044
Si	28.0855	2.330	2.4000	0.8560 ± 0.0015	92.540 ± 0.054
Cu	63.5460	8.960	2.5000	3.0730 ± 0.0181	192.71 ± 0.285
W	183.840	19.30	1.6383	9.8800 ± 0.0872	305.05 ± 0.474

Table 4.1: Data and cross sections for LTELE as a function of target material.

Table 4.1 shows the data and cross sections for LTELE as a function of different target material. It includes the atomic weight of the respective targets, the density for each target, and the thickness of each target the beam passed through. Figure 4.6 shows the inclusive cross section per nucleon at $\eta_{cm} = -2.182$ as a function of target material. It also incorporates the cross section value for hydrogen [26] extrapolated from 200 GeV/c beam momentum to 800 GeV/c beam momentum. The value was attained from the following steps:

- A $(1/N)(dN/dy)$ value was obtained from the 200 GeV/c data. Extrapolating to 800 GeV/c involved the use of

$$(\frac{1}{\sigma_{inel}})(\frac{d\sigma}{dy}) = (\frac{1}{N_{inel}})(\frac{dN}{dy}),$$

$$(\frac{d\sigma}{dy})|_{y_{lab}=1.5} = \sigma_{inel} \times (\frac{1}{N})(\frac{dN}{dy}),$$
$$(\frac{d\sigma}{dy})|_{800GeV} = 34.81(mb) \times (\frac{1}{N})(\frac{dN}{dy})|_{200GeV}.$$

- The inelastic cross section at 200 GeV/c was 32.5 ± 0.5 mb [27], total cross sections at 200 GeV/c and 800 GeV/c were 38.69 mb and 41.23 mb, respectively [28]. The 200 GeV/c σ_{inel} was extrapolated up by 7.2% (the difference between 200 GeV/c and 800 GeV/c σ_{tot}) to give an 800 GeV/c σ_{inel}=34.81 mb. With the value of $(1/N)(dN/dy)$=1.3 at 200 GeV/c, the differential cross section for hydrogen extrapolated to an 800 GeV/c beam energy was
$$(\frac{d\sigma}{dy})|_{y=1.5} = 45.25\ mb.$$

Examination of the plot implies that as the atomic mass goes up so too does the cross section for inclusive charged particle production. One would think that the σ_{pN} would be independent of the target material since $\sigma_{pN}=\frac{\sigma_{tgt}}{A^{.667}}$, and therefore a flat distribution would occur. As the plot indicates, though, it increases monotonically with atomic weight. The implication is that multiplicity comes into play. This means that the heavier and more dense the material, the more interactions occur when the beam passes through. The initial interaction produces secondary interactions which in turn produce their secondary interactions and so on, thus the increase in multiplicity.

4.4 $(d\sigma/d\eta)$ for Silicon as a Function of Tapeset Number

Another form of reference for checking beam intensity was the calculation of the cross section for inclusive particle production via the silicon target. As E771 was

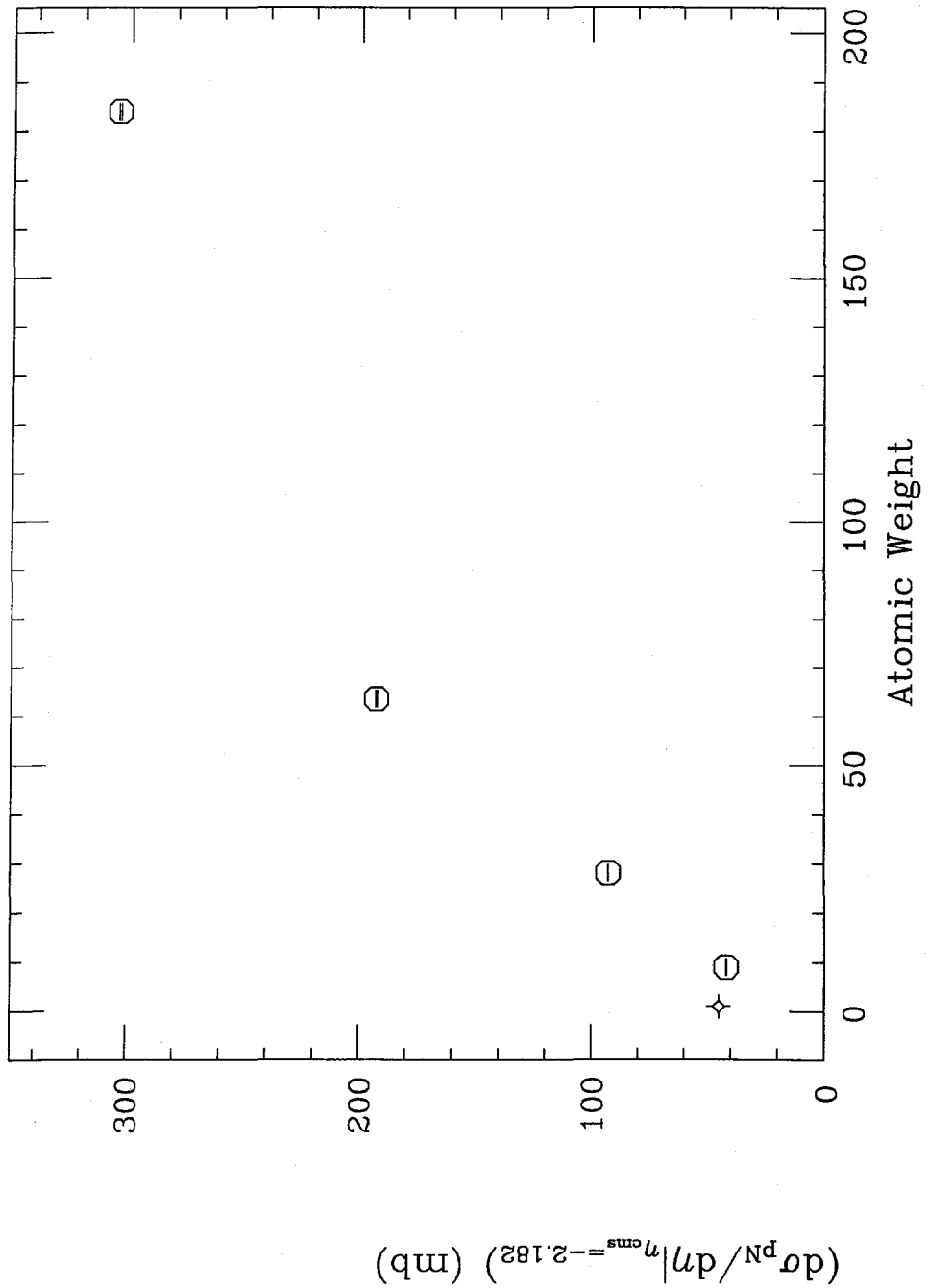

Figure 4.6: LTELE inclusive cross section as a function of target material.

originally intended to run with the silicon target, many data points were obtained from different tapeset intervals. Figure 4.7 shows a plot of $d\sigma_{pN}/d\eta$ versus Tapeset Number for the silicon target. This extended over a period of two months near the end of the run. As shown in the plot, those points at the end of the run were related to an increase in the beam intensity. This was a time when the beam intensity was pushed up to and beyond rates that some components of the spectrometer were expected to withstand. Numerous tests were also being performed. Although the lack of consistency in cross section measurements in this part of the run is not understood, it is not surprising.

Table 4.2 shows the data and cross section values for particle production using the silicon target for several tapesets sampled. These are for those data points shown in Figure 4.7.

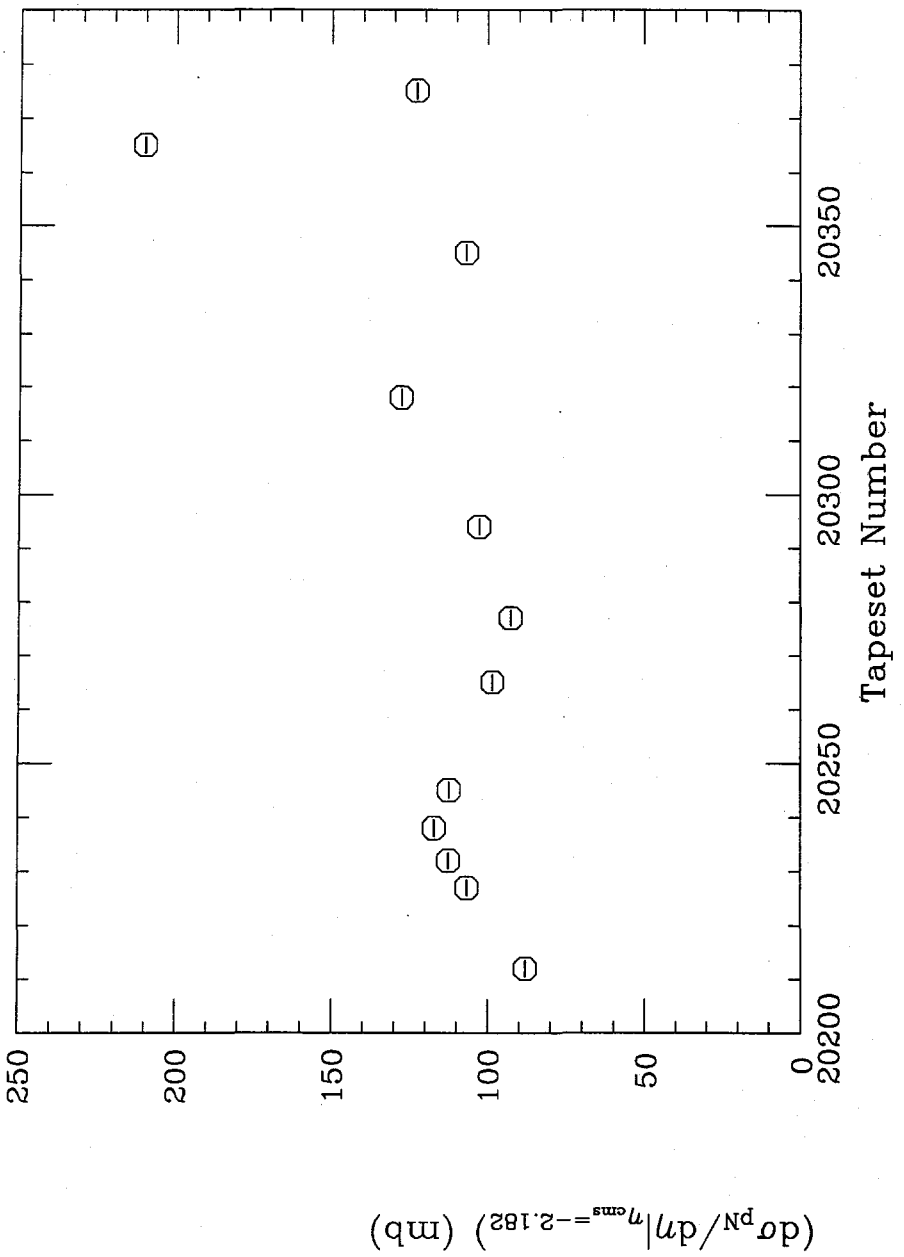

Figure 4.7: LTELE inclusive cross section as a function of tapeset number for a silicon target.

Tapeset #	$(d\sigma_{si}/d\eta)$ $(barns)$	$(d\sigma_{pN}/d\eta)$ (mb)
20212	0.813 ± .00499	87.890 ± .1779
20227	0.985 ± .00430	106.49 ± .1533
20232	1.040 ± .00180	112.43 ± .0641
20238	1.083 ± .00253	117.08 ± .0903
20245	1.038 ± .00162	112.22 ± .0577
20265	0.910 ± .00192	98.380 ± .0684
20277	0.856 ± .00151	92.540 ± .0537
20294	0.948 ± .00161	102.49 ± .0574
20318	1.180 ± .00168	127.57 ± .0596
20345	0.987 ± .00185	106.70 ± .0657
20365	1.944 ± .00725	210.16 ± .2582
20375	1.135 ± .00098	122.70 ± .0350

Table 4.2: Data and cross sections using LTELE as a function of tapeset number for the silicon target.

Chapter 5

Monte Carlo

5.1 PYTHIA and JETSET

Monte Carlo programs are a common occurrence in high energy physics. These programs are mainly written to aid experimentalists in estimating what kind of physics they will observe given a particular experimental spectrometer and a particular running mode, such as a collider run or a fixed target run. The PYTHIA [29] and JETSET [30] programs are packages developed to simulate particle production. PYTHIA's main purpose is to generate events according to specific phenomenological criteria. The resulting events are used to check theory against experiment, to aid in the design of future experiments based upon results from Monte Carlo generation programs, and to confirm or question new observations based upon the Standard Model and its predictions. JETSET, on the other hand, takes an event that PYTHIA generates and deals with the jet fragmentation aspects for that particular event. In an event generation step, a parton configuration is selected, and this in turn is fragmented into multiple hadronic decays using the electroweak and QCD theories. The step may continue on down the chain with the unstable hadrons decaying into their constituents.

As E771's main objective was the study of B physics, PYTHIA and JETSET were used to simulate a fixed target run not only for $b\bar{b}$ events, but for $c\bar{c}$ events and minimum bias events as well. These particular run modes were used to determine how strangeness might behave under certain conditions. It is with these Monte Carlo programs that one can extrapolate to an ideal "effectiveness" for obtaining differential cross sections, p_t distributions, optimal rapidity distributions, etc.

5.2 Fast Monte Carlo

A Monte Carlo program was written to simulate strange particle decays and subsequent travel of their decay products through E771's spectrometer. The main aspect of this fast routine was that it generated two tracks according to the kinematical variables of a K° particle or a Λ° particle. For simplicity, we shall describe one daughter track from the decay. The parent strange particle is generated randomly according to hypothetical rapidity and p_t distributions. Particle decay is taken to be isotropic in the rest system of the parent. Momentum is then transformed relativistically into the laboratory or the center of mass system as needed.

The daughter track proceeds through the front part of the tracking chambers where it passes through the magnetic field experiencing a p_t kick. Assuming the particle has made it this far, it is kicked off in another direction for its final journey through the rear spectrometer region. (For the purpose of this discussion, only the front and rear chambers were used. The charged particle hodoscope, the electromagnetic calorimeter, and the resistive plate counters were excluded.)

A sample plot of the simulation of two tracks traversing E771's spectrometer

is shown in Figure 5.1. The plot depicts two tracks, (A) and (B), emanating from a decay point. (Note how the tracks are extrapolated back to the origin in order to determine their acceptance within a Δx position of the target.) We follow the tracks through the magnet where they experience the B-field that changes their trajectories. The lower momentum track gets deflected the most. Only the front and rear chambers are depicted for our acceptance criteria.

The method by which particles are accepted depends on how many front chamber planes are hit and how many rear chamber planes are hit. The loosest criterion where one could theoretically get a true candidate would be the requirement of a track's traversal through at least three chamber planes upstream of the analysis magnet and at least three chamber planes downstream of the analysis magnet. A more stringent criterion of four planes hit in the front and six planes hit in the rear is used in order to determine variations in track acceptance as this is also the requirement imposed in the main tracking program.

5.2.1 Predictions of (dN/dy) and (dN/dp_t)

Two processes that were necessary inputs to the random event generator were the rapidity distribution and the p_t distribution.

When a specific rapidity interval is assumed for particle production, the experimentally detected distributions may yield different answers depending on spectrometer acceptances, efficiencies, and other such variables. The rapidity is defined as

$$y = \frac{1}{2} ln(\frac{E + p_z}{E - p_z}), \tag{5.1}$$

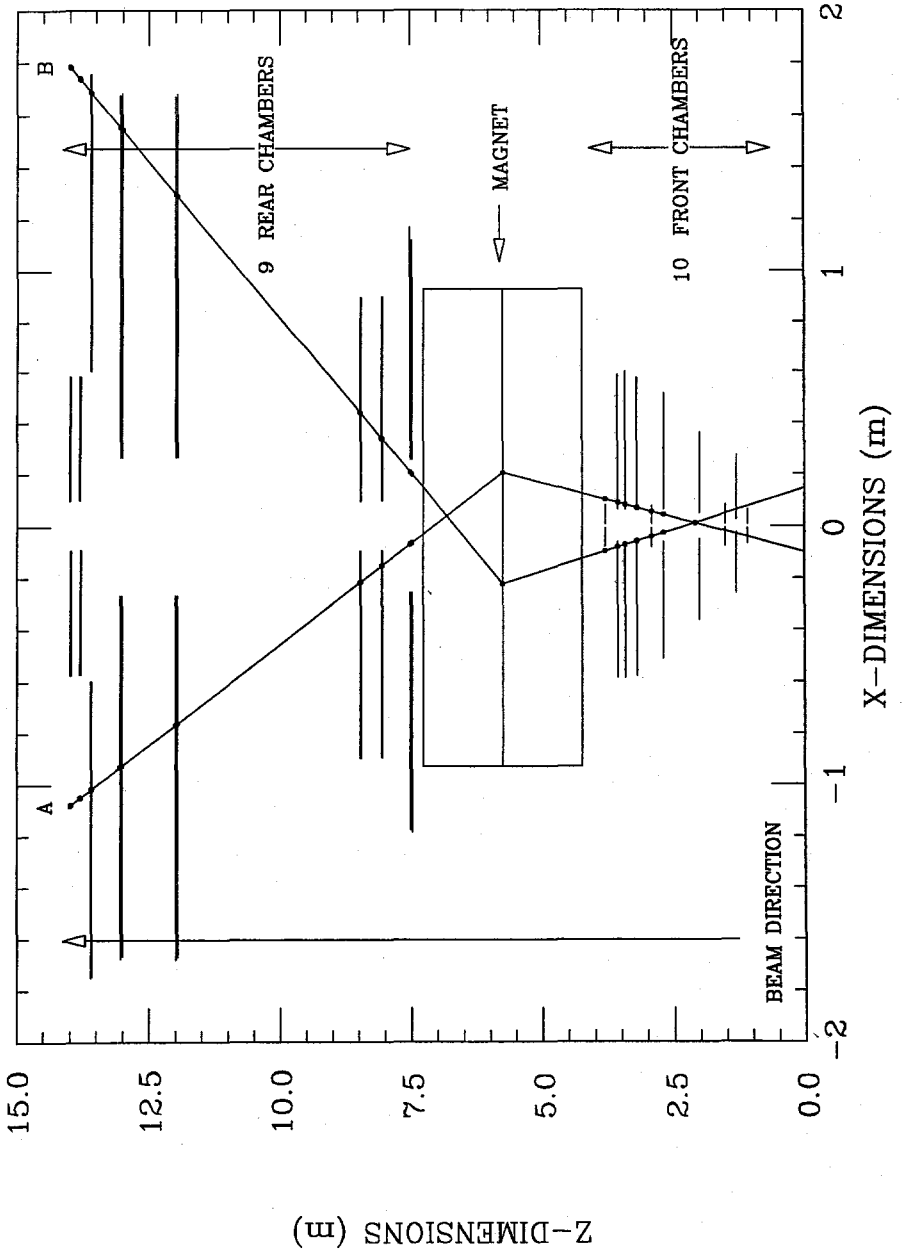

Figure 5.1: Monte Carlo simulated event through E771's spectrometer (not including the CPH, the EMC, or the RPCs).

where p_z is the longitudinal momentum along some direction of interest. Under a relativistic boost in the z-direction to a frame with velocity β, $y \rightarrow y + tanh^{-1}(\beta)$, and so the shape of the rapidity distribution dN/dy is invariant.

At 800 GeV/c beam momentum, the rapidity in the center-of-mass system had a range such at $|y_{cm}| \leq 3$. With the rapidity distribution being established and observed at lower energy experiments, a function was devised to extrapolate lower energy data to 800 GeV/c. Once these extrapolated points were plotted, a run on PYTHIA was performed for a number of beam energies. The resultant PYTHIA rapidity distribution was overlaid on both real and extrapolated data points for comparison. As it turned out, the PYTHIA run ended up following what was observed and expected. Therefore from a PYTHIA run of 800 GeV/c, a rapidity distribution was obtained, and a sixth degree polynomial was fit to this spectrum. The fitted parameter values were used as the final rapidity distribution function in the fast Monte Carlo program.

Once any function, $f(x)$, was known, we used a random number generator sequence to obtain values within the range $x_{min} \leq x \leq x_{max}$ [31]. The algorithm selected an x at random so that the probability for a given x was proportional to $f(x)$. The Monte Carlo program used this method to generate all random functions.

The resultant rapidity spectrum for the K° particles is shown in Figure 5.2. The plot shows the generated distribution and the final distribution (shaded region) after all K° tracks made it through the spectrometer and were successfully tracked. As is quite visible, the rapidity region available for particle detection is quite small

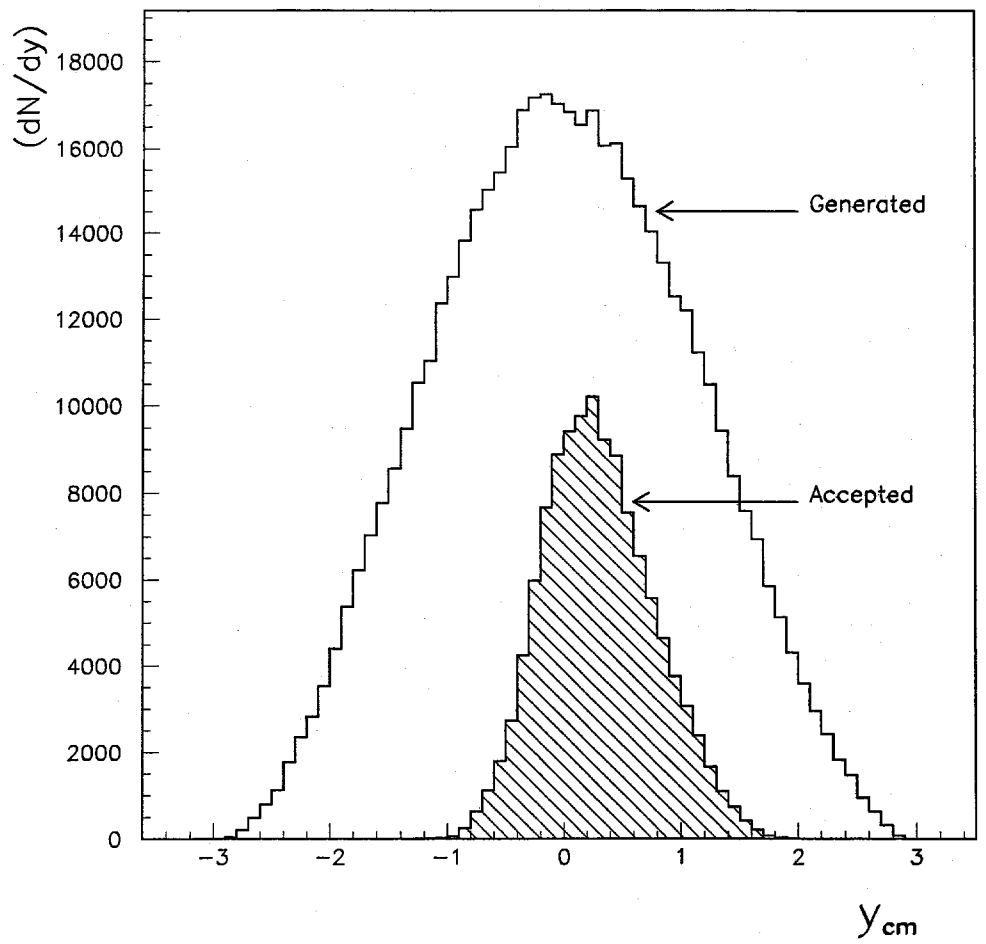

Figure 5.2: Monte Carlo rapidity distribution for K_s° particles showing the generated and accepted distributions.

due to the acceptance, and a big correction factor will be needed when attempting to get the inclusive cross section.

The generated distribution is symmetrical about the origin, but the final accepted distribution is more in the forward region. Loss of events is related to the fate of the daughter tracks from the decay. Those that were of too high momenta went straight down the beam hole and therefore were not tracked. This accounted for the loss in the forward region. Those with too low momenta may have made it through the front part of the spectrometer, but (assuming they made it to the magnet) the magnetic p_t kick would have sent them out beyond the detection capabilities of the rear chambers due to the greater deflected angles. This accounted for the loss in the backward region, and as can be seen by the plot, more tracks were accounted for in the forward region.

Figure 5.3 shows the Monte Carlo rapidity distributions for generated and accepted Λ° events. Following the same outline as described for Figure 5.2, we see a more pronounced loss of Λ° generated particles, about a factor of four greater than that for the K°'s. This may be accounted for by the fact that the Λ°'s are more massive, and due to the small Q-value, most of the momentum is transferred to the heavier proton decay product. This implies that many of the proton tracks go straight down the beam line, therefore never even having a chance of being detected by the spectrometer. Similar to the K° accepted rapidity distribution, the Λ°'s were contained in an interval from about -1.0 to 1.0 in the center-of-mass system. This was accounted for by the small spectrometer acceptance region.

The p_t distribution was also a randomly generated function. At low $\sqrt{s}$ ($\leq$ 15

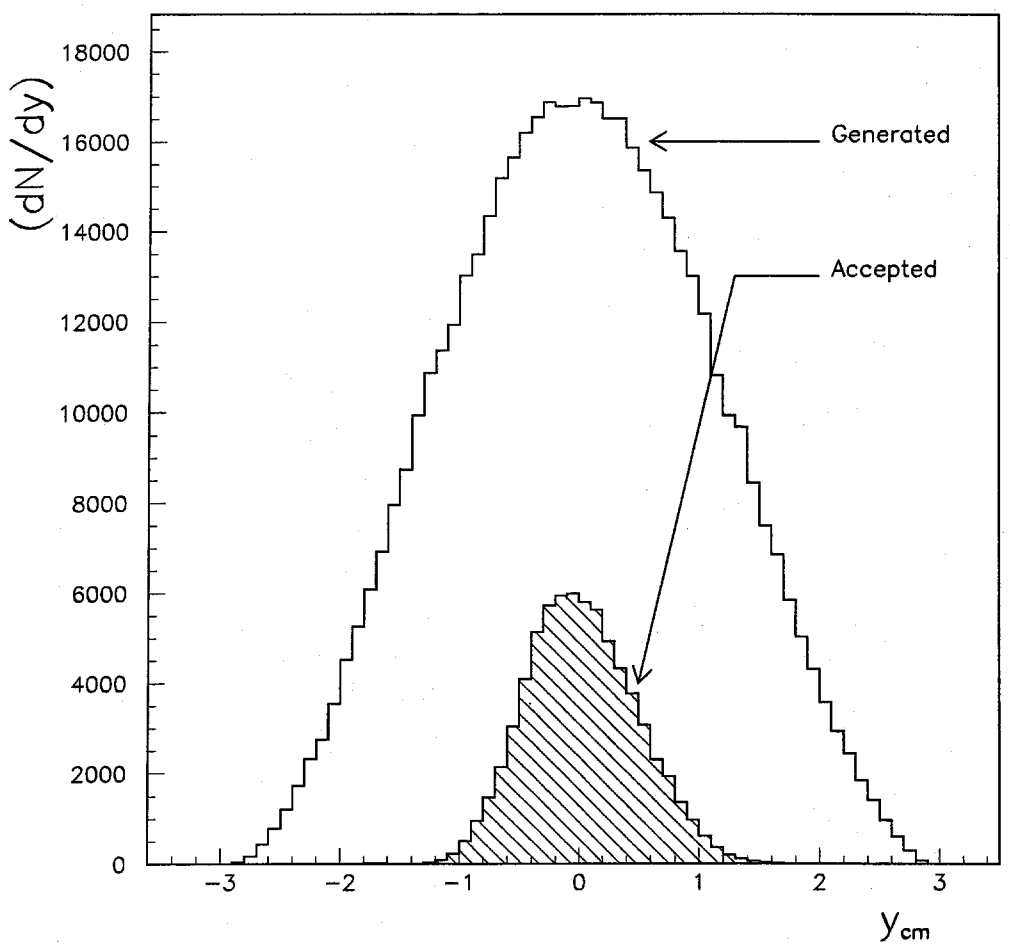

Figure 5.3: Monte Carlo rapidity distribution for Λ° particles showing the generated and accepted distributions.

GeV) transverse-momentum spectra are described relatively well by the thermodynamic model [32] where the invariant inclusive cross section falls exponentially. At low p_t the thermal model predicts the behavior of the form

$$dN/dp_t^2 \sim exp(-\alpha p_t), \tag{5.2}$$

and expansion of the above equation yields at small p_t

$$exp(-\alpha p_t) = 1 - \alpha p_t + ... \tag{5.3}$$

It has been shown that the experimental behavior of mesons with large transverse momenta in hadron-hadron collisions is consistent with the theory of quantum-chromodynamics with asymptotic freedom [33]. The approach yields the correct magnitude and an approximate $1/p_t^8$ behavior in accordance with single-particle data. A function which accommodates both the thermal model at low p_t and the power law at high p_t is

$$dN/dp_t^2 \sim \frac{1}{(1+p_t)^N} = 1 - Np_t + ... \tag{5.4}$$

Equations 5.3 and 5.4 are valid for the small p_t region where they are comparable.

A p_t distribution function for use in the Monte Carlo was achieved by running PYTHIA at 405 GeV/c to see if its p_t distribution curve resembled data at 405 GeV/c [34]. It was determined to be the case, and an attempt was made to fit the 405 GeV/c data p_t distribution curve with a double exponential. It was observed that this particular fitting algorithm did not fit well to data at high p_t, and the power law above was subsequently used yielding a good result. From this and the knowledge that PYTHIA predicted data well for a 405 GeV/c sample run, an 800

GeV/c beam momentum PYTHIA simulation was run and its p_t distribution fit using the power law.

Two slightly different parameters were obtained from PYTHIA for a run on the K°'s and a run on the Λ°'s. With the general formula being of the form,

$$dN/dp_t^2 \sim \frac{1}{(p_t^2+\alpha)^\beta}, \tag{5.5}$$

the p_t distribution for the generation of K°'s was of the form

$$dN/dp_t \sim \frac{p_t}{(p_t^2+0.5608)^{3.927}}, \tag{5.6}$$

and that of the Λ°'s was of the form

$$dN/dp_t \sim \frac{p_t}{(p_t^2+0.8717)^{3.9159}}. \tag{5.7}$$

High p_t implied the negligibility of the α term and therefore the $1/p_t^8$ behavior was observed.

The K° Monte Carlo p_t spectrum shown in Figure 5.4 is plotted as a function of the generated p_t and the accepted p_t. The shaded figure is what the final accepted spectrum looks like. It was normalized to the generated curve to show that the lower momentum tracks were lost. This was due to the fact that the lower momenta tracks, if they made it to the magnet, were deflected at a wide angle and did not pass the rear chamber hit criteria.

The Λ° Monte Carlo p_t spectrum is shown in Figure 5.5 as a function of the generated p_t and the accepted p_t. Following the same argument as given for the K°'s, the curve was normalized to the generated curve to show what particle momenta were lost. In a similar vein as the K° distribution, lower momenta tracks were lost mostly due to the spectrometer acceptance.

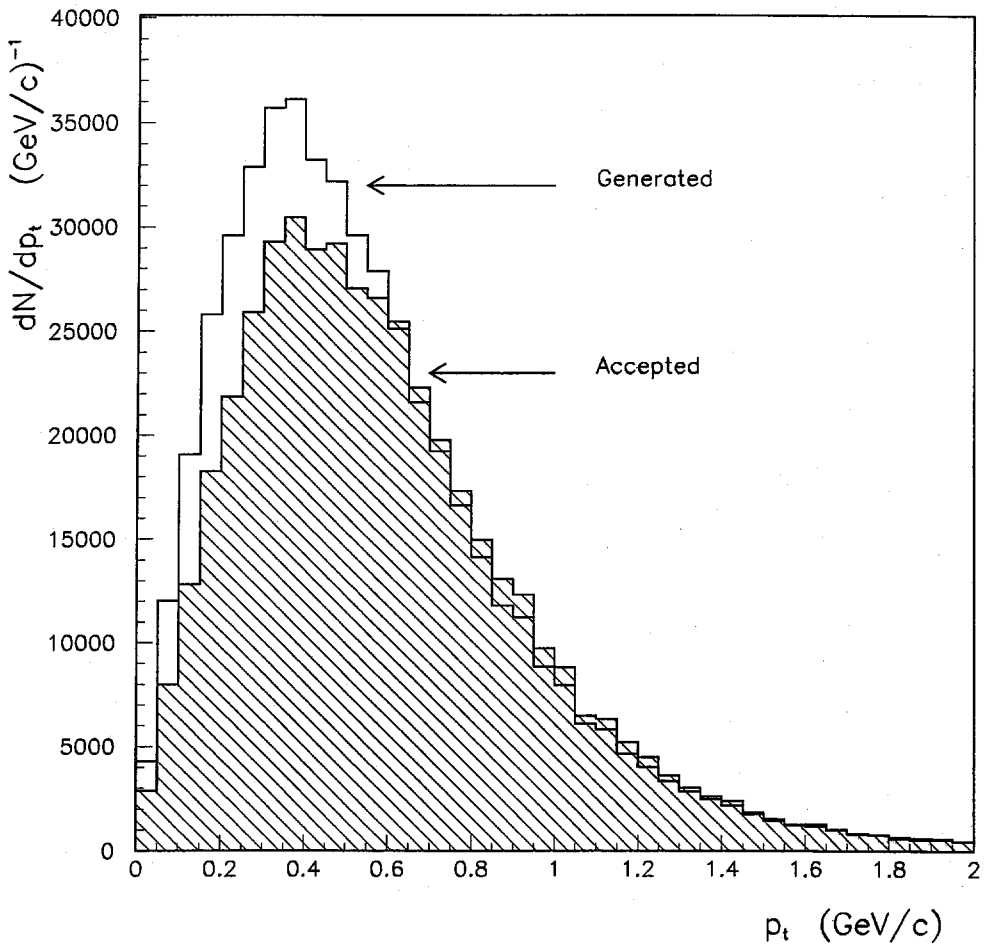

Figure 5.4: Monte Carlo p_t distribution for K_s° particles showing the generated and accepted distributions.

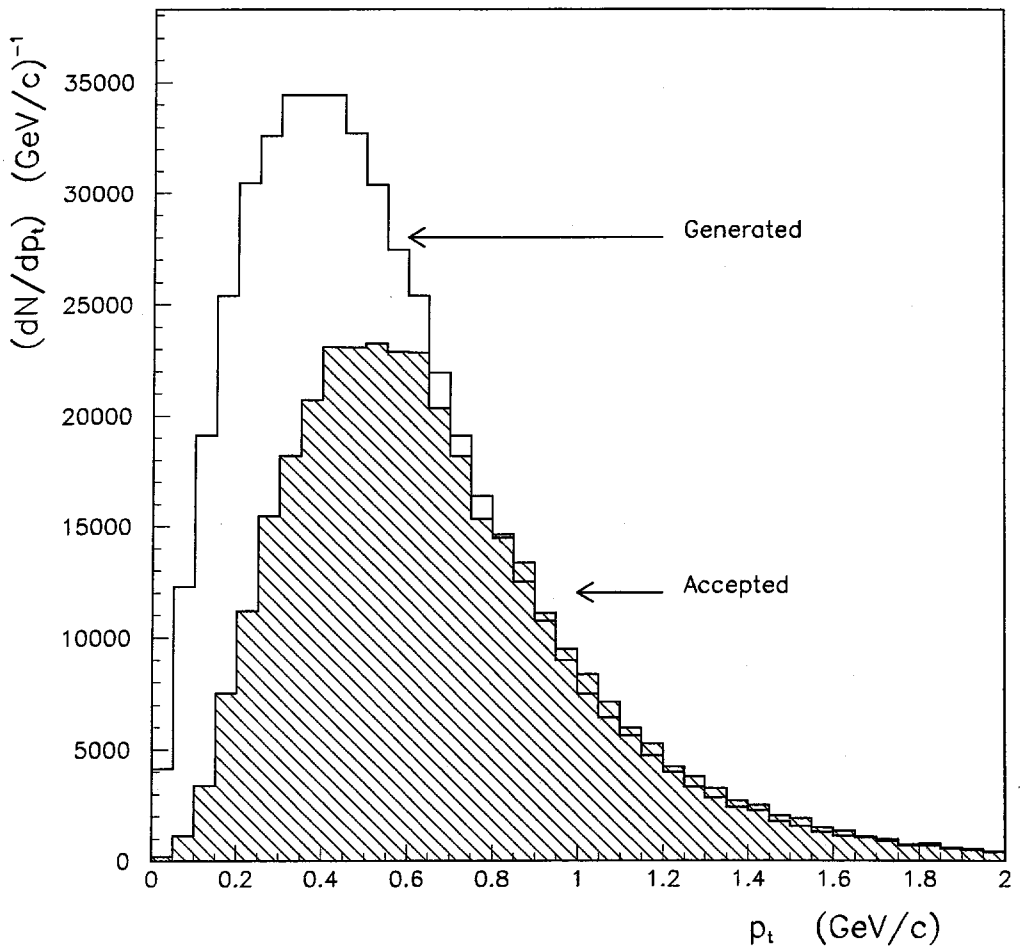

Figure 5.5: Monte Carlo p_t distribution for Λ° particles showing the generated and accepted distributions.

5.2.2 Geometrical Acceptances

The method where statistics were compiled was broken down into different subsections of the Monte Carlo routine, and these included definitions of *good* tracks, *pseudo* tracks, or *poor* tracks. The *good* tracks were the ultimate goal in physics simulations, but the others were added to see what breakdown yielded the most loss. These, of course, constituted the acceptance of a track's passage through both front and rear chambers, hitting the proper number of planes per front and rear criteria. For our intents and purposes, only the *good* tracks were used.

The final breakdown in tracking efficiencies for the K°'s and Λ°'s is summarized in Table 5.1 which illustrates the concept of different criteria on the number of planes required to be hit in the front and in the rear for acceptances. Also compared are acceptances where one includes the individual chamber efficiencies and where all chambers are assumed to be 100% efficient. From the different cuts imposed in this Monte Carlo routine, the efficiencies for the K°'s ranged from 30.13% to 17.75% and that for the Λ°'s ranged from 22.76% to 10.12%. As is obviously apparent, the poor acceptance for detection of the neutrals was due mostly to the limited spectrometer geometry. This is thus incorporated into the overlay tracking program to achieve the overlay efficiency one uses to correct up for an "ideal" spectrometer region (i.e., 100% acceptance), to be discussed in the next section.

5.3 GEANT Monte Carlo

The ultimate goal is to obtain cross sections using the proper correction factors through Monte Carlo simulations. The GEANT [35] Monte Carlo detector simula-

Particle Generated	# Planes Hit in Front	# Planes Hit in Rear	Acceptance via 100% Chamber Efficiencies	Acceptance via Individual Chamber Efficiencies
K_s°	3	3	30.1% ± 0.1%	26.5% ± 0.1%
Λ°	3	3	22.8% ± 0.1%	18.9% ± 0.1%
K_s°	4	6	24.4% ± 0.1%	17.8% ± 0.1%
Λ°	4	6	16.3% ± 0.1%	10.1% ± 0.1%

Table 5.1: E771 Monte Carlo geometrical acceptances with variations on chamber efficiencies and number of planes required to be hit.

tor program was designed for this purpose, and this program's main objectives were to track particles through a spectrometer set up for acceptance studies. It was used mostly for the simulation of secondary interactions resulting from the primary particles interacting with the detector media, etc. The physics processes implemented in GEANT included pair production, Compton scattering, the Photoelectric effect, multiple scattering, photofission, Bremsstrahlung, e^+e^- annihilations, the decay in flight of unstable particles, and hadronic interactions.

5.3.1 K° and Λ° Simulation

The fast Monte Carlo routine was used in conjunction with the GEANT program. As discussed in the previous sections, its purpose was to generate the K°'s and Λ°'s and their subsequent decays into the two charged daughters. The resultant

two decay products and their trajectories, momenta, etc., were fed into GEANT. GEANT then took them and fed them through each step of the spectrometer allowing each track to interact with chamber matter, and other such processes, as it passed through a region, say air or chamber material. In order to reproduce real events as accurately as possible by Monte Carlo techniques, GEANT simulated the physics processes in small step modules.

Once an event made a successful completion through the GEANT simulator, it was stored in a file for later use in the *overlay* tracking analysis. The meaning behind the overlay analysis is that a GEANT generated track is overlaid on a real data event for event reconstruction. This is to determine how well the tracking program is at tracking a known particle that exists among all the other chamber hit points in the event. If an event has too many hits in some chamber planes, the overlay efficiency will be worse than for an event that has fewer chamber hit points since the track reconstruction will be relatively harder to do.

As shown in Figure 5.1, an LED triggered minimum bias event shows the front and rear chamber planes and the associated hits per chamber plane. As can be seen, the hit density is quite high for the front chamber planes, and not as dense for the rear planes. An LED triggered event usually had a much smaller multiplicity than the single and double muon triggered events, so it can be imagined that overlay tracking on muon triggered events would yield a relatively low reconstruction efficiency due to the high hit density. In order to get a total differential cross section, the overlay tracking was used on the LED minimum bias triggered events.

The process where an event is overlaid requires the GEANT generated track's

hit points to be immersed in the real event's hit points. The main tracking program (to be discussed in Chapter 6) then tracks the original event plus the extra GEANT hit points as the overlay event. The main purpose is to determine whether the original track will be reproduced. If it is not, which occurred quite frequently, then there was a loss in tracking efficiency. This needed to be accounted for and corrected. It was determined that the tracking efficiency was 48% efficient per track, and due to the decay of a V° into its two constituents, this further reduced the tracking efficiency to 25%.

5.3.2 Event Reconstruction Efficiencies

There were five steps involved in getting the tracking overlay efficiency and the correction factor. They were:

- Finding the number of neutral particles seen within a cut interval, a cut interval being the requirement that a particle decay a specified distance from the main interaction target, the two daughter tracks intersect within a small Δz region, and sometimes the imposition of the tracks being coplanar for cleaner signal peaks. The method used for extracting the signal over the background was by a Gaussian fit to the signal mass peak with a polynomial fit for the background.

- Calculating the correction factor for the number of entries. This required taking the ratio of the number of entries counted for the overlay mass distribution to the number of entries counted for the real data mass distribution. This correction factor was used to correct for the number of real data V°'s

seen in the overlay plots since we only wanted to count the number of overlaid V°'s to get at the overlay efficiency.

- Calculating the number of overlay neutral particles seen within a cut interval. This was determined by the form

$$xsig_{ov} = sig_{ov} - (\frac{N_{ov}}{N_{evt}})sig_{true} \ ,$$

where sig_{ov} was the number of overlay V°'s fitted by a Gaussian for the signal, $(\frac{N_{ov}}{N_{evt}})$ was the number of entries correction factor, and sig_{true} was the number of true V°'s from the real data sample obtained from a Gaussian fit to the signal peak.

- Calculating the overlay efficiency by

$$\epsilon_{ov} = \frac{xsig_{ov}}{N_{tot}} \ ,$$

where N_{tot} was the total number of Monte Carlo events analyzed.

- Calculating the correction factor, which was defined as

$$N_{corr} = \frac{x_{sig}}{\epsilon_{ov}} \ .$$

The overlay event reconstruction efficiencies are an integral part in the determination of the V° cross section. The efficiencies will vary for the type of particle tracked, be it the K° or the Λ°.

Chapter 6

Neutral Particle Selection Criteria

6.1 E771 Main Tracking Program

The E771 main spectrometer tracking program reconstructed the full set of tracks that traversed the spectrometer region for a particular trigger criterion being satisfied. This method of tracking was broken down into several steps such as looking for a muon triggered event in order to proceed with the main tracking, and if such a muon candidate was found, performing rear tracking analysis along with the front tracking analysis and the vertex reconstruction algorithm.

A muon triggered event was realized by the triple coincidence of a track through the three RPCs, each sandwiched between layers of concrete and steel absorbers in order to disallow the passage of hadrons and allow for the passage of the most energetic muons $\geq$ 10 GeV/c in the central region and $\geq$ 6 GeV/c in the outer wing region. Once an event was tagged as having a muon trigger in it, the event was saved for later reconstruction.

The tracking begins by finding 2-dimensional x view tracks and 2-dimensional y view tracks. Next, their 3-dimensional trajectories are found by linking the x-views and y-views with the stereo hits (the U and V planes). A similar procedure

is used for the front tracking, finding the 2-dimensional x view tracks and the 2-dimensional y view tracks, and subsequently finding their 3-dimensional trajectories by linking the x-views and y-views with the stereo hits. Once the front and rear tracks are found, a method used for the "matching" of the front and rear tracks is implemented to match front and rear track segments at the magnet. In order for the front and rear segments to be considered a match, the difference in the x intercept value for the front and rear segments must be less than 0.8 *cm*, the difference in the y intercept value for the front and rear segments must be less than 1.8 *cm*, and the front and rear y slope difference must be less than 5 *mrad*.

The primary vertex calculation evolved from a crude determination of the interaction primary vertex. This method for determining the vertex required the reconstruction of the beam tracks. As the beam protons approached the targets, they left in their wake hits in the beam silicon planes, three planes in X and three planes in Y. The beam tracks were then reconstructed from these hits, and from this a crude determination of the interaction primary vertex was possible. X and Y tracks were then sought in the silicon tracker planes near the location of the crude primary vertex. The searching algorithm allowed for a window of 8 *mm* in X and 8 *mm* in Y around the crude primary vertex. A χ^2 method was applied where the least χ^2 was desired for the fitting procedure, and a minimum of three hits per track was required in five planes of the X view and five planes of the Y view. The χ^2 was defined as

$$\chi^2 = \sum_{j=1}^{n} \frac{\delta_j^2}{\sigma_j^2}, \tag{6.1}$$

with the distance of closest approach (impact parameter) between a track and

the primary vertex position being defined by δ_j for the jth track, and the error in the jth track being defined by σ_j. The looping of the j=1, n tracks only dealt with 2-dimensional tracks since 3-dimensional tracking was difficult due to the lack of stereo (U and V) planes in the silicon tracker. If a χ^2 value of around 200 was obtained, it was determined that a primary vertex was found, otherwise the procedure was repeated with the remaining tracks in order to achieve a reasonable χ^2 measurement.

A tracking display program, developed at the University of Virginia, was written to allow the display of any region of the E771 spectrometer. This was useful in allowing users to view candidate tracks in any region they wished. If the front part of the spectrometer was desired, a switch could be activated to allow the observation of tracks in that vicinity. This was an interactive program which allowed the user to determine invariant masses, create and/or delete tracks, and so on. A sample display of matched and unmatched tracks is shown in Figure 6.1 which gives a view of the whole spectrometer. This particular plot was from a sample run of LED triggered events defined as minimum bias events. The dashed lines in the plot indicate tracks that were not matched for front/rear combinations, and the solid lines are those where matched tracks occurred for both front and rear track segments. A high density of chamber hits existed near the beam region upstream of the analysis magnet. Tracks are drawn using the number of hits each chamber plane gets. If a particular line passes through four planes of hit chambers, say, then it is considered a track candidate.

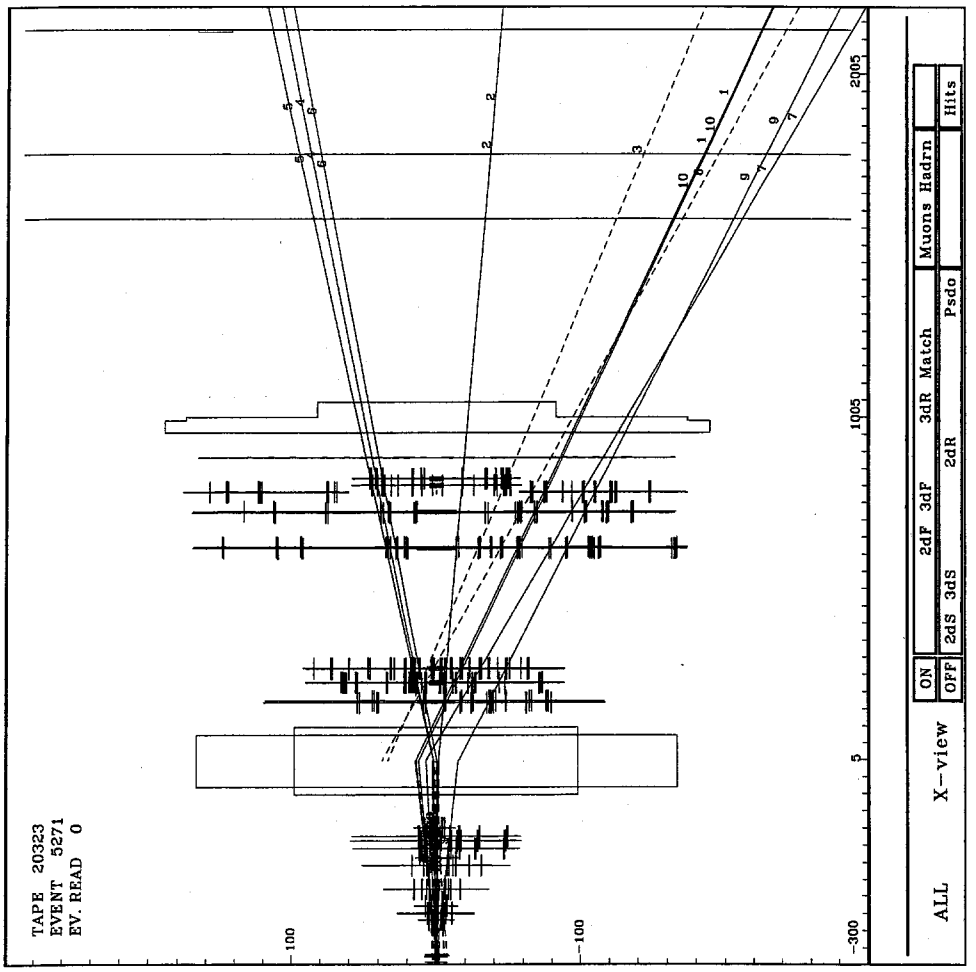

Figure 6.1: Sample display of a tracked LED (minimum bias) event. The solid lines indicate those tracks that were matched in the front and rear, where the dashed lines indicate no front-rear matched combinations.

6.2 Neutral Strange Particle Analysis Routine

A separate analysis routine was written for the extraction of neutral strange particle production (NSPP). This analysis routine used the results from the main tracking program. As detailed in Chapter 3, the raw data were written to 8 *mm* gigabyte data tapes, and the main tracking program's results yielded Data Summary Tapes (DST's). Due to the large number of events written to tape, it was desirable that the processed event information be compressed in order to achieve the smallest event record while maintaining the relevant event information. "Trash tracks", for example, that did not meet specific tracking criteria were not recorded onto the DST's. The DST's were further reduced in record size to allow for faster analysis procedures. The further reduced data were labeled DSA, DSB, and finally DSC, "C" being the most tuned output tapes for this thesis. "Bare bones" information relevant to neutral strange particle production was retained on the DSC's, information such as slope and intercept values, number of tracks per event, momenta information, covariance matrices, primary vertex information, and other such relevant parameters.

The main aspect of the NSPP program was the invariant mass calculation. The mass is calculated via

$$M = \sqrt{(E_a + E_b)^2 - (\vec{P}_a + \vec{P}_b)^2}, \tag{6.2}$$

with $\vec{P}_a$ and $\vec{P}_b$ being further reduced to

$$|\vec{P}_a| = \sqrt{P_{xa}^2 + P_{ya}^2 + P_{za}^2}, \tag{6.3}$$

and

$$|\vec{P_b}| = \sqrt{P_{x_b}^2 + P_{y_b}^2 + P_{z_b}^2}. \tag{6.4}$$

"a" and "b" refer to the two charged tracks. The momentum of a track was defined by its change in slope as it traversed the magnet and experienced a p_t kick. The momentum in the xz-plane was defined as

$$p_{xz} \quad (GeV/c) = \frac{0.821}{|sin(\theta_{rear}) - sin(\theta_{front})|}, \tag{6.5}$$

where 0.821 GeV/c was the magnet induced p_t kick, $sin(\theta_{rear})$ the xz projected angle the track makes with respect to the beam axis (the x slope of the rear track) after it has traversed the magnet, and $sin(\theta_{front})$ the projected angle the track makes with respect to the beam axis (the x slope of the front track) before encountering the magnet.

Another aspect of the NSPP program was the calculation of the decay vertex of the V°. This was relevant in studies extracting the signal from the noise (to be discussed later). A variable describing the distance of the V° from the primary interaction was defined as

$$z_{dcy} = z_v^w - z_{vtx}, \tag{6.6}$$

where z_{vtx} was the z position of the primary interaction vertex, and z_v^w, the weighted average for the z-coordinate of the V° vertex in the x-z plane and the y-z plane,

$$z_v^w = \frac{(\frac{1}{\delta z_v})_{rms} \cdot z_v + (\frac{1}{\delta z_v^{'}})_{rms} \cdot z_v^{'}}{(\frac{1}{\delta z_v})_{rms} + (\frac{1}{\delta z_v^{'}})_{rms}}. \tag{6.7}$$

z_v was the decay z-position found in the x-z plane and $z_v^{'}$ was the decay z-position found in the y-z plane. δz_v and $\delta z_v^{'}$ were the errors in the z-position in the x-z and

y-z planes, respectively, as obtained from the error matrix of the track fitting.

Once the decay vertex was found, cuts could be imposed on decay regions, such as the requirement that the V° decay a specified distance from the main interaction region. These different cuts were imposed to extract a good signal to background ratio. With the K° and Λ° being of a relatively long life, the requirement of a decay a finite distance from the main target reduced the number of high background combinatoric tracks as well as a reduction in the V° candidates.

Once the decay position was found, and the two daughter tracks were obtained, a Δz cut was placed on the allowable difference in z position for track intersections in the x-z plane and intersections in the y-z plane. Δz was defined as

$$\Delta z = z_x - z_y, \tag{6.8}$$

with z_x being the z-coordinate of the two track intersection seen in the x-z view, and z_y being the z-coordinate of the two track intersection seen in the y-z view. In Figure 6.2, the Δz spectrum is plotted for all events, and it is readily noticeable that the spectrum begins to form its peak at around 20 *cm*. Various tests were performed on different $|\Delta z|$ cuts in order to extract the best possible signal. Optimum cut values varied when looking at the K°'s as compared to the Λ°'s. To reduce analysis CPU time, cuts were imposed on the z_{dcy} of the V° and its $|\Delta z|$ value.

Another step used to get a good signal peak involved searching for coplanar events, that is, events where the V° and its constituents were all produced in the same plane. This particular method used the "double cross dot product". The

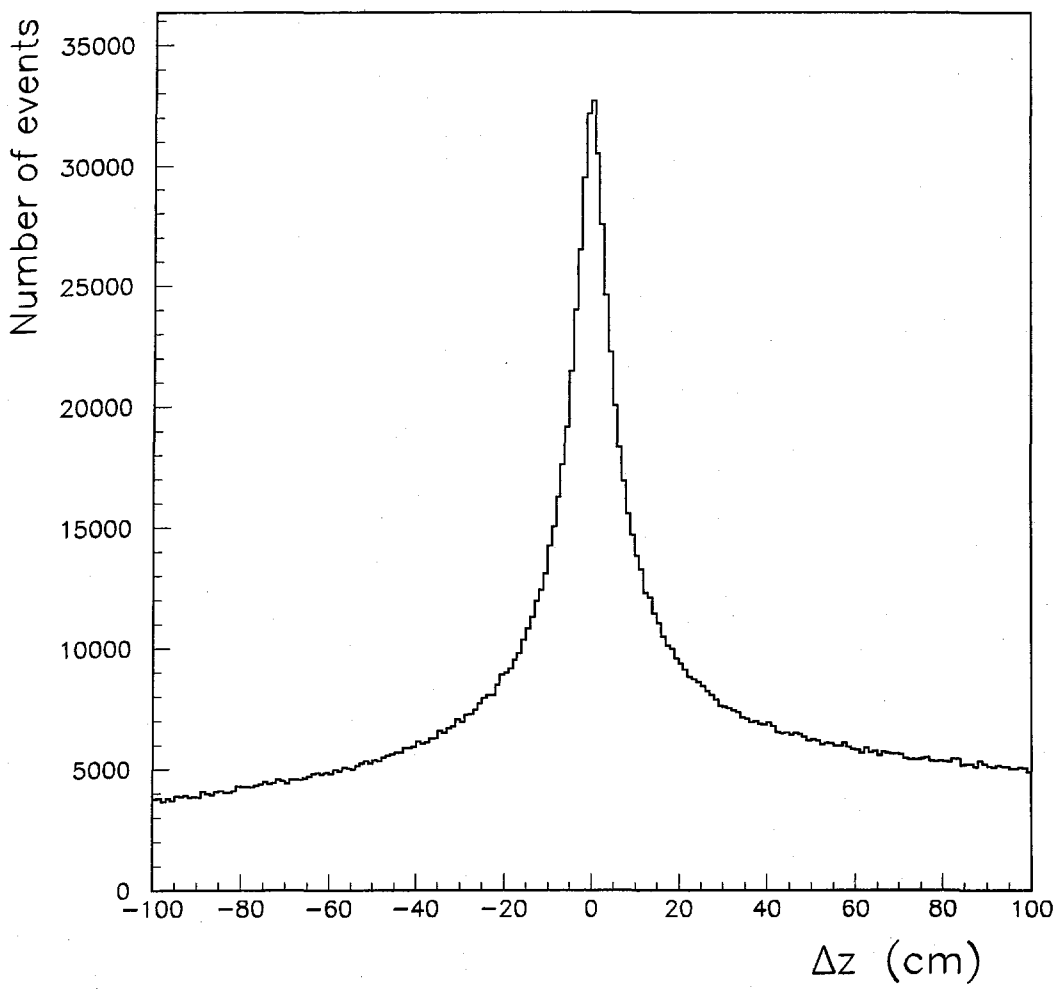

Figure 6.2: Δz distribution for two charged tracks.

variable used for cuts was

$$cos(\theta) = \frac{(\vec{V} \times \vec{a}) \cdot (\vec{b} \times \vec{V})}{|\vec{V} \times \vec{a}||\vec{b} \times \vec{V}|}, \tag{6.9}$$

where $\vec{V}$, $\vec{a}$, and $\vec{b}$ were the momentum vectors of the V° and the first and second decay products, respectively. If a truly coplanar situation existed, this implied that $cos(\theta) = 1$. It was determined that an optimum cut off for coplanarity acceptance was $cos(\theta) \geq 0.95$. It is readily observable, by Figure 6.3, that most tracks in this data analysis were non-coplanar, therefore with the tight cut on coplanarity, many background events were significantly reduced, yet the signal was reduced as well. It still proved to be a valuable cut in terms of a good signal to background ratio when performing mass spectrum fits.

6.3 K° Invariant Mass Plots

One of the main goals of this thesis is to measure good cross section values for K° and Λ° production. In order to do this, a method was developed whereby clean mass peaks were obtained for the V°'s. Figure 6.4 shows an example of the evolution of the K° peak becoming more pronounced as an attempt to increase the signal/background ratio was made. Plot (a) shows the raw mass spectrum, for unlike sign charged tracks, without the imposition of any cuts. Due to the many combinatorial background pairs, there is absolutely no indication of the existence of any neutral strange particles. With the lifetime of the K° being 0.892×10^{-10} *sec* and that of the Λ° being 2.63×10^{-10} *sec*, their respective $c\tau$ lengths are 2.6 *cm* and 7.89 *cm*. (The $c\tau$ of the B_s meson, on the other hand, is 402 μm at rest, four

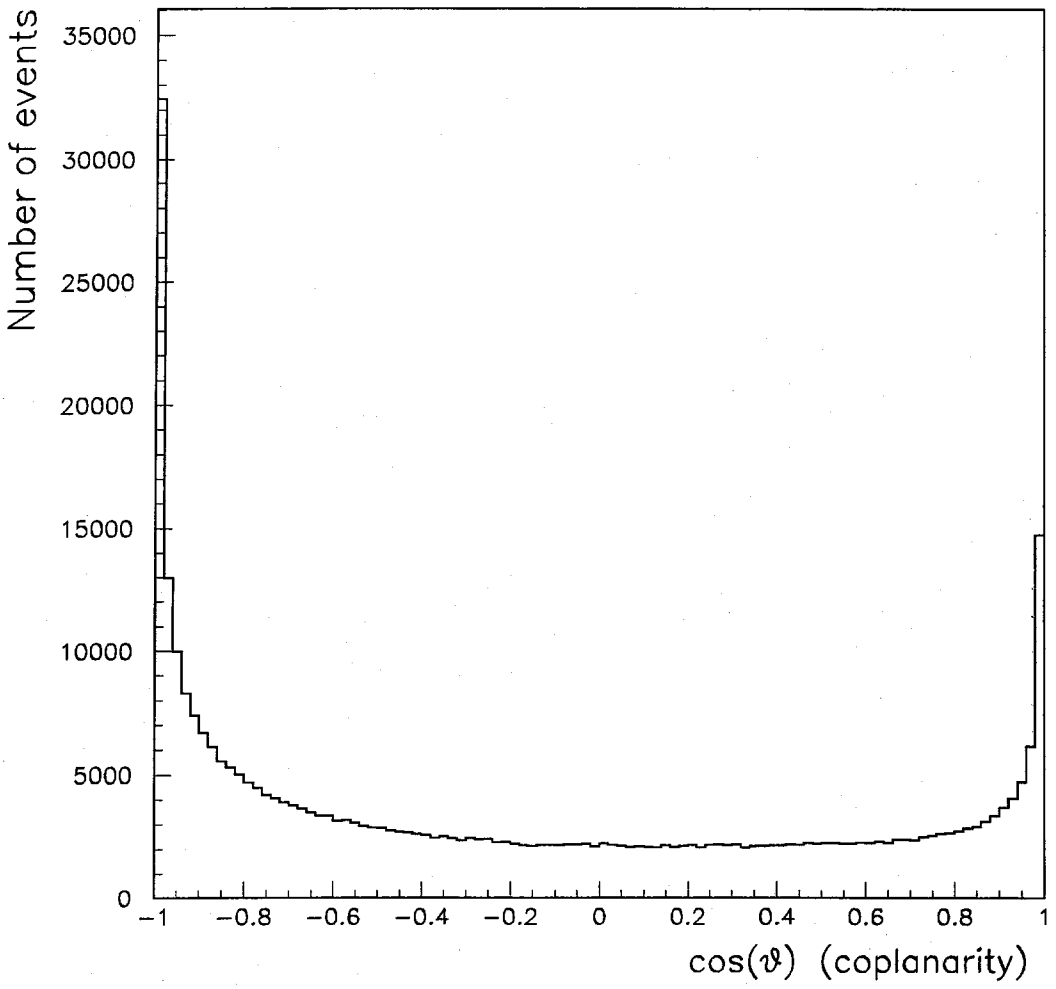

Figure 6.3: $cos(\theta)$ distribution for decay of the K_s° into its two constituents.

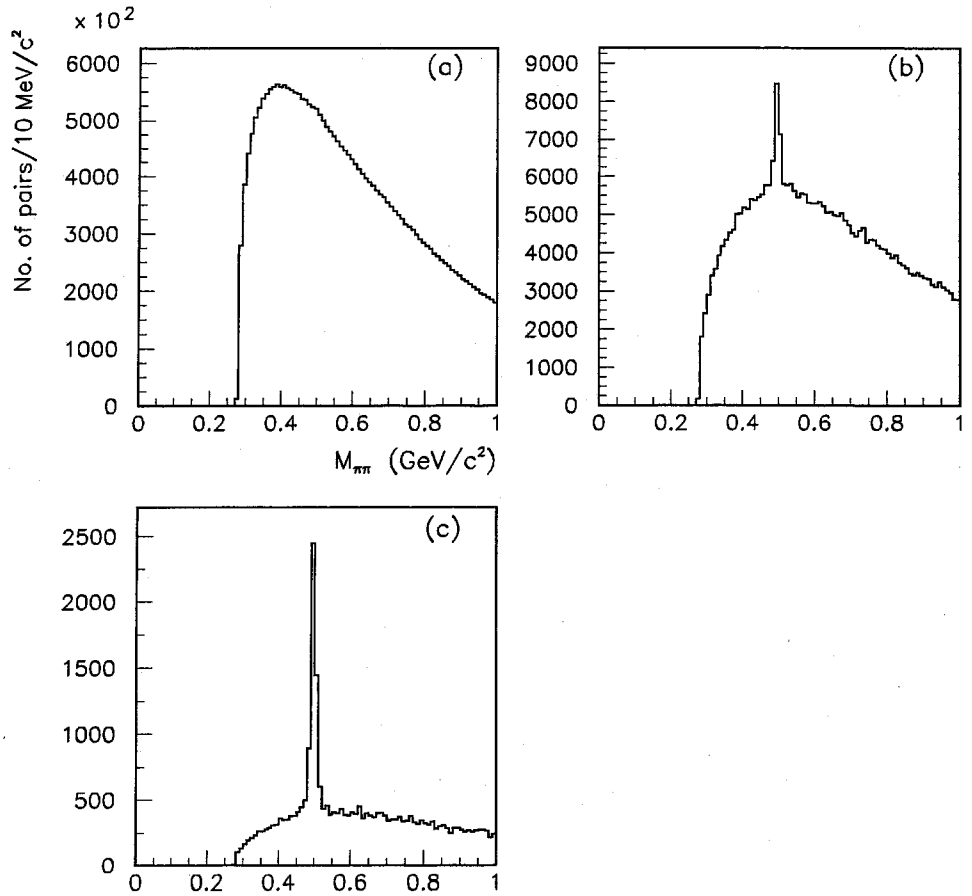

Figure 6.4: Invariant mass distributions for $K_s^\circ, \overline{K_s^\circ} \rightarrow \pi^\pm\pi^\mp$ for unlike sign charged tracks.

orders of magnitude different from the K° and Λ°.) With the particles Lorentz boosted, their decay lengths are increased as a function of the V° momentum. This four orders of magnitude difference allowed for a requirement of the V°'s to have decayed a specified distance from the main interaction target. Plot (b) is a result of such a cut. The background begins to get cut out allowing for the observation of a K° peak. Not only was a z_{dcy} cut imposed for this figure but a Δz cut as well, with z_{dcy} greater than 30 cm and $|\Delta z|$ less than 10 cm. Plot (c) is a final plot with a good signal to background ratio for the K°'s. This plot has the same cuts as in (b), with the added condition that the tracks be coplanar, with $cos(\theta)$ $\geq$ 0.95. The K° has both lower average momentum and a greater energy release (Q-value) on decay than the Λ°. This implies large decay opening angles for the K°, and thus permits tighter cuts on Δz and coplanarity.

As Figure 6.4 shows the K° invariant mass plots for unlike sign charged tracks, Figure 6.5 shows the exact same plots but for like sign charged tracks. This is to show that no K° peak occurs for like sign tracks, as a neutral Kaon only decays into two oppositely charged particles. The plot in (a) shows the invariant mass without any cuts imposed, and plot (b) shows the invariant mass with a z_{dcy} cut greater than 30 cm and a $|\Delta z|$ cut less than 10 cm, and finally plot (c) shows the invariant mass with the same cuts as in (b) but with the added condition that the tracks be coplanar.

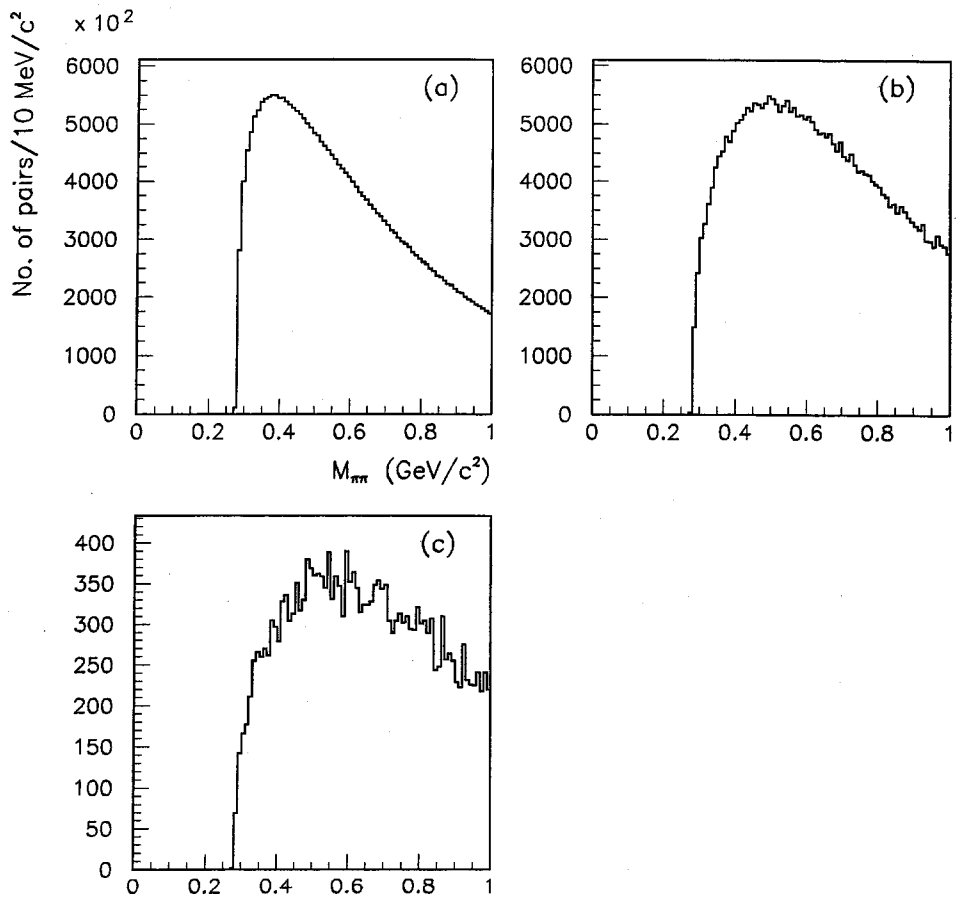

Figure 6.5: Invariant mass distributions for $K_s^\circ, \overline{K_s^\circ} \rightarrow \pi^\pm\pi^\pm$ for like sign charged tracks.

6.4 $\Lambda^\circ/\overline{\Lambda^\circ}$ Invariant Mass Plots

A method similar to that used for the K° mass plots was followed for the Λ°'s, with an added condition on the momentum of one of the constituent tracks. The proton momentum, on average, is larger than the pion momentum with the proton carrying about 87% of the Λ° momentum and, therefore, it will be oriented almost in the direction of flight of the Λ° and point towards the interaction vertex. The Λ°, having a very small phase space, imparts most of its momentum to the proton, the more massive of the two decay products. This in turn yields a high momentum track which experiences a relatively low p_t kick as compared to its π^- companion. Due to this phenomenon, the proton and pion have a relatively small opening angle between them as compared to that of the K°'s constituents. As a result, the calculation of the extrapolated tracks back to the original decay vertex has a bigger error in the Δz condition. Looser Δz cuts had to be imposed on the Λ°'s in order not to lose the signal as compared to more stringent cuts on the Kaons.

Since it was determined that the proton would always have the greater momentum of the two decay products, a cut was made that the momentum of the proton (anti-proton) be greater than a constant multiplied by the momentum of the pion. This factor was determined from a Monte Carlo run for a plot of the momentum of the proton versus the momentum of the pion, as depicted in Figure 6.6. As shown in the plot, the momentum of the proton was indeed generally much greater than that of the pion, and therefore, a clear characteristic line displayed itself from which the multiplicative factor of 3.33 was determined.

With this added condition in the invariant mass spectra plots for the Λ°'s,

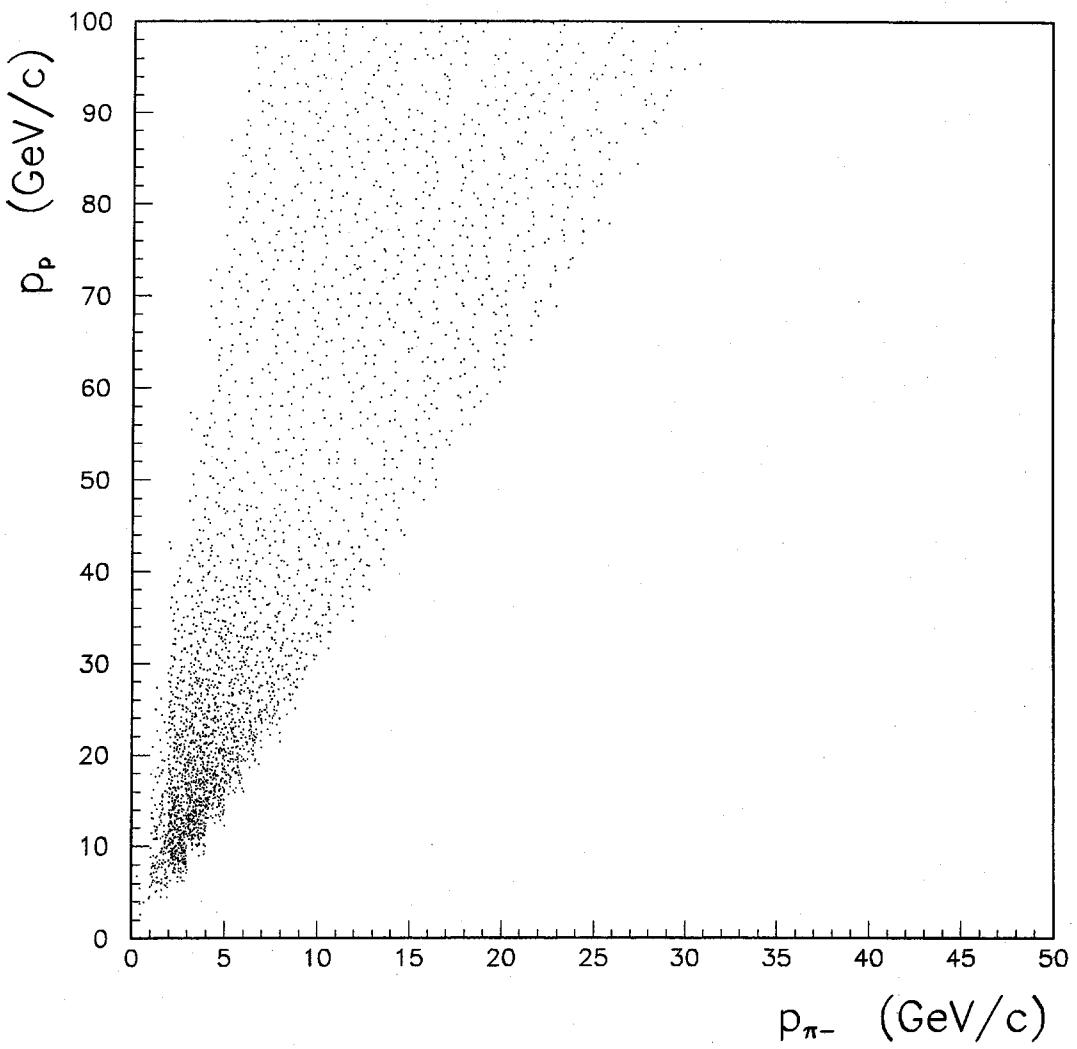

Figure 6.6: Monte Carlo distribution of p_p vs. p_{π^-} for Λ° decays.

Figure 6.7 shows the different steps used in extracting a clean peak. Plot (a) shows the invariant mass without any cuts. Plot (b) shows the invariant mass with a z_{dcy} cut $\geq$ 30 cm from the main target and a $|\Delta z|$ cut $\leq$ 10 cm. Plot (c) shows the invariant mass with the same conditions as (b) but with the added requirement that the momentum of the proton is greater than 3.33 times the momentum of the pion. Plot (d) shows the invariant mass with the same conditions as (c) but with an added requirement that the tracks be coplanar. The wide bump centered at 1.15 GeV/c^2 is indicative of the Ξ^- mass distribution. Although its mass is 1.32 GeV/c^2, the bump has a different mass value which is produced by pairing the proton with the pion from the cascade decay rather than the pion from the lambda decay. This is commonly called the "wrong pion", as shown in Figure 6.8.

Figure 6.9 shows some plots of the invariant mass spectrum for $\Lambda^\circ \rightarrow \overline{p}\pi^-$ or $p\pi^+$, like sign pairs (similar procedure for $\overline{\Lambda^\circ}$). The plot in (a) shows the invariant mass without any cuts imposed. Plot (b) shows the invariant mass with a z-decay cut $\geq$ 30 cm from the main target and a $|\Delta z|$ cut $\leq$ 10 cm. Plot (c) shows the invariant mass with the same conditions as (b) but with the added requirement that the momentum of the proton is greater than 3.33 times the momentum of the pion. Plot (d) is the invariant mass with the same conditions as (c) but with an added requirement that the tracks be coplanar. It is apparent that no mass peak is observed due to the fact that a neutral decays into two oppositely charged tracks.

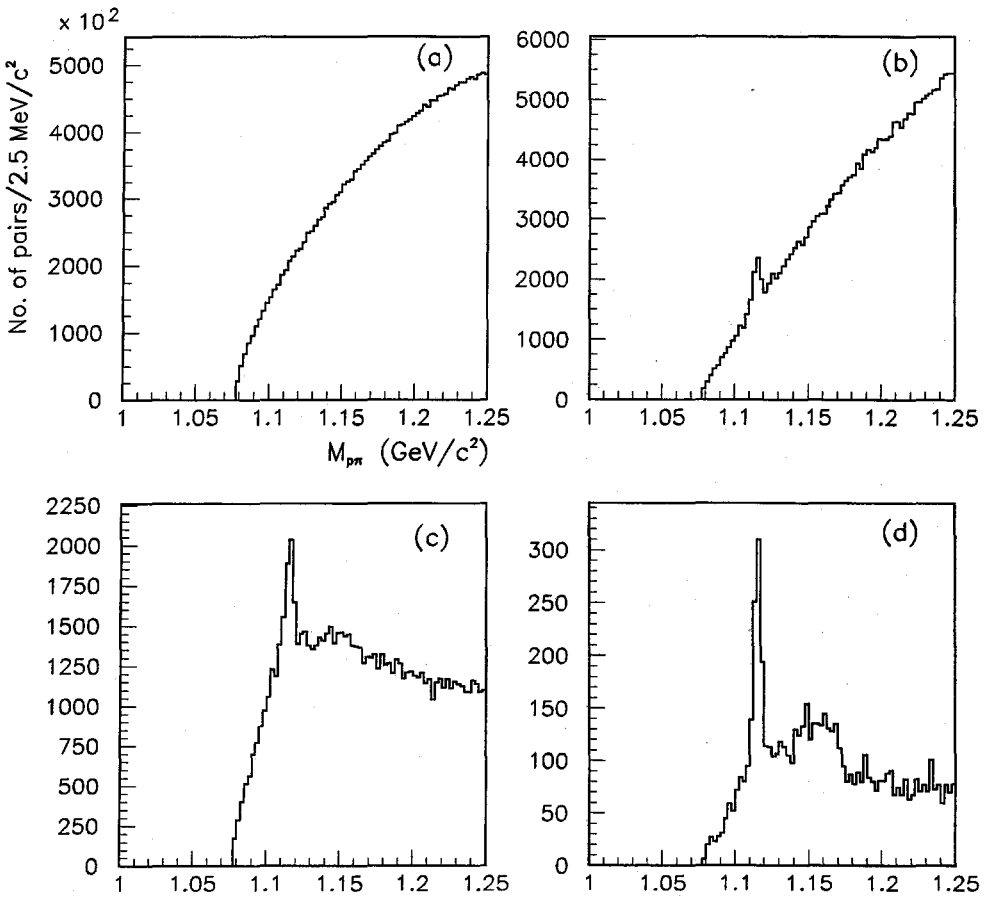

Figure 6.7: Invariant mass distributions for $\Lambda^\circ, \overline{\Lambda^\circ} \rightarrow p^\pm\pi^\mp$ for unlike sign charged tracks.

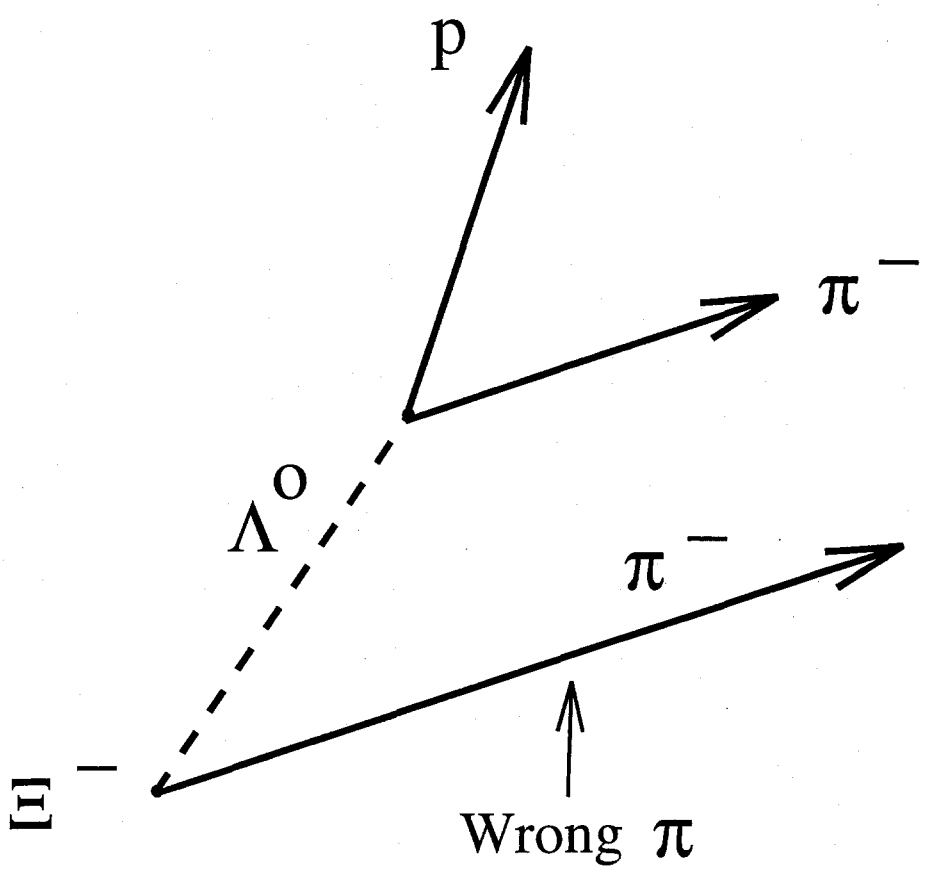

Figure 6.8: Decay mode for $\Xi^- \rightarrow \Lambda^\circ + \pi^-$. Shown is how the wrong π mass may be assigned to the Λ° mass to yield a wide peak distribution at 1.15 GeV/c^2.

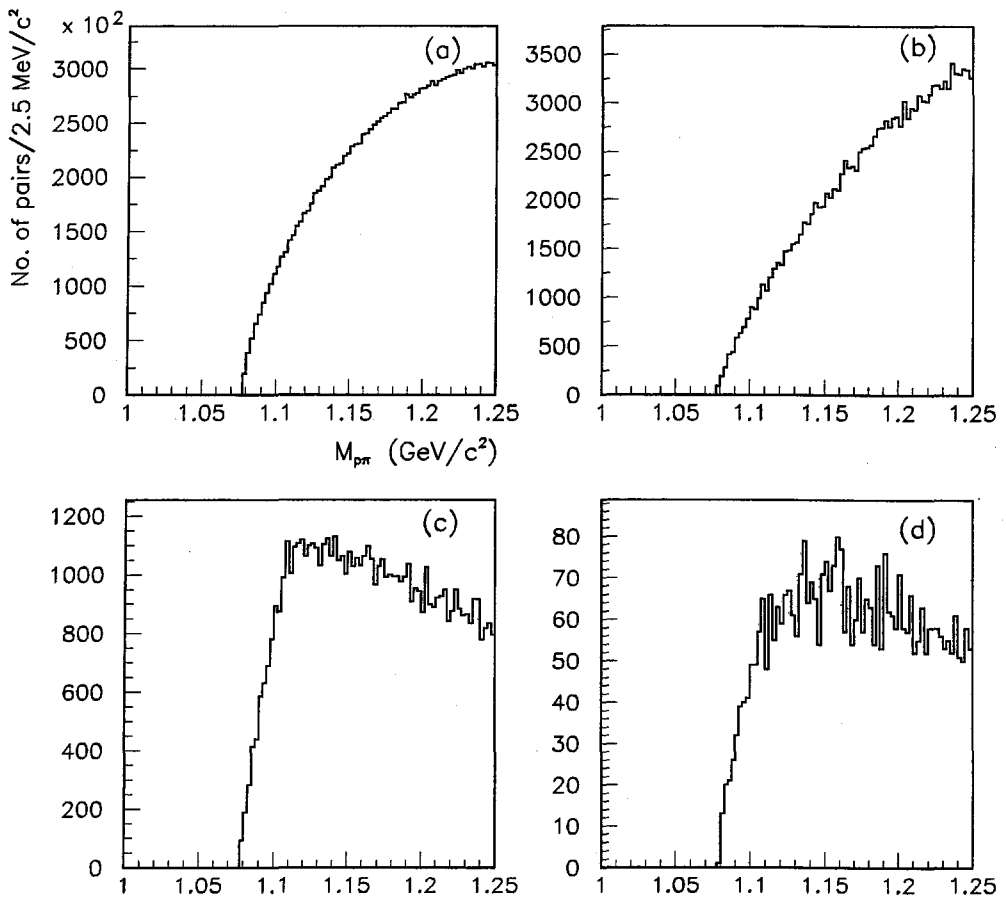

Figure 6.9: Invariant mass distributions for $\Lambda^{\circ}, \overline{\Lambda^{\circ}} \rightarrow p^{\pm}\pi^{\pm}$ for like sign charged tracks.

6.5 K°, Λ°, and $\overline{\Lambda^\circ}$ Particle Mis-Identification

It is difficult to distinguish particle decays without some form of particle identification scheme, such as measuring a track's momentum vector and its velocity. E771 was able to calculate the momentum of tracks, yet there did not exist a Cherenkov counter to aid in the completion of the particle identification step. To this end, an event tagged as a K° may not have necessarily been a K°. In order to obtain a correct estimation for total cross section production for a particular decay, the error in particle identification had to be taken into account and corrected. A method to aid in distinguishing K° decays from Λ° decays used the Podolanski-Armenteros plot [36], defined as the magnitude of the p_t distribution of one of the daughter tracks relative to the direction of flight of the parent track versus the asymmetry in the momentum of the two daughter tracks (shown in Figure 6.10), defined as

$$\alpha = (P_L^+ - P_L^- / P_L^+ + P_L^-). \tag{6.10}$$

Figure 6.11 shows the theoretical Podolanski-Armenteros plot for the K° and $\Lambda^\circ/\overline{\Lambda^\circ}$ decays. As observed from the plot, there exists a region where a clear overlap occurs for particle indistinguishability. It is at these regions where one must perform the correction factors.

Figure 6.12 shows the Podolanski-Armenteros plot for the K°, Λ°, and $\overline{\Lambda^\circ}$ decays from data. It is shown for the unlike sign track pairs in the mass cut interval of $\pm$ 30 MeV/c^2 for the K°'s and $\pm$ 10 MeV/c^2 for the $\Lambda^\circ/\overline{\Lambda^\circ}$'s. As seen from this plot, there is a wide band where it would be quite difficult to distinguish the particles. A method was devised to correct for this.

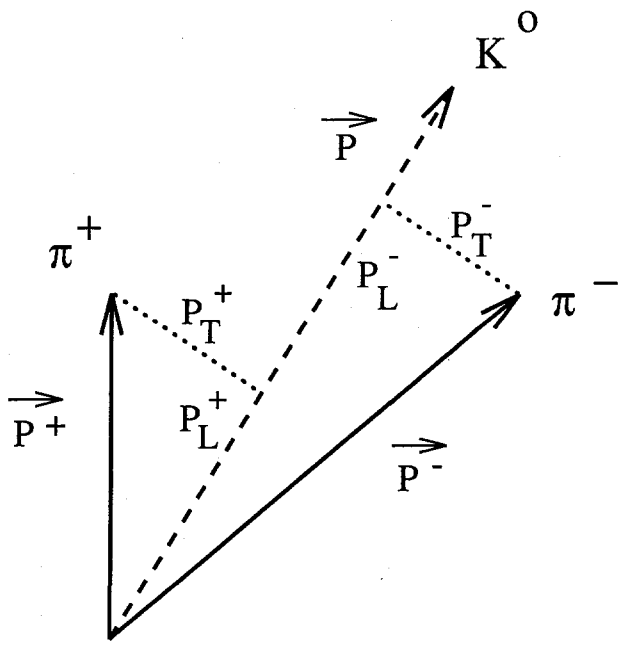

$$p_t = \frac{|\vec{P}^+ X \vec{P}|}{|\vec{P}|} = \frac{|\vec{P}^- X \vec{P}|}{|\vec{P}|}$$

$$\alpha = \frac{P_L^+ - P_L^-}{P_L^+ + P_L^-}$$

Figure 6.10: Decay distribution of the $K_s^\circ \rightarrow \pi^+ + \pi^-$, using the Podolanski-Armenteros variables, p_t and α.

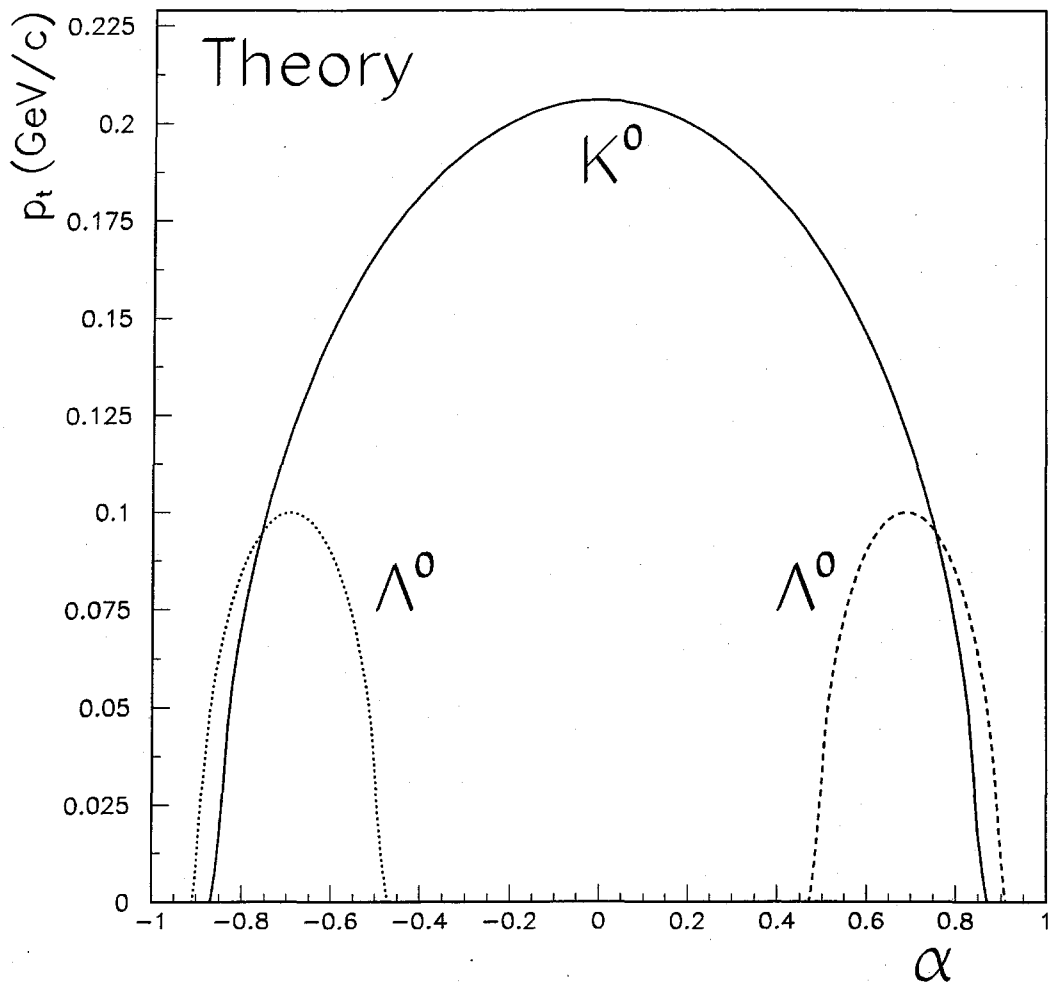

Figure 6.11: Podolanski-Armenteros theoretical plot of p_t vs. α for the $K_s^\circ \rightarrow \pi^+\pi^-$, $\Lambda^\circ \rightarrow p\pi^-$, and $\overline{\Lambda^\circ} \rightarrow \overline{p}\pi^+$ decays.

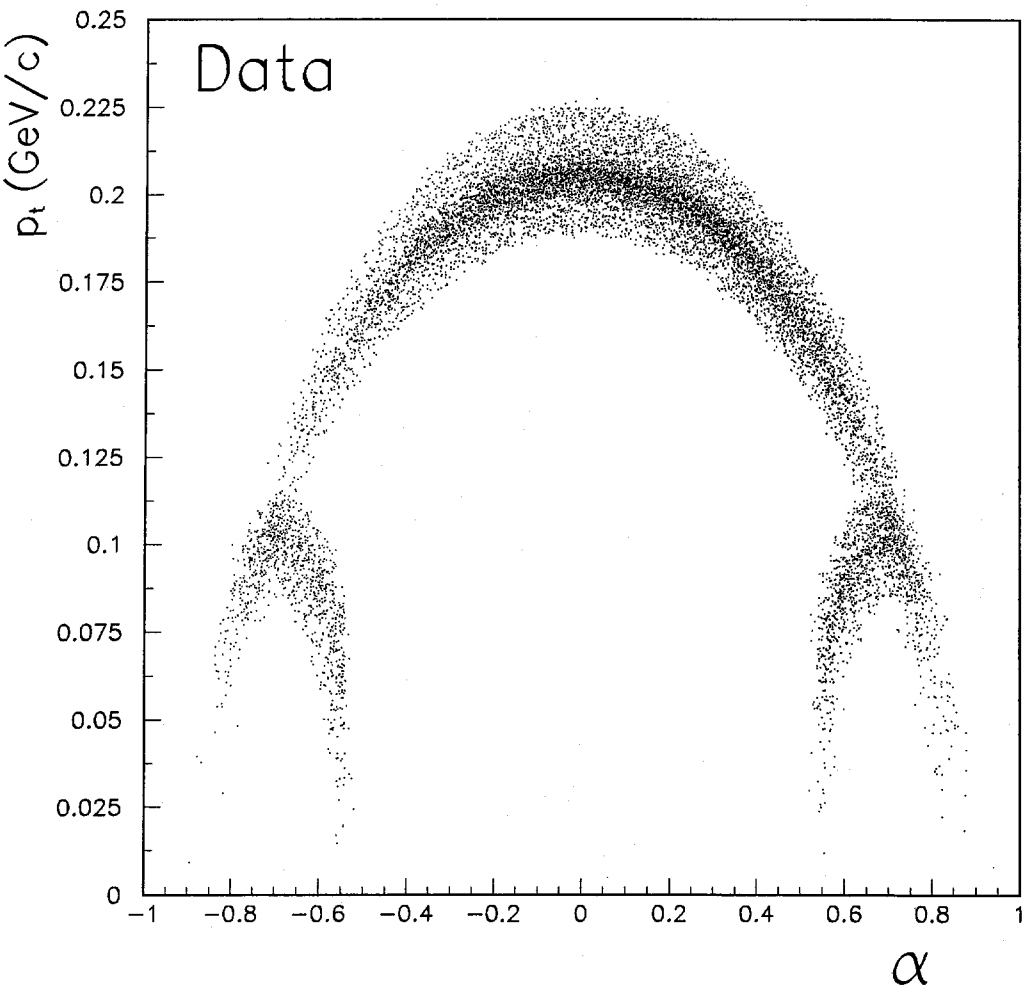

Figure 6.12: Podolanski-Armenteros data plot of p_t vs. α for the $K_s^\circ \rightarrow \pi^+\pi^-$, $\Lambda^\circ \rightarrow p\pi^-$, and $\overline{\Lambda^\circ} \rightarrow \overline{p}\pi^+$ decays.

The particle mis-identification procedure will be described for the K°'s (a similar procedure was followed for the Λ°'s). To estimate the percentage of particle mis-identification, a five step procedure was used to eliminate the ambiguities:

- Count the total number of pairs within $\pm$ 30 MeV of the K° mass value .
- If one is looking at the K° interval, then re-assign the mass value to fit for the Λ°'s.
- Re-calculate the mass value and plot its spectrum in order to perform a mass fit.
- Use a Gaussian distribution to fit the mass region in order to get the number of mis-identified particles.
- Take the ratio of the number of identified K°'s to the number of mis-identified K°'s to find the percentage of contamination.

With the above procedures utilized, the K°'s contained 1% contamination, as compared to 14% contamination for the Λ°'s and $\overline{\Lambda^{\circ}}$'s.

Chapter 7

Minimum Bias Events

Total cross sections for Kaon and Lambda production were obtainable since there existed a minimum bias trigger known as the *LED Trigger*. There did exist what was known as the *minimum bias trigger*, but it was in reality biased by accepting only those events where at least four hits were detected in the silicon tracker. Total cross sections can only be calculated in unbiased environments.

7.1 The LED Trigger

A trigger defined as the LED trigger [37] was used to obtain cross section measurements on unbiased events. It was specifically designed to monitor the Electromagnetic Calorimeter gain calibration and pedestals. An LED pulser that was located within the electromagnetic calorimeter housing was triggered by the prescaled RF signal that came from the accelerator. This pulse drove 96 LEDs. The generated light signal from the 96 LEDs was transmitted through one of 12 optical filters which then shone on a bundle of optical fibers. Each of the fibers led to a different glass block of the calorimeter.

Although the pulser was used to light up the LEDs, it also sent a TTL pulse to

the counting room where the logic electronics were located. There, after some logic, which synchronized it with the nearest RF pulse, the pulse went to a TRIGGER OR module which produced the LED trigger. Although the LED trigger usually ran at a typical rate of a few Hertz, it was able to operate at 100 Hz. The LED trigger was also useful in the sense that it allowed for the monitoring of the spectrometer and data acquisition system even during times of no beam.

7.2 Overlay and Data (dN/dy) and (dN/dp_t)

In order for one to obtain an absolute cross section for the production of any particle, one must be able to run an overlay program on the real data to obtain the "overlay efficiency" (to be discussed later). This is then used to correct up to the number of particles that would have been seen had one been dealing with a 100% efficient spectrometer. The overlay Monte Carlo program must have some input variables in order to simulate the spectrometer acceptances as best it can.

For our case, two input distributions had to be simulated, the rapidity distribution and the p_t distribution. Their relevant generation procedures have already been described in detail in Chapter 5. The only difference is that the overlay generation mechanism takes the process one step further. A particle is randomly generated by the fast Monte Carlo program. If it is accepted through the spectrometer, then it is sent to the GEANT simulation program. This then takes the track and simulates true physics phenomena, such as bremsstrahlung, multiple scattering, and other processes. The final surviving track's relevant characteristics, such as its p_t value, its p_x, p_y, and p_z coordinates, its slope and intercept values,

are saved for use in the overlay tracking program. The overlay tracking consists of taking the GEANT simulated track (its hit points), overlaying it on a real data event, and seeing if the main tracking program will reconstruct that sequence of points as the original track, or whether it will lose the track due to too many hits in each chamber plane.

Figure 7.1 shows a comparison of the real data and Monte Carlo overlay for the Kaons using a LED trigger for the rapidity distribution. The same technique may be used for the single muon triggered events and the double muon triggered events. (a) shows the assumed input Monte Carlo rapidity distribution (dashed curve) superimposed on the overlay accepted curve (solid curve), both normalized to the same area for comparison. As is immediately observable, the spectrometer acceptance dramatically cuts the rapidity distribution. The overlay accepted rapidity distribution is asymmetrical and favors the forward region. (b) shows the overlay efficiency, ϵ, i.e., the ratio of the overlay accepted events to the input Monte Carlo generated events. The efficiency is at its peak at a rapidity value around 0.5. (c) shows the superposition of the real data curve (solid) and the overlay data curve (dashed) both normalized to the same area to show the relative behavior of the overlay to data. The relative agreement with the overlay demonstrates the degree of validity of the Monte Carlo generator. The last plot (d) shows the final corrected rapidity distribution. This distribution was obtained by taking the ratio of the real data events to the overlay efficiency (i.e., overlay efficiency is that for accepting events within a specified rapidity interval).

The input p_t distribution used in the Monte Carlo routine for the generation

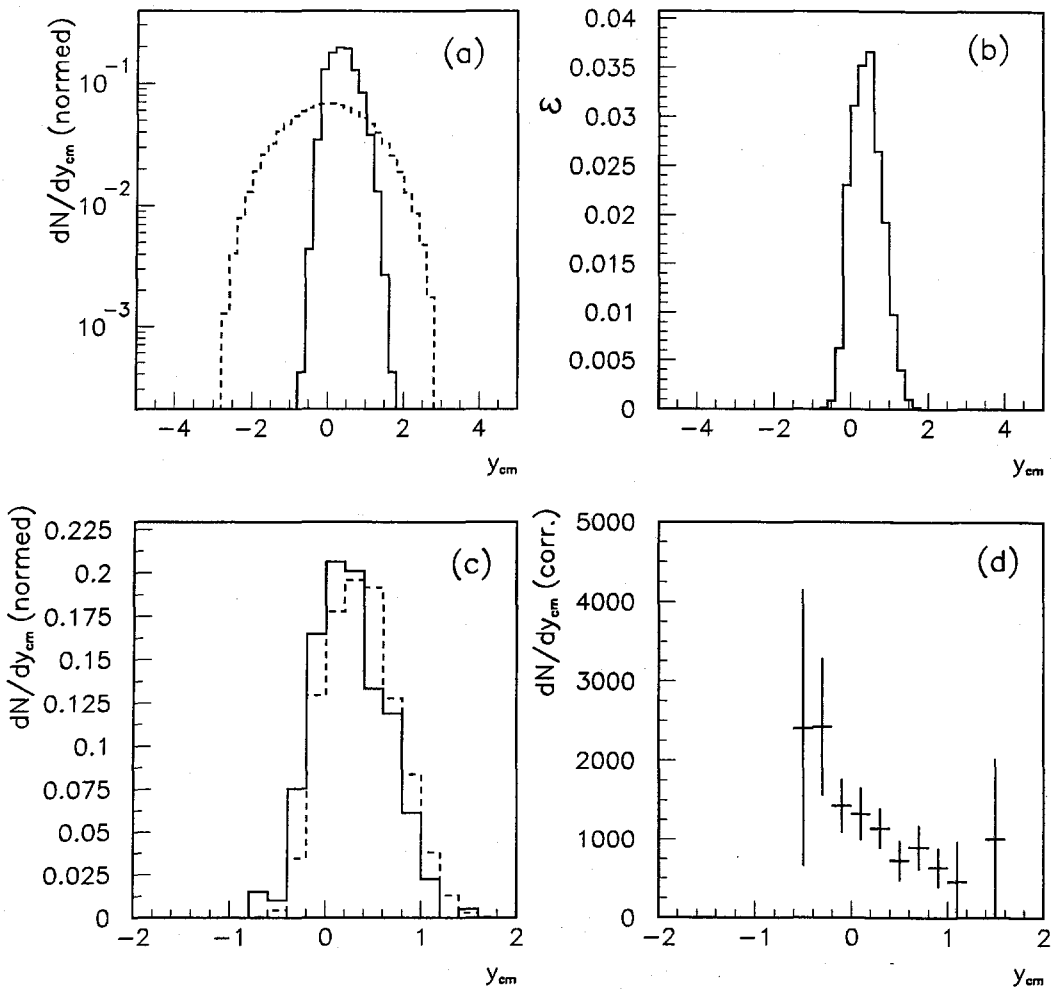

Figure 7.1: Overlay and data rapidity distribution plots for the K°'s using the LED triggered events. (a) is the input Monte Carlo rapidity distribution (dashed curve) superimposed on the overlay accepted distribution (solid curve), both with the same area normalization. (b) is the overlay efficiency, ϵ. (c) is the superposition of the uncorrected real data (solid) and the overlay data (dashed), both normalized to the same area. (d) is the final efficiency corrected rapidity distribution.

of the K°'s was of the form

$$dN/dp_t \sim p_t/(p_t + 0.5608)^{3.927}. \tag{7.1}$$

As discussed in Chapter 5, this distribution was fit to lower energy p_t distributions and extrapolated to simulate an 800 GeV/c p_t distribution.

The results of the overlay run compared to real data are shown in Figure 7.2. This figure shows the p_t distribution curves for overlay generated events and real data events for the K°'s using LED triggered events. The same may be extrapolated to the single muon triggered events and the double muon triggered events. (a) is the input Monte Carlo p_t distribution (dashed curve) overlaid on the p_t accepted curve (solid curve), both normalized to show their relative overlaps. (b) is the overlay efficiency, i.e., the ratio of the overlay p_t distribution to the input Monte Carlo generated p_t distribution. (c) shows the real data (solid curve) p_t distribution and the overlay p_t distribution (dashed curve) normalized to the same area and superposed on each other to display the approximate agreement in the curves for real data and the Monte Carlo generated overlay distribution. (d) is the final corrected p_t distribution. This distribution is achieved by taking the ratio of the real data p_t distribution to the overlay efficiency (i.e., overlay efficiency is that for accepting events within a specified p_t interval).

Figure 7.1 and Figure 7.2 showed the rapidity and p_t distributions for the K°'s. The exact same procedure was repeated for the Λ°'s and $\overline{\Lambda^{\circ}}$'s, and therefore their spectra will not be displayed.

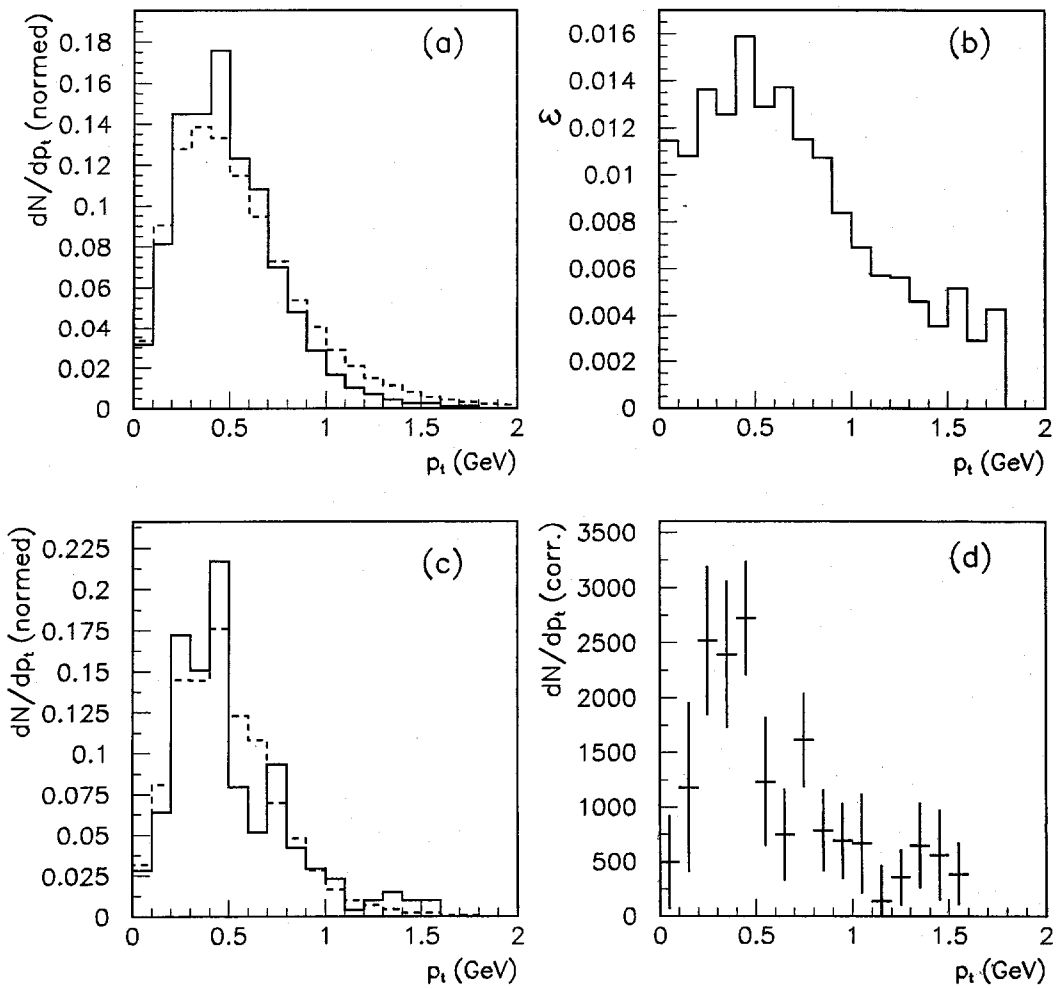

Figure 7.2: Overlay and data p_t distribution for the K°'s using the LED triggered events. (a) is the input Monte Carlo p_t distribution (dashed curve) superimposed on the overlay accepted curve (solid curve), both normalized to the same area. (b) is the overlay efficiency, ϵ. (c) is the superposition of the real data (solid) and the overlay data (dashed), both normalized to the same area. (d) is the final efficiency corrected p_t distribution.

7.3 K°

Due to the fact that the K° is a relatively long lived particle (as compared to the B-meson), its decay vertex may be well calculated. The K° may come about from the decay of

$$B_d^\circ \rightarrow J/\psi + K_s^\circ.$$

The detection of this particular decay mode was not observed in E771 due to its relatively small branching ratio. However, interesting information may be obtained from the observation of the K° particle, such as differences from its behavior at lower energy. This section will deal with its properties, mainly the calculation of its cross section, and a study of its p_t, rapidity, x_f, and multiplicity distributions. Some of these results will be compared to PYTHIA.

7.3.1 P_t Distribution

In order to achieve the most reasonable p_t distribution, one must apply cuts within the K°'s mass region. The K° p_t distribution was obtained by restricting the acceptance to only those events whose mass was within $\pm$ 30 MeV of the K° mass value. If they met this criterion, the p_t distribution was then plotted. But there still existed a background region below the mass signal peak. This had to be accounted for and subtracted from the final p_t distribution plot. In order to do this, a fit was performed on the K° mass plot, where a Gaussian was used to fit the signal peak (N_s) and a polynomial was used to fit the background (N_b). A ratio of N_s/N_b was obtained, and this ratio was subsequently used in conjunction with the p_t distribution subtraction algorithm.

The way this was incorporated into the problem was the following: For the p_t distribution, plot the distribution for those events that have unlike sign tracks (signal plot, $N_{\pm}$), and then plot the same p_t distribution for those events that have like sign tracks (background plot, N_{LS}). The p_t distribution plotted using the like sign tracks has to be normalized to the p_t distribution plotted using the unlike sign tracks in some way suitable for background subtraction. In order to do this, we must renormalize the like-sign (N_{LS}) to be the same as the N_b, so each like sign event has to be multiplied by the ratio N_b/N_{LS}. This is then subtracted from the $N_{\pm}$ distribution, thus yielding the true p_t distribution.

Figure 7.3 is the K° true p_t distribution, the same figure shown three times for each of three different fitting functions to obtain the $< p_t >$ value. The three different functions are:

$$dN/dp_t = P1 \cdot p_t \cdot exp(-p_t \cdot P2), \tag{7.2}$$

$$dN/dp_t = P1 \cdot p_t \cdot exp(-\sqrt{p_t^2 + m^2}/P2), \tag{7.3}$$

$$dN/dp_t = (P1 \cdot p_t)/(p_t + P2)^{P3}. \tag{7.4}$$

The parameters $P1$, $P2$, and $P3$ are the fitted parameter values obtained from each of the individual fits.

Plot (a) is the K° p_t distribution using Equation (7.2) as the fitting function, where $P1$ and $P2$ are the fitted parameters for the given exponential function. Plot (b) is the K° p_t distribution using Equation (7.3) as the fitting function for the distribution, where $P1$ and $P2$ are the fitted parameters for this function involving the transverse energy (thermal exponential fit). Plot (c) is the K° p_t distribution

with a "power law" fit of the form from Equation (7.4), where $P1$, $P2$, and $P3$ are the fitted parameters for this function.

Each of the three different fitting functions yielded similar values for the $< p_t >$, and the greatest discrepancy between the values was 0.061 GeV/c. The $K^\circ < p_t >$ value, averaged for all three fitting algorithms, yielded a value of

$$< p_t >=0.45 \pm 0.03 \text{ GeV/c},$$

where the systematic error is the standard deviation of the three different fits.

As is observable from the p_t distribution plots, the fittings were only performed on a p_t interval greater than about 0.5 GeV/c. This was due to the loss of particles in the lower p_t region, as can be seen from the PYTHIA generated and accepted distributions (Section 5.2.1).

The three different fits used to get the average p_t values were model dependent and did not look at the low p_t region. This was explained by the fact that the low p_t particles were lost when simulated to traverse E771's spectrometer region. An alternative for getting the average p_t was to average directly the p_t values for the whole distribution as the final p_t distribution was corrected for the spectrometer acceptance. The procedure was the same as that used for getting the three model dependent $< p_t >$ values. That is, one had to normalize the background p_t distribution to the signal p_t distribution in order to perform the proper subtraction to get the correct p_t distribution. The distribution had to be overlay corrected for losses at small p_t. Then the simple average of the corrected p_t distribution was formed without performing any fitting procedures. The $< p_t >$ value obtained for the K°'s using this method was

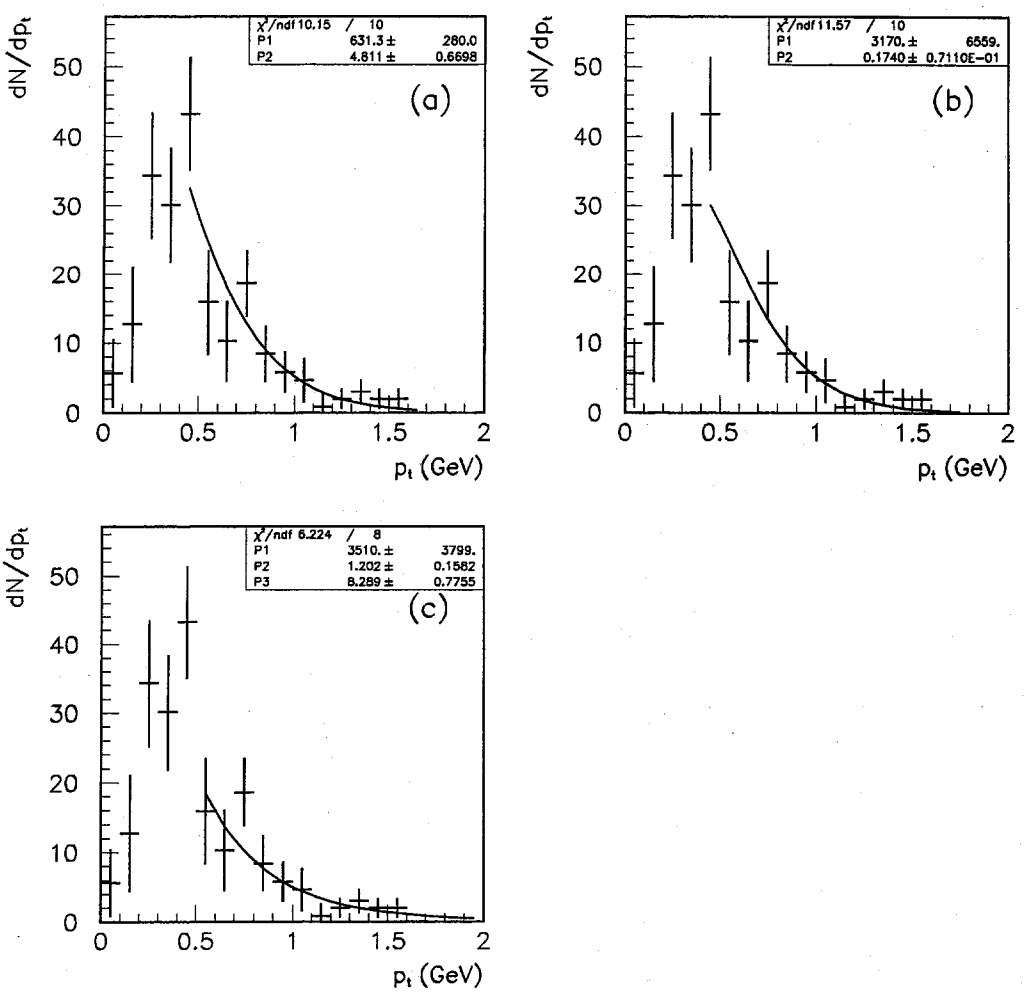

Figure 7.3: The K° p_t distribution from LED triggered events. The same plot is shown three times for each of three different fitting functions. (a) uses Equation (7.2) as the fit, (b) uses Equation (7.3) as the fit, and (c) uses Equation (7.4) as the fit.

$$< p_t >=0.60\pm0.11\ GeV/c.$$

It is noted that the latter procedure used to fit the $< p_t >$ yielded a higher value than that obtained from the three different fits. This is explainable by the fact that the power law fit described above generally gave a lower value than did the other two fits.

7.3.2 Multiplicity, Rapidity, and x_f Distributions

The multiplicity (N_c), rapidity (y_{cm}), and Feynman-x (x_f) distributions were all obtained the same way the p_t distribution was. That is, those events that were within ± 30 MeV of the K° mass peak were kept and their respective distributions plotted.

With all the track's information given with respect to laboratory coordinates, the rapidity in the laboratory frame is

$$y_{lab} = \frac{1}{2} ln(\frac{E + P_l}{E - P_l}). \tag{7.5}$$

The rapidity in the center of mass system is

$$y_{cm} = y_{lab} + y_{tx}, \tag{7.6}$$

where

$$y_{tx} = \frac{1}{2} ln(\frac{1 - \beta_{cm}}{1 + \beta_{cm}}). \tag{7.7}$$

E is the particle's energy, P_l its longitudinal momentum, and

$$\beta_{cm} = P_{beam}/(\sqrt{P_{beam}^2 + m_p^2} + m_p).$$

P_{beam} is the beam momentum, and m_p is the proton mass.

Feynman's x variable, x_f, in the center of mass system, is given in terms of

$$x_f = \frac{2 \cdot p_{z(cm)}}{\sqrt{s}}, \tag{7.8}$$

where $p_{z(cm)} = \gamma_{cm} \cdot (P_z - \beta_{cm} \cdot E)$.

Figure 7.4 shows the uncorrected distributions (uncorrected for efficiency and acceptance) for the K° multiplicity, rapidity, and Feynman-x for the LED triggered events. (a) is the charged particle multiplicity distribution, with $< N_c >$=7.2±3.1. (b) is the rapidity distribution in the center of mass system. The rapidity distribution is more pronounced in the forward direction. This means that those particles that are produced in the rear direction tend not to be accepted by the outer perimeters of the tracking chambers due to their relatively small fiducial volume. (c) is the Feynman-x distribution in the center of mass system.

7.3.3 Minimum Bias PYTHIA

A Monte Carlo PYTHIA program was run in order to determine how close to nature it comes when Monte Carlo events are subjected to an experimental acceptance similar to that encountered by real events. As described earlier, PYTHIA is a program that can simulate different types of events, such as minimum bias events, charm enhanced events, or beauty enhanced events. For this section, we will discuss a program written to simulate minimum bias events and the effect of spectrometer acceptance on them.

An event is PYTHIA generated and then forced to pass through the spectrometer region. It encounters the magnet where it experiences a p_t kick and thus deflected to traverse the rear chambers. The Monte Carlo program checks to see

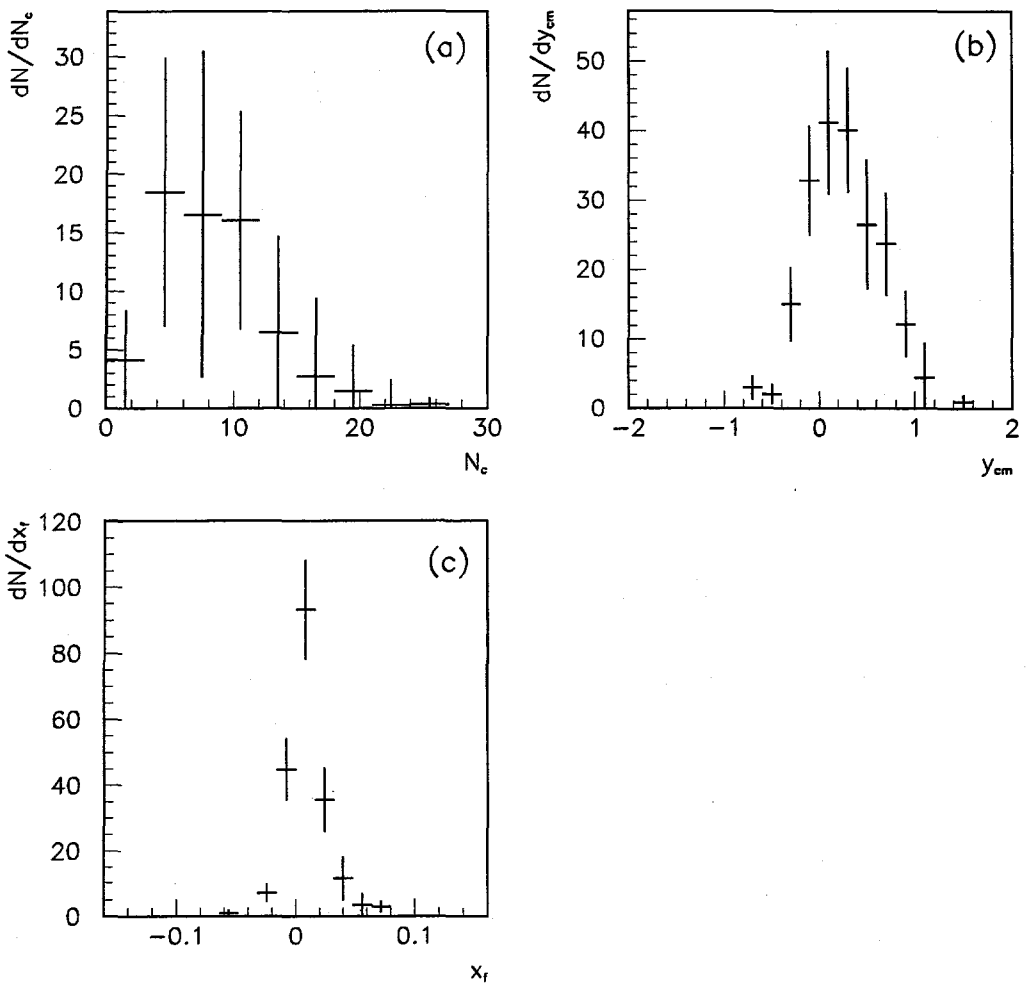

Figure 7.4: (a) N_c, (b) y_{cm}, and (c) center of mass x_f distributions for the K° LED triggered events. These distributions are not corrected for full spectrometer acceptance.

that each track of the event hits at least three chamber planes in the front and at least three chamber planes in the rear (the minimal hits required). If two tracks of a generated K° pass the front chamber and rear chamber hit criteria, this event is accepted and its relevant information, such as p_t, are plotted or put in counters for later use. The relevant pieces of information extracted from PYTHIA that may be compared to data are the average multiplicity value for those events that had K°'s in them, the average multiplicity value for all events irrespective of whether the event contained a K°, the number of K°'s generated (here generated means that the particle did not necessarily make it through the spectrometer acceptance region) per generated multiplicity, the number of K°'s generated per event, and the average p_t value.

7.3.4 Comparison of Data to PYTHIA

A comparison of real data events to those PYTHIA generated is used to determine how close PYTHIA is able to predict experiment. Table 7.1 shows a comparison of PYTHIA events to real data events for the study of K° produced particles in the minimum bias events. The first column of the table is the average charged particle multiplicity for an event that contained a K°. PYTHIA predicted a value of 3.17 while the data had a value of 7.2±3.1, more than twice the number of tracks per event in the spectrometer acceptance than PYTHIA's prediction (if we exclude the error bars). There may be two reasons for this: (1) PYTHIA has a reputation for underestimating multiplicity in some situations. (2) The real data used a nuclear target, and PYTHIA was run assuming a free nucleon-nucleon collision.

The second column is the average multiplicity for all events, irrespective of whether they had a K° in them. PYTHIA's number of 1.97 is lower than its value for when a K° is required to have been in the event. This N_c cannot be calculated for real data because the LED triggered minimum bias events may have contained empty track events. That is, with the LED being pre-scaled to trigger every 4.1 million buckets per 53.1 MHz, the possibility existed that no interaction occurred, hence no charged track multiplicities.

The third column is the average number of K°'s generated (not necessarily accepted by the spectrometer region) per raw charged multiplicity for the PYTHIA run. The value obtained from data is what would have been the produced number when correcting up with the tracking overlay efficiency. PYTHIA's generated value was in relative agreement with what was observed from data.

The fourth column is the average number of K°'s PYTHIA generated per event to compare to the average number of K°'s produced per event when corrected up with the tracking overlay efficiency. PYTHIA predicts a number approximately twice that of what data observed.

Finally, the last column is the mean p_t for the K°, where PYTHIA agrees relatively well with the result obtained from the data events of 0.417 GeV/c.

The conclusion one may draw from a comparison of PYTHIA and data is that not all parameters are in agreement. The main discrepancy exists between the multiplicity values and the number of K°'s produced per event. It must be emphasized here that the real data used in Table 7.1 was corrected for acceptance and overlay efficiency.

	$< N >_{K^\circ\ evt}$	$< N >_{evt}$	$< \frac{K^\circ(gen)}{N_{all}} >$	$< \frac{K^\circ(gen)}{evt} >$	$< p_t >_{K^\circ}$ (GeV/c)
PYTHIA	3.170 ± 0.004	1.97 ± 0.004	0.1114 ± 0.0001	0.219 ± 0.001	0.446 ± 0.001
DATA	7.2 ± 3.1	-	-	0.0902 ± 0.0115	0.4167 ± 0.0475

Table 7.1: Comparison of minimum bias PYTHIA generated events and data events for K° produced particles with no muon trigger imposed.

7.3.5 Mass Fitting Algorithm

In order to achieve proper resolutions, proper cross sections, and proper distributions, one must have a relatively good mass fitting procedure. The main process behind most of the physics involved in obtaining multiple distributions and cross sections lies in the way the mass peak spectrum is fit. If it is poorly fit, it may yield spurious results. This section will deal with the method used in fitting the mass peak.

As in most mass distribution plots, the signal peak is seen above some background region. In order to extract the true number of signal events within its mass interval, two fits are performed on the curve, a Gaussian fit for the signal peak and a polynomial fit for the background. Note that for the Gaussian fit, there could have theoretically been three parameters to fit, the multiplicative parameter, the mean mass parameter, and the standard deviation parameter. The mean mass parameter was fixed at the K° mass value, so only two parameters were fit. Figure 7.5 is an example of the evolution of the fitting procedure. Plot (a) is a Gaussian fit to the signal peak, where the limits on the tail edges of the fit are varied somewhat in order to obtain the best fit. It also includes a straight line fit

for a pre-determination of the background in the peak region. This means that once the signal peak is obtained, the straight line fit allows for a "cut-off" of the signal peak in order to fit the background in the neighborhood of the peak region, as shown in (b). It shows what the distribution looks like with the mass peak extracted and replaced by a straight line. It allows one to fit a polynomial to the curve, as shown by the line fit. (c) is then just a curve of what the polynomial distribution is like from the background fit. This is used to extract the number of track pairs in the background region within $\pm$ 30 MeV of the K° mass peak. (d) is the culmination of the fitting procedure. It shows the Gaussian fit to the signal peak and the polynomial fit to the background. Many algorithms were tried. This one was uniformly applicable to all situations and gave the most reproducible results independent of the choice of the fitting interval.

The Gaussian fit itself is not used to determine the number of K°'s. The steps used for obtaining the number of true K°'s involves the following:

- Count the total number of mass pairs within $\pm$ 30 MeV of the K° mass value. Take this to be the preliminary number of signal plus background ($N_s + N_b = N_F$) pairs, the total number of pairs.

- From a polynomial fit on the background, count the number of pairs within $\pm$ 30 Mev of the K° mass value under the curve. Take this to be the number of background pairs (N_b).

- Subtract the number of background pairs from the total number of pairs. This result gives us the total number of signal pairs.

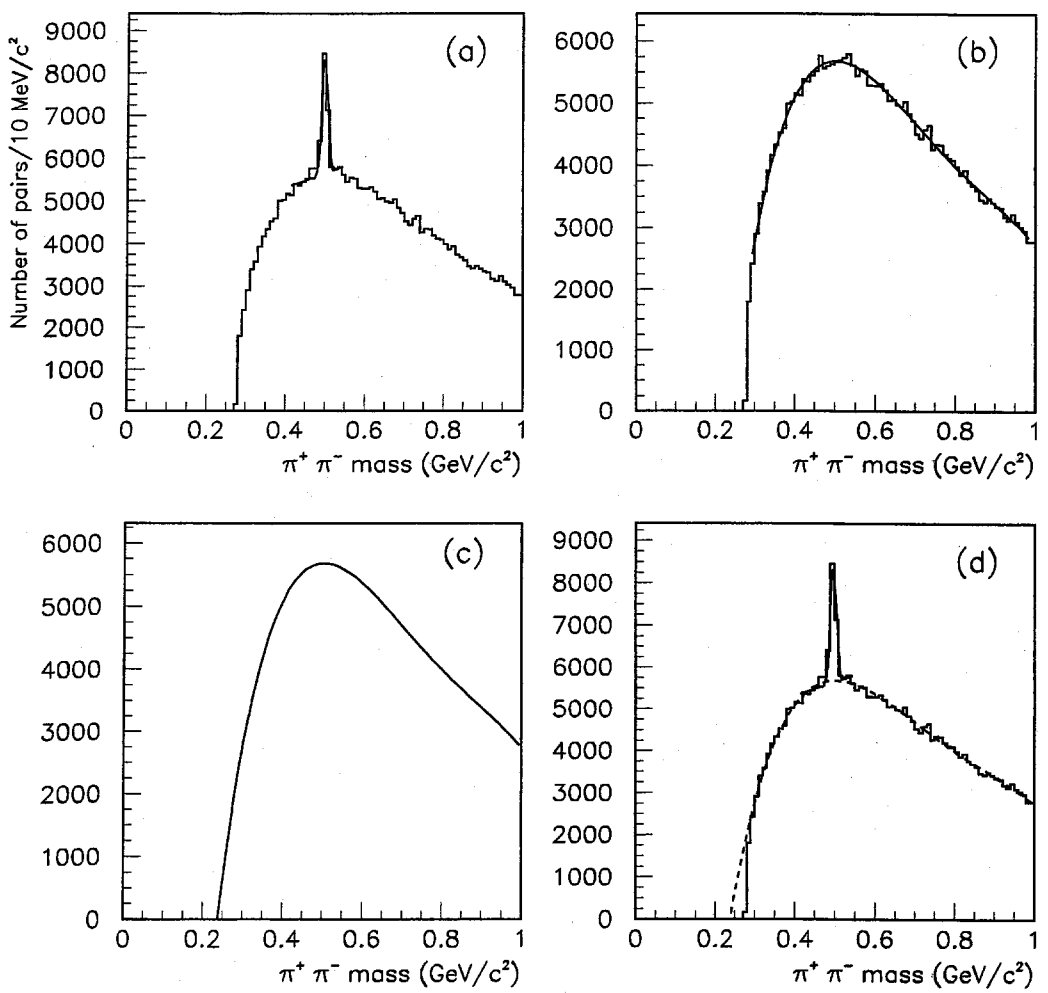

Figure 7.5: Sample K° mass fitting algorithm. (a) is the mass distribution with a Gaussian fit to the signal. (b) is the same as (a) but with the signal peak subtracted in order to fit the background. (c) is the polynomial curve drawn out as a result of the fit to the background. (d) is the final distribution showing the Gaussian fit to the signal and the polynomial fit to the background.

- The final ratio of N_s/N_b may be obtained and used for further analyses.

Figure 7.6 shows a Gaussian fit to the K° mass signal peak and a straight line fit for a pre-determination for the background region, where the function used for the signal part of the fit was of the form

$$dN/dm^* = P(1) \cdot exp(-(x - p(2))^2/(2 \cdot p(3)^2)). \tag{7.9}$$

Allowing the mass to be a fitted parameter illustrates the fact that one is fitting the K° correctly with respect to its mass value, with a mean mass value $P(2) = 0.497\ GeV/c^2$.

7.3.6 K° Cross Section

The method used to obtain the K° cross section involved fitting the mass distribution for a wide range of cuts. These mostly involved a combination of cuts on the z-decay position of the K° and its $|\Delta z|$ parameter, that is, the difference in the distance of closest approach of the two daughter tracks and a measure of its uncertainty, both cuts already discussed in Chapter 6.2. The method for calculating the cross section involves the following steps:

- Fit the real data K° mass plots in order to get the absolute number of K°'s detected within a specified z-decay and $|\Delta z|$ interval.
- Fit the overlay data K° mass plots in order to get the number of tracks returned from the original input distribution.
- Calculate the overlay efficiency from overlay data mass plots.

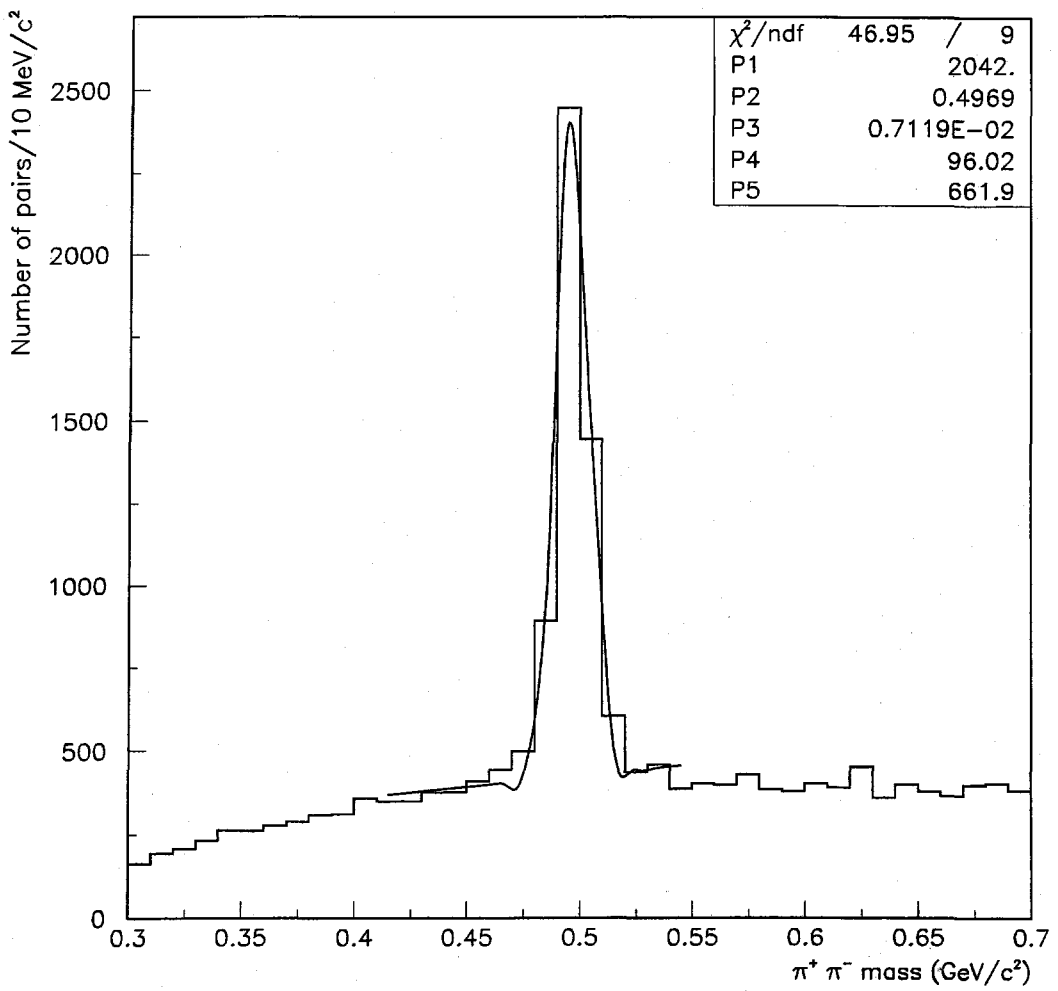

Figure 7.6: Fitted Gaussian distribution to the $K_s^\circ \rightarrow \pi^+\pi^-$ mass peak.

- Calculate the number of K°'s corrected up by the overlay efficiency. This final number is the one that will be used in the cross section calculation.

Figure 7.7 shows a sampling of mass distributions for a variety of z-decay cuts and $|\Delta z|$ cuts. The first row shows the K° mass plots for a fixed z-decay length greater than 5 cm from the main interaction vertex and with increasingly tighter cuts imposed on the $|\Delta z|$ of the two daughter tracks. As the $|\Delta z|$ cuts are made tighter, the peak appears more defined. The ideal case would be a situation where the $|\Delta z|$ of the two tracks is 0.0 cm, implication of originating from the same decay point. Making too tight a $|\Delta z|$ cut would result in the loss of good K° events. The second row shows the K° mass plots for a fixed z-decay length greater than 10 cm from the main interaction vertex and with tighter cuts imposed on the $|\Delta z|$ of the two daughter tracks in each column. The process where a K° candidate is required to have decayed a distance from the main interaction vertex is plausible due the particle's relatively long lifetime. This then allows for the exclusion of unwanted background events. Of course, as in any cut imposed, too tight a cut will inevitably lead to loss in the number of K°'s observed. The third and fourth rows show the K° mass plots for fixed z-decay lengths greater than 30 cm and 50 cm, respectively, from the main interaction vertex and with increasingly tighter cuts imposed on the $|\Delta z|$ of the two daughter tracks in each column. All mass spectra in this figure were plotted irrespective of whether they were coplanar tracks. Each vertical scale is the number of pairs per 10 MeV/c^2, and each horizontal scale is the mass value in GeV/c^2.

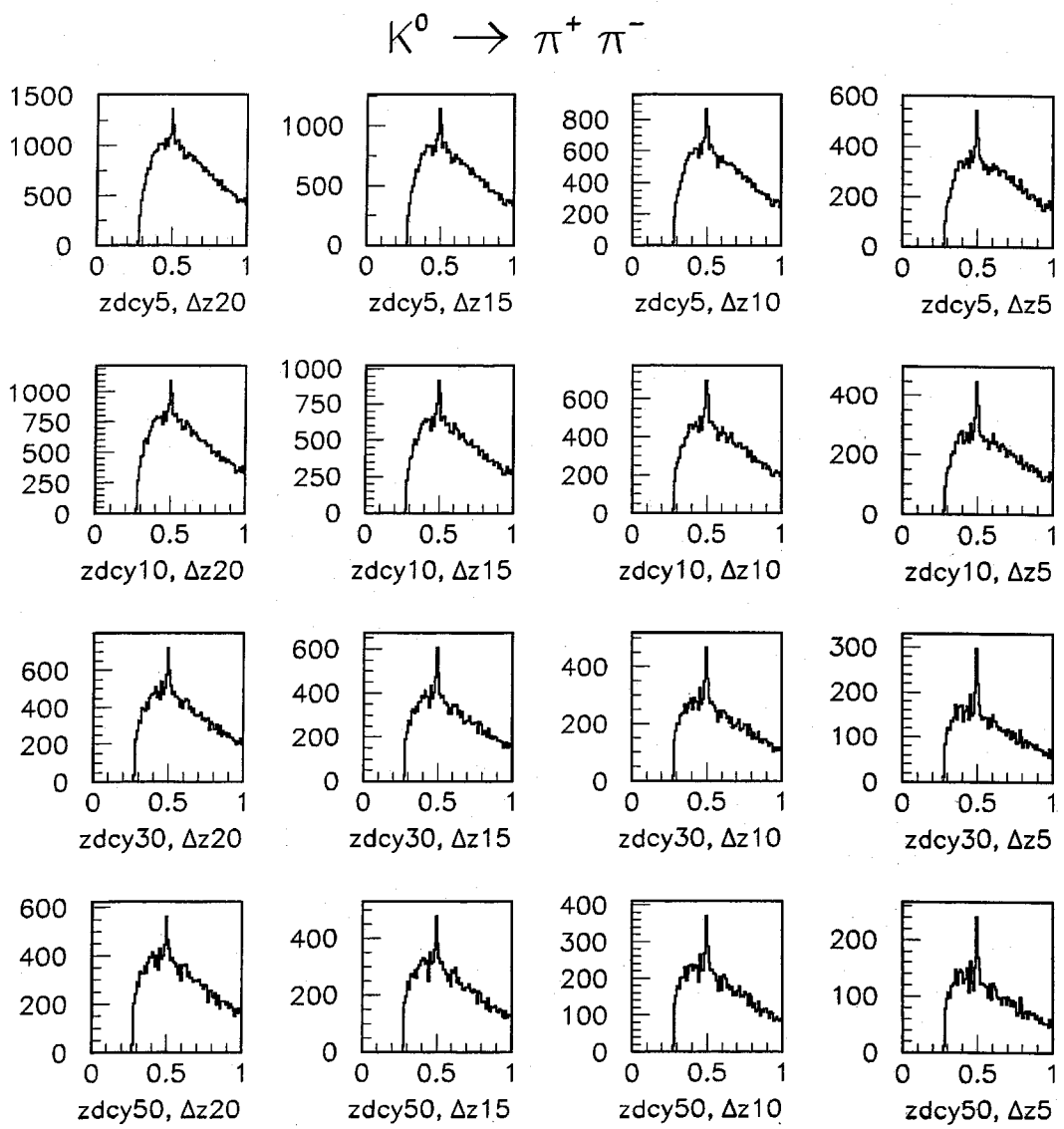

Figure 7.7: K° mass distributions from minimum bias triggered events for various z-decay and $|\Delta z|$ cuts, with no coplanarity criterion imposed. Each horizontal scale is the mass value in GeV/c^2, and each vertical scale is the number of pairs per 10 MeV/c^2.

Figure 7.8 follows the same logic as that described for Figure 7.7 with the added condition that the tracks be coplanar, as previously described in Chapter 6.2. The columns detail the progression in the cuts on $|\Delta z|$ while the rows detail the progression in the cuts on the z-decay of the particle from the main interaction vertex. A coplanarity cut produces a much better mass spectrum by eliminating those tracks in the background region that were non-coplanar. Each vertical scale is the number of pairs per 10 MeV/c^2, and each horizontal scale is the mass value in GeV/c^2.

Figure 7.9 is a plot of the raw number of K°'s as a function of the $|\Delta z|$ cuts for the K° events. The multiple curves are for individual fixed z-decay cuts. The plots show the raw number for both non-coplanarity cut events and for coplanarity cut events. Visual inspection of the plots shows a marked difference in the number of events seen without the coplanarity cut and for those with the coplanarity cut. The non-coplanarity cut events range in value from as high as 690 to as low as 160. The coplanar events, though, range in value from a high of 320 to a low of 120 (this includes all possible $|\Delta z|$ and z_{dcy} cuts), a much smaller swing in values. The systematic error assigned to these values was extracted from the swing in the value of the numbers for a fixed $|\Delta z|$ cut.

Figure 7.10 is a plot of the overlay efficiency, ϵ, versus $|\Delta z|$ for the K° overlay events. The multiple curves are for individual fixed z-decay cuts. The efficiency increases as the cuts are made less stringent. These efficiency curves include both the coplanar tracks and the non-coplanar tracks.

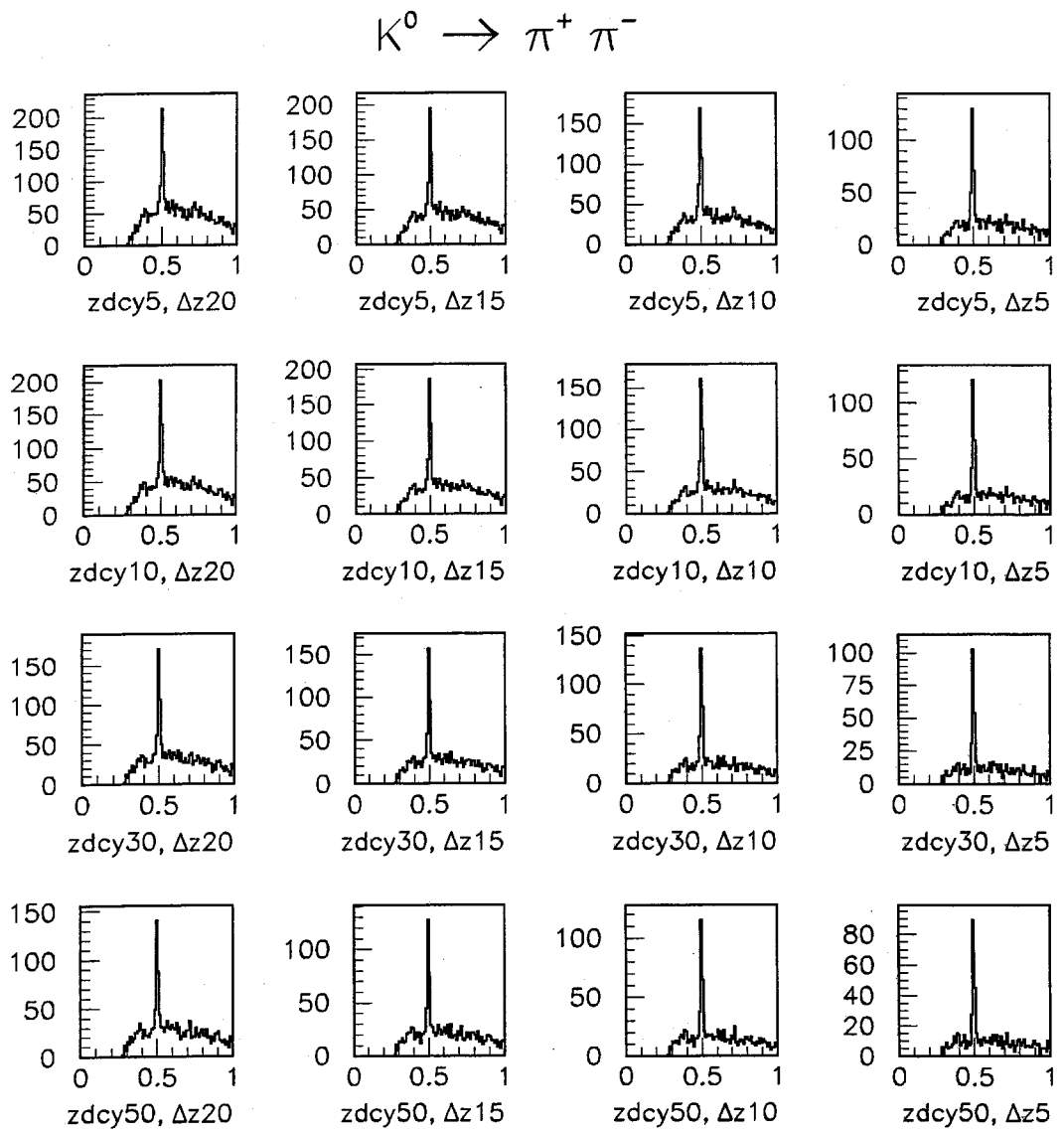

Figure 7.8: K° mass distributions from minimum bias triggered events for various z-decay and $|\Delta z|$ cuts, with a coplanarity criterion imposed. Each horizontal scale is the mass value in GeV/c^2, and each vertical scale is the number of pairs per 10 MeV/c^2.

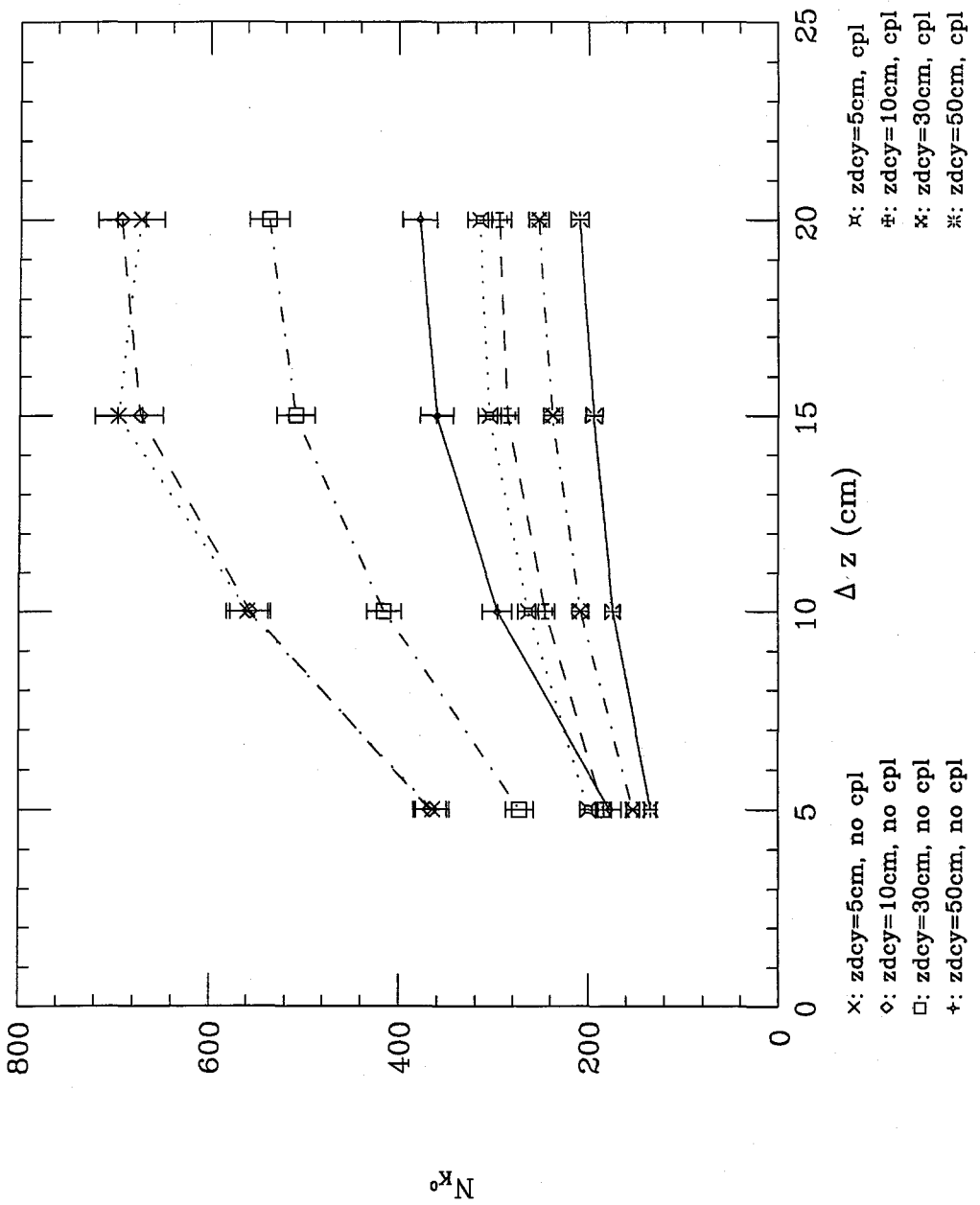

Figure 7.9: Total number of K°'s, $N_{K^{\circ}}$, as a function of $|\Delta z|$ and z-decay cuts. Shown are curves for coplanar tracks and curves for non-coplanar tracks.

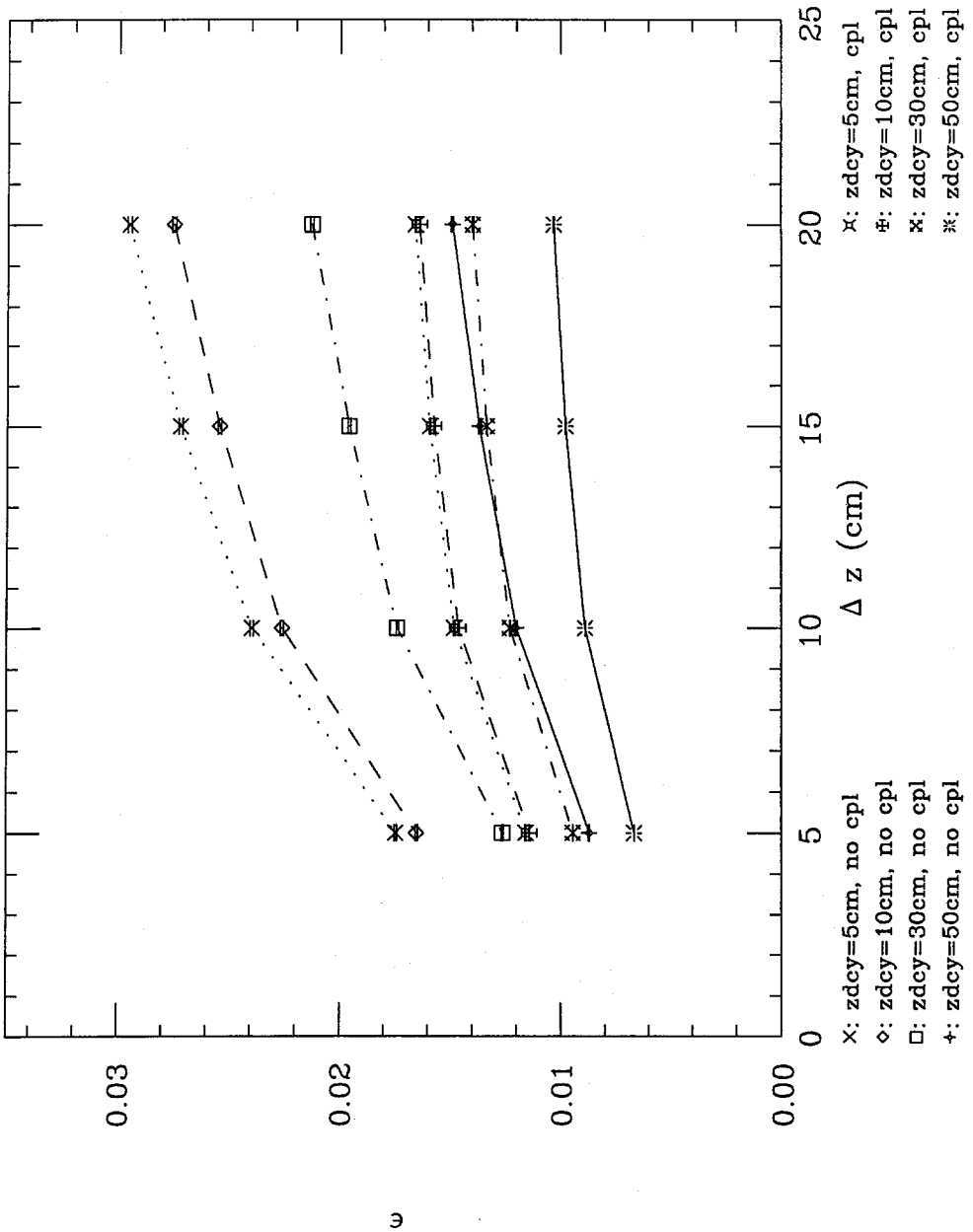

Figure 7.10: Overlay efficiency, ϵ, for tracking a K° as a function of $|\Delta z|$ and z-decay cuts. Shown are curves for coplanar tracks and curves for non-coplanar tracks.

Figure 7.11 shows the plot of the corrected number of K°'s, (N_K°/ϵ), using the raw number of K° events and the overlay efficiency versus the $|\Delta z|$ cuts. The curved lines represent different z-decay value parameters. Ideally all the points on this plot would be a single number for corrected K°'s if it were possible to estimate the overlay efficiency perfectly.

Once the corrected number of K°'s was determined from the overlay efficiency values, a cross section calculation was performed. If the total number of K° events is known, and the total number of beam particles is known, the estimated cross section is

$$\sigma^{si}_{K_s^\circ \to \pi^+\pi^-} = (\frac{A_{si}}{\rho_{si} \cdot N_A \cdot x})(\frac{N_{K_s^\circ \to \pi^+\pi^-}}{N_{beam}}), \tag{7.10}$$

where $A_{si} = 28.09$, the atomic weight of silicon, $\rho_{si} = 2.33\ g/cm^3$, the density of silicon, $x = 0.36\ cm$ (tracker) + 2.4 cm (target), the length of the silicon target and silicon tracker. The number of beam particles, from 33 tapesets analyzed (see last section), was defined as

$$N_{beam} = 4.691 \times 10^{12}(LiveBeam) \times (\frac{13(LED/sec)}{53.1 \times 10^6 HzRF}). \tag{7.11}$$

Although there were 4.691×10^{12} beam particles, one must multiply by the fraction of spills having LED triggers. In each spill there were 13 LED pulses per second, and the RF was pulsed at 53.1 MHz. The number of beam particles was

$$N_{beam} = 1.148 \times 10^6. \tag{7.12}$$

In order to get $N_{K_s^\circ \to \pi^+\pi^-}$, the overlay efficiency corrected number of K°'s had to be extracted, see Figure 7.11. Its mean value, taking into account the systematic

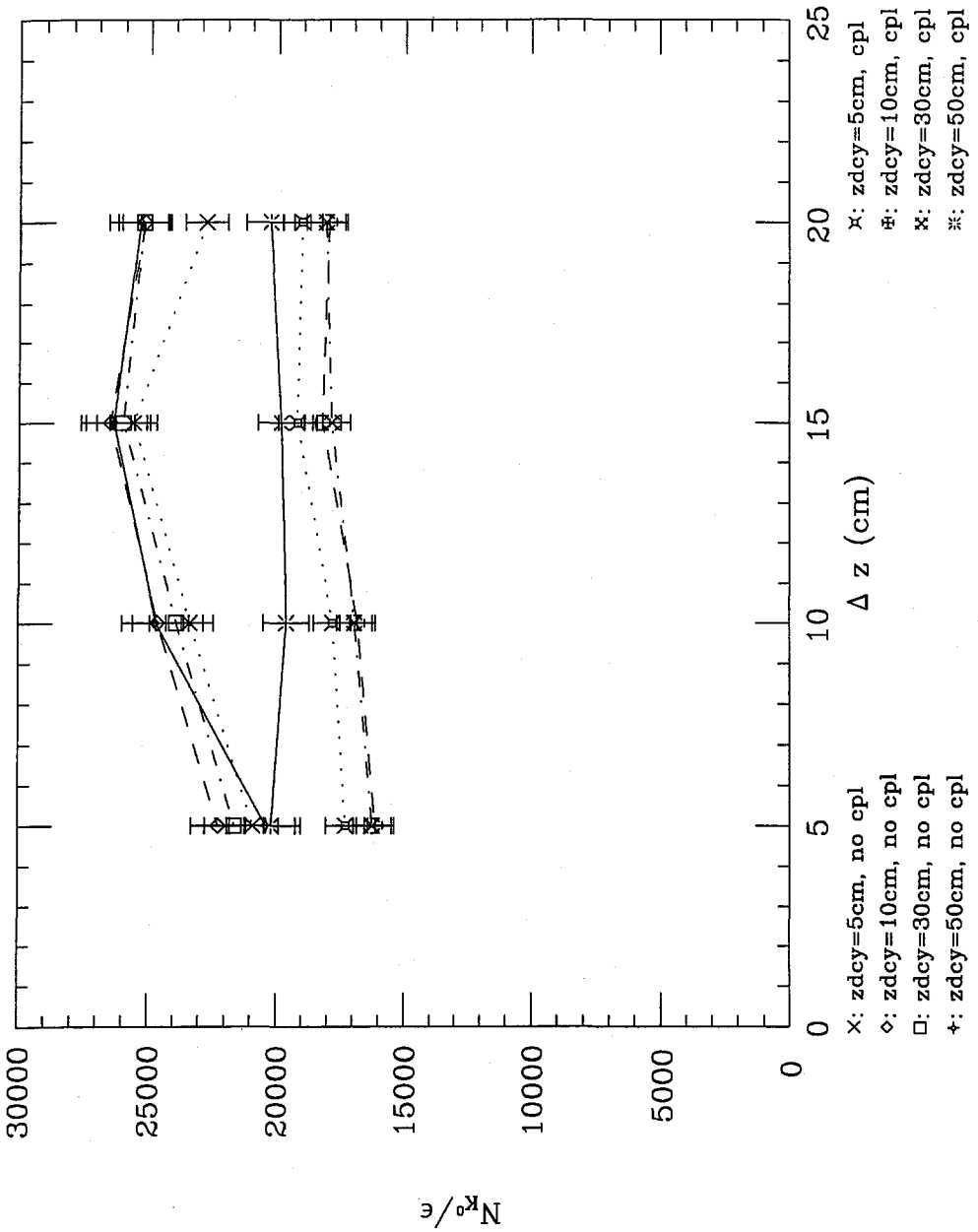

Figure 7.11: Corrected number of K° events, N_{K°/ϵ, as a function of $|\Delta z|$ and z-decay cuts. Shown are curves for coplanar tracks and curves for non-coplanar tracks.

fluctuations, was 20,500. The cross section calculation further reduced to

$$\sigma^{si}_{K^\circ_s \to \pi^+\pi^-} = (\frac{20.02}{x(cm)})(\frac{20,500}{1.148 \times 10^6}), \tag{7.13}$$

$$\Rightarrow \sigma^{si}_{K^\circ_s \to \pi^+\pi^-} = 129.54\ mb.$$

We now want to determine the cross section for K° production per nucleon, so

$$\sigma^{pN}_{K^\circ_s \to \pi^+\pi^-} = \frac{\sigma^{si}_{K^\circ_s \to \pi^+\pi^-}}{28.0855} = 4.612 mb. \tag{7.14}$$

The decay mode of $K^\circ_s \to \pi^+\pi^-$ was the only one tracked for this analysis. In order to include all possible decay modes, such as the decay of the K°_s into two neutral pions, and the decay of the K°_L, the cross section must be corrected up by

$$\sigma^{pN}_{K^\circ} = 2 \times \frac{\sigma^{pN}_{K^\circ_s \to \pi^+\pi^-}}{.6861} = \sigma^{pN}_{K^\circ_s} + \sigma^{pN}_{K^\circ_L}, \tag{7.15}$$

where the value of 0.6861 in the denominator is the branching ratio for the decay into two charged pions. Correcting for the $\Lambda^\circ/\overline{\Lambda^\circ}$ contamination, we end up with an estimated K° cross section of

$$\sigma^{pN}_{K^\circ} = 13.31 \pm 0.65 \text{ (sys.) } mb.$$

In order to compare this result to those calculated at lower beam energies and some at higher beam energies, a plot is made of σ_{tot} versus beam momentum for world data [38] as shown in Figure 7.12. The world data cross section values came from such sources as the MIRABELLE hydrogen bubble chamber at the Serpukhov accelerator, the Argonne National Laboratory 12-foot hydrogen bubble chamber, the CERN 2-meter hydrogen bubble chamber, the Brookhaven 80-inch deuterium filled bubble chamber, the Fermilab 30-inch hydrogen bubble chamber, and the Fermilab 15-foot bubble chamber.

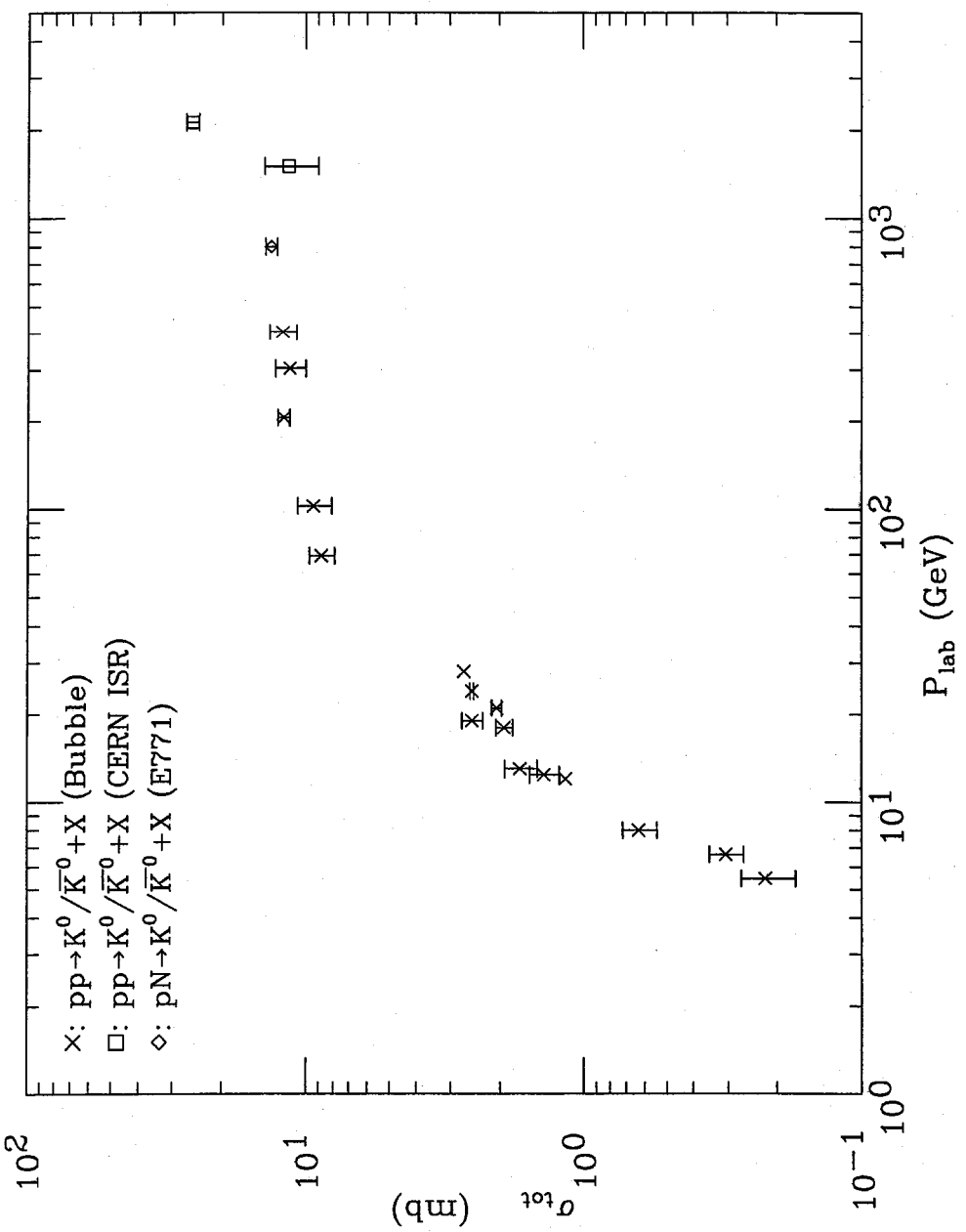

Figure 7.12: E771 estimated σ_{tot} for K° production versus P_{lab} compared to world data.

The plot of the various cross sections at different beam momenta seems to indicate a plateauing effect. At lower beam energy, the cross sections increase quite rapidity, but they level off in their values as the beam energy increases above 400 GeV/c. E771's data point is on par with the trend of an increasing cross section with increasing beam energy, yet at a lower rate when such high energies are attained.

7.3.7 $(d\sigma/dy)|_{y=0}$

The value obtained for the total K° production cross section depended critically on the correctness of the assumed rapidity distribution. A more direct measurement involving fewer assumptions is that of $(d\sigma/dy)|_{y=0}$. This measurement has been made at the lower energies as well, and so the result obtained for this thesis will be compared and analyzed with respect to other values.

The method used in obtaining $(d\sigma/dy)|_{y=0}$ consists of the following steps:

- Generate Monte Carlo events from an input rapidity distribution.
- Overlay these events on real data and track them to obtain an estimate of the detected rapidity distribution, one where the spectrometer region and acceptances have been taken into account.
- Choose a rapidity interval (chosen as $-0.4 < y < 1.4$ for statistics reasons) from the Monte Carlo and Monte Carlo Overlay regions in order to get a ratio of Monte Carlo events to Monte Carlo Overlay events. Use this ratio to get the overlay efficiency within the specified rapidity interval.

- Fit the K° mass peak for those pairs that were within the specified interval region in order to obtain $\Delta N/\Delta y$.

Once $\Delta N/\Delta y$ for the specified rapidity interval is known, it can be corrected to zero rapidity. This is achieved by multiplying $\Delta N/\Delta y$ by the Monte Carlo (M.C.) correction factor, *beta*, which converts the average $\Delta N/\Delta y$ over the interval to its peak value at $y = 0.0$, thus

$$(dN/dy)|_{y=0} = (\Delta N/\Delta y)|_{-.4<y<1.4} \times \beta. \tag{7.16}$$

The cross section at $y = 0$ is

$$(\frac{d\sigma}{dy})|_{y=0} = (\frac{dN}{dy})|_{y=0}(\frac{1}{N})(\frac{A_{wt}}{\rho N_A x},) \tag{7.17}$$

where N is the number of beam particles, A_{wt} is the atomic weight of silicon, ρ is the density of silicon, N_A is Avogadro's number, and x is the thickness of the silicon target. With all values factored in and correcting for $\Lambda^\circ/\overline{\Lambda^\circ}$ contamination, the K° cross section at zero rapidity is

$$(\frac{d\sigma}{dy})|_{y=0} = 1.46 \pm 0.06 \ \ (stat.) \ \ mb. \tag{7.18}$$

Figure 7.13 is a plot of the K° $(\frac{d\sigma}{dy})|_{y=0}$ for this experiment compared to world data [39], where a $ln(s)$ curve is forced to pass through E771's data point. This pattern indicates a behavior similar to the one observed for the total cross section value, that is, it increases quickly up to some energy, but eventually rises in a much slower fashion. The $ln(s)$ curve was plotted in order to show how the slowly increasing values correspond with past results.

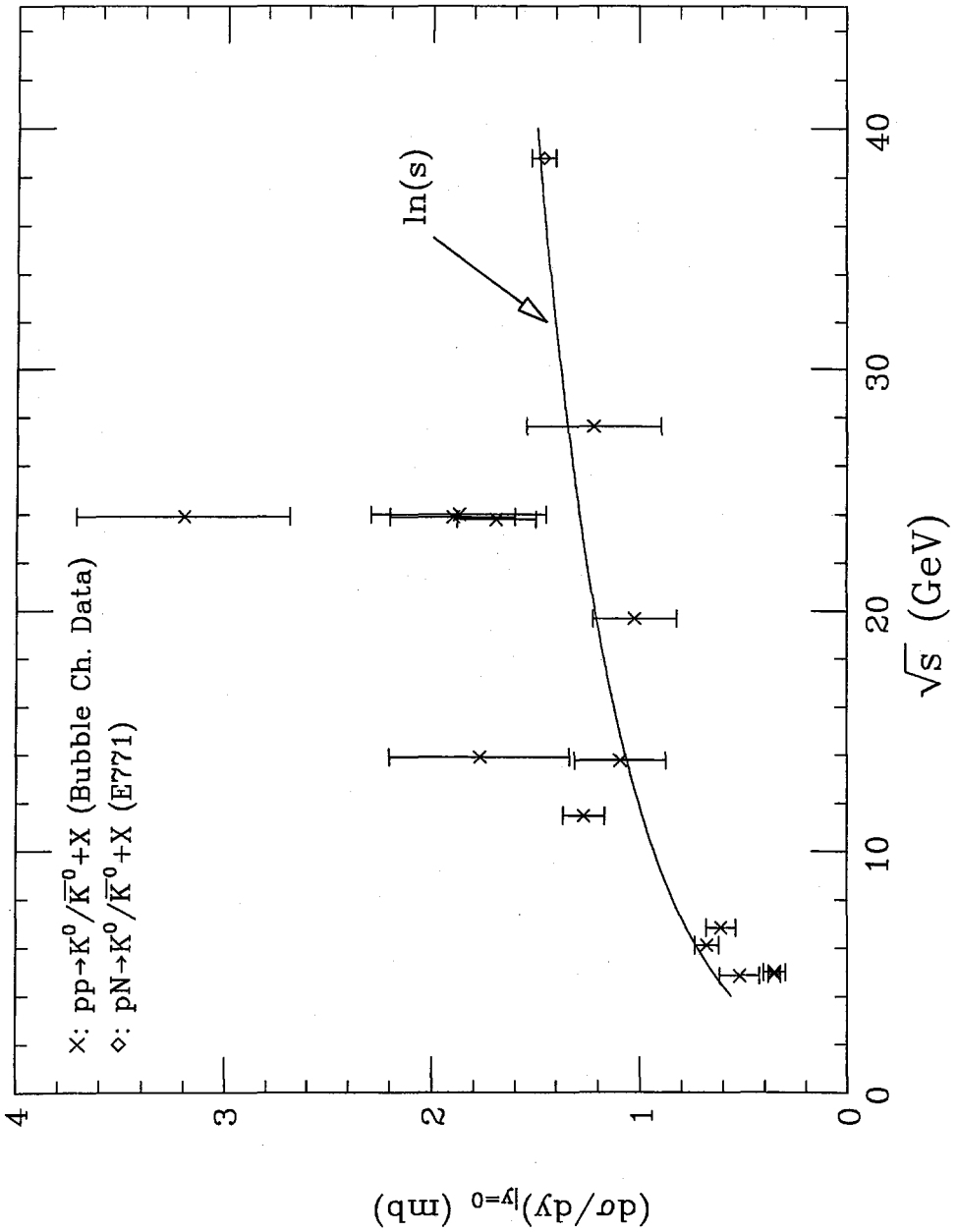

Figure 7.13: K° $(d\sigma/dy)_{y=0}$ versus $\sqrt{s}$ compared to world data with a $ln(s)$ curve drawn through E771's data point.

7.4 Λ°

Since the Λ° has a lifetime comparable to the K°, its decay vertex may be well calculated. The detection of the Λ°'s for this thesis was through the decay of

$$\Lambda^\circ \rightarrow p + \pi^-.$$

The total cross section and $(\frac{d\sigma}{dy})|_{y=0}$ will be calculated and compared to previous world data values. A study of its p_t, rapidity, x_f, and multiplicity distributions will also be performed. Some of these results will be compared to PYTHIA.

7.4.1 P_t Distribution

In order to achieve the most reasonable p_t distribution, one must apply cuts within the Λ° mass region. The Λ° p_t distribution is obtained by restricting the acceptance of only those events whose mass is within $\pm$ 10 MeV of the Λ° mass value. If they meet this criterion, the p_t distribution is plotted. There exists a background region below the mass peak, and this has to be accounted for and subtracted from the final p_t distribution plot. A background subtraction was made using the same procedure described for the K°'s in Section 7.3.1. The resulting true p_t distribution is shown in Figure 7.14.

Figure 7.14 shows the Λ° p_t distribution, the same figure plotted three times for each of three different fitting functions to obtain the $< p_t >$ value. The three different fitting functions are:

$$dN/dp_t = P1 \cdot p_t \cdot exp(-p_t \cdot P2), \tag{7.19}$$

$$dN/dp_t = P1 \cdot p_t \cdot exp(-\sqrt{p_t^2 + m^2}/P2), \tag{7.20}$$

$$dN/dp_t = (P1 \cdot p_t)/(p_t + P2)^{P3}. \tag{7.21}$$

The parameters $P1$, $P2$, and $P3$ are the fitted parameter values obtained from each of the individual fits. Points at low p_t are not used to constrain the fits because of the experimental loss of low p_t events.

(a) is the Λ° p_t distribution using Equation (7.19) as the fitting function, where $P1$ and $P2$ are the fitted parameters for the given exponential function. (b) is the Λ° p_t distribution using Equation (7.20) as the fitting function for the distribution, where $P1$ and $P2$ are the fitted parameters for this function involving the transverse energy (thermal exponential fit). (c) is the Λ° p_t distribution using Equation (7.21) as the power law fit to the distribution, where $P1$, $P2$, and $P3$ are the fitted parameters for this function.

Each of the three different fitting functions yielded similar values for the $< p_t >$, and taking the average of all three values from the three different fitting algorithms gave a value of

$$< p_t > = 0.51 \pm 0.11 \text{ GeV/c},$$

where the error was obtained from the systematic variation in the three fits.

The three different fits used to get the average p_t values were model dependent and did not look at the low p_t region. This was explained by the fact that the low p_t particles were lost when simulated to traverse E771's spectrometer region. An alternative for getting the average p_t was to average directly the p_t values for the whole distribution as the final p_t distribution was corrected for the spectrometer acceptance. The procedure was the same as that used for getting the three model dependent $< p_t >$ values. That is, one had to normalize the background p_t dis-

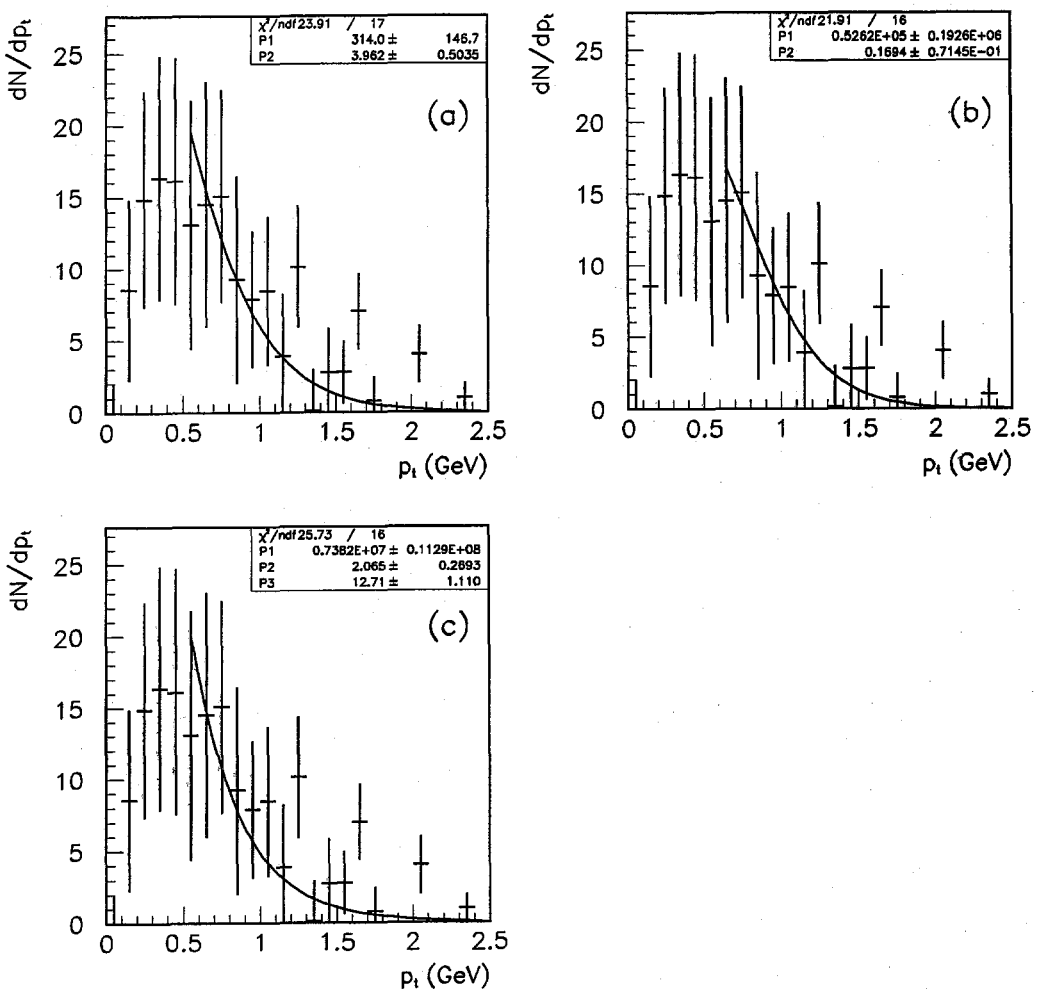

Figure 7.14: The Λ° p_t distribution from LED triggered events. The same plot is shown three times for each of three different fitting functions. (a) uses Equation (7.19) as the fit, (b) uses Equation (7.20) as the fit, and (c) uses Equation (7.21) as the fit.

tribution to the signal p_t distribution in order to perform the proper subtraction to get the correct p_t distribution. The distribution had to be overlay corrected for losses at small p_t. Then the simple average of the corrected p_t distribution was formed without performing any fitting procedures. The $< p_t >$ value obtained for the Λ°'s using this method was

$$< p_t >=0.53\pm0.17\ GeV/c.$$

It is noted that the latter procedure used to fit the $< p_t >$ yielded a higher value than that obtained from the three different fits. This is explainable by the fact that the power law fit described above generally gave a lower value than did the other two fits.

7.4.2 Multiplicity, Rapidity, and x_f Distributions

The N_c, y_{cm}, and x_f distributions were all obtained the same way the p_t distribution was. That is, those events that were within $\pm$ 10 MeV of the Λ° mass peak were kept and their respective distributions plotted. Otherwise, the calculational procedure is the same as that described for the K°'s in section 7.3.2.

Figure 7.15 shows the Λ° multiplicity, y_{cm}, and x_f distributions for the LED triggered events. (a) is the multiplicity distribution, with $< N_c >$=5.3 $\pm$ 2.6. (b) is the rapidity distribution plotted in the center of mass system. The rapidity distribution is more pronounced in the forward direction. This leads one to the conclusion that those produced in the rear direction were not accepted due to the limited spectrometer acceptance region, as observed from the Monte Carlo run. (c) is the Feynman-x distribution plotted in the center of mass system. The x_f

distribution follows the same qualitative behavior as the y_{cm} distribution.

We will now compare these distributions to those obtained from PYTHIA generated events after they have been subjected to the spectrometer acceptance.

7.4.3 Minimum Bias PYTHIA

A Monte Carlo PYTHIA program was run in order to determine how close to nature PYTHIA comes when the generated events are subjected to the same experimental acceptance. As described earlier, PYTHIA can simulate a myriad of events, such as minimum bias events, charm enhanced events, or beauty enhanced events. For this section, we will discuss a program written to simulate minimum bias events.

An event is PYTHIA generated and tracked through the spectrometer region using experimental selection criteria as was done for the K°'s in section 7.3.3.

The relevant information extracted from PYTHIA that may be compared to data consist of the average multiplicity value for those events that had Λ°'s in them, the average multiplicity value for all events, irrespective of whether the event contained a Λ°, the number of Λ°'s generated (here generated means that the particle did not necessarily make it through the spectrometer acceptance region) per generated multiplicity, the number of Λ°'s generated per event, and the average p_t value.

Since we are dealing with LED triggered events in the real data, this does not necessarily mean that a true interaction occurred for each LED trigger. The possibility existed for the LED to have triggered, but there may not have been a

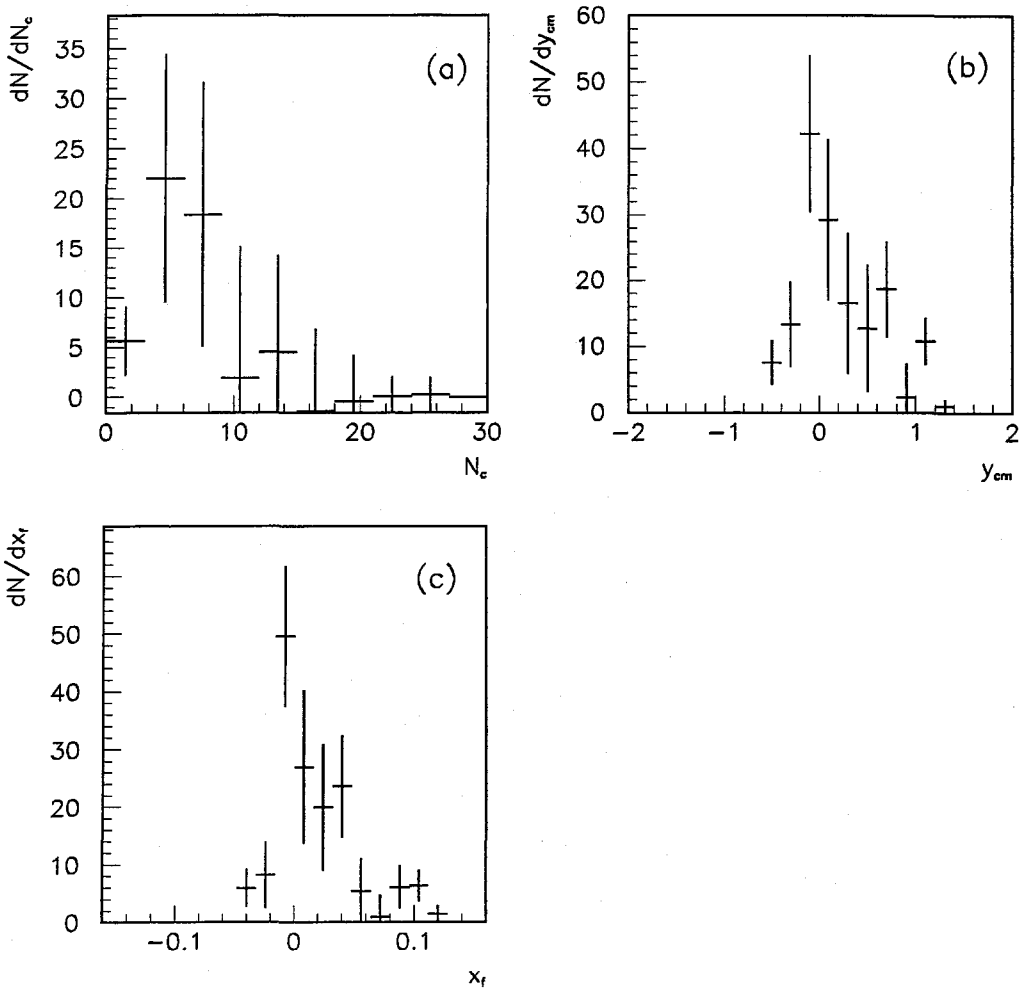

Figure 7.15: (a) N_c, (b) y_{cm}, and (c) center of mass x_f distributions for the Λ° LED triggered events. These distributions are not corrected for full spectrometer acceptance.

beam interaction. The track multiplicity would inevitably be lower than what a true minimum biased event would have recorded .

7.4.4 Comparison of Data to PYTHIA

A comparison of real data events to those PYTHIA generated is used to determine how close PYTHIA is able to predict experiment. Table 7.2 shows a comparison of PYTHIA events to real data events for the study of Λ° produced particles for minimum bias events. The first column of the table is the average multiplicity for an event that contained a Λ°. PYTHIA predicted the value 3.18 while data had the value 5.3±2.6, more than the number of tracks per event than PYTHIA predicted. The second column is the average multiplicity for all events, irrespective of whether they had a Λ° in them. The number from experimental data may be considered a lower limit since LED events without a Λ° may not have had an interaction in the silicon target. PYTHIA's number of 1.97 is lower than its value for when a Λ° is required to have been in the event. The third column contains the average number of Λ°'s generated (not necessarily that they were accepted through the spectrometer region for PYTHIA's definition, and corrected up for 4π acceptance for data) per raw charged multiplicity. Again, experimental data here are unreliable for the LED triggered events. The fourth column is the average number of Λ°'s generated per event. PYTHIA and data values agree within errors, but this experimental data point is a lower limit for LED triggers. The last column contains the $< p_t >$ for the Λ°, and the two values for PYTHIA and data agree within errors.

	$< N >_{\Lambda^\circ}$	$< N >_{evt}$	$< \frac{\Lambda^\circ(gen)}{N_{all}} >$	$< \frac{\Lambda^\circ(gen)}{evt} >$	$< p_t >_{\Lambda^\circ}$ (GeV)
PYTHIA	3.18 ± 0.07	1.97 ± 0.004	0.0543 ± 0.0004	0.1069 ± 0.0007	0.426 ± 0.004
DATA	5.3±2.6	-	-	0.0894 ± 0.0138	0.50 ± 0.06

Table 7.2: Comparison of minimum bias PYTHIA generated events and data events for Λ° produced particles with no muon trigger imposed.

A preliminary conclusion drawn from the comparisons is that PYTHIA does not exactly predict data too well. Discrepancies exist, and these may be accounted for by taking into account that PYTHIA may not allow for some specified physics processes.

7.4.5 Mass Fitting Algorithm

As outlined in Section 7.3.5, one needs to obtain a good mass peak distribution in order to perform physics calculations, such as cross section calculations. This section will describe the method used for fitting the Λ°'s.

As in most mass distribution plots, cuts are performed in order to enhance the signal distribution over the background. Two fits are performed to obtain the number of mass pairs seen within a specified region. A Gaussian fit is used for the signal peak, and a polynomial is used to fit the background region. A Gaussian fit to the signal peak may involve three parameters to fit, the multiplicative parameter, the mean mass parameter, and the standard deviation parameter. The mean mass parameter was fixed at the Λ° mass value, so only two parameters were fit. Figure 7.16 is an example of the evolution of the fitting procedure. (a)

shows a Gaussian fit to the signal peak, where the limits on the tail edges of the fit are varied somewhat in order to obtain the best fit. It also shows a straight line fit for a pre-determination on the background region. This means that once the signal peak is obtained, the straight line fit allows for a "cut-off" of the signal peak in order to fit a polynomial to the background peak, as shown in (b). This plot displays what the distribution looks like with the mass peak cut out. It allows one to fit a polynomial to the curve. (c) is then just what the polynomial distribution follows from the background fit. This is used to extract the number of track pairs in the background region within $\pm$ 10 MeV of the Λ° mass value. Plot (d) is the culmination of the fitting procedure. It shows the Gaussian fit to the signal peak and the polynomial fit for the background distribution.

The procedure for getting the number of pairs in the signal region and the number of pairs in the background region involves the following steps:

- Without the aid of fitting, count the total number of pairs within $\pm$ 10 MeV of the Λ° mass value. Take this to be the preliminary number of signal plus background pairs, the total number of pairs.

- Use the polynomial fit to the background to evaluate the number of pairs within $\pm$ 10 MeV of the Λ° mass value under the curve. Take this to be the number of background pairs.

- Subtract the number of background pairs from the total number of pairs. This result gives us the total number of signal pairs.

- The final ratio of N_s/N_b may thus be obtained and used for further analyses.

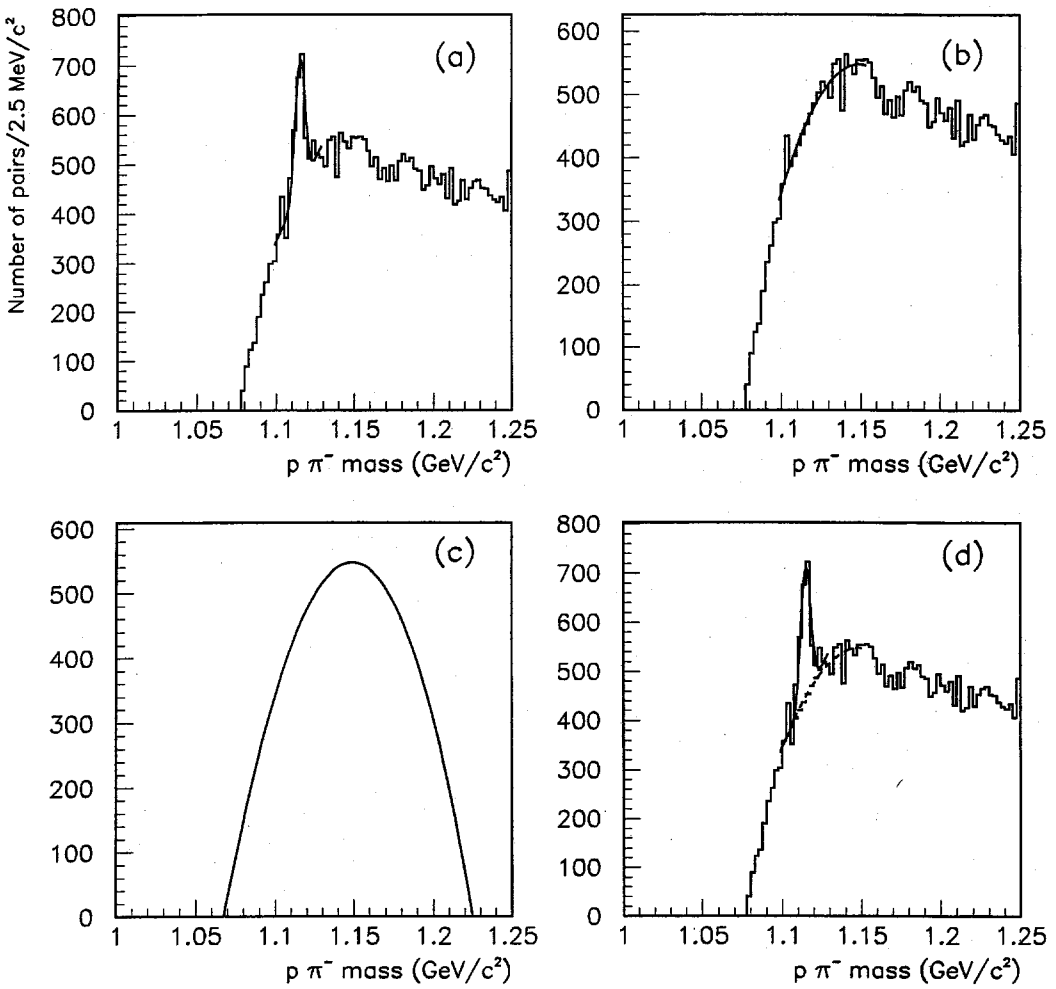

Figure 7.16: Sample Λ° mass fitting algorithm. (a) is the mass distribution with a Gaussian fit to the signal. (b) is the same as (a) but with the signal peak subtracted in order to fit the background. (c) is the polynomial curve drawn out as a result of the fit to the background. (d) is the final distribution showing the Gaussian fit to the signal and the polynomial fit to the background.

Figure 7.17 shows a Gaussian fit to the $\Lambda^\circ \rightarrow p + \pi^-$ mass signal peak and a straight line fit for a pre-determination for the background region, where the function used for the signal part of the fit was of the form

$$dN/dm^* = P(1) \cdot exp(-(x - p(2))^2/(2 \cdot p(3)^2)).$$

This is to illustrate the fact that one is fitting the Λ° right within its mass value, with its mean mass value $P(2)$= 1.115 GeV/c^2.

7.4.6 Λ° Cross Section

The method used to achieve the Λ° cross section involved fitting the mass distribution obtained when using various cuts. These mostly involved a combination of cuts on the z-decay position of the Λ° and its $|\Delta z|$ parameter, that is, the uncertainty in the z position of the decay vertex. The methods for both cuts already have been discussed in Chapter 6. The steps leading to the Λ° cross section involve the following:

- Fit the real data Λ° mass plots in order to get the absolute number of pairs produced within a z-decay and $|\Delta z|$ interval.
- Fit the overlay data Λ° mass plots in order to get the number of tracks returned from the original input distribution.
- Calculate the overlay efficiency from overlay decays on real data.
- Calculate the number of Λ°'s corrected up by the overlay efficiency. This final number is the one that will be used in the cross section calculation.

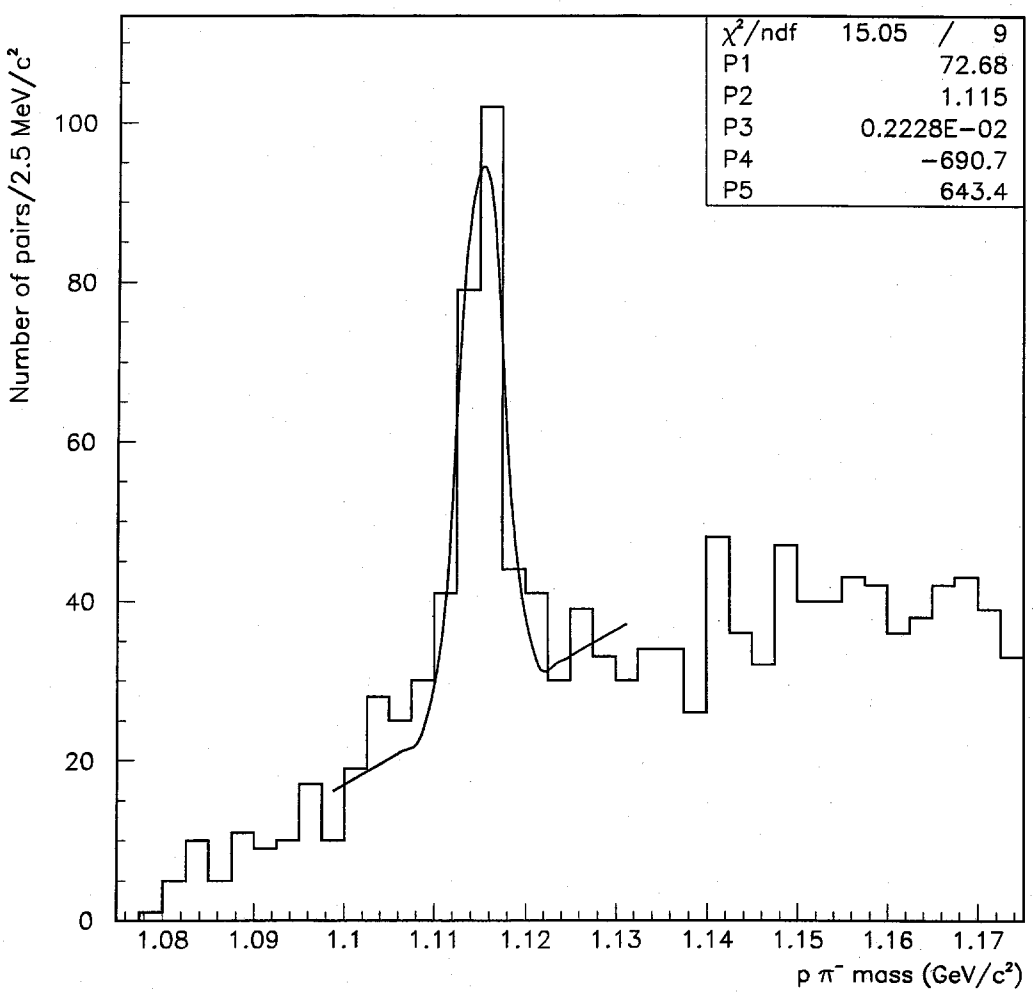

Figure 7.17: Fitted Gaussian distribution to the $\Lambda^\circ \rightarrow p + \pi^-$ mass peak.

Figure 7.18 shows a sampling of mass distributions for a variety of z-decay cuts and $|\Delta z|$ cuts. The first row shows the Λ° mass plot for a fixed z-decay length greater than 5 cm from the main interaction vertex and with increasingly tighter cuts imposed on the $|\Delta z|$ of the two daughter tracks. As the $|\Delta z|$ cuts are made tighter, the peak appears more defined.

The $|\Delta z|$ cuts imposed on the Λ°'s are looser than those imposed on the K°'s due to the low Q value in the Λ° decay. A high momentum particle produces two decay tracks that are of a small opening angle, in general. Due to this fact, the extrapolation back of two daughter decay tracks to their production site needs to allow for a greater ambiguity in the $|\Delta z|$ value. Thus, with the Λ°'s displaying the above characteristics, $|\Delta z|$ cuts ≤ 40 cm, ≤ 30 cm, ≤ 20 cm, and ≤ 10 cm were applied for the Λ°'s. One had to be careful not to allow too loose a $|\Delta z|$ cut since extraneous crossing tracks may get counted.

The second, third, and fourth rows of Figure 7.18 show the Λ° mass plots for fixed z-decay lengths greater than 10 cm, 30 cm, and 50 cm, respectively, from the main interaction vertex and with increasingly tighter cuts imposed on the $|\Delta z|$ of the two daughter tracks in each column. The further away from the main interaction vertex a particle decays, and if it is relatively long lived, as the K°'s and Λ°'s are, the further reduction in the background noise. Due to the low amount of statistics obtained for the LED triggered events, there is even a smaller amount of Λ°'s reproduced. All mass spectra in this figure were plotted irrespective of whether they were coplanar tracks. Each vertical scale is the number of pairs per 2.5 MeV/c^2, and each horizontal scale is the mass value in GeV/c^2.

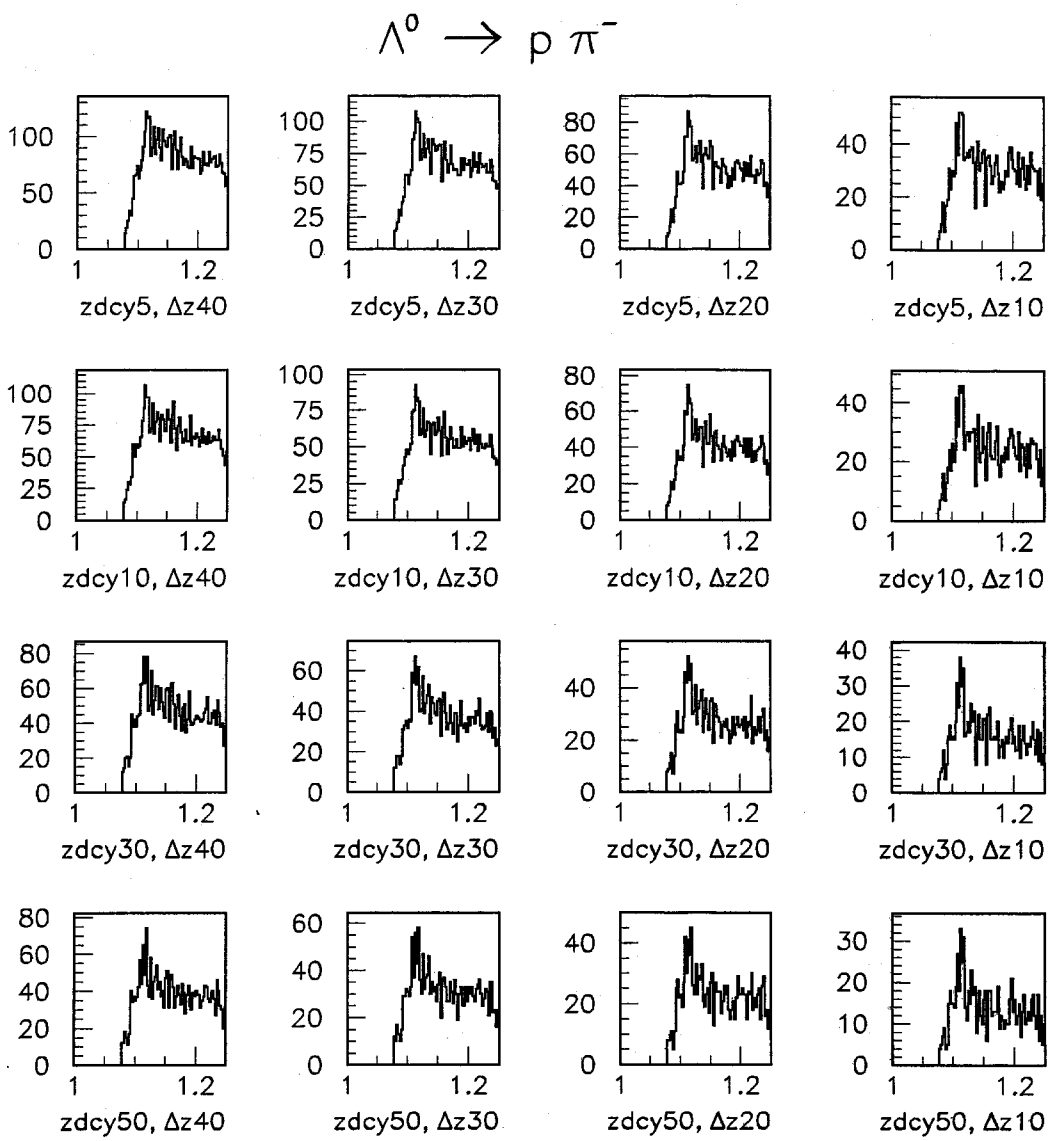

Figure 7.18: Λ° mass distributions from minimum bias triggered events for various z-decay and $|\Delta z|$ cuts, with no coplanarity criterion imposed. Each horizontal scale is the mass value in GeV/c^2, and each vertical scale is the number of pairs per 2.5 MeV/c^2.

Figure 7.19 follows the same logic as that described for Figure 7.18 with the added condition that the tracks be coplanar, as previously described in Chapter 6. The columns detail the progression in the cuts on $|\Delta z|$ while the rows detail the progression in the cuts on the z-decay of the particle from the main interaction vertex. A coplanarity cut produces a somewhat cleaner mass peak, although it results in much lower statistics. Each vertical scale is the number of pairs per 2.5 MeV/c^2, and each horizontal scale is the mass value in GeV/c^2.

Figure 7.20 is a plot of the raw number of Λ°'s versus the $|\Delta z|$ cuts for the Λ° events. The multiple curves are for individual fixed z-decay cuts. The plots show the raw number for both non-coplanarity cut events and for coplanarity cut events. Visual inspection of the plots shows a marked difference in the number of events seen without the coplanarity cut and for those with the coplanarity cut. There exists a big jump in the raw number of events, with the coplanarity cut plots lumped together. The systematic error in these values can be extracted from the swing in the value of the numbers.

Figure 7.21 is the overlay efficiency versus $|\Delta z|$ for the Λ° overlay events. The multiple curves are for individual fixed z-decay cuts. The efficiency increases as the cuts are made less stringent. These efficiency curves include both the coplanar pairs and the non-coplanar pairs. The coplanar tracks show an efficiency curve that plateaus as the $|\Delta z|$ cut is opened more.

Figure 7.22 is the corrected number of Λ°'s, $(N^\circ_\Lambda/\epsilon)$, using the raw number of Λ° events and the overlay efficiency versus the $|\Delta z|$ cuts. The curved lines represent different z-decay value parameters. As is readily observable, the coplanar and non-

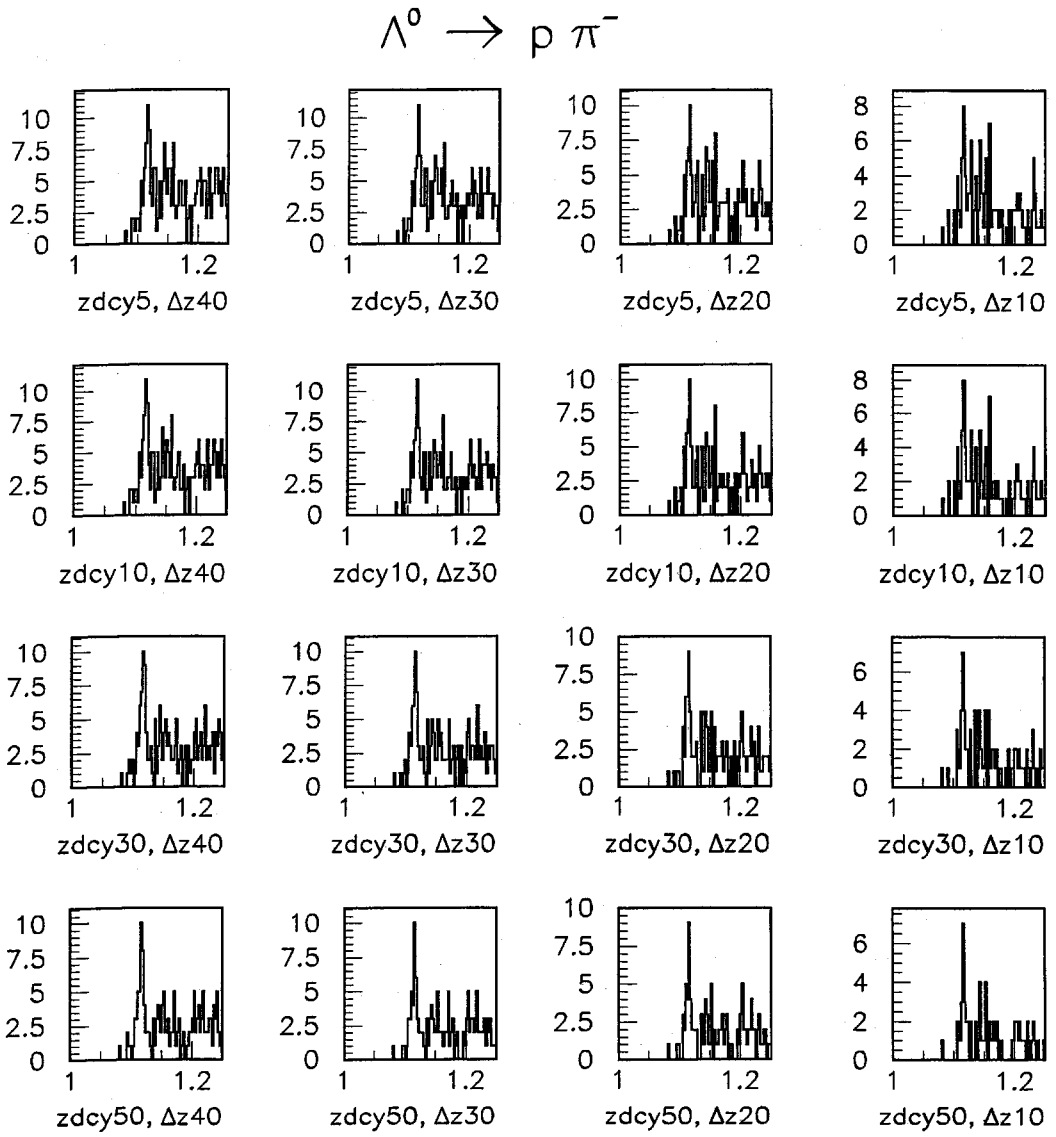

Figure 7.19: Λ° mass distributions from minimum bias triggered events for various z-decay and $|\Delta z|$ cuts, with a coplanarity criterion imposed. Each horizontal scale is the mass value in GeV/c^2, and each vertical scale is the number of pairs per 2.5 MeV/c^2.

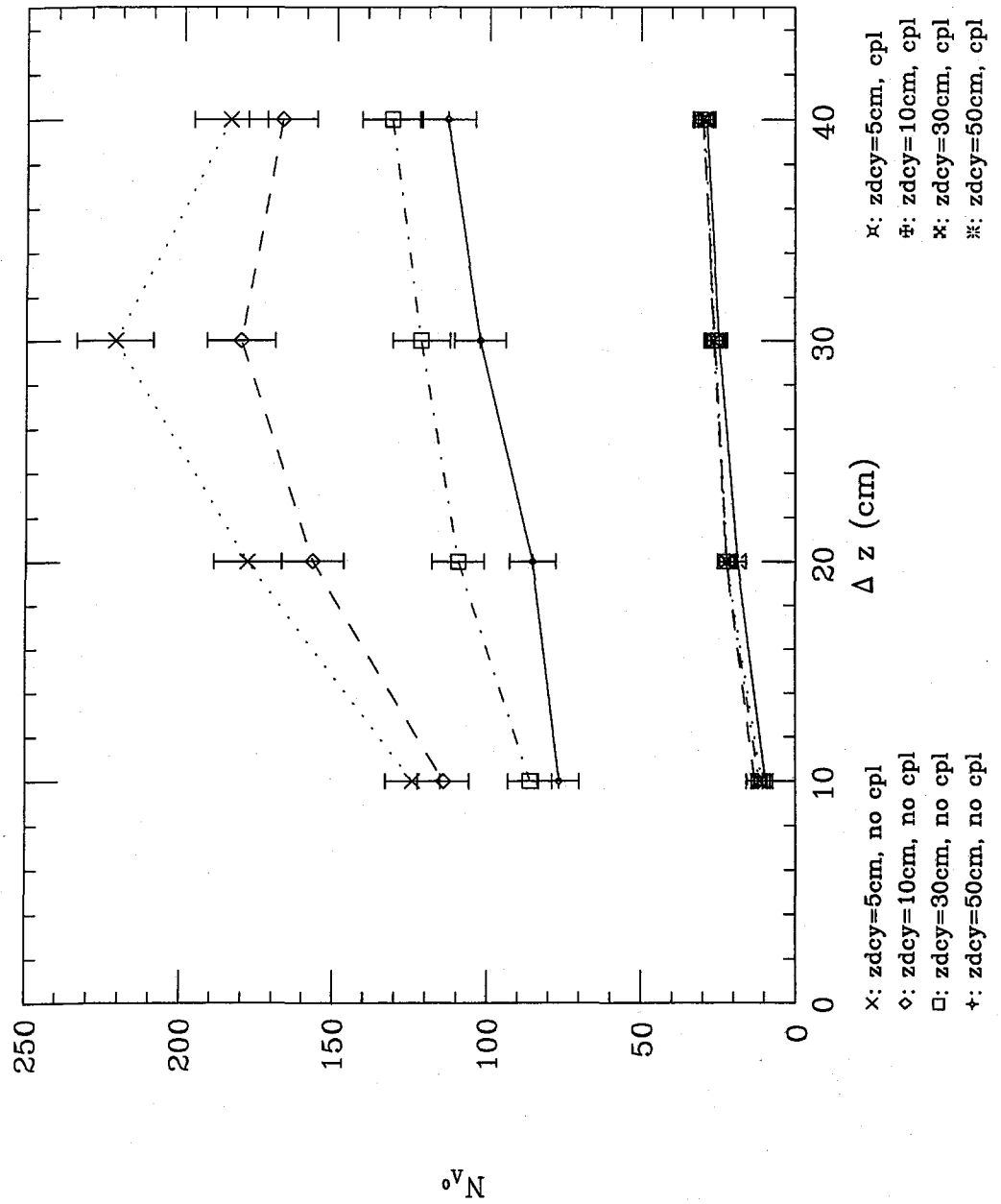

Figure 7.20: Total number of Λ°'s, N_{Λ°, as a function of $|\Delta z|$ and z-decay cuts, with the curved lines representing different z-decay cuts. Shown are curves for coplanar tracks and curves for non-coplanar tracks.

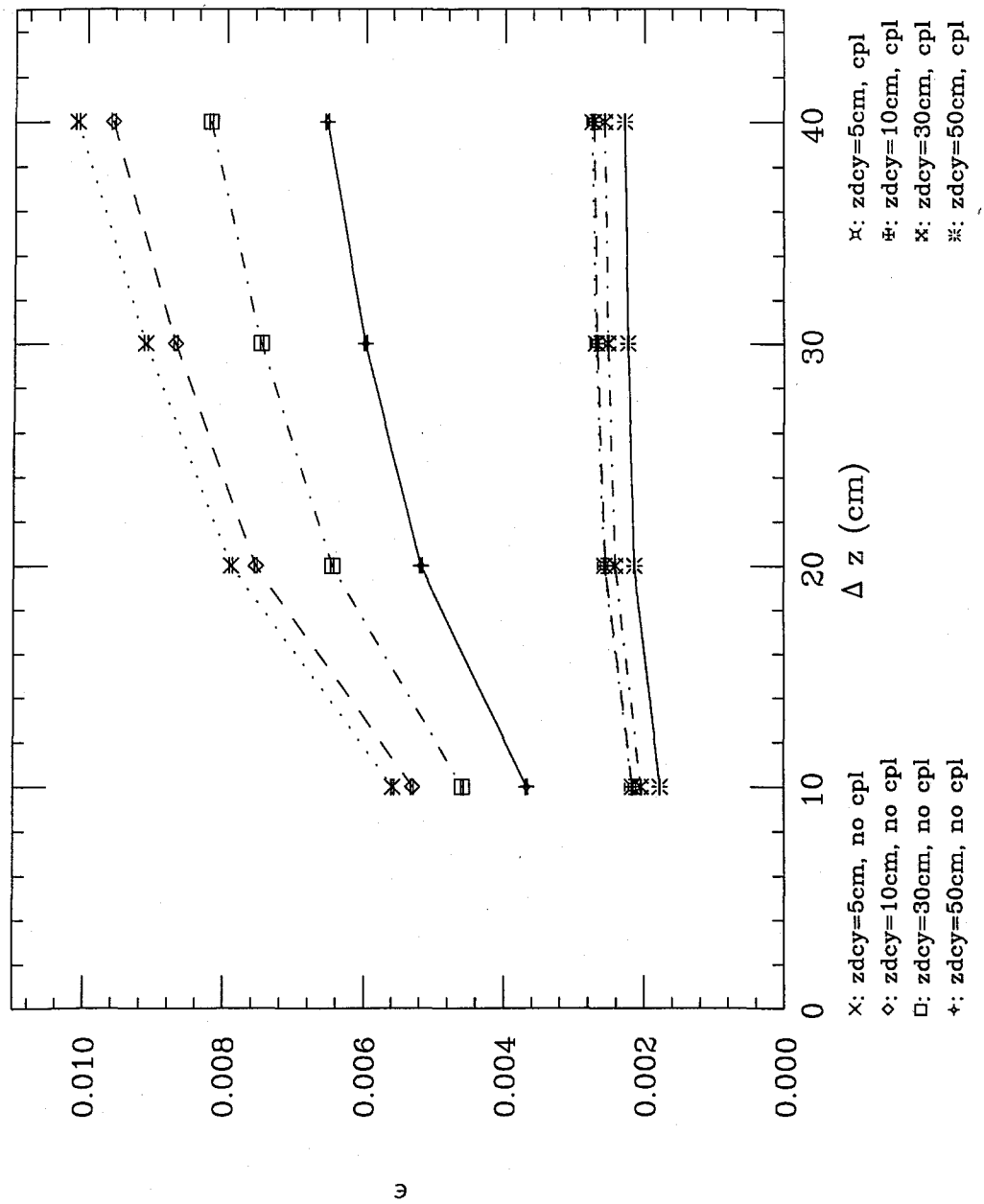

Figure 7.21: Overlay efficiency, ϵ, for tracking a Λ° as a function of $|\Delta z|$ and z-decay cuts, with the curved lines representing different z-decay cuts. Shown are curves for coplanar tracks and curves for non-coplanar tracks.

coplanar results differ by a factor of about four. This may be due to the fact that so few Λ°'s were seen, and hence a poor overlay efficiency corrected value resulted. Due to such a high discrepancy in these pairs, the cross section was calculated using events that did not have the coplanarity cut imposed.

Once the corrected number of Λ°'s was determined from the overlay efficiency values, a cross section calculation was performed. If the total number of Λ° events is known, and the total number of beam particles is known, the cross section thus is

$$\sigma^{si}_{\Lambda^\circ \to p\pi^-} = (\frac{A_{si}}{\rho_{si} \cdot N_A \cdot x})(\frac{N_{\Lambda^\circ \to p\pi^-}}{N_{beam}}). \tag{7.22}$$

$A_{si} = 28.09$ is the atomic weight of silicon. $\rho_{si} = 2.33\ g/cm^3$ is the density of silicon, and $x = 0.36\ cm$ (tracker) $+ 2.4\ cm$ (target) is the length of the silicon target and silicon tracker. The number of beam particles, from 33 tapesets analyzed (see last section of this chapter), was defined as

$$N_{beam} = 4.691 \times 10^{12} \text{ (Live Beam)} \times (\frac{13(LED/sec)}{53.1 \times 10^6 HzRF}).$$

Although there were 4.691×10^{12} beam particles, one must multiply by the fraction of LED triggers taken. In each spill there were 13 LED pulses per second, and the RF was pulsed at 53.1 MHz. The number of beam particles was

$$N_{beam} = 1.148 \times 10^6.$$

In order to get $N_{\Lambda^\circ \to p\pi^-}$, the overlay efficiency corrected number of Λ°'s had to be extracted, see Figure 7.22. Its mean value, taking into account the systematic fluctuations, was 20,250. The cross section calculation further reduces to

$$\sigma^{si}_{\Lambda^\circ \to p\pi^-} = (\frac{20.02}{x(cm)})(\frac{20,250}{1.148 \times 10^6}), \tag{7.23}$$

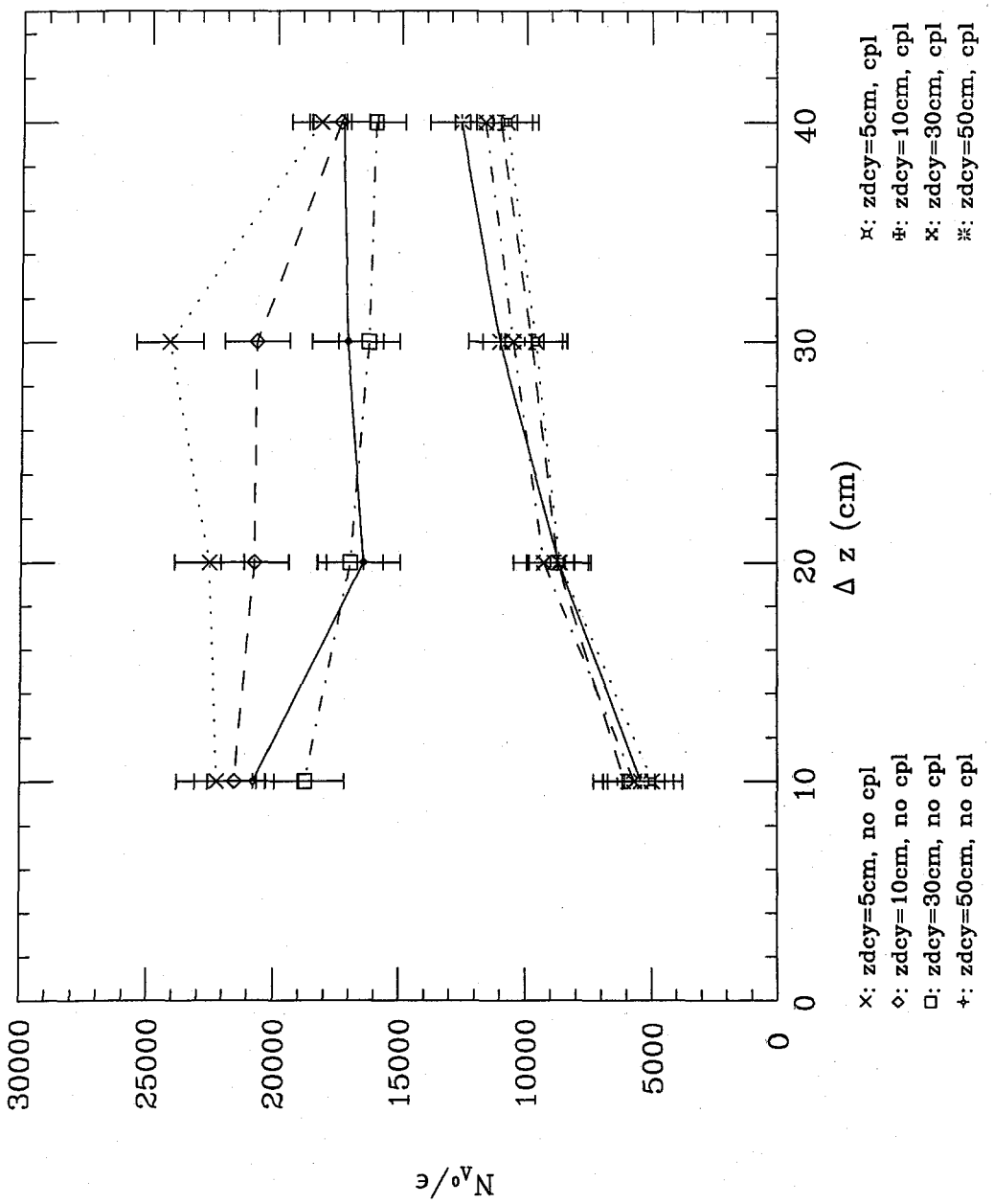

Figure 7.22: Corrected number of Λ°, $N_{\Lambda^\circ}/\epsilon$, as a function of $|\Delta z|$ and z-decay cuts, with the curved lines representing different z-decay cuts. Shown are curves for coplanar tracks and curves for non-coplanar tracks.

$$\Rightarrow \sigma^{si}_{\Lambda^\circ \to p\pi^-} = 127.96\ mb.$$

We now want to determine the cross section for Λ° production per nucleon, and

$$\sigma^{pN}_{\Lambda^\circ \to p\pi^-} = \frac{\sigma^{si}_{\Lambda^\circ \to p\pi^-}}{28.0855} = 4.556\ \ mb. \tag{7.24}$$

The decay mode of $\Lambda^\circ \to p\pi^-$ was the only one tracked for this analysis. In order to include all possible decay modes, such as the decay of the Λ° into a neutron and a neutral pion, the cross section must be corrected up by

$$\sigma^{pN}_{\Lambda^\circ} = \frac{\sigma^{pN}_{\Lambda^\circ \to p\pi^-}}{0.639}, \tag{7.25}$$

where 0.639 in the denominator is the branching ratio for the decay into a p and a π^-. Correcting for K° contamination, we end up with the Λ° estimated cross section of

$$\sigma^{pN}_{\Lambda^\circ} = 6.06 \pm 1.09\ (\text{sys.})\ mb,$$

where the systematic error is taken from the root-mean-square deviation of points at $|\Delta z| \leq 10\ cm$ in Figure 7.22.

In order to compare this result to those calculated at lower beam energy, Figure 7.23 is the σ_{tot} versus beam momentum for world data [38]. The world data cross section values came from sources like the MIRABELLE hydrogen bubble chamber from the Serpukhov accelerator, the Argonne National Laboratory 12-foot hydrogen bubble chamber, the CERN 2-meter hydrogen bubble chamber, the Brookhaven 80-inch deuterium filled bubble chamber, the Fermilab 30-inch hydrogen bubble chamber, and the Fermilab 15-foot bubble chamber.

The world data cross sections at different beam momenta indicate a plateau effect. The E771 data point, though, seems to lead to an indication of increasing

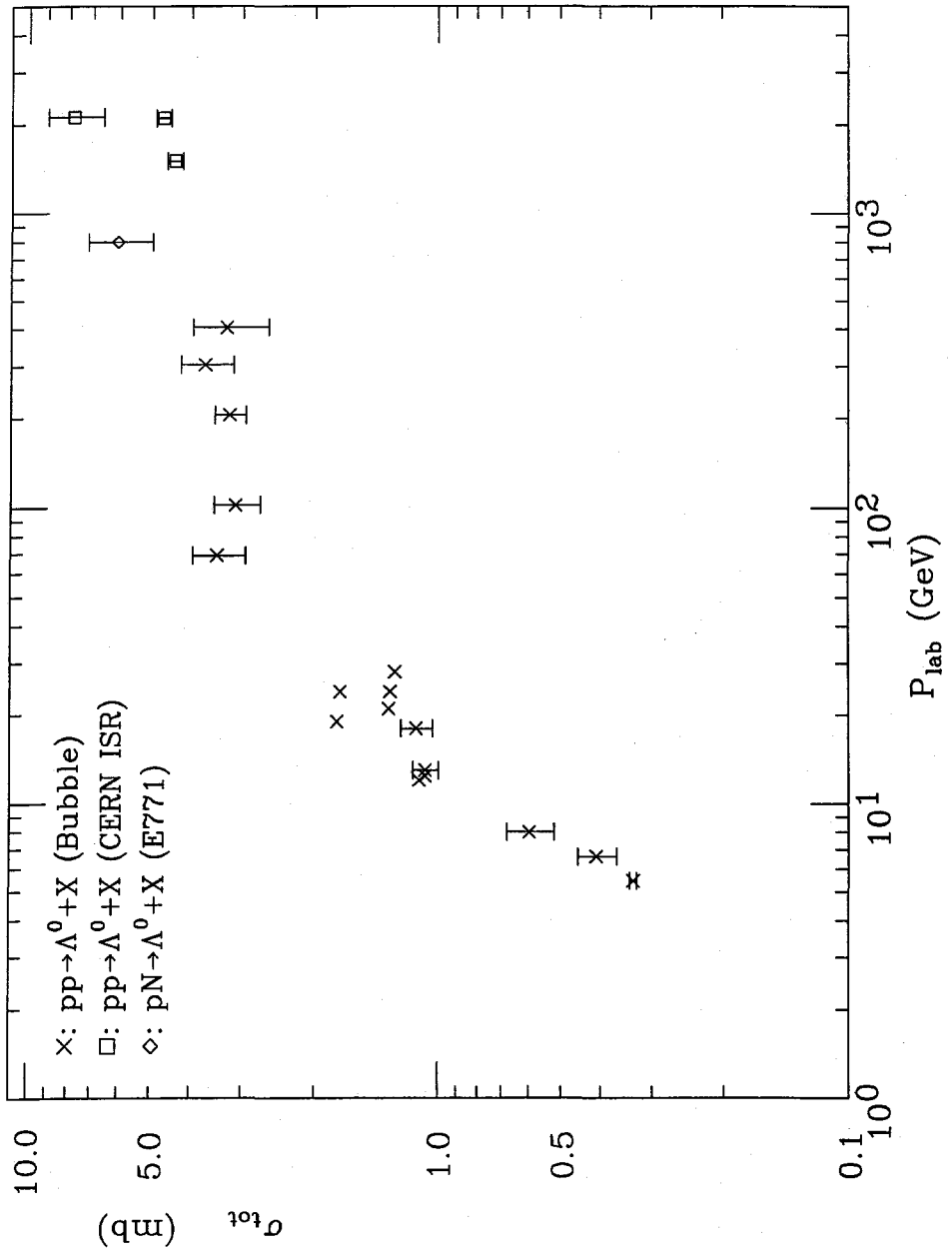

Figure 7.23: Λ° σ_{tot} versus P_{lab} compared to world data.

value as the beam energy increases. As pointed out earlier, E771's data point is a good estimation of the cross section and not an actual measurement since it depended on assumed input rapidity and p_t functions.

7.4.7 $(d\sigma/dy)|_{y=0}$

The Λ° cross section at zero rapidity is a directly measured quantity in this experiment. Since the measurement has been performed at the lower beam energies, this result will be compared and analyzed with respect to other values.

The method used in obtaining $(d\sigma/dy)|_{y=0}$ consists of the following steps:

- Generate Monte Carlo events from an input rapidity distribution.
- Overlay these events on real data and track them to obtain an estimate of the detected rapidity distribution, one where the spectrometer region and acceptances have been taken into account.
- Choose a rapidity interval (chosen as -0.4 < y < 1.4 for statistics reasons) from the Monte Carlo and Monte Carlo Overlay regions in order to get a ratio of Monte Carlo events to Monte Carlo Overlay events. Use this ratio to get the overlay efficiency within the specified rapidity interval.
- Fit the Λ° mass peak for those pairs that were within the specified interval region in order to obtain $\Delta N/\Delta y$.

Once $\Delta N/\Delta y$ for the specified rapidity interval is known, it can be corrected to zero rapidity. This is achieved by multiplying $\Delta N/\Delta y$ by the Monte Carlo (M.C.)

correction factor, β, i.e.,

$$(dN/dy)|_{y=0} = (\Delta N/\Delta y)|_{-0.4<y<1.4} \times \beta.$$

The cross section, thus at $y = 0$ is

$$(\frac{d\sigma}{dy})|_{y=0} = (\frac{dN}{dy})|_{y=0}(\frac{1}{N})(\frac{A_{wt}}{\rho N_A x},) \tag{7.26}$$

where N is the number of Λ° pairs within the zero rapidity range, A_{wt} is the atomic weight of silicon, ρ is the density of silicon, N_A is Avogadro's number, and x is the thickness of the silicon target. With all values factored in and correcting for K° contamination, the Λ° cross section at zero rapidity is

$$(\tfrac{d\sigma}{dy})|_{y=0} = 0.40 \pm 0.08 \text{ (stat.) } mb.$$

Figure 7.24 shows the Λ° $(\frac{d\sigma}{dy})|_{y=0}$ for this experiment compared to world data [40]. E771's point indicates a plateauing effect for the cross section value in the zero rapidity region.

7.5 $\overline{\Lambda^\circ}$

Since the $\overline{\Lambda^\circ}$ has a lifetime comparable to the K°, much longer lived than the B-meson, its decay vertex may be well calculated. The detection of the $\overline{\Lambda^\circ}$'s for this thesis was through the decay of

$$\overline{\Lambda^\circ} \rightarrow \overline{p} + \pi^+.$$

The estimated total cross section and $(\frac{d\sigma}{dy})|_{y=0}$ will be calculated and compared to previous world data values. At issue will be whether these cross sections are following expected trends. A study of its p_t , rapidity, x_f, and multiplicity distributions will also be performed. Some of these results will be compared to PYTHIA, and an attempt to draw some correlation will be made.

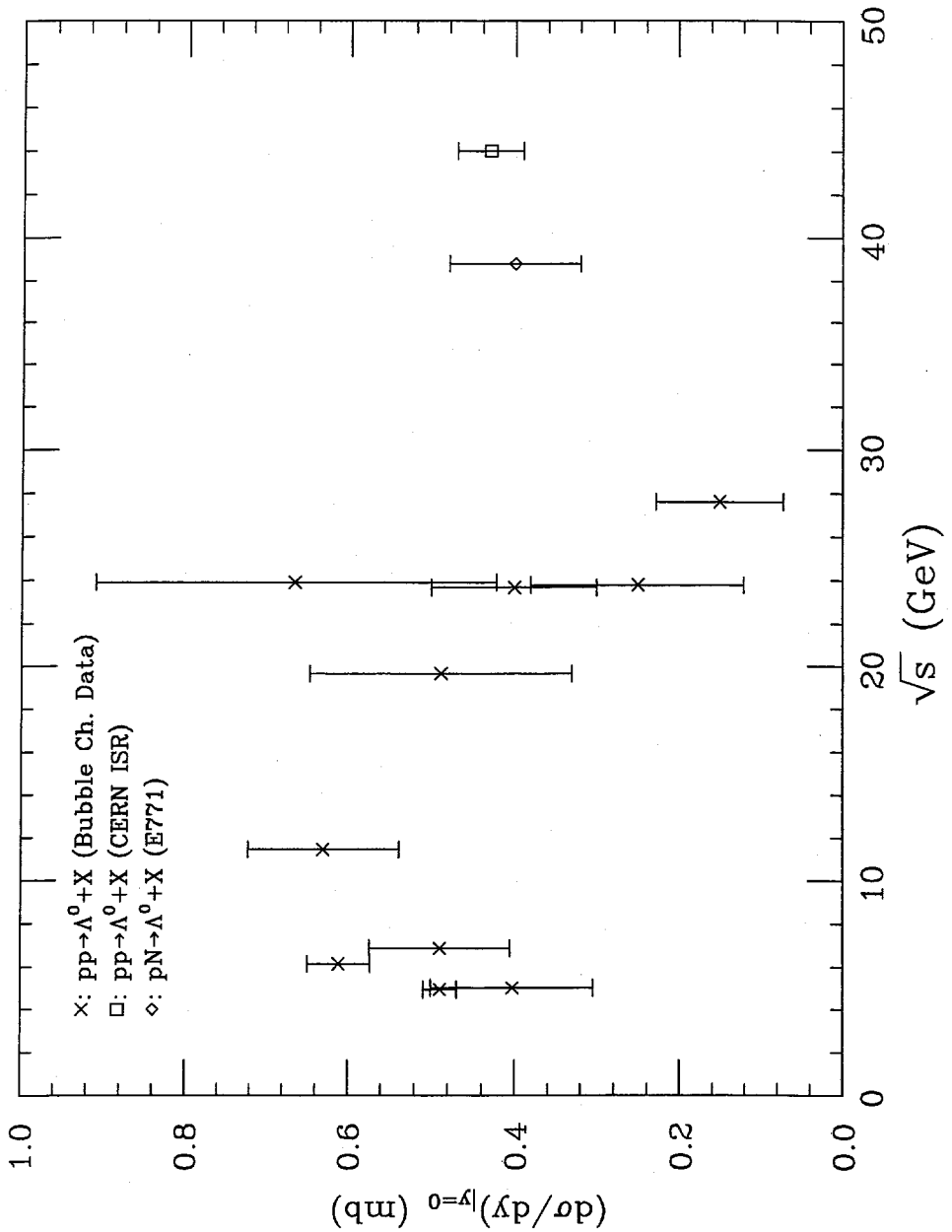

Figure 7.24: Λ° $(d\sigma/dy)_{y=0}$ versus $\sqrt{s}$ compared to world data.

7.5.1 P_t Distribution

As previously discussed for the K° and Λ° p_t distributions, selected cuts were also applied to the $\overline{\Lambda^\circ}$ mass region to obtain the most reasonable p_t distribution. The $\overline{\Lambda^\circ}$ p_t distribution was obtained by restricting the acceptance of only those events whose mass values were within $\pm$ 10 MeV of the $\overline{\Lambda^\circ}$ mass value. If they met this criterion, the p_t distribution was plotted. There existed a background region below the mass peak, and this had to be accounted for and subtracted from the final p_t distribution plot. In order to do this, a fit was performed on the $\overline{\Lambda^\circ}$ mass plot, where a Gaussian was used to fit the signal peak (N_s), and a straight line was used as a pre-determination for the background distribution. A polynomial was used to fit the background (N_b). A ratio of N_s/N_b was obtained which was subsequently used in conjunction with the p_t distribution subtraction algorithm. The way this was incorporated into the problem was the following: For the p_t distribution, plot the distribution for those events that have unlike sign tracks (signal plot, $N_\pm$), and then plot the same p_t distribution for those events that have like sign tracks (background plot, N_{LS}). The p_t distribution using the like sign tracks has to be normalized to the p_t distribution using the unlike sign tracks in some way suitable for background subtraction. In order to do this, we must renormalize the like sign pairs (N_{LS}) to be the same as the N_b, so each like sign event has to be multiplied by the ratio N_b/N_{LS}. This is then subtracted from the $N_\pm$ distribution, yielding the true p_t distribution curve.

Figure 7.25 shows the $\overline{\Lambda^\circ}$ true p_t distribution, the same figure plotted three times for each of three different fitting functions to obtain the $< p_t >$ value. The

three different fitting functions are:

$$dN/dp_t = P1 \cdot p_t \cdot exp(-p_t \cdot P2), \tag{7.27}$$

$$dN/dp_t = P1 \cdot p_t \cdot exp(-\sqrt{p_t^2 + m^2}/P2), \tag{7.28}$$

$$dN/dp_t = (P1 \cdot p_t)/(p_t + P2)^{P3}. \tag{7.29}$$

The parameters $P1$, $P2$, and $P3$ are the fitted parameter values obtained from each of the individual fits. (a) is the $\overline{\Lambda^\circ}$ p_t distribution using Equation (7.27) as the fit to the distribution, where $P1$ and $P2$ are the fitted parameters for the given exponential function. (b) is the $\overline{\Lambda^\circ}$ p_t distribution using Equation (7.28) as the fit to the distribution, where $P1$ and $P2$ are the fitted parameters for this function involving the transverse energy (thermal exponential fit). (c) is the $\overline{\Lambda^\circ}$ p_t distribution using the power law Equation (7.29) as the fit to the distribution, where $P1$, $P2$, and $P3$ are the fitted parameters for this function. Note that the fitted curve to the p_t distribution does not start at 0.0 GeV, but at a value near 0.4 GeV. As shown by the Monte Carlo p_t generated and accepted distributions (see Section 5.2.1, Figure 5.4), the accepted curve only follows the characteristic nature of the Monte Carlo at higher p_t values. This indicates that the lower p_t events cannot be used in a fit without correction for losses.

Each of the three different fitting functions yielded similar values for the $< p_t >$, and taking the average of all three values from the three different fitting algorithms gave a value

$$< p_t > = 0.421 \pm 0.096 \text{ GeV/c},$$

where the systematic error was the *rms* deviation of the three fits.

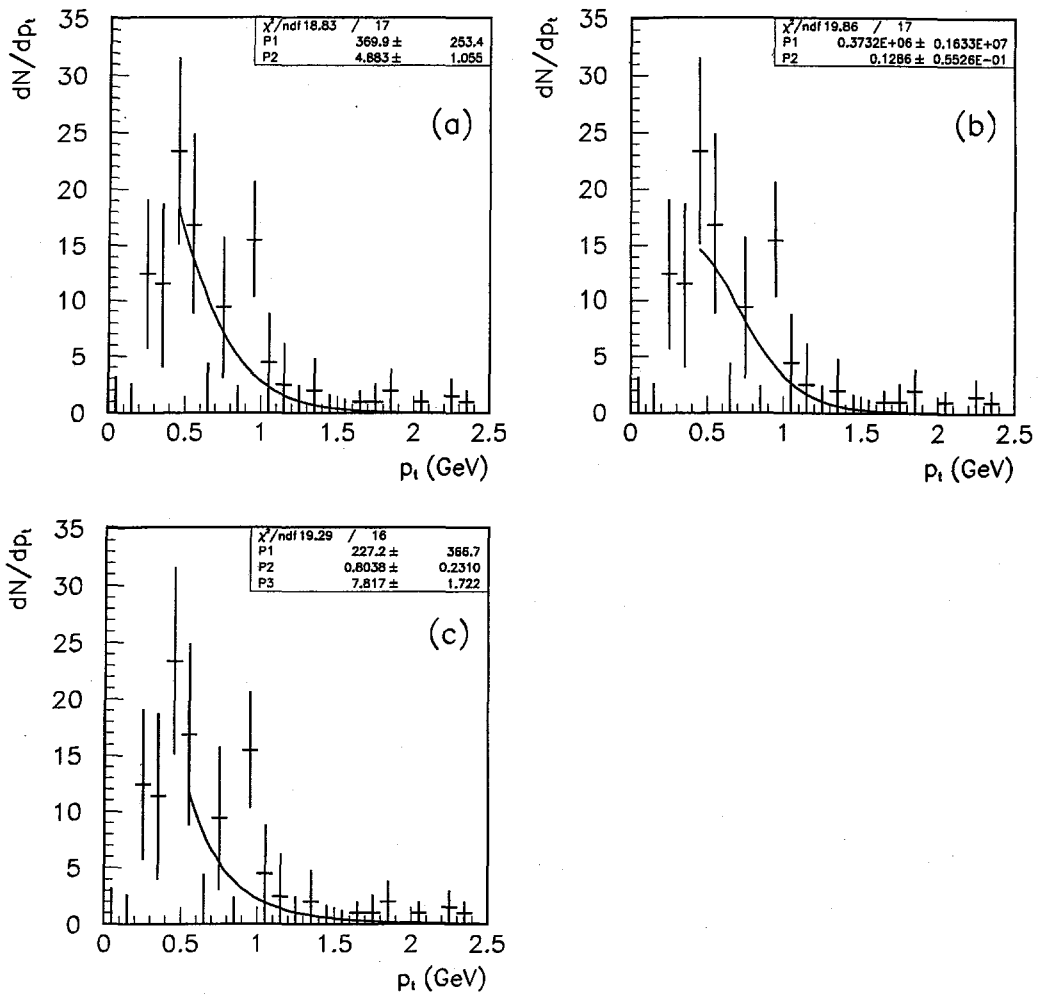

Figure 7.25: The $\overline{\Lambda^\circ}$ p_t distribution from LED triggered events. The same plot is shown three times for each of three different fitting functions. (a) uses Equation (7.27) as the fit, (b) uses Equation (7.28) as the fit, and (c) uses Equation (7.29) as the fit.

The three different fits used to get the average p_t values were model dependent and did not look at the low p_t region. This was explained by the fact that the low p_t particles were lost when simulated to traverse E771's spectrometer region. An alternative for getting the average p_t was to average directly the p_t values for the whole distribution as the final p_t distribution was corrected for the spectrometer acceptance. The procedure was the same as that used for getting the three model dependent $< p_t >$ values. That is, one had to normalize the background p_t distribution to the signal p_t distribution in order to perform the proper subtraction to get the correct p_t distribution. The distribution had to be overlay corrected for losses at small p_t. Then the simple average of the corrected p_t distribution was formed without performing any fitting procedures. The $< p_t >$ value obtained for the $\overline{\Lambda^\circ}$'s using this method was

$$< p_t >=0.60\pm0.17\ GeV/c.$$

It is noted that the latter procedure used to fit the $< p_t >$ yielded a higher value than that obtained from the three different fits. This is explainable by the fact that the power law fit described above generally gave a lower value than did the other two fits.

7.5.2 Multiplicity, Rapidity, and x_f Distributions

The N_c, y_{cm}, and x_f distributions were all obtained the same way the p_t distribution was. That is, those events that were within $\pm$ 10 MeV of the $\overline{\Lambda^\circ}$ mass peak were kept and their respective distributions plotted. The $\overline{\Lambda^\circ}$ mass peak was fit with a Gaussian to the signal and a straight line for the pre-determination of the

background distribution. The signal peak was "cut" out from the distribution in order to be left with the background region which was fitted using a polynomial curve. The ratio of signal to background was used as the normalization factor for the like sign tracked events for the "background" distribution. The normalized background distribution plot was subtracted from the signal plot in order to get the "true" distribution.

With all the tracking information given with respect to laboratory coordinates, the rapidity in the center of mass system is obtained by a transformation from the rapidity in the laboratory frame. Thus

$$y_{lab} = \frac{1}{2} ln(\frac{E + P_l}{E - P_l}), \tag{7.30}$$

and

$$y_{tx} = \frac{1}{2} ln(\frac{1 - \beta_{cm}}{1 + \beta_{cm}}). \tag{7.31}$$

Then

$$y_{cm} = y_{lab} + y_{tx}. \tag{7.32}$$

y_{tx} is the transformation equation, E is the particle's energy, and P_l is the longitudinal momentum. $\beta_{cm} = P_{beam}/(\sqrt{P_{beam}^2 + m_p^2} + m_p)$, where P_{beam} is the beam momentum and m_p the proton mass.

When looking at the center of mass system, Feynman's x variable is defined as

$$x_f = \frac{2 \cdot p_{z(cm)}}{\sqrt{s}}, \tag{7.33}$$

where $p_{z(cm)} = \gamma_{cm} \cdot (P_z - \beta_{cm} \cdot E)$.

The charged multiplicity distribution was defined as those tracks that were

spectrometer accepted. They were not corrected up for full 4π steradian acceptance via the overlay efficiency routine.

Figure 7.26 is the $\overline{\Lambda^{\circ}}$ N_c, y_{cm}, and x_f distributions for the LED triggered events. (a) is the raw charged multiplicity distribution, only spectrometer accepted tracks. Its average value was $< N_c >$=7.5±3.0. The rapidity distribution, as calculated in the center of mass system, is shown in (b). Closer observation reveals how the distribution is more pronounced in the forward direction. Those in the backward region were not accepted due to the limited spectrometer acceptance. The Feynman-x distribution, in the center of mass system, is shown in (c). It follows the same qualitative shape of y_{cm}.

7.5.3 Minimum Bias PYTHIA

A Monte Carlo PYTHIA program was implemented to simulate the generation of minimum bias events. PYTHIA was used so that comparisons may be made between data and theory.

An event is PYTHIA generated and simulated to pass through the spectrometer region. Charged tracks encounter the magnet where they experience a p_t kick and are deflected to traverse the rear chambers. The Monte Carlo program checks to see that each track of the event hits at least three chamber planes upstream of the analysis magnet and at least three chamber planes downstream of the analysis magnet. If two tracks of a generated $\overline{\Lambda^{\circ}}$ pass the front chamber and rear chamber hit criteria, the event is accepted and its relevant information, such as p_t, is plotted or put in counters for later use. The relevant information extracted from PYTHIA

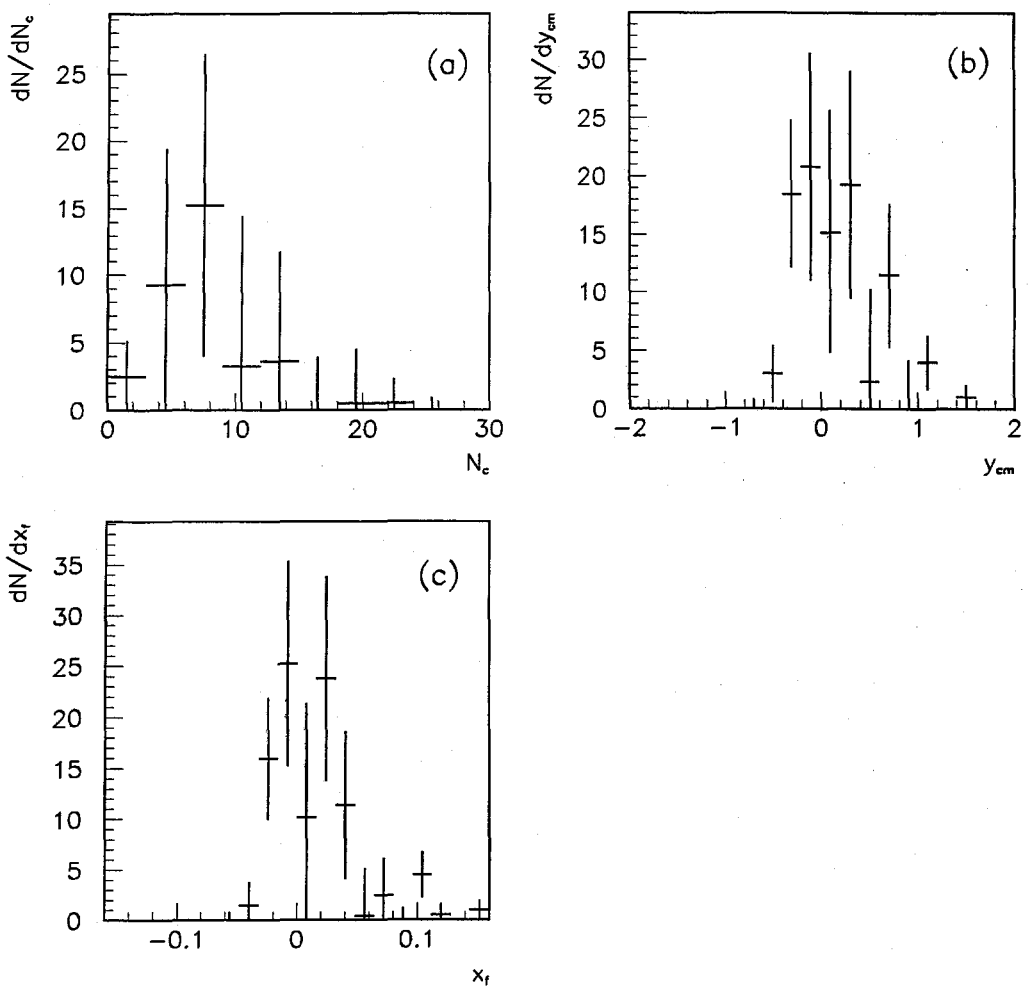

Figure 7.26: (a) N_c, (b) y_{cm}, and (c) center of mass x_f distributions for the $\overline{\Lambda^\circ}$ LED triggered events. These distributions are not corrected for full spectrometer acceptance.

that may be compared to data consists of the average charged multiplicity value for those events that had $\overline{\Lambda^\circ}$'s in them, the average charged multiplicity value for all events, irrespective of whether the event contained a $\overline{\Lambda^\circ}$, the number of $\overline{\Lambda^\circ}$'s generated (where "generated" means that the particle did not necessarily make it through the spectrometer acceptance region) per generated multiplicity, the number of $\overline{\Lambda^\circ}$'s generated per event, and the average p_t value.

7.5.4 Comparison of Data to PYTHIA

A comparison of real data events to those PYTHIA generated is used to determine how well theory can predict nature. Table 7.3 is a comparison of PYTHIA events to real data events for the study of $\overline{\Lambda^\circ}$ produced particles for minimum bias events. The first column is the average multiplicity accepted by the spectrometer for an event that contained a $\overline{\Lambda^\circ}$. PYTHIA predicted a value of 3.1 and data's value was 7.5, more than twice the number of tracks per event that PYTHIA predicted. The second column contains the average multiplicity accepted by the spectrometer for all events, irrespective of whether they had a $\overline{\Lambda^\circ}$ in them. PYTHIA cannot be compared to data's multiplicity value since the LED triggered events may not have necessarily contained an interaction. The third column contains the average number of $\overline{\Lambda^\circ}$'s generated per raw charged spectrometer accepted multiplicity. The context of "generated" for the PYTHIA generated events is that the $\overline{\Lambda^\circ}$ particles were not required to have passed the spectrometer acceptance criteria. As seen in the table, a comparison was not made with data since the value obtained for data is not the true multiplicity due to the LED triggered events. The fourth column

is the average number of $\overline{\Lambda^\circ}$'s generated per event. PYTHIA and data disagree in this category. The last column is the $< p_t >$ for the $\overline{\Lambda^\circ}$, and the two values for PYTHIA and data are within agreement.

	$< N >_{\overline{\Lambda^\circ}}$	$< N >_{evt}$	$< \frac{\overline{\Lambda^\circ}(gen)}{N_{all}} >$	$< \frac{\overline{\Lambda^\circ}(gen)}{evt} >$	$< p_t >_{\overline{\Lambda^\circ}}$ (GeV)
PYTHIA	3.1 ± 0.1	1.971 ± 0.004	0.012 ± 0.018	0.0235 ± 0.0003	0.442 ± 0.004
DATA	7.5 ± 3.0	-	-	0.0530 ± 0.0052	0.409 ± 0.089

Table 7.3: Comparison of minimum bias PYTHIA generated events and data events for $\overline{\Lambda^\circ}$ produced particles with no muon trigger imposed.

A comparison of PYTHIA and data shows that PYTHIA under predicts the number of $\overline{\Lambda^\circ}$'s generated per event and the average charged multiplicity. This is indicative of the fact that PYTHIA is known to under represent the actual number of charged tracks per event. The $< p_t >$ values were in relative agreement. A preliminary conclusion one may reach is that PYTHIA may be a good indicator of what nature could hypothetically do, but there are more physics processes that have to be taken into account to explain some of the discrepancies that exist.

7.5.5 Mass Fitting Algorithm

As Section 7.4.5 described the mass fitting algorithm routine for the Λ°'s, the same procedure is used for the $\overline{\Lambda^\circ}$'s, except for its decay being into the $\overline{p}$ and π^+. The same Gaussian fit was used for the signal peak, a straight line for the predetermination to the background region, and a polynomial fit for the background region.

The actual number obtained for pairs in the signal region and pairs in the background region involves the following steps:

- Count the total number of pairs within $\pm$ 10 MeV of the $\overline{\Lambda^\circ}$ mass value. Take this to be the preliminary number of signal + background pairs, the total number of pairs ($N_T = N_s + N_b$).
- From a polynomial fit on the background distribution, determine the number of pairs within $\pm$ 10 MeV of the $\overline{\Lambda^\circ}$ mass value under the curve. Take this to be the number of background pairs.
- Subtract the number of background pairs from the total number of pairs. This result gives us the total number of signal pairs.
- The final ratio of N_s/N_b may be obtained and used for further analyses.

7.5.6 $\overline{\Lambda^\circ}$ Cross Section

The method used to obtain the $\overline{\Lambda^\circ}$ cross section involved fitting the mass distribution for specific cuts. These mostly involved a combination of cuts on the z-decay position of the $\overline{\Lambda^\circ}$ and its $|\Delta z|$ parameter. The method for calculating the cross section involves the following steps:

- Fit the real data $\overline{\Lambda^\circ}$ mass plots in order to get the absolute number of $\overline{\Lambda^\circ}$'s detected within a specified z-decay and $|\Delta z|$ interval.
- Fit the overlay data $\overline{\Lambda^\circ}$ mass plots in order to get the number of tracks returned from the original input distribution.

- Calculate the overlay efficiency from overlay data mass plots.
- Calculate the number of $\overline{\Lambda^\circ}$'s corrected up by the overlay efficiency. This final number is the one that will be used in the cross section calculation.

Figure 7.27 shows a sampling of mass distributions for various z-decay cuts and $|\Delta z|$ cuts. The first row shows the $\overline{\Lambda^\circ}$ mass plot for a fixed z-decay length greater than 5 *cm* from the main interaction vertex and with increasingly tighter cuts imposed on the $|\Delta z|$ of the two daughter tracks. As the $|\Delta z|$ cuts are made tighter, the peak appears more defined. The $|\Delta z|$ cuts imposed on the $\overline{\Lambda^\circ}$'s are looser than those imposed on the K°'s due to the high momentum the $\overline{\Lambda^\circ}$ imparts to its two constituents. A high momentum particle produces two decay tracks that are of a small opening angle, in general, and thus experience less of a p_t kick when traversing the magnet as compared to a less massive and lower momentum particle. Due to this fact, the extrapolation back of two daughter decay tracks to their production site needs to allow for a greater ambiguity in the $|\Delta z|$ value. Thus, with the $\overline{\Lambda^\circ}$'s displaying the above characteristics, $|\Delta z|$ cuts ≤ 40 *cm*, ≤ 30 *cm*, ≤ 20 *cm*, and ≤ 10 *cm* were applied to the $\overline{\Lambda^\circ}$'s.

The second, third, and fourth rows of Figure 7.27 show the $\overline{\Lambda^\circ}$ mass plots for fixed z-decay lengths greater than 10 *cm*, 30 *cm*, and 50 *cm*, respectively, from the main interaction vertex with tighter cuts imposed on the $|\Delta z|$ of the two daughter tracks in each column. The further away from the main interaction vertex a particle decays, and if it is relatively long lived, as the K°'s and $\overline{\Lambda^\circ}$'s are, the further the reduction in the background noise. Due to the low amount of statistics obtained for the LED triggered events, there is even a smaller amount of $\overline{\Lambda^\circ}$'s obtained.

All mass spectra in this figure were plotted irrespective of whether there were coplanar tracks. Each vertical scale is the number of pairs per 2.5 MeV/c^2, and each horizontal scale is the mass value in GeV/c^2.

Figure 7.28 follows the same logic as that described for Figure 7.27 with the added condition that the tracks be coplanar, as previously described in Chapter 6. The columns detail the progression in the cuts on $|\Delta z|$ while the rows detail the progression in the cuts on the z-decay of the particle from the main interaction vertex. A coplanarity cut in this instance pretty much wipes out the mass peak due to the low statistics accumulated, so that no further use is made of the coplanarity cut. Each vertical scale is the number of pairs per 2.5 MeV/c^2, and each horizontal scale is the mass value in GeV/c^2.

Figure 7.29 shows a plot of the raw number of $\overline{\Lambda^\circ}$'s versus the $|\Delta z|$ cuts for the $\overline{\Lambda^\circ}$ events. It must be pointed out that, unlike the plots for the K°'s and the Λ°'s, due to the loss of the $\overline{\Lambda^\circ}$ signal peak, all subsequent $N_{\overline{\Lambda^\circ}}$, overlay efficiency, and $N_{\overline{\Lambda^\circ}}/\epsilon$ plots only contain events that had no coplanarity cut imposed. The multiple curves are for individual fixed z-decay cuts. The plots show the raw number for non-coplanarity cut events . The systematic error in these values was extracted from the *rms* swing in the value of the numbers.

Figure 7.30 is the overlay efficiency versus $|\Delta z|$ for the $\overline{\Lambda^\circ}$ overlay events. The multiple curves are for individual fixed z-decay cuts. The efficiency increases as the cuts are made less tight.

Figure 7.31 is the corrected number of $\overline{\Lambda^\circ}$'s, $(N_{\overline{\Lambda^\circ}}/\epsilon)$, using the raw number of $\overline{\Lambda^\circ}$ events and the overlay efficiency versus the $|\Delta z|$ cuts. The curved lines

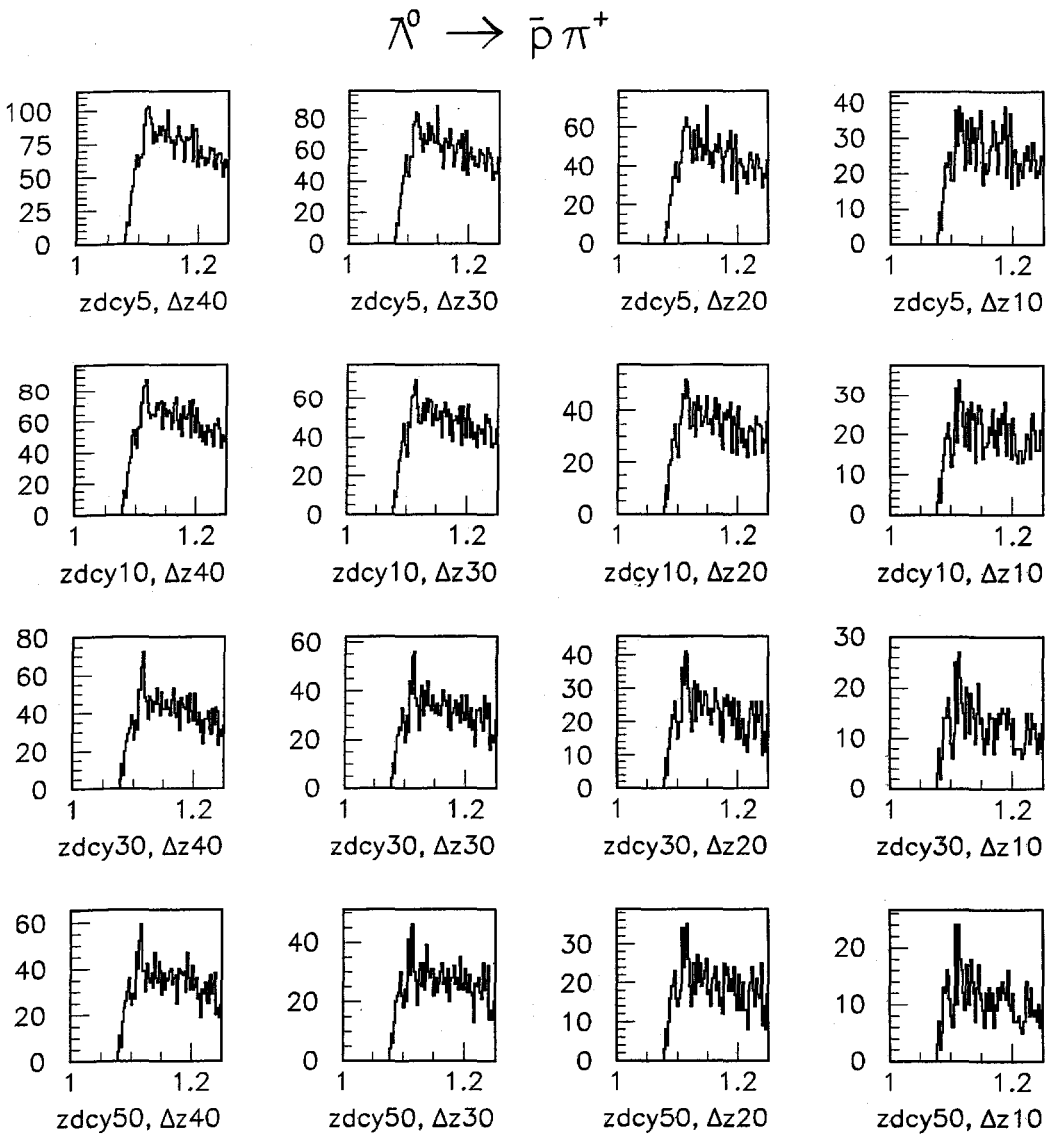

Figure 7.27: $\overline{\Lambda^\circ}$ mass distributions from minimum bias triggered events for various z-decay and $|\Delta z|$ cuts, with no coplanarity criterion imposed. Each horizontal scale is the mass value in GeV/c^2, and each vertical scale is the number of pairs per 2.5 MeV/c^2.

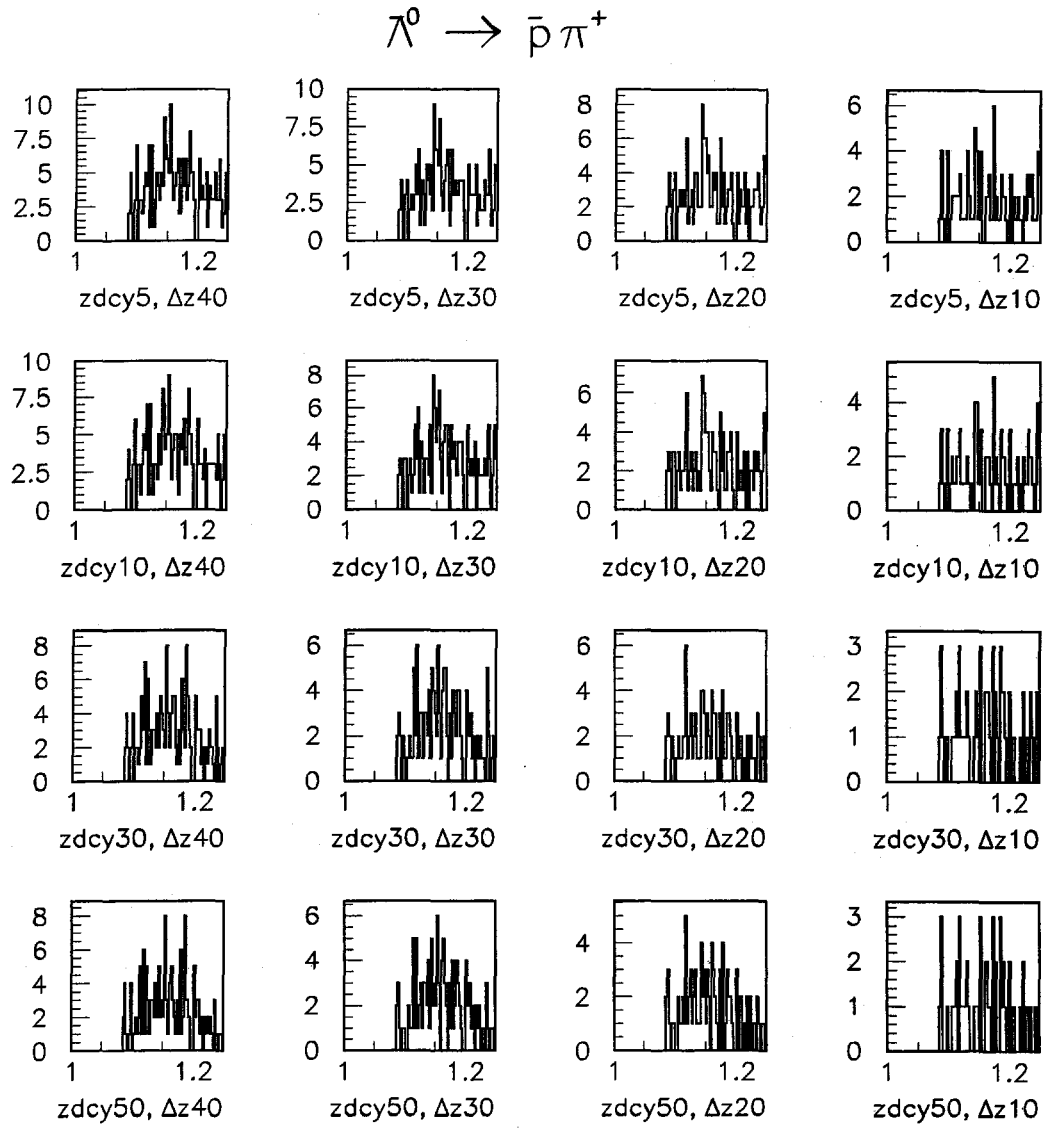

Figure 7.28: $\overline{\Lambda^\circ}$ mass distributions from minimum bias triggered events for various z-decay and $|\Delta z|$ cuts, with a coplanarity criterion imposed. Each horizontal scale is the mass value in GeV/c^2, and each vertical scale is the number of pairs per 2.5 MeV/c^2.

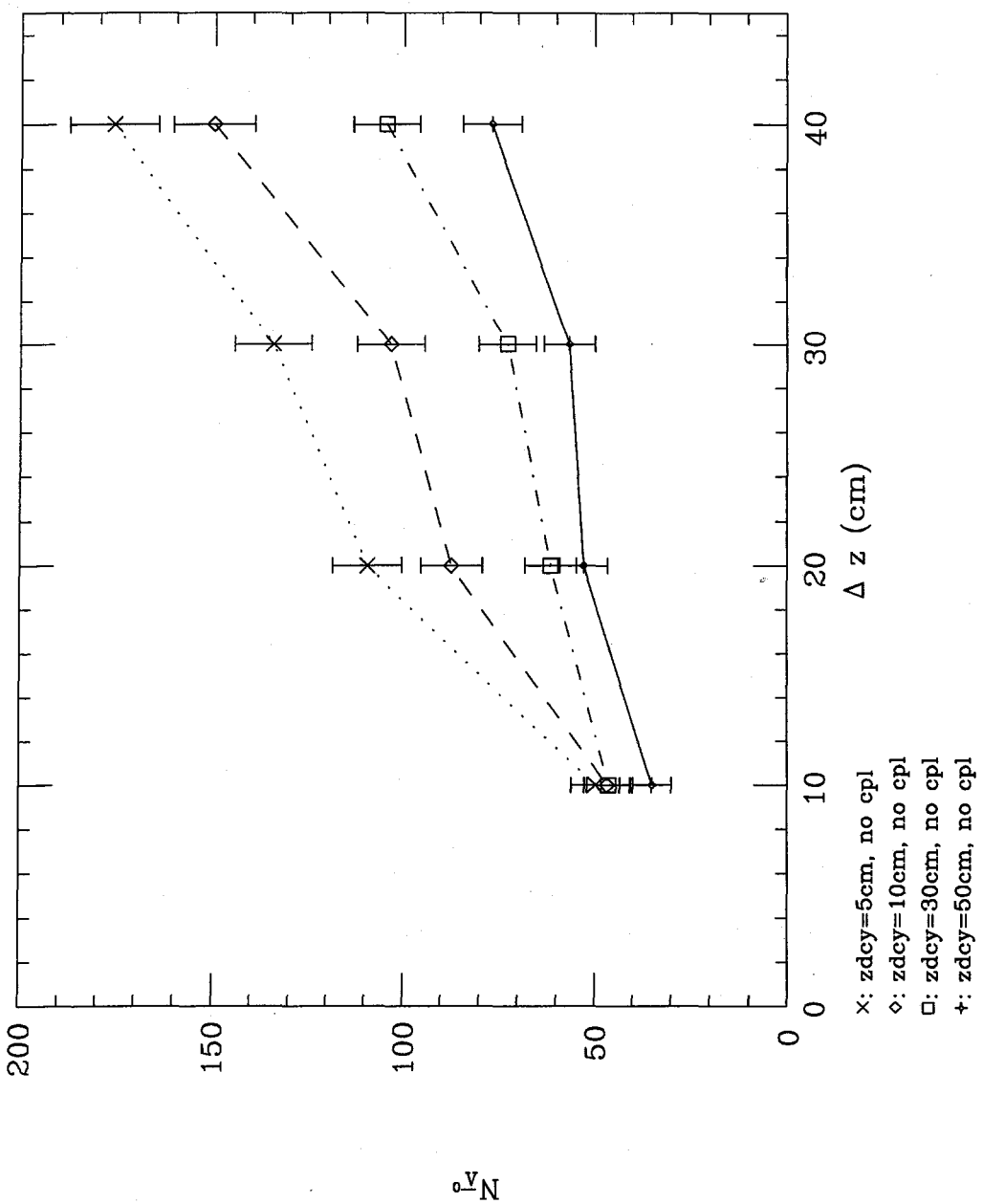

Figure 7.29: Total number of $\overline{\Lambda^\circ}$'s, $N_{\overline{\Lambda^\circ}}$, as a function of $|\Delta z|$ and z-decay cuts, with the curved lines representing different z-decay cuts.

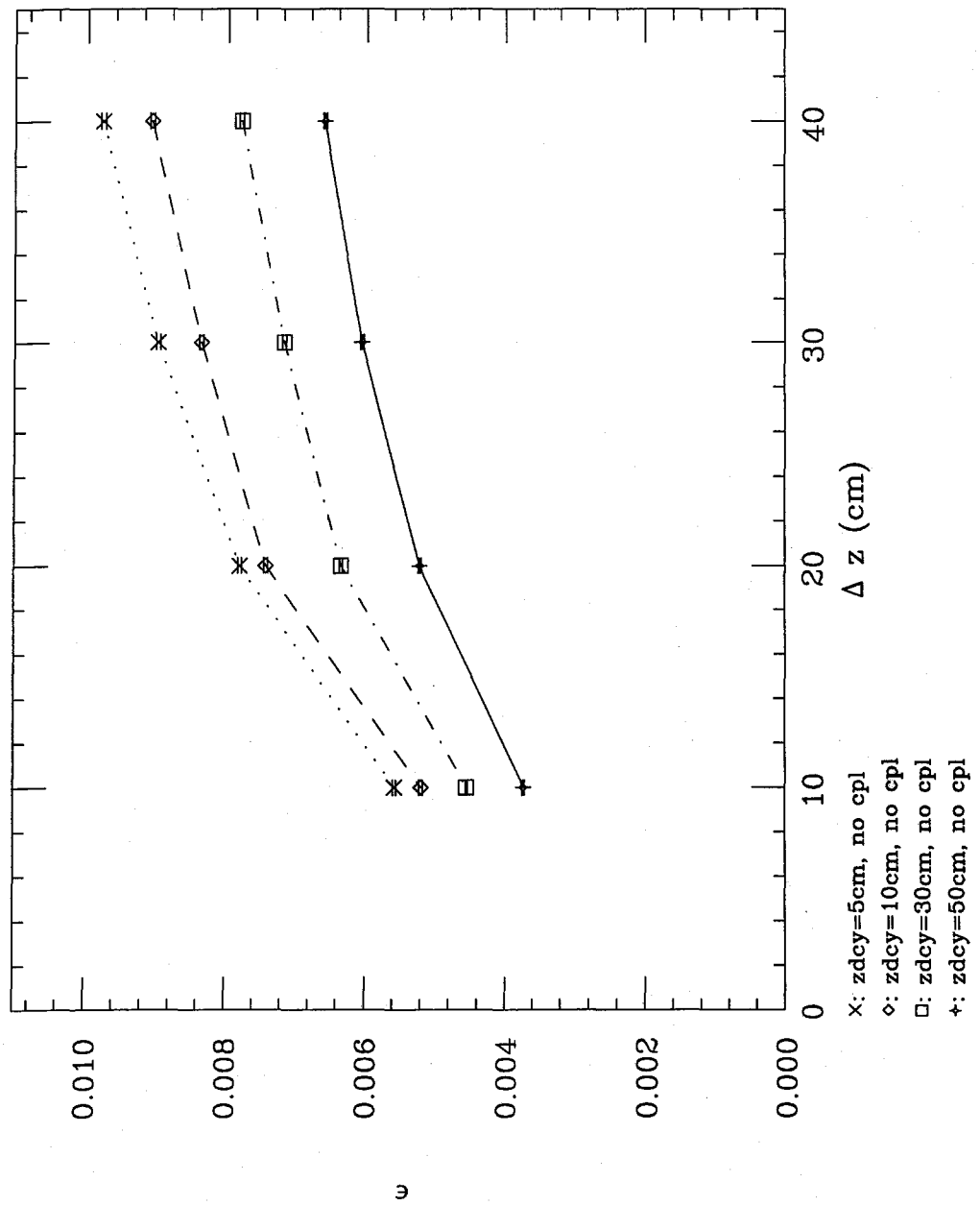

Figure 7.30: Overlay efficiency, ϵ, for tracking a $\overline{\Lambda^{\circ}}$ as a function of $|\Delta z|$ and z-decay cuts, with the curved lines representing different z-decay cuts.

represent different z-decay value parameters.

Once the corrected number of $\overline{\Lambda^\circ}$'s was determined from the overlay efficiency values, a cross section calculation was performed. If the total number of $\overline{\Lambda^\circ}$ events is known, and the total number of beam particles is known, the cross section is

$$\sigma^{si}_{\overline{\Lambda^\circ}\to\overline{p}\pi^+} = (\frac{A_{si}}{\rho_{si}\cdot N_A\cdot x})(\frac{N_{\overline{\Lambda^\circ}\to\overline{p}\pi^+}}{N_{beam}}). \tag{7.34}$$

$A_{si} = 28.09$ is the atomic weight of silicon, $\rho_{si} = 2.33\ g/cm^3$ is the density of silicon, and $x = 0.36\ cm$ (tracker) + 2.4 cm (target) is the length of the silicon target plus the silicon tracker. The number of beam particles, from 33 tapesets analyzed (see last section of this chapter), was defined as

$$N_{beam} = 4.691\times 10^{12}(LiveBeam)\times(\frac{13(LED/sec)}{53.1\times 10^6 HzRF}). \tag{7.35}$$

Although there were 4.691×10^{12} beam particles, one must multiply by the fraction of LED events seen. In each spill there were 13 LED pulses per second, and the RF was pulsed at 53.1 MHz. The number of beam particles was

$$N_{beam} = 1.148\times 10^6.$$

In order to get $N_{\overline{\Lambda^\circ}\to\overline{p}\pi^+}$, the overlay efficiency corrected number of $\overline{\Lambda^\circ}$'s had to be extracted, see Figure 7.31. Its mean value, taking into account the systematic fluctuations, was 10,500. The cross section calculation further reduced to

$$\sigma^{si}_{\overline{\Lambda^\circ}\to\overline{p}\pi^+} = (\frac{20.02}{x(cm)})(\frac{10,500}{1.148\times 10^6}), \tag{7.36}$$

$$\Rightarrow \sigma^{si}_{\overline{\Lambda^\circ}\to p\pi^-} = 66.35\ mb.$$

We now want to determine the cross section for $\overline{\Lambda^\circ}$ production per nucleon, thus

$$\sigma^{pN}_{\overline{\Lambda^\circ}\to\overline{p}\pi^+} = \frac{\sigma^{si}_{\overline{\Lambda^\circ}\to\overline{p}\pi^+}}{28.0855} = 2.362\ \ mb. \tag{7.37}$$

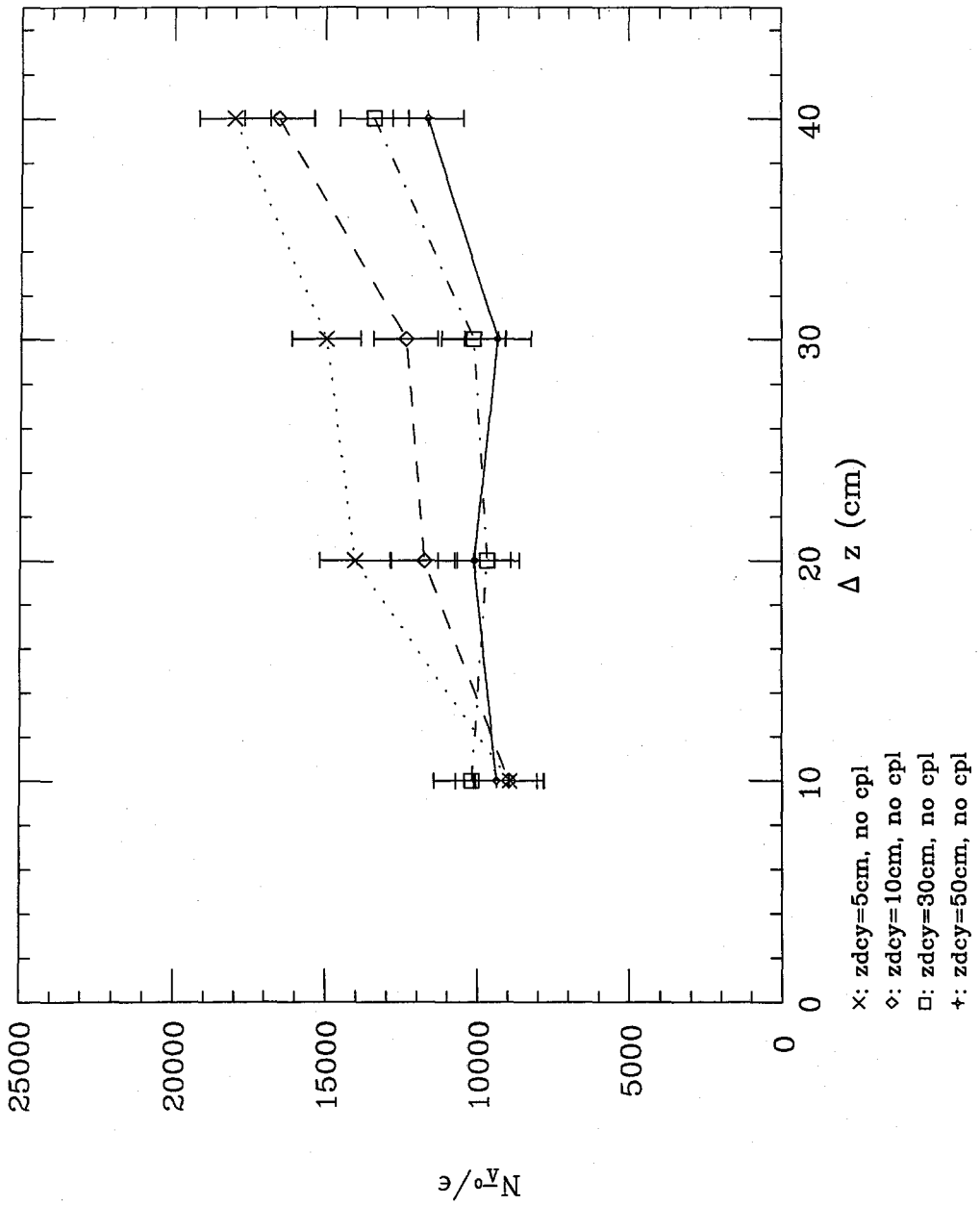

Figure 7.31: Corrected number of $\overline{\Lambda^o}$, $N_{\overline{\Lambda^o}}/\epsilon$, as a function of $|\Delta z|$ and z-decay cuts, with the curved lines representing different z-decay cuts.

The decay mode of $\overline{\Lambda^\circ} \rightarrow \overline{p}\pi^+$ was the only one tracked for this analysis. In order to include all possible decay modes, such as the decay of the $\overline{\Lambda^\circ}$ into a neutron and a neutral pion, the cross section must be corrected up by

$$\sigma^{pN}_{\overline{\Lambda^\circ}} = \frac{\sigma^{pN}_{\overline{\Lambda^\circ}\rightarrow\overline{p}\pi^+}}{0.639},$$

where the value of 0.639 in the denominator is the branching ratio for the decay into a $\overline{p}$ and a π^+. Correcting for K° contamination, we end up with the $\overline{\Lambda^\circ}$ cross section value

$$\sigma^{pN}_{\overline{\Lambda^\circ}} = 3.15 \pm 0.45 \text{ (sys.) } mb.$$

In order to compare this result to those calculated at lower beam energies, a plot is made of σ_{tot} versus beam momentum for world data [41]. It is shown in Figure 7.32. The world data cross section values came from sources as the MIRABELLE hydrogen bubble chamber at the Serpukhov accelerator, the Argonne National Laboratory 12-foot hydrogen bubble chamber, the CERN 2-meter hydrogen bubble chamber, the Brookhaven 80-inch deuterium filled bubble chamber, the Fermilab 30-inch hydrogen bubble chamber, and the Fermilab 15-foot bubble chamber.

The plot of the world data cross sections at different beam momenta indicates a continuous increase in cross section as the beam energy increases. It does not appear to indicate a plateauing effect as seen for Λ° production.

7.5.7 $(d\sigma/dy)|_{y=0}$

The $\overline{\Lambda^\circ}$ cross section at zero rapidity was directly measured, and as this procedure has been performed at lower beam energies, the result will be compared with

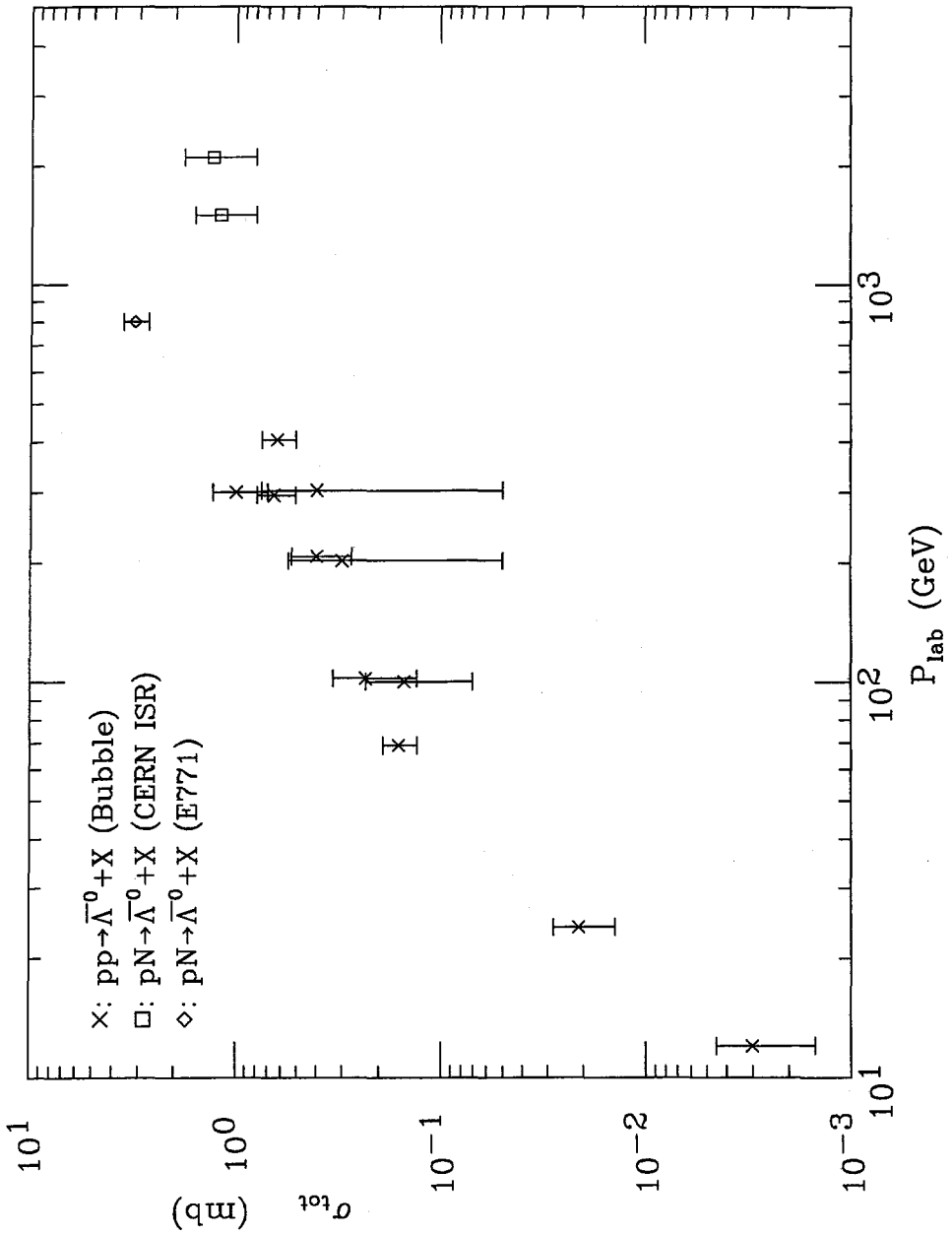

Figure 7.32: $\overline{\Lambda^\circ}$ σ_{tot} versus P_{lab} compared to world data.

respect to world data values.

The method used in obtaining $(d\sigma/dy)|_{y=0}$ consists of the following steps:

- Generate Monte Carlo events from an input rapidity distribution.
- Overlay these events on real data and track them to obtain an estimate of the detected rapidity distributions, one where the spectrometer region and acceptances have been taken into account.
- Choose a rapidity interval (chosen as $-0.4 < y < 1.4$ for statistics reasons) from the Monte Carlo and Monte Carlo Overlay regions in order to get a ratio of Monte Carlo events to Monte Carlo Overlay events. Use this ratio to get the overlay efficiency within the specified rapidity interval.
- Fit the $\overline{\Lambda^\circ}$ mass peak for those pairs that were within the specified Δy interval region in order to obtain $\Delta N/\Delta y$.

Once the average $\Delta N/\Delta y$ for the rapidity interval is known, it can be corrected to zero rapidity. This is achieved by multiplying $\Delta N/\Delta y$ by the Monte Carlo (M.C.) correction factor, β, which converts the average $\Delta N/\Delta y$ over the interval to its peak value at y=0, so

$$(dN/dy)|_{y=0} = (\Delta N/\Delta y)|_{-.4<y<1.4} \times \beta. \tag{7.38}$$

The cross section at $y = 0$ is

$$(\frac{d\sigma}{dy})|_{y=0} = (\frac{dN}{dy})|_{y=0}(\frac{1}{N})(\frac{A_{wt}}{\rho N_A x},) \tag{7.39}$$

where N is the number of beam particles, A_{wt} is the atomic weight of silicon, ρ is the density of silicon, N_A is Avogadro's number, and x is the thickness of the

silicon target. With all values factored in and correcting for K° contamination, the $\overline{\Lambda^\circ}$ cross section at zero rapidity is

$$(\frac{d\sigma}{dy})|_{y=0} = 0.32 \pm 0.09 \text{ (stat.) } mb.$$

Figure 7.33 shows the $\overline{\Lambda^\circ}$ $(\frac{d\sigma}{dy})|_{y=0}$ for this experiment compared to world data [42]. Comparison of the data points shows that E771's value seems to indicate a slower increase in the cross section, yet a definite continual increase in value as a function of increasing energy.

7.6 Signal/Background Ratios

A good sampling of the V° mass distributions was obtained by applying various z-decay and $|\Delta z|$ cuts. From these variances, a range of signal/background ratios was obtained out of a sample of 214,873 tracked LED (minimum bias) triggered events.

The signal/background ratios for the K° mass distributions ranged from as low as 0.12 to as high as 0.30 when all track pairs were taken into consideration, that is, the mass distributions contained both non-coplanar and coplanar tracks. The signal/background ratios for the K° mass distributions ranged from as low as 0.95 to as high as 2.26 when only coplanar tracks were considered. It is apparent how the ratio increased significantly, showing how the coplanarity cut had a great influence in getting rid of the background combinatorics.

The signal/background ratios for the Λ° mass distributions ranged from as low as 0.22 to as high as 0.40 when all track pairs were taken into consideration, that

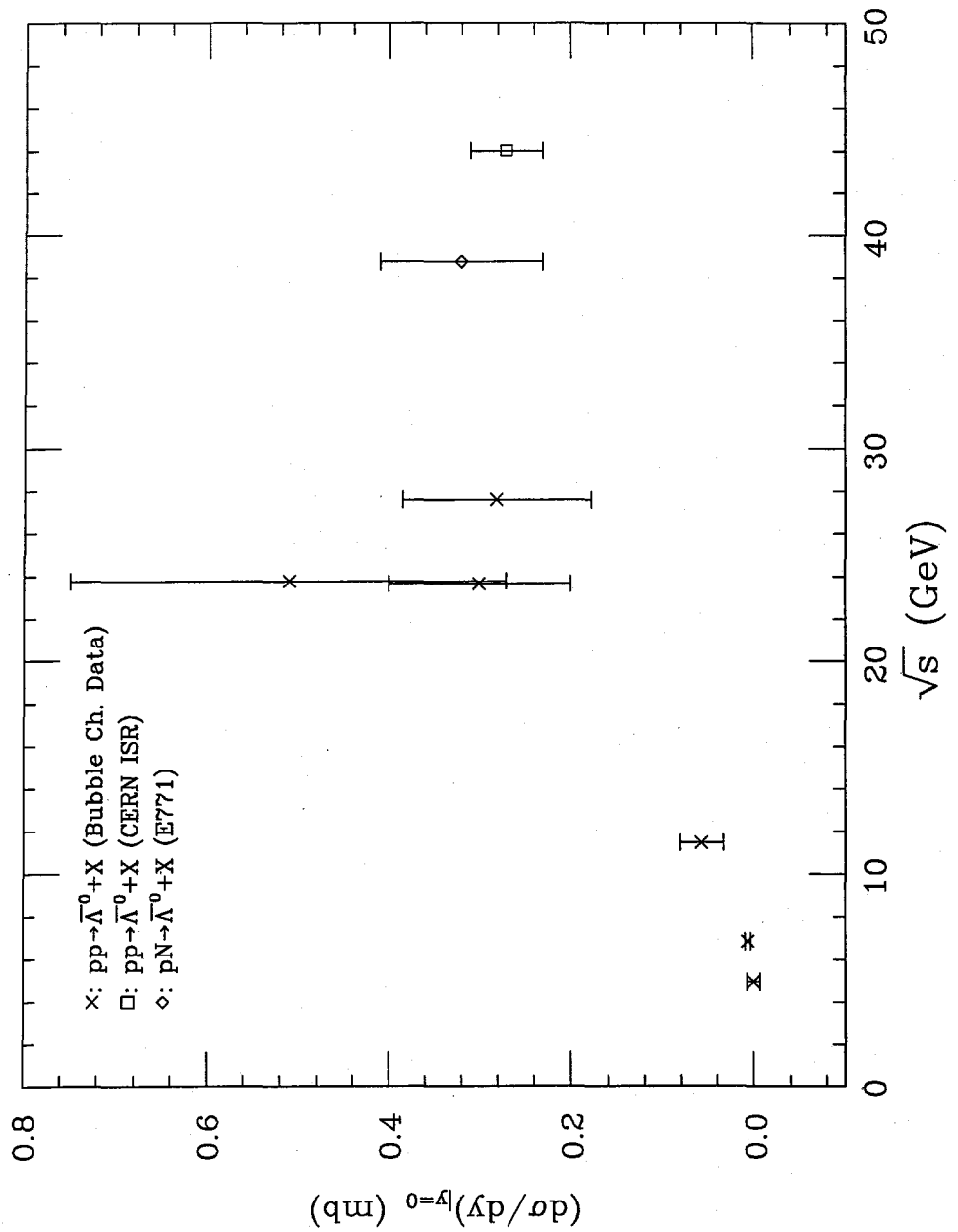

Figure 7.33: $\overline{\Lambda^\circ}$ $(d\sigma/dy)_{y=0}$ versus $\sqrt{s}$ compared to world data.

is, for the mass distributions containing both non-coplanar tracks and coplanar tracks. The signal/background ratios for the Λ° mass distributions ranged from a low of 1.23 to a high of 1.89, again showing how the coplanar cut increased the signal peak and decreasing the background region.

The signal/background ratios for the $\overline{\Lambda^\circ}$ mass distributions ranged from as low as 0.29 to as high as 0.52 when all track pairs were taken into consideration, that is, for the mass distributions containing both non-coplanar tracks and coplanar tracks. The signal/background ratios for the $\overline{\Lambda^\circ}$ mass distributions were unobtainable due to the low return on the $\overline{\Lambda^\circ}$ mass peak spectrum. It can be predicted that had more statistics been analyzed, the coplanar cut on the $\overline{\Lambda^\circ}$ would also have increased the ratios.

7.7 Data Sets Analyzed for Minimum Bias Events

Fermilab's accelerator complex was in fixed target mode from around April 1991 until January 8, 1992. During this time, E771 was in its transitional mode from upgrading pre-existing devices to full operation. Proportional wire chambers, hodoscopes, and veto counters were among the pre-existing devices to be upgraded. The new RPC chambers were installed, but it took a while to get all the FASTBUS readout electronics for the silicon detectors in place and in operation.

E771 did not begin accumulating its physics phase of the run until December 1, 1991. During this time, 138 tapesets of data were written, where a tapeset consisted of twelve 2.239 GByte tapes. This consisted of a total of 1,656 tapes where approximately 200,000 events were written to a single tape. Those events

that were triggered and tracked as LED events comprised approximately 700 events per tape of approximately 200,000 written events, roughly 1 LED tracked event per 286 events.

Tables 7.4 and 7.5 are lists of the tapesets that were analyzed to form a sample of LED events. Contained in these tables are the tapeset numbers, the JM sequence numbers (12 tapes) per tapeset number, and the total number of LED events that were tracked.

Tapeset # (TS)	JM Sequence Numbers	Total LED Tracked Events	# Events per Tapeset	Beam Particles Per TS ($\times 10^6$)
TS20323	JM2655 → JM2666	8,708	2,599,870	188,378
TS20324	JM2667 → JM2678	7,064	2,310,467	154,954
TS20326	JM2691 → JM2702	6,571	2,344,088	156,584
TS20327	JM2703 → JM2714	6,295	2,527,303	153,684
TS20328	JM2715 → JM2726	7,029	2,522,100	152,786
TS20332	JM2763 → JM2774	7,220	2,360,380	154,345
TS20333	JM2775 → JM2786	4,661	1,412,757	122,182
TS20335	JM2799 → JM2810	6,216	2,123,412	130,349
TS20336	JM2811 → JM2822	7,617	2,209,095	153,389
TS20338	JM2835 → JM2846	7,553	2,318,188	162,800
TS20339	JM2847 → JM2858	3,449	1,362,216	92,218
TS20340	JM2859 → JM2870	7,322	2,257,829	166,926
TS20341	JM2871 → JM2882	8,701	2,454,109	191,636
TS20342	JM2883 → JM2894	8,914	2,394,066	192,046
TS20343	JM2895 → JM2906	7,529	2,508,079	166,913
TS20344	JM2907 → JM2918	6,682	2,060,624	152,000
TS20345	JM2919 → JM2930	6,420	2,213,425	158,591

Table 7.4: Run statistics for minimum bias triggered events.

Tapeset # (TS)	JM Sequence Numbers	Total LED Tracked Events	# Events per Tapeset	Beam Particles Per TS ($\times 10^6$)
TS20347	JM2943 → JM2954	6,860	1,978,941	133,036
TS20348	JM2955 → JM2966	6,997	1,956,212	126,901
TS20350	JM2979 → JM2990	6,803	2,316,825	151,126
TS20351	JM2991 → JM3002	7,441	2,450,670	154,093
TS20353	JM3015 → JM3026	7,356	2,230,024	155,260
TS20354	JM3027 → JM3038	7,766	2,390,938	171,054
TS20355	JM3039 → JM3050	6,696	2,117,654	150,784
TS20357	JM3063 → JM3074	8,408	2,372,247	179,489
TS20362	JM3123 → JM3134	2,743	865,214	42,780
TS20363	JM3135 → JM3146	2,609	1,512,057	43,962
TS20365	JM3159 → JM3170	7,268	2,402,271	146,551
TS20366	JM3171 → JM3182	6,594	2,142,963	135,204
TS20368	JM3195 → JM3206	5,274	1,906,832	110,308
TS20374	JM3267 → JM3278	4,424	1,337,283	97,878
TS20375	JM3279 → JM3290	6,346	2,042,344	155,297
TS20377	JM3303 → JM3314	2,604	1,159,281	88,080

Table 7.5: Run statistics for minimum bias triggered events. (Continuation of Table 7.4.)

Chapter 8

Single-μ Triggered Events

The single muon triggered events consisted only of those events that contained a high p_t muon trigger, usually of the value $p_t \geq 0.8$ GeV/c or $p_t \geq 1.0$ GeV/c. As discussed in Chapter 3.1, E771 wrote approximately 60 million single muon triggered events to data tapes. Of the 60 million single muon triggered events, approximately 1.6 million single muon tracked events were used for this analysis.

8.1 Raw K° Events, Overlay Efficiency, Corrected K° Acceptance

The procedures that will be described for fitting the K° events, for calculating the overlay efficiency, and for obtaining the corrected K° acceptances are the same as those employed for the minimum bias events.

Compared to the minimum bias (LED triggered) events, the single muon triggered events produced mass spectra with a significantly larger number of K°'s. Figure 8.1 shows such a sampling of the K° mass distribution with different z-decay and $|\Delta z|$ cuts. These plots did not require that the tracks be coplanar.

The first row of plots is the mass distribution for a fixed z-decay length greater

than 5 cm from the main interaction vertex, while the progression of columns is for increasingly tighter cuts imposed on the distance of closest approach of the two daughter tracks, $|\Delta z|$. The second row is the mass distribution for a fixed z-decay length greater than 10 cm from the main interaction vertex, while the columns are for $|\Delta z|$ cuts $\leq$ 20 cm, $\leq$ 15 cm, $\leq$ 10 cm, and $\leq$ 5 cm. The third row is the mass distribution for a fixed z-decay length greater than 30 cm from the main interaction vertex, while the columns are for $|\Delta z|$ cuts $\leq$ 20 cm, $\leq$ 15 cm, $\leq$ 10 cm, and $\leq$ 5 cm. The last row is the mass distribution for a fixed z-decay length greater than 50 cm from the main interaction vertex, while the columns are for $|\Delta z|$ cuts $\leq$ 20 cm, $\leq$ 15 cm, $\leq$ 10 cm, and $\leq$ 5 cm. The combination of tighter cuts increases the signal to noise ratio.

Recall that a coplanar K° event met the criterion that

$$cos(\theta) = \frac{(\vec{V} \times \vec{a}) \cdot (\vec{b} \times \vec{V})}{|\vec{V} \times \vec{a}||\vec{b} \times \vec{V}|} \geq 0.95, \tag{8.1}$$

where $\vec{V}$ was the parent particle vector, and $\vec{a}$ and $\vec{b}$ were the first and second decay product vectors.

Figure 8.2 follows the same convention as that described for Figure 8.1 with the added condition that the tracks be coplanar. A comparison of the two figures shows a significant improvement of the signal to noise ratio, thus enabling good fitting procedures to be performed.

Figure 8.3 is one example of the information extracted from the mass plots. It shows the raw number of K°'s as a function of the $|\Delta z|$ cuts. The lines drawn through sets of different coordinated symbols refer to the different z-decay values. The looser the $|\Delta z|$ cut is, e.g., $\leq$ 20 cm, and the closer to the main interaction

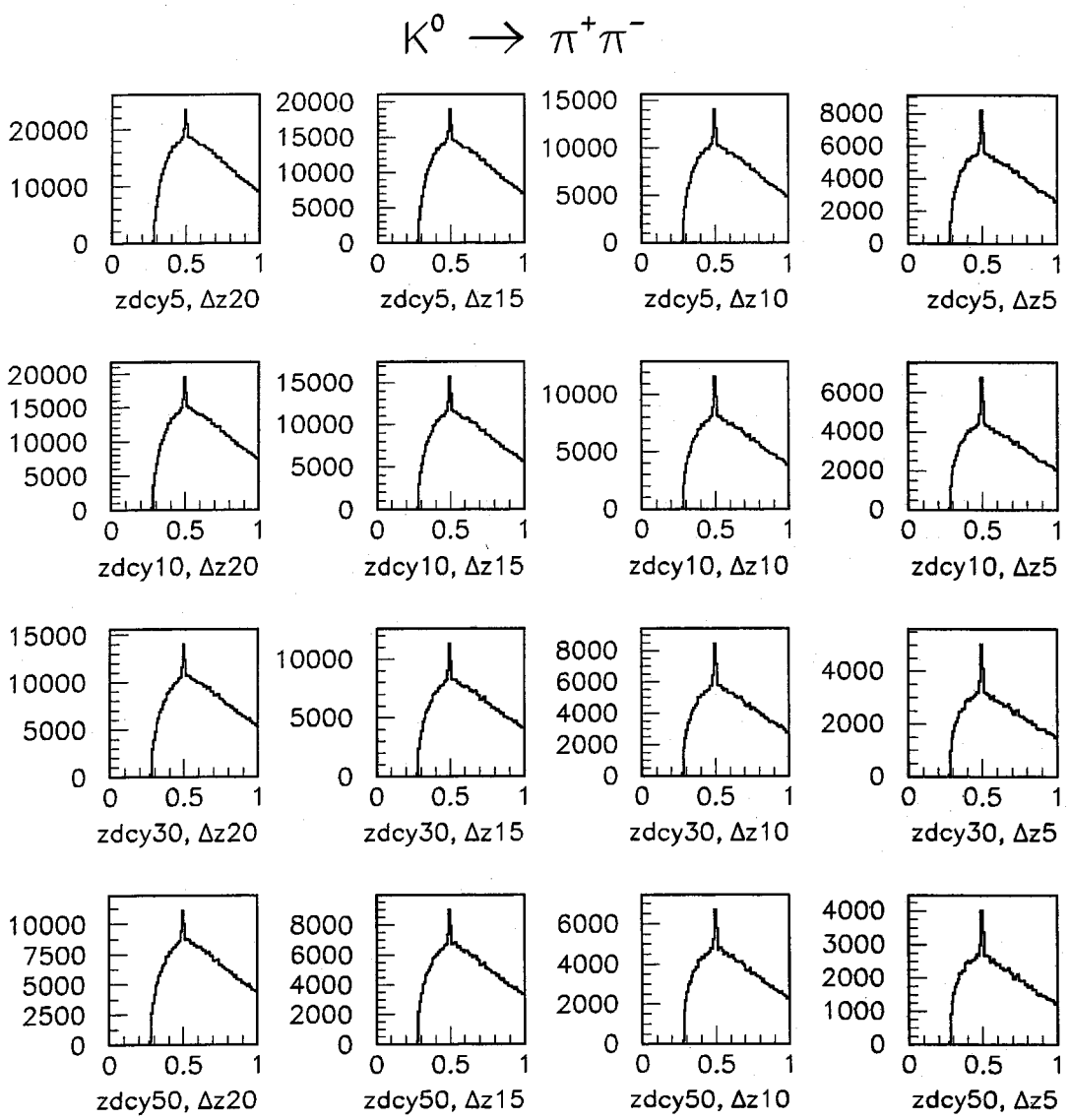

Figure 8.1: K° mass distributions from single muon triggered events for different z-decay and $|\Delta z|$ cuts, with no coplanarity cut imposed. Each horizontal scale is the mass value in GeV/c^2, and each vertical scale is the number of pairs per 10 MeV/c^2.

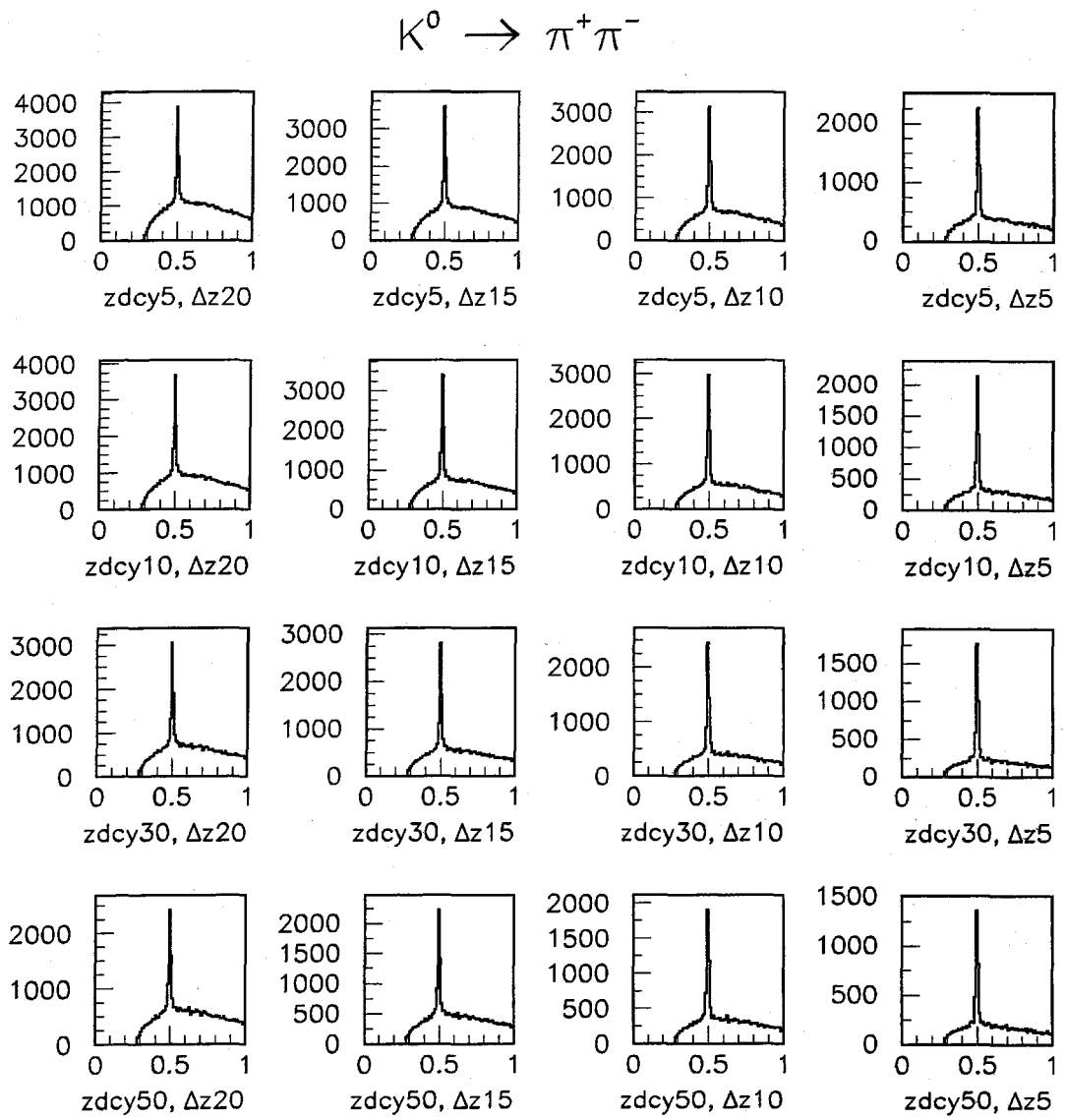

Figure 8.2: K° mass distributions from single muon triggered events for different z-decay and $|\Delta z|$ cuts, with a coplanarity criterion imposed. Each horizontal scale is the mass value in GeV/c^2, and each vertical scale is the number of pairs per 10 MeV/c^2.

vertex the decay of the K°, the greater the K° yield. This plot shows a set of lines for which the coplanarity cut was not implemented and another set of lines for which a coplanarity cut was implemented. It is interesting to note that there is a greater deviation in the raw number of K°'s counted for those events where no coplanarity cut was required, whereas those events where a coplanarity cut was implemented show a much smaller variation. This is due to a better mass fit on a well defined signal peak when the coplanarity cut was activated.

The overlay efficiency for tracking an event within a pre-determined cut interval, is shown in Figure 8.4. It is plotted as a function of $|\Delta z|$, where the lines, dashes, dots, and dot-dashes joining their respective symbols are the different z-decay cuts from the main interaction vertex. For single muon triggered events, the efficiency is in the range of 0.3% to 1.5%, a very low acceptance.

Figure 8.5 shows the corrected number of K°'s, correcting up the raw number of K°'s by the overlay efficiency, versus the $|\Delta z|$ cuts. The individual symbols are for different z-decay cuts from the main interaction. This plot shows a close agreement (some overlaps) between the values obtained for those pairs that had coplanar tracks and those pairs that did not require the tracks to be coplanar. This is in much better agreement than that from the LED triggered events, see Figure 7.11, and is probably due to the fact that more statistics were obtained for the single muon triggered events, thus reducing the systematic deviations.

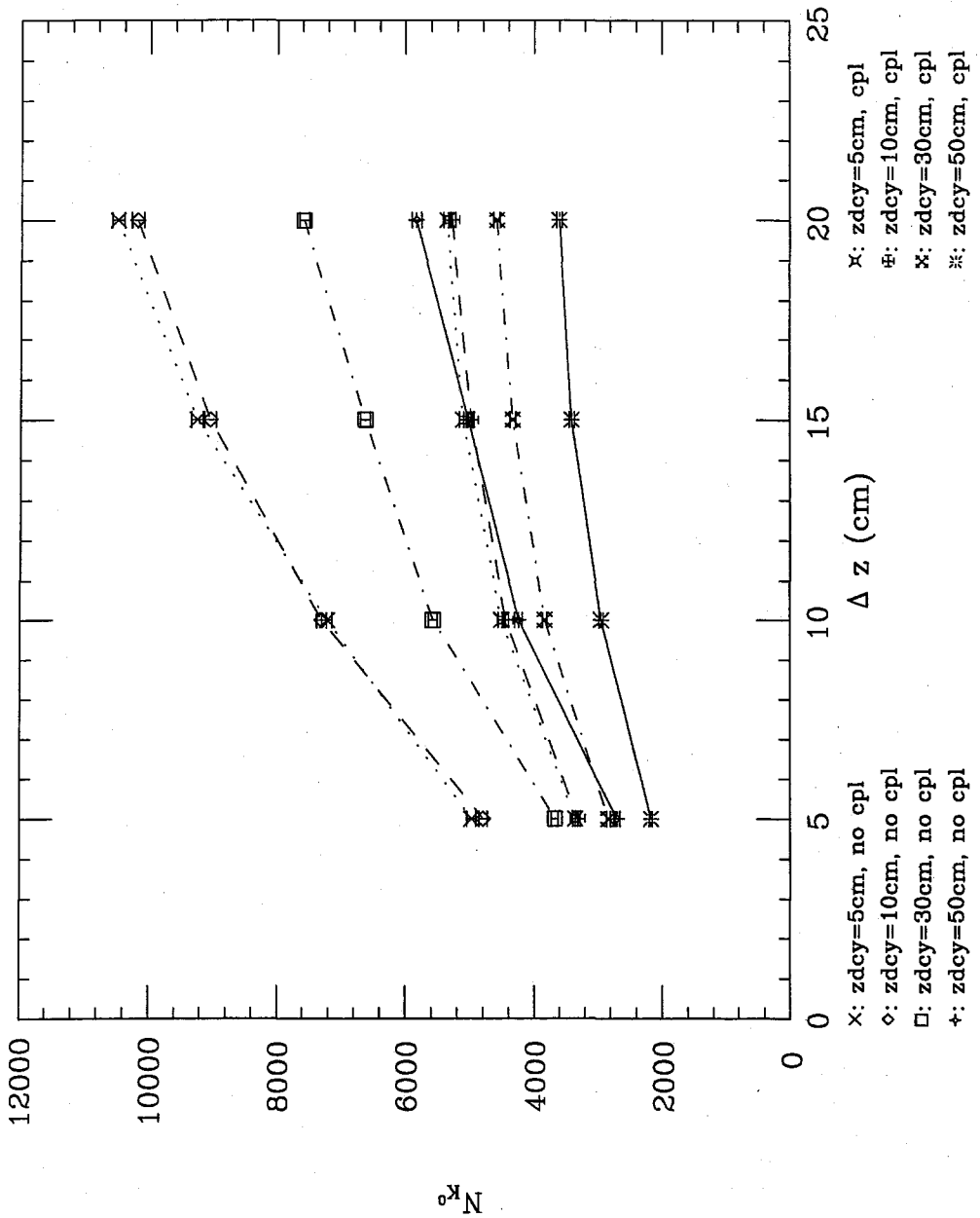

Figure 8.3: Total number of K°'s, $N_{K^{\circ}}$, as a function of $|\Delta z|$ and z-decay cuts. Shown are curves for coplanar tracks and curves for non-coplanar tracks.

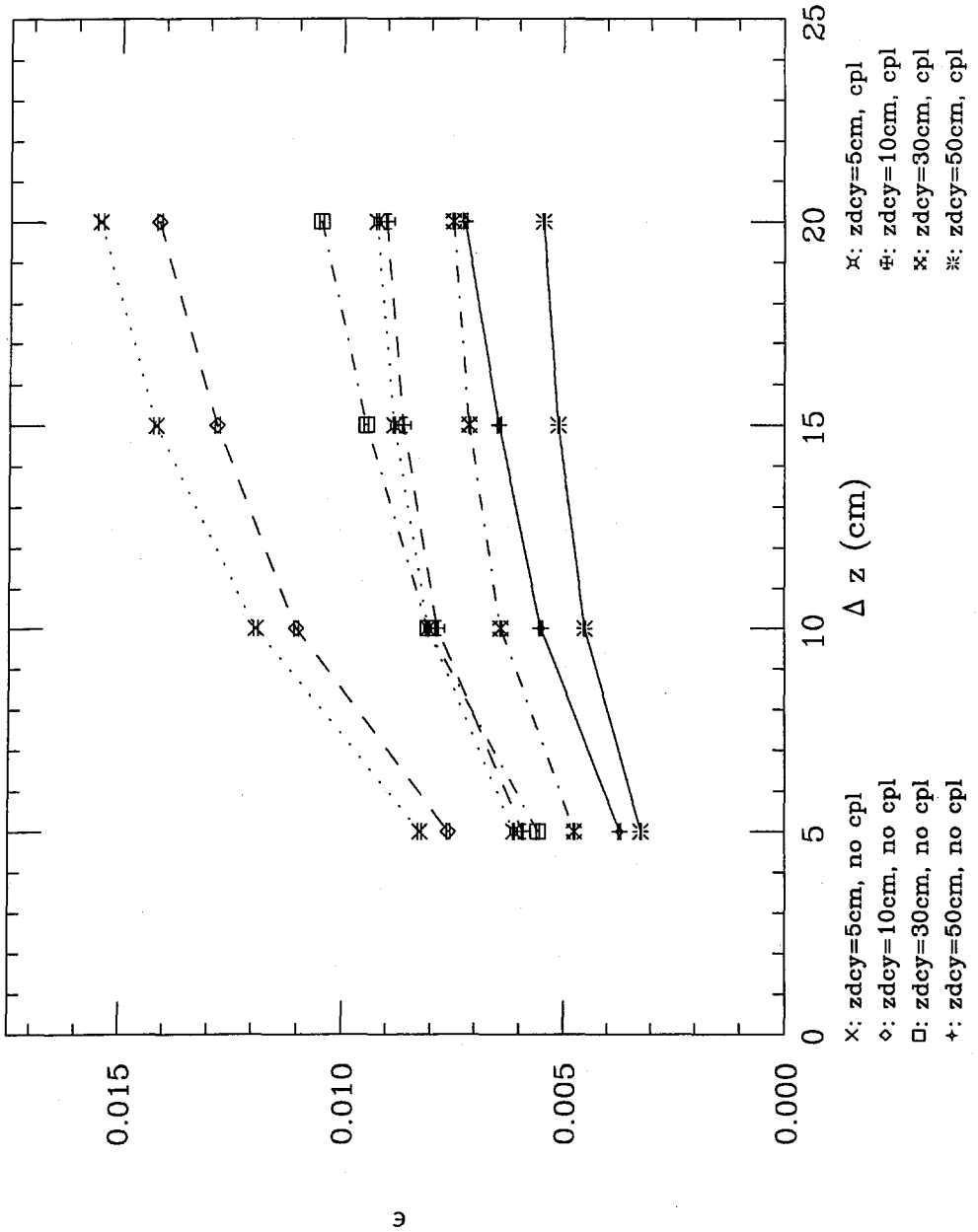

Figure 8.4: Overlay efficiency, ϵ, for tracking a K° as a function of $|\Delta z|$ and z-decay cuts. Shown are curves for coplanar tracks and curves for non-coplanar tracks.

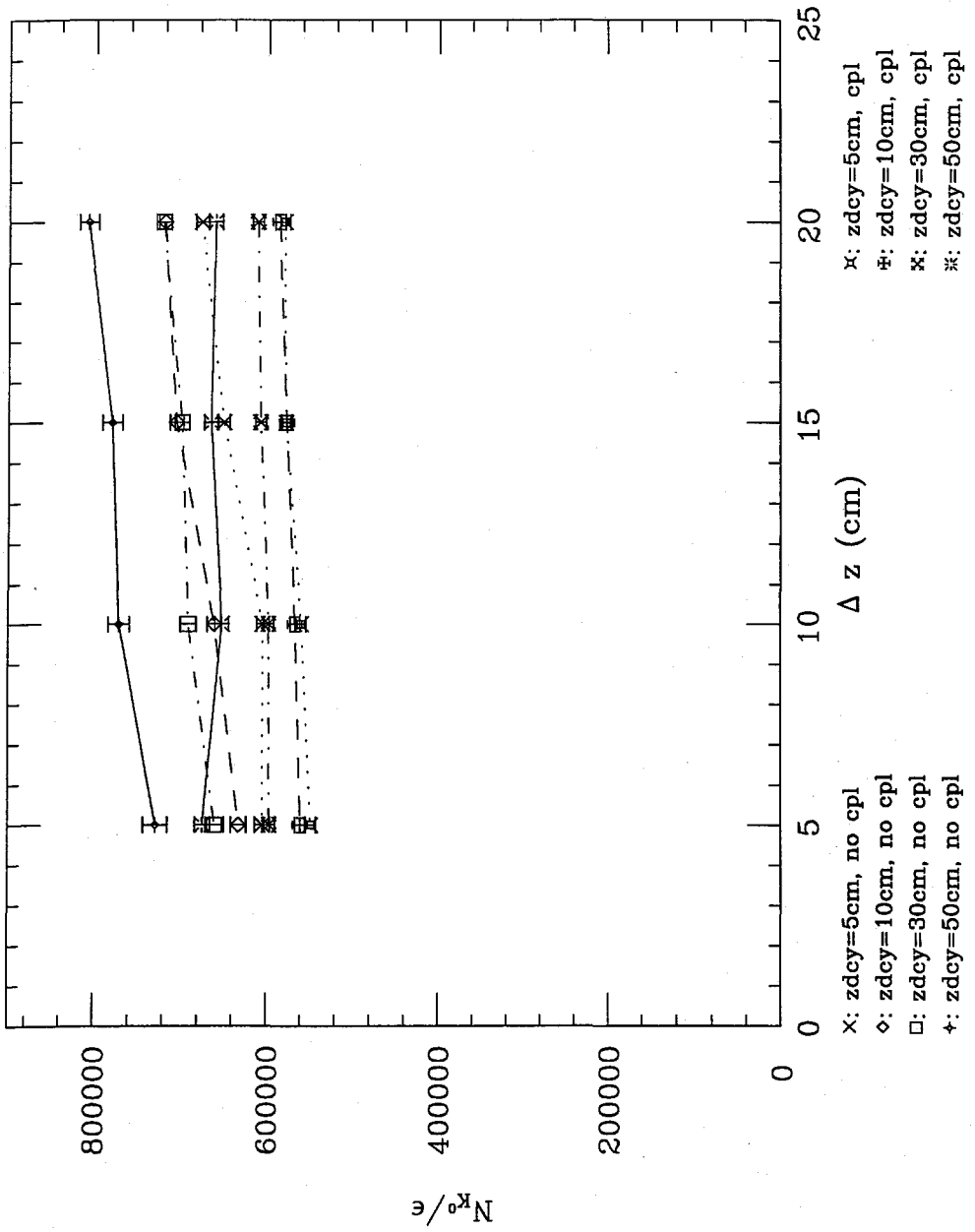

Figure 8.5: Corrected number of K°'s, $N_{K^{\circ}}/\epsilon$, as a function of $|\Delta z|$ and z-decay cuts. Shown are curves for coplanar tracks and curves for non-coplanar tracks.

8.2 K° p_t, Multiplicity, Rapidity, and x_f Distributions

Important K° characteristics from single muon triggered events, such as the average p_t, the charged multiplicity (N_c), the rapidity and x_f distributions, will be discussed and compared to PYTHIA results.

8.2.1 Data

As discussed in Sections 7.3.1, 7.4.1, and 7.5.1, a good p_t distribution is achieved by applying several cuts within the mass region of the K° in order to extract a distribution that would most likely come from a K° event. The p_t distribution was obtained by accepting only those events whose mass values were within $\pm$ 30 MeV of the K° mass value. If they met this criterion, the p_t distribution was plotted. As can be seen by Figures 8.1 and 8.2, a background distribution existed beneath the mass peak. This had to be accounted for and subtracted from the final p_t distribution plot. A fit was performed on the K° mass plot, using a Gaussian to fit the signal (N_s) and a polynomial to fit the background (N_b). The p_t distribution was plotted for those events that had unlike sign tracks (signal plot, $N_\pm$), and it was also plotted for those events that had like sign tracks (background plot, N_{LS}). The like sign distribution had to be normalized to the unlike sign distribution. Each like sign event was multiplied by the ratio N_b/N_{LS} in order to normalize background to signal. This resultant distribution was then subtracted from the $N_\pm$ distribution, giving the true p_t distribution curve.

Figure 8.6 is the K° true p_t distribution, shown three times for three different fitting functions to the curve in order to extract the $< p_t >$ value. The three

different fitting functions are:

$$dN/dp_t = P1 \cdot p_t \cdot exp(-p_t \cdot P2), \tag{8.2}$$

$$dN/dp_t = P1 \cdot p_t \cdot exp(-\sqrt{p_t^2 + m^2}/P2), \tag{8.3}$$

$$dN/dp_t = (P1 \cdot p_t)/(p_t + P2)^{P3}. \tag{8.4}$$

$P1$, $P2$, and $P3$ are the fitted parameter values obtained from each of the individual fits. (a) is the K° p_t distribution using Equation (8.2) as a fit, where $P1$ and $P2$ are the fitted parameters for this particular exponential function. (b) is the distribution using Equation (8.3) as a fit, where $P1$ and $P2$ are the fitted parameters for this function involving the transverse energy (thermal exponential fit). (c) is the distribution using Equation (8.4) as a fit, where $P1$, $P2$, and $P3$ are its fitted parameters.

Each of the three different fitting functions yielded similar values for the $< p_t >$, and the greatest discrepancy between the values was 0.143 GeV/c. The $K^\circ < p_t >$ value, averaged for all three fitting algorithms, is

$$< p_t > = 0.56 \pm .07 \text{ GeV/c},$$

where the systematic error was the *rms* deviation in the three different fits.

The three different fits used to get the average p_t values were model dependent and did not look at the low p_t region. This was explained by the fact that the low p_t particles were lost when simulated to traverse E771's spectrometer region. An alternative for getting the average p_t was to average directly the p_t values for the whole distribution as the final p_t distribution was corrected for the spectrometer acceptance. The procedure was the same as that used for getting the three model

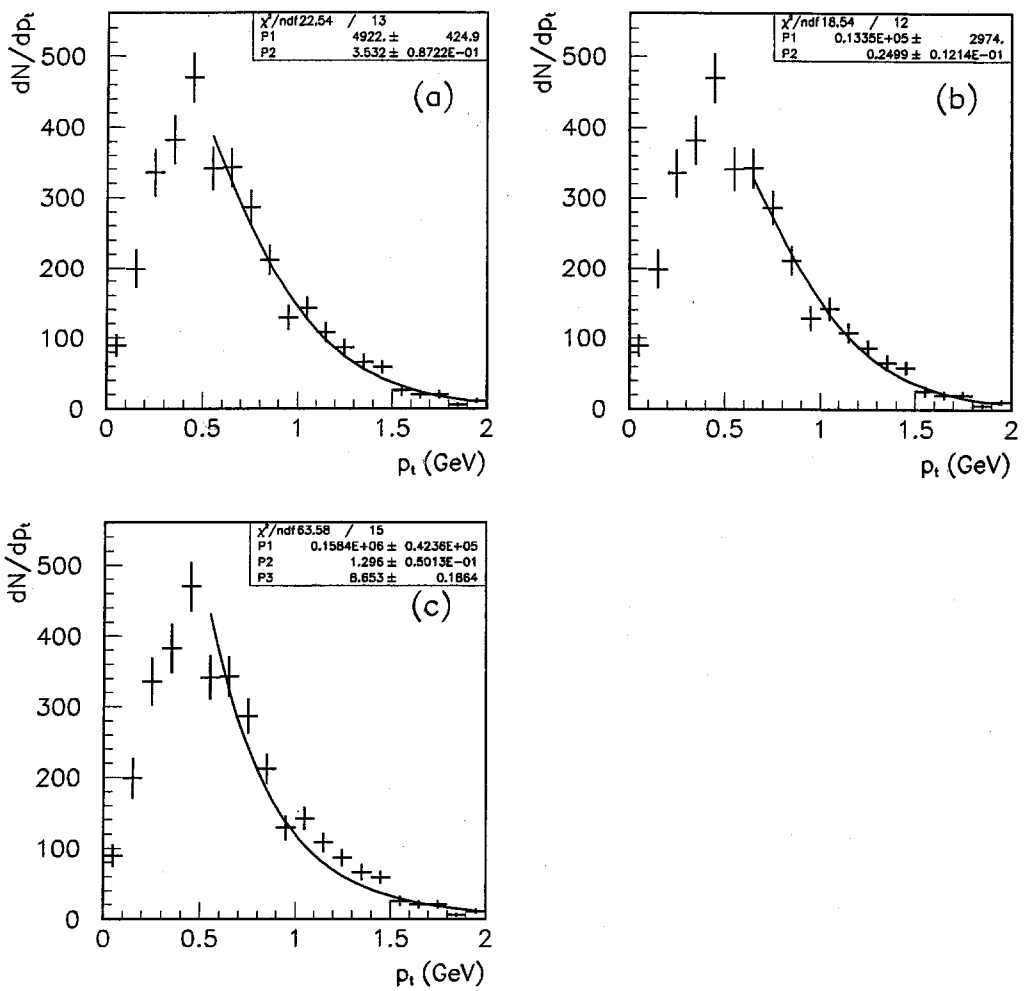

Figure 8.6: The K° p_t distribution from single muon triggered events. The same plot is shown three times for each of three different fitting functions. (a) uses Equation (8.2) as the fit, (b) uses Equation (8.3) as the fit, and (c) uses Equation (8.4) as the fit.

dependent $< p_t >$ values. That is, one had to normalize the background p_t distribution to the signal p_t distribution in order to perform the proper subtraction to get the correct p_t distribution. The distribution had to be overlay corrected for losses at small p_t. Then the simple average of the corrected p_t distribution was formed without performing any fitting procedures. The $< p_t >$ value obtained for the K°'s using this method was

$$< p_t >=0.76\pm0.06\ GeV/c.$$

It is noted that the latter procedure used to fit the $< p_t >$ yielded a higher value than that obtained from the three different fits. This is explainable by the fact that the power law fit described above generally gave a lower value than did the other two fits.

The multiplicity (N_c), rapidity (y_{cm}), and Feynman-x (x_f) distributions were all obtained the same way the p_t distribution was. That is, the background events had to be normalized to the signal events and subtracted from the signal events in order to get their true distributions.

As the main tracking program calculated a track's relevant information in the lab system, the rapidity distribution in the center of mass system had to be transformed from the lab system. The rapidity in the laboratory frame is defined as

$$y_{lab} = \frac{1}{2}ln(\frac{E+P_l}{E-P_l}), \tag{8.5}$$

with a transformation of the form

$$y_{tx} = \frac{1}{2}ln(\frac{1-\beta_{cm}}{1+\beta_{cm}}), \tag{8.6}$$

to give

$$y_{cm} = y_{lab} + y_{tx}. \tag{8.7}$$

E is the particle's energy and P_l its longitudinal momentum.

$$\beta_{cm} = P_{beam}/(\sqrt{P_{beam}^2 + m_p^2} + m_p),$$

where P_{beam} is the beam momentum and m_p the proton mass.

Feynman's x variable, x_f, in the center of mass system, is defined as

$$x_f = \frac{2 \cdot p_{z(cm)}}{\sqrt{s}}, \tag{8.8}$$

where $p_{z(cm)} = \gamma_{cm} \cdot (P_z - \beta_{cm} \cdot E)$.

Shown in Figure 8.7 are the K° N_c, y_{cm}, and x_f distributions for the single muon triggered events. These are distributions for events that had K°'s in them. (a) is the charged particle multiplicity distribution, N_c. Its mean value is $< N_c >$ $= 11.7 \pm 0.4$. (b) is the center of mass system rapidity distribution, y_{cm}. Inspection of this distribution shows an asymmetry in acceptance more in the forward direction. Due to the limited spectrometer acceptance, this may account for the low acceptance of those particles produced in the backward direction. (c) is the Feynman-x distribution, x_f, in the center of mass system. This distribution follows the same qualitative behavior as the y_{cm} distribution.

8.2.2 Minimum Bias PYTHIA

A Monte Carlo PYTHIA program was used to simulate E771's run conditions. This was used to compare data to theoretical predictions. PYTHIA can be programmed to simulate different types of events, such as minimum bias events, charm enhanced events, or beauty enhanced events. A minimum bias program, designed to run only for those events that contained at least one muon trigger, was written in order to incorporate PYTHIA's random generation process with certain

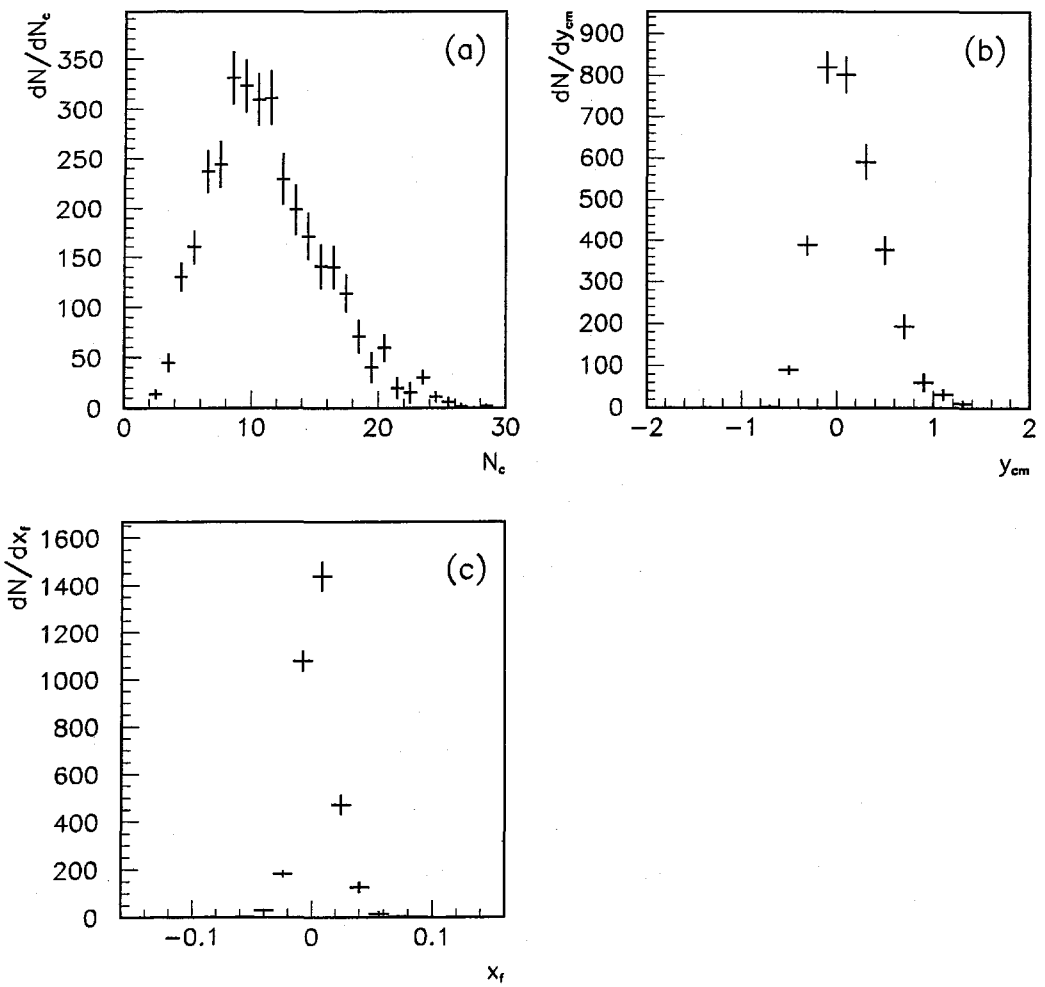

Figure 8.7: (a) N_c, (b) y_{cm}, and (c) center of mass x_f distributions for K°'s from single muon triggered events. These distributions are not corrected for full spectrometer acceptance.

restrictions imposed.

In order to simulate a single muon trigger for a PYTHIA event, a search is performed on muon particles. Once a muon is tagged, the program calculates whether its p_t was great enough to allow for its passage through the RPCs. If so, it is counted as a single muon trigger. We continue with the event by looking for the neutral strange particles. The V° particle is simulated to pass through the spectrometer region. It encounters the magnet where it experiences a p_t kick and deflected to traverse the rear chambers. The program checks to see that each track of the V° particle hits at least three upstream chamber planes and three downstream chamber planes. If the two daughter tracks pass the front and rear chamber hit criteria, the event is accepted and its relevant information plotted or put in counters for later use. The relevant information used from PYTHIA for comparison purposes consisted of obtaining the average multiplicity value for those events that had K°'s in them, obtaining the average multiplicity value for all events, irrespective of whether the event contained a K°, the number of K°'s generated ("generated" here meaning 4π full acceptance), the number of K°'s generated per event, and the average p_t value.

8.2.3 Comparison of Data to PYTHIA

Table 8.1 is a comparison of PYTHIA events to real data events for the study of K° produced particles for a minimum bias run with the condition that the analyzed events contain single muon triggers. The first column is the average raw charged multiplicity for an event that contains a K°. A big discrepancy exists between

what PYTHIA predicts and what is experimentally observed. The difference is more than three times greater for data. This indicates that requiring a single muon to be a trigger for a minimum bias produced event did not increase the PYTHIA multiplicity value. The second column is the average charged multiplicity for all events, and this does not take into account whether or not a K° was present. A comparison of data and PYTHIA reveals behavior similar to their difference for the raw charged multiplicity, but the interesting point is that when a K° is required to have been in the event in order to count the multiplicity value, the average charged multiplicity per event increases compared to that for all events. The third column is the average number of K°'s generated (with the definition of "generated" standing for overlay acceptance corrections for the experimental data) per raw charged multiplicity. PYTHIA predicted more K°'s than what was experimentally observed. The last column is the $< p_t >$ for the K°'s, where PYTHIA's value is somewhat lower than data.

	$< N >_{K^\circ}$	$< N >_{evt}$	$< \frac{K_s^\circ(gen)}{N_{all}} >$	$< \frac{K_s^\circ(gen)}{evt} >$	$< p_t >_{K_s^\circ}$ (GeV)
PYTHIA	3.73 ± 0.02	2.820 ± 0.005	0.1081 ± 0.0001	0.308 ± 0.007	0.444 ± 0.005
DATA	11.7 ± 0.4	9.451 ± 0.004	0.042 ± .004	0.399 ± 0.039	0.566 ± 0.014

Table 8.1: Comparison of minimum bias single muon triggered PYTHIA generated events and data events for K° produced particles.

As in the minimum bias events for no trigger criterion, PYTHIA and data were in agreement for some values, while they had discrepancies for others. An explanation may be that PYTHIA tends to under predict the true multiplicity,

hence the subsequent disagreement in some of the parameters.

8.3 Raw Λ° Events, Overlay Efficiency, Corrected Λ° Acceptance

The procedures that will be described for fitting the Λ° events, for calculating the overlay efficiency, and for obtaining the corrected Λ° acceptances are the same as those employed for the minimum bias events.

Compared to the minimum bias (LED triggered) events, the single muon triggered events contained a larger statistics sample, and therefore the Λ° mass peak was well observed. Figure 8.8 is an example of the Λ° mass distribution with different z-decay and $|\Delta z|$ cuts. These plots did not require that the pairs be coplanar, where a coplanar event met the criterion that

$$cos(\theta) = \frac{(\vec{V} \times \vec{a}) \cdot (\vec{b} \times \vec{V})}{|\vec{V} \times \vec{a}||\vec{b} \times \vec{V}|} \geq 0.95. \tag{8.9}$$

$\vec{V}$ is the parent particle vector, and $\vec{a}$ and $\vec{b}$ are the first and second decay product vectors. The first row of plots is the mass distribution for a fixed z-decay length greater than 5 cm from the main interaction vertex, while the progression of columns has increasingly tighter $|\Delta z|$ cuts applied. The second row is the mass distribution for a fixed z-decay length greater than 10 cm from the main interaction vertex, and the columns are $|\Delta z|$ cuts $\leq$ 40 cm, $\leq$ 30 cm, $\leq$ 20 cm, and $\leq$ 10 cm. The third and fourth rows are the mass distributions for fixed z-decay lengths greater than 30 cm and 50 cm, respectively, from the main interaction vertex, and the columns are the same $|\Delta z|$ cuts as those described for the second row of

plots. The combination of tighter cuts increases the signal peak, thus increasing the signal to noise ratio.

Figure 8.9 follows the same convention as Figure 8.8 with the added condition that the tracks be coplanar. A comparison of the two figures shows a significant improvement of the signal to noise ratio, thus enabling good fitting procedures to be performed.

Figure 8.10 is one example of the information extracted from the mass plots. It is the raw number of Λ°'s as a function of the $|\Delta z|$ cuts. The lines drawn through a set of different coordinated symbols refer to the different z-decay values. The looser the $|\Delta z|$ cut is, e.g., $\leq 40\ cm$, and the closer to the main interaction vertex the decay of the Λ°, the more Λ°'s are produced. This plot shows a set of lines where the coplanarity cut was not implemented, and another set of lines shows plots where a coplanarity cut was implemented. It is interesting to note that there is a greater deviation in the raw number of Λ°'s counted for those events where no coplanarity cut was required, whereas those events where a coplanarity cut was implemented show a much smaller variance. This may be attributable to the fact that a cleaner signal peak was obtained when the coplanarity cut was activated.

The overlay efficiency (ϵ) for tracking an event within a specified cut interval, is shown in Figure 8.11. It is plotted as a function of $|\Delta z|$, where the lines, dashes, dots, and dot-dashes joining their respective symbols are the various z-decay cuts from the main interaction vertex. The overlay efficiency for tracking Λ° events is much smaller than that for the K°'s, ranging from 0.18% to a maximum of 0.56%, whereas that for the K°'s ranged from a minimum of 0.3% to a maximum of 1.5%,

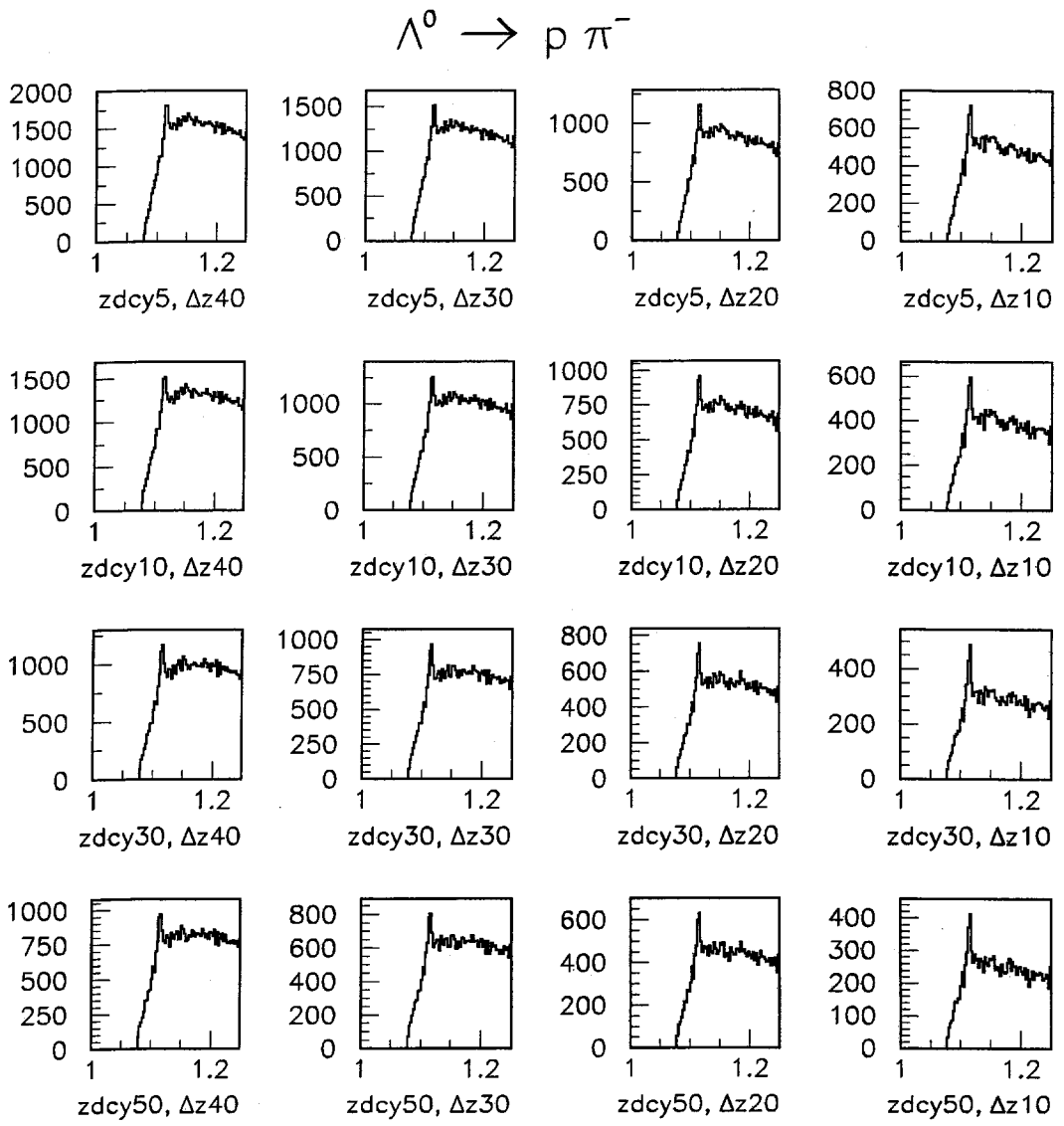

Figure 8.8: Λ° mass distributions from single muon triggered events using different z-decay and $|\Delta z|$ cuts, with no coplanarity cut imposed. Each horizontal scale is the mass value in GeV/c^2, and each vertical scale is the number of pairs per 2.5 MeV/c^2.

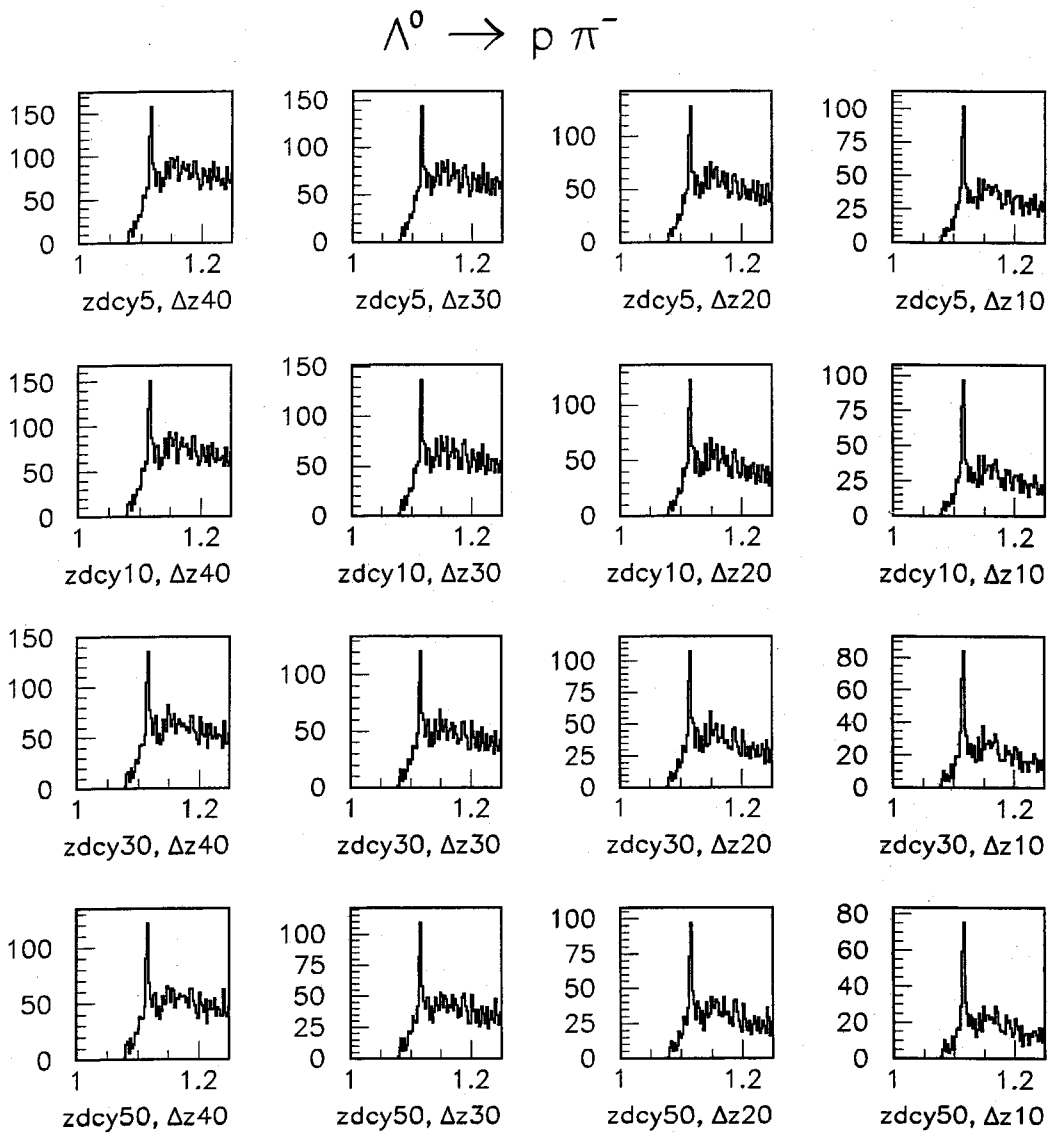

Figure 8.9: Λ° mass distributions from single muon triggered events using different z-decay and $|\Delta z|$ cuts, with a coplanarity cut imposed. Each horizontal scale is the mass value in GeV/c^2, and each vertical scale is the number of pairs per 2.5 MeV/c^2.

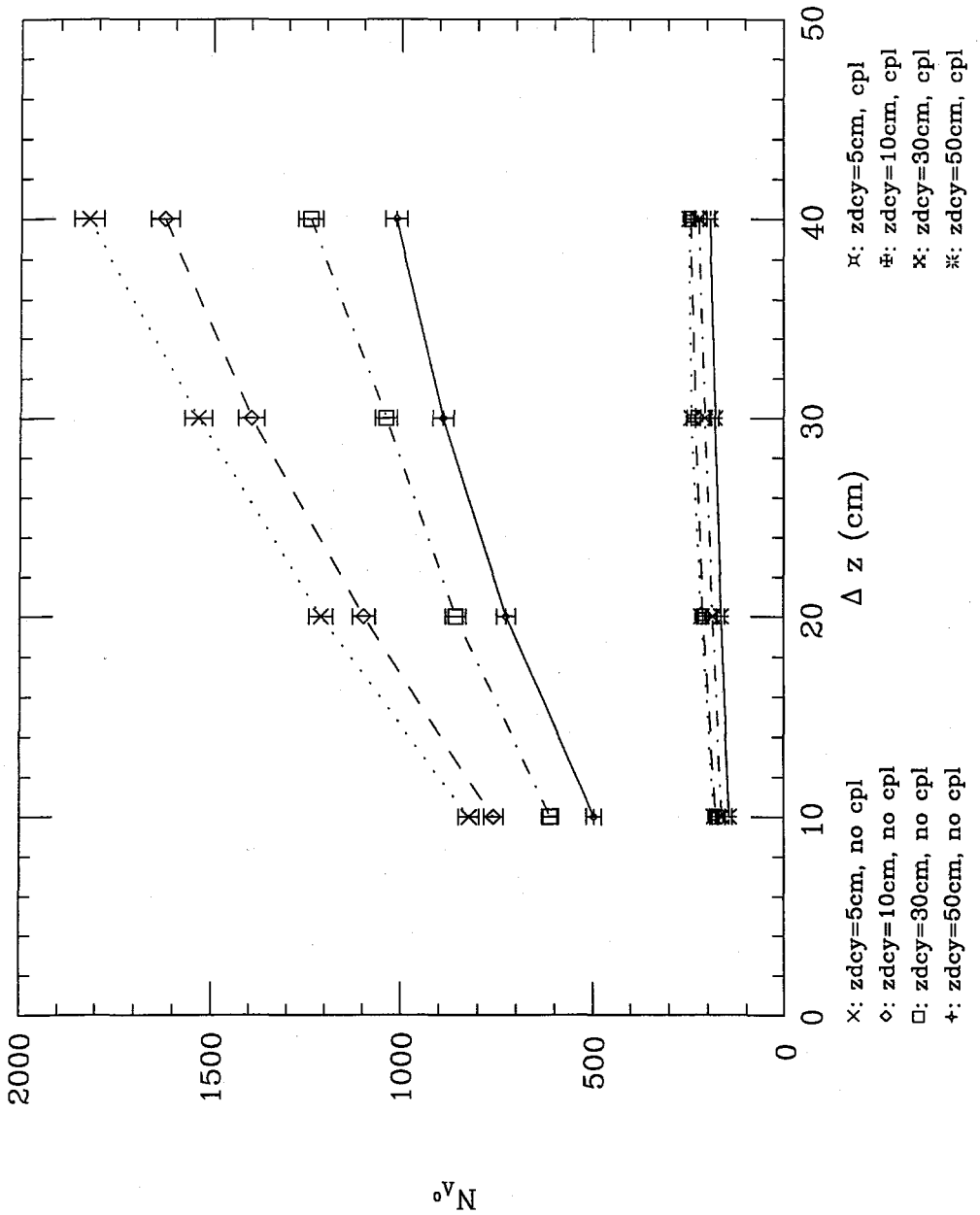

Figure 8.10: Total number of Λ°'s, $N_{\Lambda^{\circ}}$, as a function of $|\Delta z|$ and z-decay cuts. Shown are curves for coplanar tracks and curves for non-coplanar tracks.

indicative of the tremendous difficulty for tracking Λ°'s.

Figure 8.12 is a plot of the corrected number of Λ°'s ($N_{\Lambda^\circ}/\epsilon$), correcting the raw number of Λ°'s by the overlay efficiency, versus the $|\Delta z|$ cuts. The different symbols indicate the various imposed z-decay cuts from the main interaction vertex. A definite discrepancy exists between those tracks that were coplanar and those that were not required to be coplanar. The coplanar tracks, although in more of a systematic agreement than those tracks that did not require the coplanarity criterion, ended up with a lower corrected number of Λ°'s. This may be attributed to the fact that the coplanar tracks originally contained a small amount of statistics, the overlay efficiency was too low, and so the final result produced a noticeably different mean for the corrected number of Λ°'s than those that did not require coplanar tracks.

8.4 Λ° p_t, Multiplicity, Rapidity, and x_f Distributions

Important Λ° characteristics from single muon triggered events, such as the p_t, N_c, y_{cm}, and x_f distributions, will be discussed, and their relevant extracted information will be compared to PYTHIA.

8.4.1 Data

As there was a different number of cuts applied to the mass spectrum in order to achieve the best signal/background ratio, a good p_t distribution was obtained. If the invariant mass of track pairs was within $\pm$ 10 MeV of the Λ° mass value, the p_t was plotted. Since a background distribution existed beneath the mass peak,

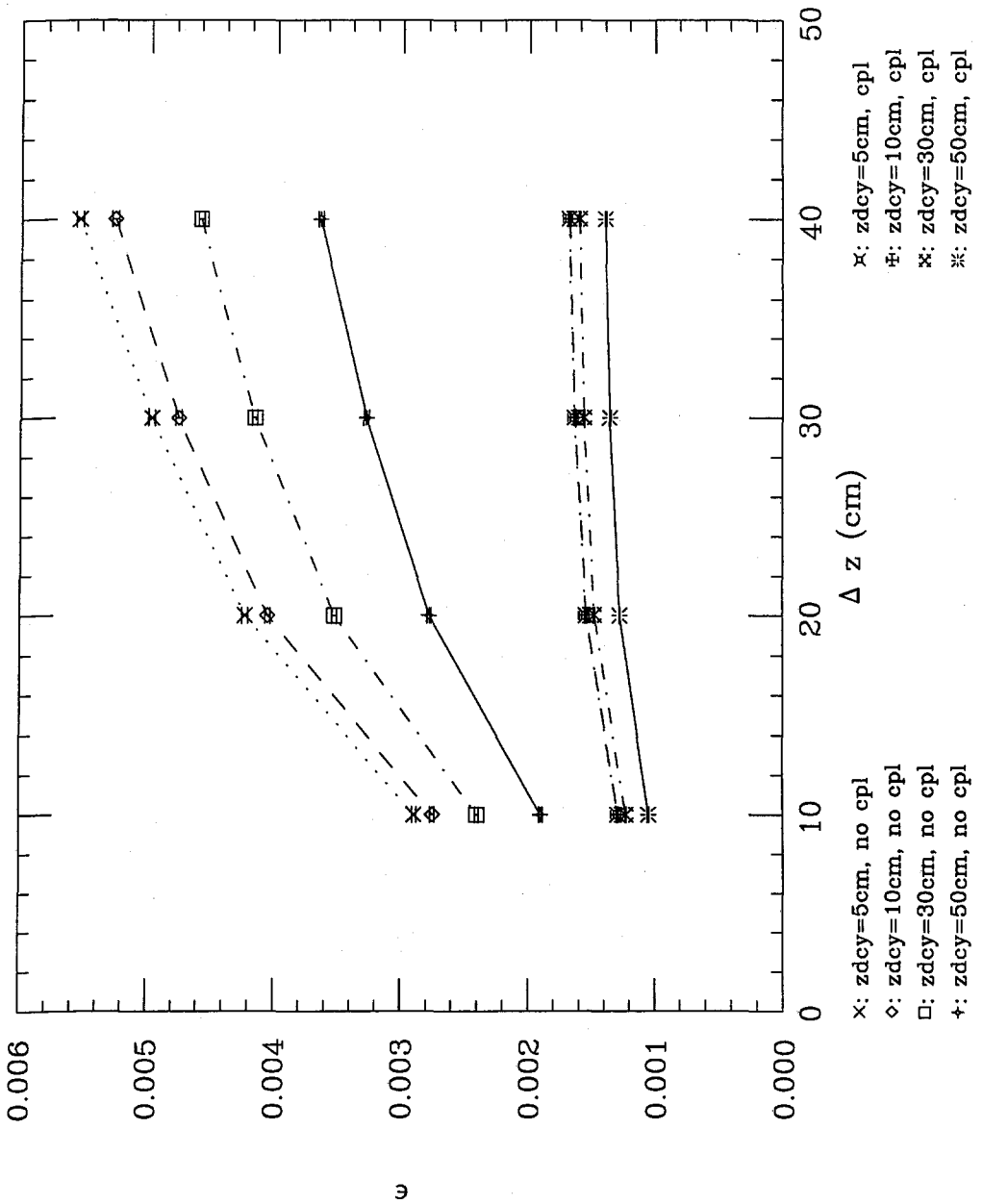

Figure 8.11: Overlay efficiency, ϵ, for tracking a Λ° as a function of $|\Delta z|$ and z-decay cuts. Shown are curves for coplanar tracks and curves for non-coplanar tracks.

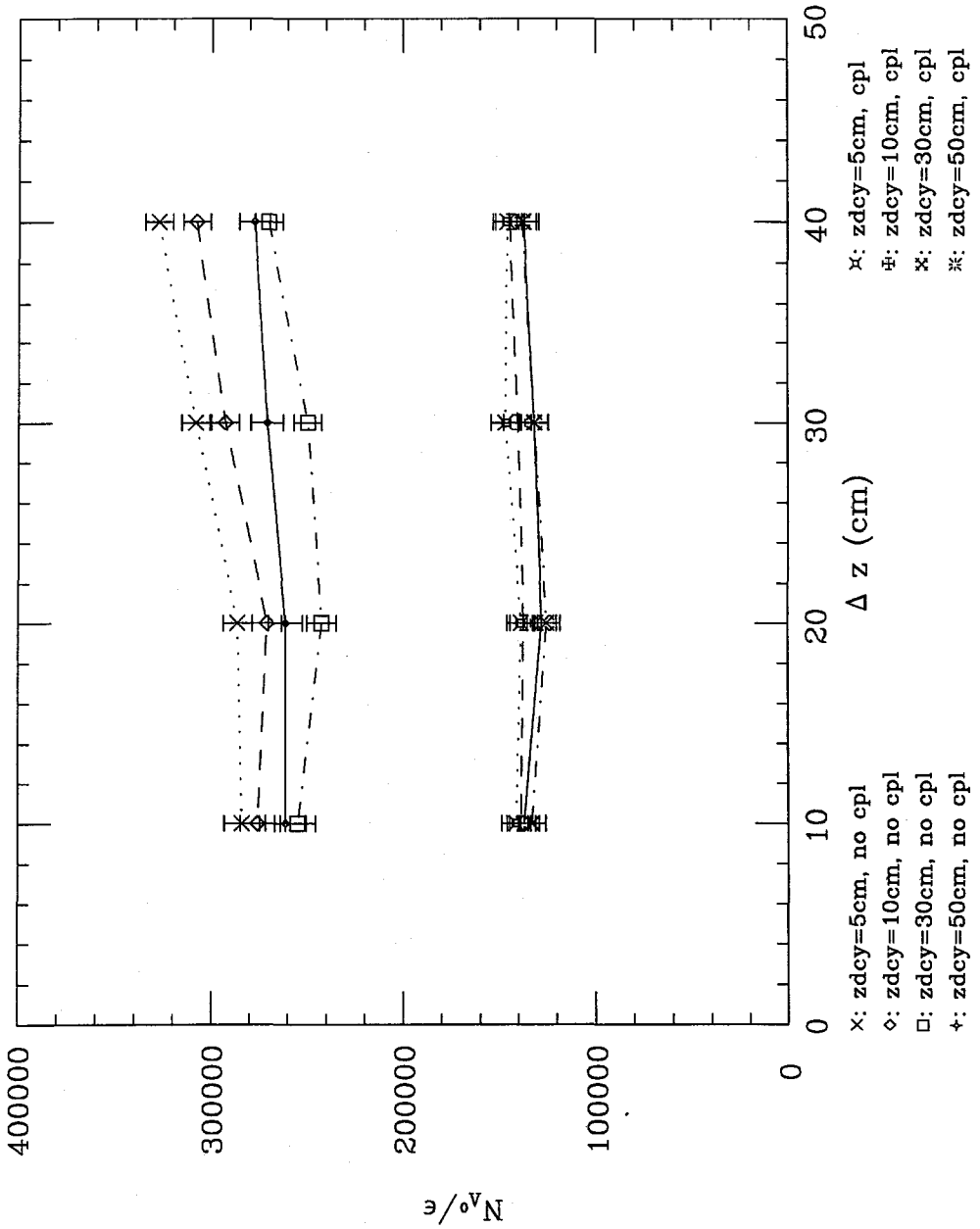

Figure 8.12: Corrected number of Λ^0's, N_{Λ^0}/ϵ, as a function of $|\Delta z|$ and z-decay cuts. Shown are curves for coplanar tracks and curves for non-coplanar tracks.

a normalization and subtraction algorithm was implemented. The p_t distribution was plotted for events that had unlike sign tracks (signal plot, $N_{\pm}$) and like sign tracks (background plot, N_{LS}). The p_t distribution for the like sign tracks was normalized to the p_t distribution for the unlike sign tracks to obtain the proper background subtraction.

Figure 8.13 is the corrected p_t distribution. It is shown three times, each with a different fitted p_t function. The three different fitting functions are:

$$dN/dp_t = P1 \cdot p_t \cdot exp(-p_t \cdot P2), \tag{8.10}$$

$$dN/dp_t = P1 \cdot p_t \cdot exp(-\sqrt{p_t^2 + m^2}/P2), \tag{8.11}$$

$$dN/dp_t = (P1 \cdot p_t)/(p_t + P2)^{P3}. \tag{8.12}$$

$P1$, $P2$, and $P3$ are the fitted parameter values obtained from each of the individual fits. (a) is the Λ° p_t distribution using Equation (8.10) as a fit, where $P1$ and $P2$ are the fitted parameters for this exponential function. (b) is the Λ° p_t distribution using Equation (8.11) as a fit, where $P1$ and $P2$ are the fitted parameters for this function involving the transverse energy (thermal exponential fit). (c) is the Λ° p_t distribution using Equation (8.12) for the fit, where $P1$, $P2$, and $P3$ are the fitted parameters for this function.

Each of the three different fitting functions yielded similar values for the $< p_t >$, and the greatest discrepancy between the values was 0.27 GeV/c. The Λ° $< p_t >$ value, averaged for all three fitting algorithms was

$$< p_t > = 0.47 \pm 0.15 \text{ GeV/c},$$

where the systematic error was the *rms* deviation in the three fits. The two

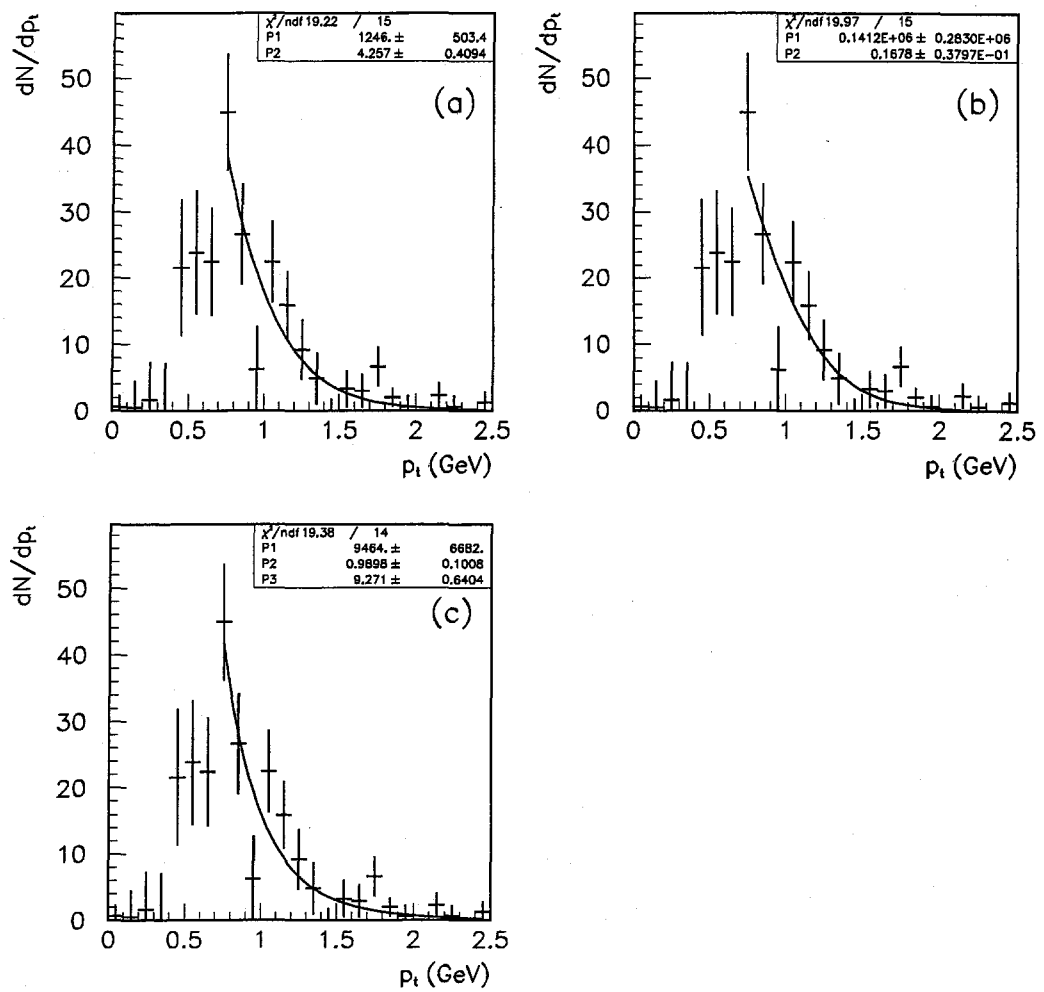

Figure 8.13: The Λ° p_t distribution from single muon triggered events. The same plot is shown three times for each of three different fitting functions. (a) uses Equation (8.10) as the fit, (b) uses Equation (8.11) as the fit, and (c) uses Equation (8.12) as the fit.

exponential fits were in close agreement, and the power law fit proved on average to give a lower $< p_t >$.

The three different fits used to get the average p_t values were model dependent and did not look at the low p_t region. This was explained by the fact that the low p_t particles were lost when simulated to traverse E771's spectrometer region. An alternative for getting the average p_t was to average directly the p_t values for the whole distribution as the final p_t distribution was corrected for the spectrometer acceptance. The procedure was the same as that used for getting the three model dependent $< p_t >$ values. That is, one had to normalize the background p_t distribution to the signal p_t distribution in order to perform the proper subtraction to get the correct p_t distribution. The distribution had to be overlay corrected for losses at small p_t. Then the simple average of the corrected p_t distribution was formed without performing any fitting procedures. The $< p_t >$ value obtained for the Λ°'s using this method was

$$< p_t >=0.96\pm0.32\ GeV/c.$$

It is noted that the latter procedure used to fit the $< p_t >$ yielded a higher value than that obtained from the three different fits. This is explainable by the fact that the power law fit described above generally gave a lower value than did the other two fits.

The multiplicity, rapidity, and Feynman-x distributions were all obtained the same way the p_t distribution was. Those events that were within $\pm$ 10 MeV of the Λ° mass peak were retained and their respective distributions plotted.

The rapidity, defined in the laboratory frame, is

$$y_{lab} = \frac{1}{2} ln(\frac{E + P_l}{E - P_l}). \tag{8.13}$$

A transformation is performed to convert to the center of mass system,

$$y_{tx} = \frac{1}{2} ln(\frac{1 - \beta_{cm}}{1 + \beta_{cm}}), \tag{8.14}$$

so in the center of mass system

$$y_{cm} = y_{lab} + y_{tx}. \tag{8.15}$$

E is the particle energy and P_l its longitudinal momentum.

$$\beta_{cm} = P_{beam}/(\sqrt{P_{beam}^2 + m_p^2} + m_p),$$

where P_{beam} is the beam momentum and m_p the proton mass.

Feynman's x variable, x_f, in the center of mass system, is defined as

$$x_f = \frac{2 \cdot p_{z(cm)}}{\sqrt{s}}, \tag{8.16}$$

where $p_{z(cm)} = \gamma_{cm} \cdot (P_z - \beta_{cm} \cdot E)$.

Figure 8.14 is the Λ° multiplicity, rapidity, and Feynman-x distributions from the single muon triggered event sample. (a) is the charged particle multiplicity provided a Λ° existed in the event. Its mean value is $< N_c > = 11.8 \pm 1.5$. (b) is the rapidity distribution in the center of mass system. This distribution is more pronounced in the forward direction than the backward region due to the low geometrical acceptance at wide angles. (c) is the center of mass x_f distribution. It too has a low backward acceptance, and its qualitative shape is similar to that for the rapidity distribution.

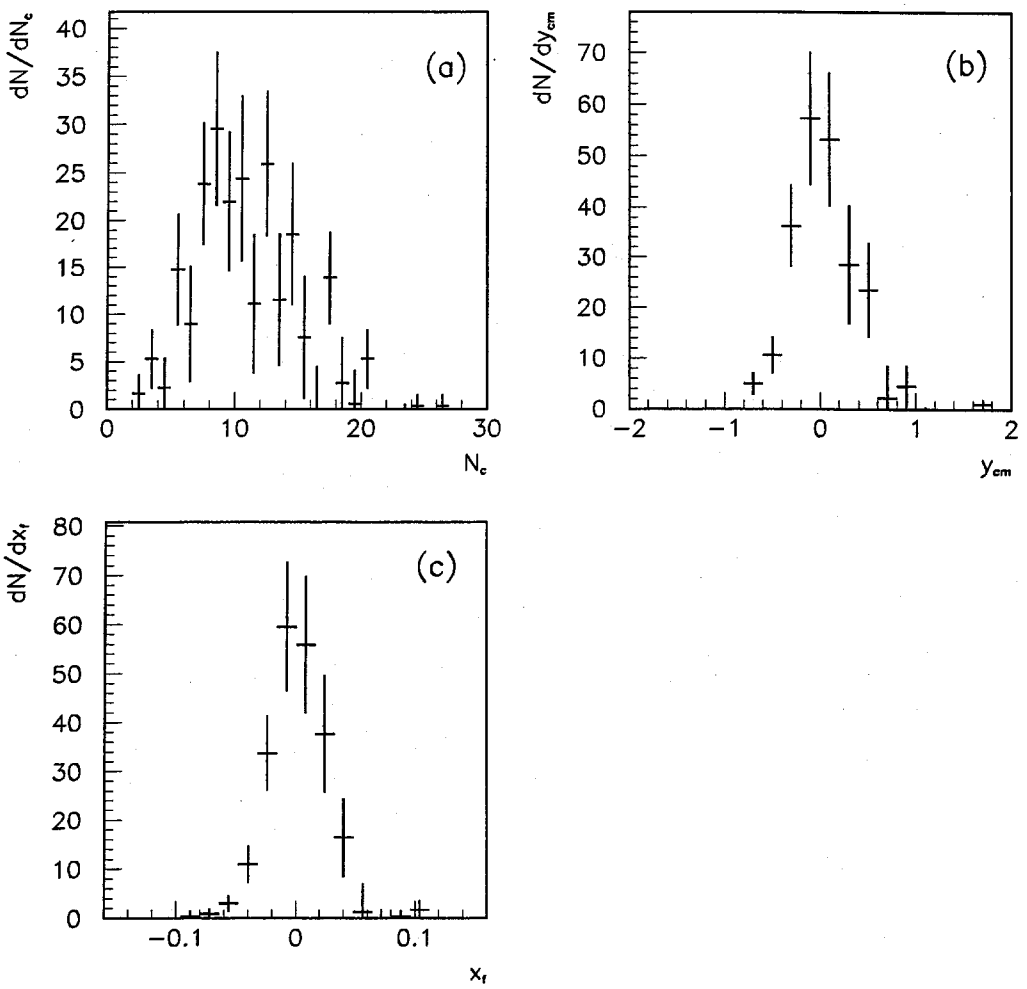

Figure 8.14: (a) N_c, (b) y_{cm}, and (c) center of mass x_f distributions for Λ^0's from single muon triggered events. These distributions are not corrected for full spectrometer acceptance.

8.4.2 Minimum Bias PYTHIA

As described in Section 8.3.2, a Monte Carlo PYTHIA program was run to simulate the decays of Λ° particles using a muon trigger.

In order to simulate a single muon trigger for a PYTHIA event, a search is performed on muon particles. Once a muon is tagged, the program calculates whether its p_t was great enough to allow for its passage through the RPCs. If so, it is counted as a single muon trigger. We continue with the event by looking for the neutral strange particles. The V° particle is simulated to pass through the spectrometer region. It encounters the magnet where it experiences a p_t kick and deflected to traverse the rear chambers. The program checks to see that each track of the V° particle hits at least three upstream chamber planes and three downstream chamber planes. If the two daughter tracks pass the front and rear chamber hit criteria, the event is accepted and its relevant information plotted or put in counters for later use. The relevant information used from PYTHIA for comparison purposes consisted of obtaining the average multiplicity value for those events that had Λ°'s in them, obtaining the average multiplicity value for all events, irrespective of whether the event contained a Λ°, the number of Λ°'s generated ("generated" here standing for 4π steradian acceptance), the number of Λ°'s generated per event, and the average p_t value.

8.4.3 Comparison of Data to PYTHIA

Table 8.2 is a comparison of PYTHIA events to real data events for the study of Λ° produced particles for a minimum bias run with the condition that the ana-

lyzed events contain single muon triggered events. The first column is the average multiplicity for an event that contained a Λ°. PYTHIA's value is dramatically different from what was observed experimentally. The requirement of a muon to have been a "trigger" in the event did not influence an increase in the multiplicity. The data value, though, is influenced by the muon, indicative of the fact that many tracks were present in the event. The second column is the average multiplicity for all events, irrespective of whether a Λ° was in the event. PYTHIA and data disagree, with PYTHIA more than three times too low. The third column is the average number of Λ°'s generated (where "generated" for data meant taking into account the overlay efficiency correction for 4π steradian) per raw charged multiplicity. PYTHIA predicts more Λ°'s produced per charged multiplicity than what was experimentally observed. The fourth column is the average number of Λ°'s generated per event. PYTHIA's value is in relative agreement with data. The last column is the $< p_t >$ for the Λ°'s. PYTHIA and data are in agreement within errors.

	$< N >_{\Lambda^\circ}$	$< N >_{evt}$	$< \frac{\Lambda^\circ(gen)}{N_{all}} >$	$< \frac{\Lambda^\circ(gen)}{evt} >$	$< p_t >_{\Lambda^\circ}$ (GeV)
PYTHIA	3.9 ± 0.3	2.820 ± 0.005	0.0390 ± 0.0001	0.111 ± 0.004	0.51 ± 0.02
DATA	11.8 ± 1.5	9.451 ± 0.004	0.018 ± .001	0.17 ± 0.01	0.47 ± 0.05

Table 8.2: Comparison of minimum bias single muon triggered PYTHIA generated events and data events for Λ° produced particles.

As in the minimum bias events for no trigger criterion, PYTHIA and data were in agreement for some values, while they had big disagreements in others.

The biggest disagreements involved the multiplicity values. PYTHIA consistently under predicted the multiplicity, and so this affected the ratio of the number of Λ°'s generated per charged multiplicity, giving a higher value for PYTHIA than for data.

8.5 Raw $\overline{\Lambda^{\circ}}$ Events, Overlay Efficiency, Corrected $\overline{\Lambda^{\circ}}$ Acceptance

The procedures that were discussed in Chapter 7 for fitting the $\overline{\Lambda^{\circ}}$ events, for calculating the overlay efficiency, and for obtaining the corrected $\overline{\Lambda^{\circ}}$ acceptances will be used in the single muon triggered events for the $\overline{\Lambda^{\circ}}$ analysis.

Although a greater amount of data was accumulated for the single muon triggered events as compared to the LED triggered events, the actual observation of the $\overline{\Lambda^{\circ}}$ was somewhat difficult due to the high background combinatorics, as shown in Figure 8.15. This figure is the $\overline{\Lambda^{\circ}}$ mass distribution for different z-decay and $|\Delta z|$ cuts. The first through fourth rows of the figure are the mass distributions for z-decay cuts greater than 5 *cm* from the main interaction vertex, greater than 10 *cm* from the main interaction vertex, greater than 30 *cm* from the main interaction vertex, and greater than 50 *cm* from the main interaction vertex, respectively. The first through the fourth columns show the mass distribution for $|\Delta z|$ cuts $\leq$ 40 *cm*, $\leq$ 30 *cm*, $\leq$ 20 *cm*, and $\leq$ 10 *cm*, respectively. With the loosest cut applied, it is relatively difficult to distinguish a mass peak, but it becomes more visible as the cuts are made tighter. Figure 8.15 is the $\overline{\Lambda^{\circ}}$ mass distribution for all events, irrespective of whether they were coplanar.

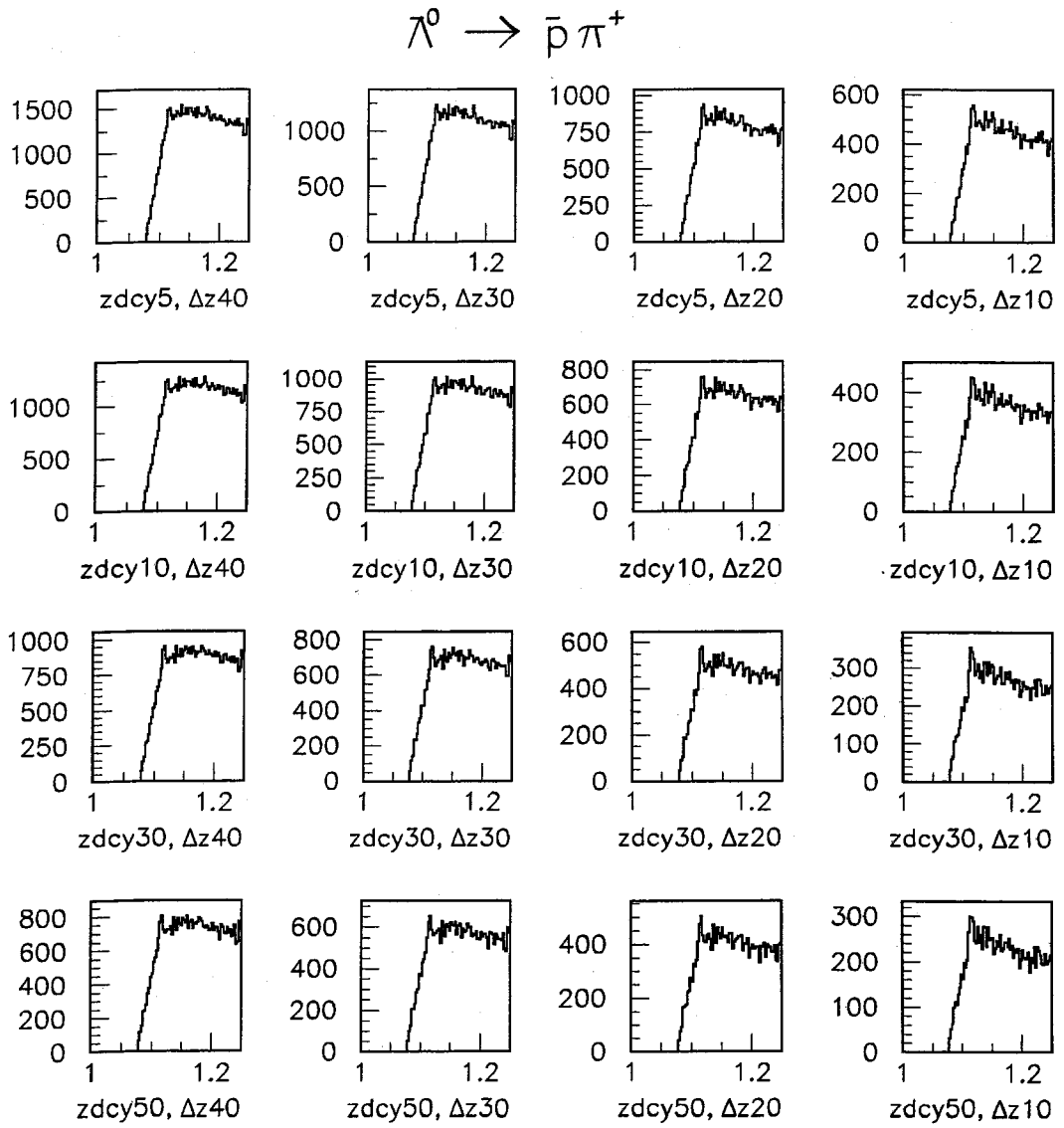

Figure 8.15: $\overline{\Lambda^\circ}$ mass distributions from single muon triggered events for different z-decay and $|\Delta z|$ cuts, with no coplanarity cut imposed. Each horizontal scale is the mass value in GeV/c^2, and each vertical scale is the number of pairs per 2.5 MeV/c^2.

Figure 8.16 follows the same convention as that described for Figure 8.15 with the added condition that the tracks be coplanar. Coplanarity is defined as

$$cos(\theta) = \frac{(\vec{V} \times \vec{a}) \cdot (\vec{b} \times \vec{V})}{|\vec{V} \times \vec{a}||\vec{b} \times \vec{V}|} \geq 0.95. \tag{8.17}$$

$\vec{V}$ is the parent particle vector, and $\vec{a}$ and $\vec{b}$ the first and second decay product vectors. A comparison of Figures 8.15 and 8.16 shows an increased mass peak, yet the coplanarity criterion significantly reduces the statistics.

The significance of Figures 8.15 and 8.16 is brought out by observing the number of $\overline{\Lambda^\circ}$'s produced, by calculating the overlay tracking efficiency for $\overline{\Lambda^\circ}$ acceptance, and by calculating the corrected number of $\overline{\Lambda^\circ}$'s using the overlay efficiency number. Figure 8.17 is the raw number of $\overline{\Lambda^\circ}$'s as a function of $|\Delta z|$ cuts. The lines drawn through sets of different symbols refer to the different z-decay values. The looser the $|\Delta z|$ cut is, and the closer the decay of the $\overline{\Lambda^\circ}$ to the main interaction vertex, the more $\overline{\Lambda^\circ}$'s are produced, yet the background is also high. Contained in this plot are sets of lines pertaining to different classes of z-decay cuts for non-coplanar as well as coplanar tracked events. Examination of the plot shows how those tracks that were required to be coplanar yielded close numbers for the number of $\overline{\Lambda^\circ}$'s seen, whereas those tracks that did not require coplanarity had high deviations. The non-coplanar tracks gave numbers that were expected, that is, the looser the cuts, the more $\overline{\Lambda^\circ}$'s would be produced.

The overlay efficiency for tracking an event within a specified cut interval is shown in Figure 8.18. It is plotted as a function of $|\Delta z|$, where the lines, dashes, dots, and dot-dashes joining the different symbols are the various z-decay cuts from the main interaction vertex. The overlay efficiency for tracking $\overline{\Lambda^\circ}$ events is

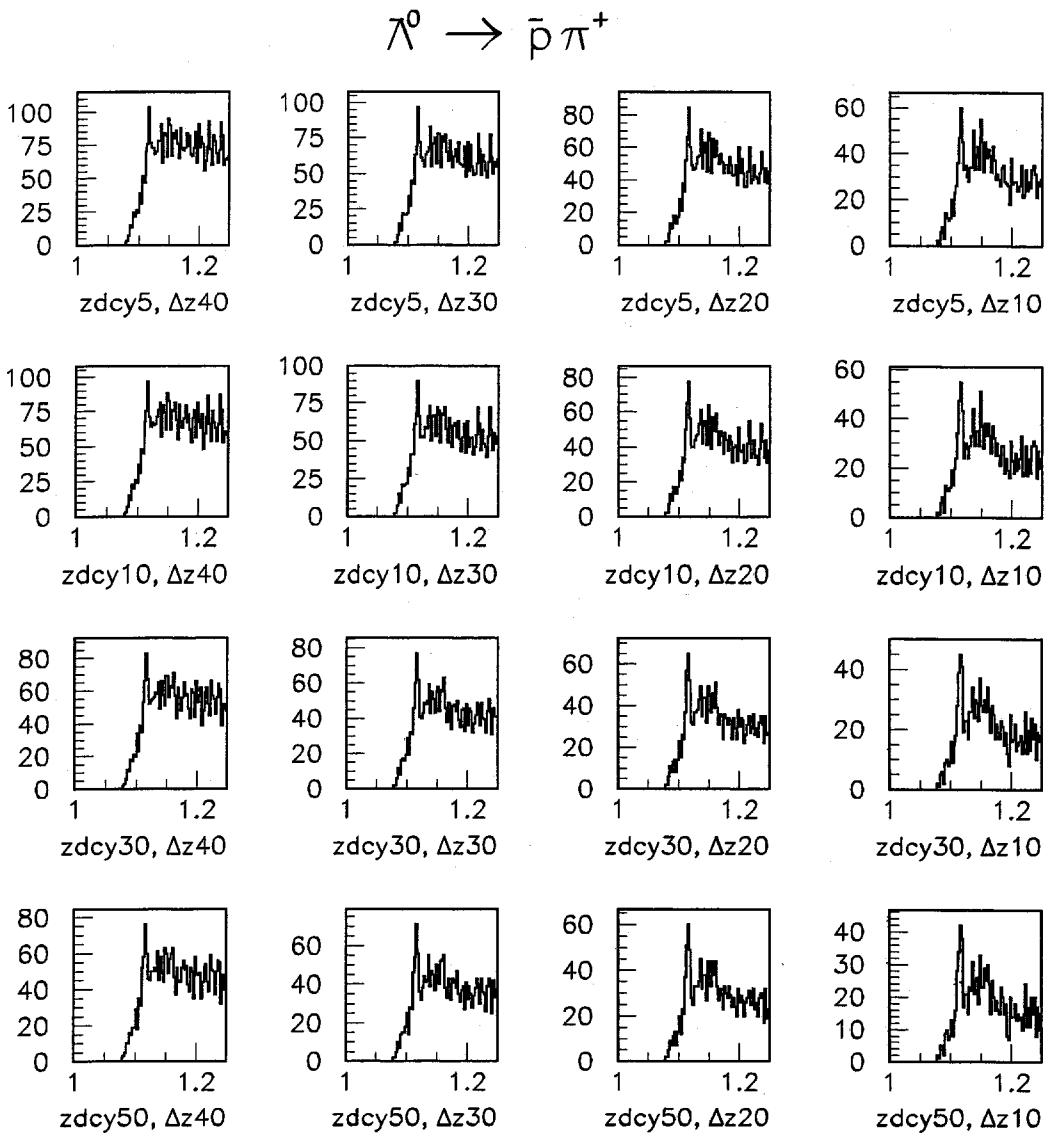

Figure 8.16: $\overline{\Lambda^\circ}$ mass distributions from single muon triggered events for different z-decay and $|\Delta z|$ cuts, with a coplanarity cut imposed. Each horizontal scale is the mass value in GeV/c^2, and each vertical scale is the number of pairs per 2.5 MeV/c^2.

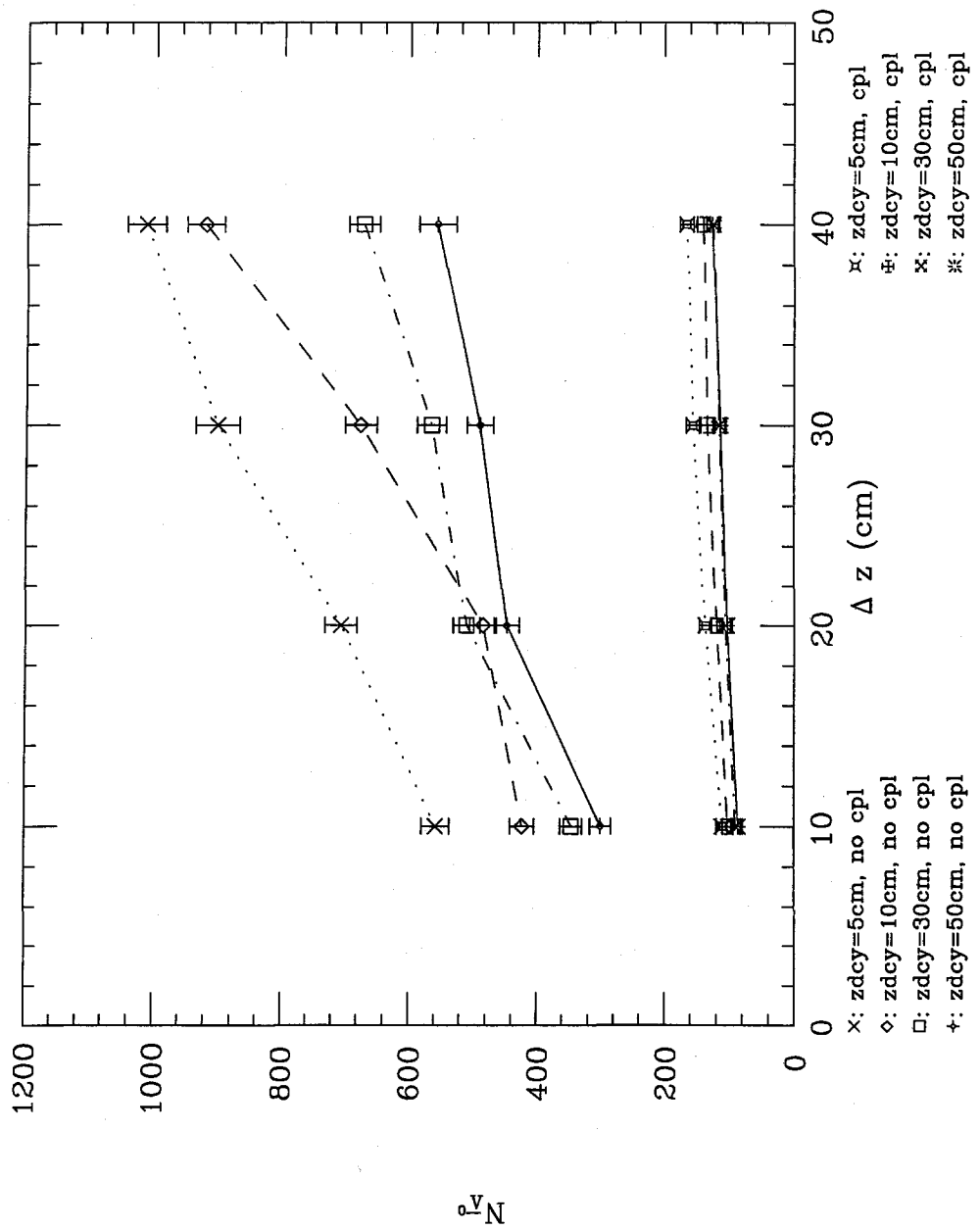

Figure 8.17: Total number of $\overline{\Lambda^\circ}$, $N_{\overline{\Lambda^\circ}}$, as a function of $|\Delta z|$ and z-decay cuts. Shown are curves for coplanar tracks and curves for non-coplanar tracks.

quite small ranging from a minimum of 0.18% to a maximum of 0.57%, comparable to those measured for Λ° production. The quoted efficiency values were for tracks where no coplanarity criterion was imposed. Due to the loss of events when the coplanarity cut was applied, poor fits were obtained, and so the overlay efficiency was not measured for them.

Figure 8.19 is the corrected number of $\overline{\Lambda^\circ}$'s (the corrected number of $\overline{\Lambda^\circ}$'s is achieved by taking the ratio of the raw number of $\overline{\Lambda^\circ}$'s to the overlay efficiency, $(N_{\overline{\Lambda^\circ}}/\epsilon)$, versus the $|\Delta z|$ cuts. The different symbols are for different z-decay cuts from the main interaction vertex. A much larger fluctuation occurs for those tracks where no coplanar tracks were required, whereas those tracks that were required to be coplanar yielded much better agreements.

8.6 $\overline{\Lambda^\circ}$ p_t, Multiplicity, Rapidity, and x_f Distributions

Important $\overline{\Lambda^\circ}$ characteristics from single muon triggered events, such as the $< p_t >$, the charged particle multiplicity (N_c), the rapidity (y_{cm}), and the Feynman-x (x_f) distributions, will be discussed, and their relevant extracted information will be compared to PYTHIA.

8.6.1 Data

To obtain a p_t distribution that is most likely to come from a $\overline{\Lambda^\circ}$ event, one must apply cuts within the mass region of the $\overline{\Lambda^\circ}$ in order to obtain the best possible mass distribution for fitting purposes. A fit was performed on the $\overline{\Lambda^\circ}$ mass plot using a Gaussian to fit the signal peak (N_s) and a polynomial to fit the background

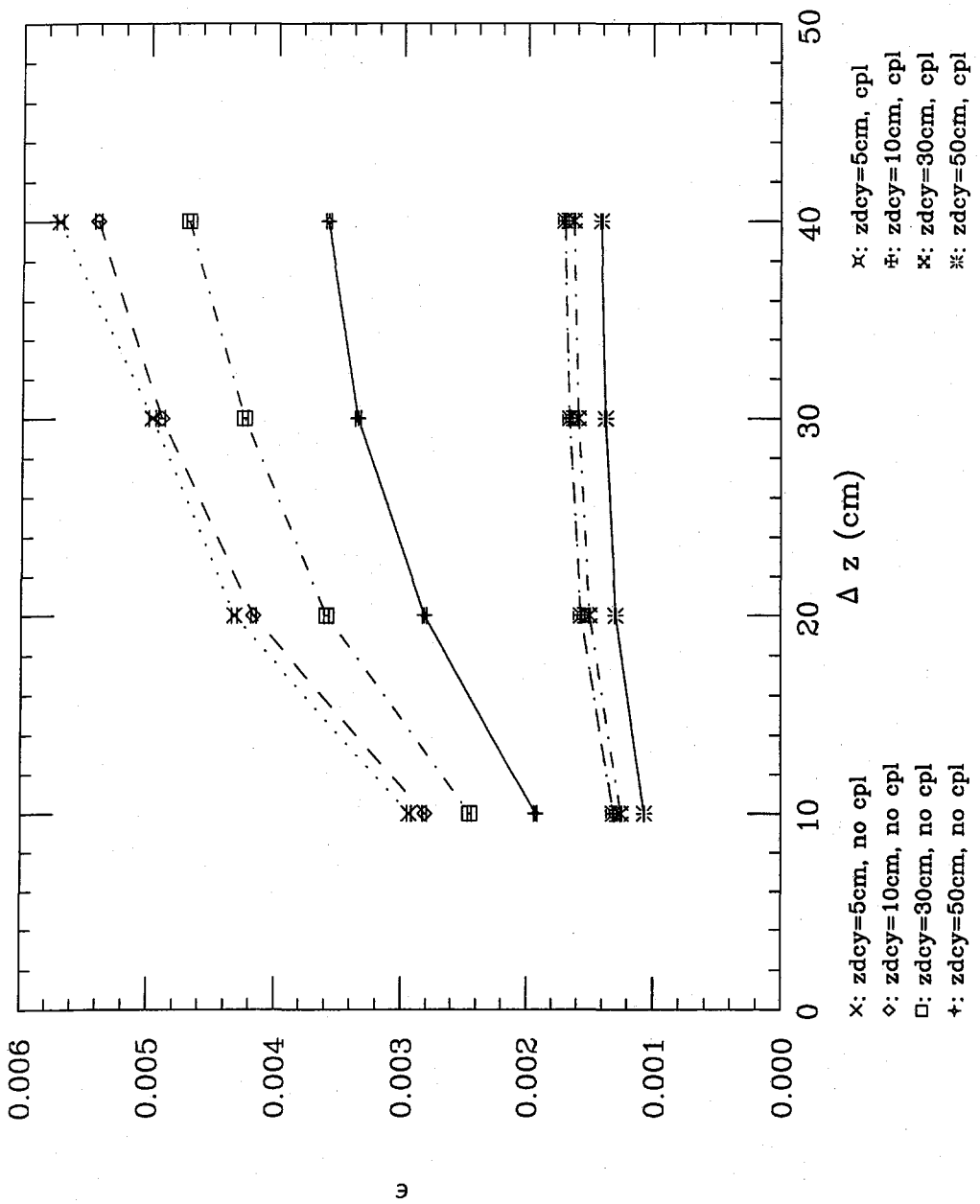

Figure 8.18: Overlay efficiency, ϵ, for tracking a Λ° as a function of $|\Delta z|$ and z-decay cuts. Shown are curves for coplanar tracks and curves for non-coplanar tracks.

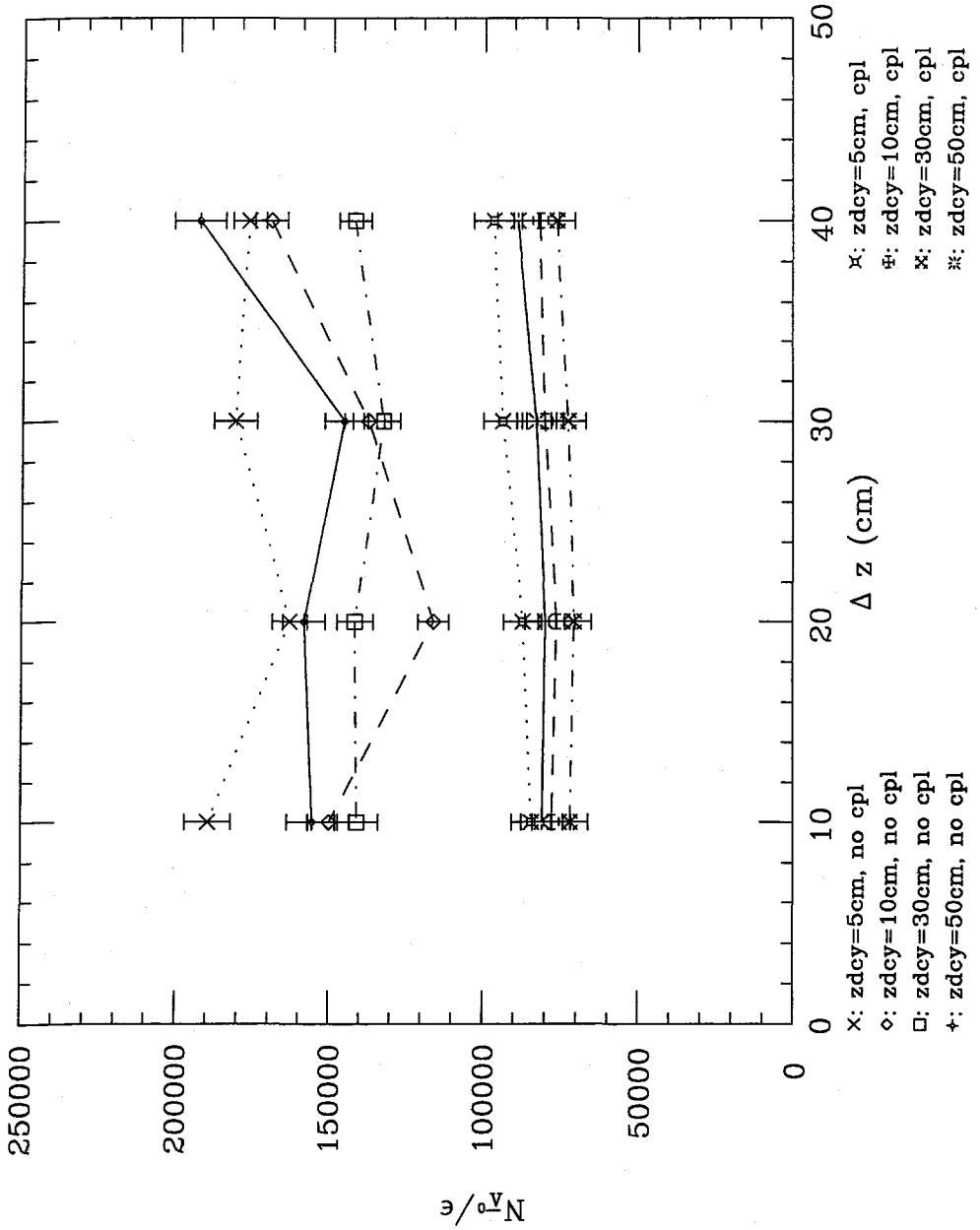

Figure 8.19: Corrected number of $\overline{\Lambda^0}$'s, $N_{\overline{\Lambda^0}}/\epsilon$, as a function of $|\Delta z|$ and z-decay cuts. Shown are curves for coplanar tracks and curves for non-coplanar tracks.

(N_b). The p_t distribution was obtained by restricting the acceptance of only those events whose mass values were within $\pm$ 10 MeV of the $\overline{\Lambda^\circ}$ mass value. If they met this criterion, the p_t distribution was plotted. As seen in Figures 8.15 and 8.16, a background distribution was quite prevalent in those events where no coplanarity cut was imposed. The background also existed in those tracks where coplanar tracks were required, but to a much smaller extent. The background region had to be accounted for and subtracted from the final p_t distribution plot. To achieve the true p_t distribution, the p_t distribution for those events that had unlike sign tracks (signal plot, $N_\pm$) was plotted. The same distribution was made for those events that had like sign tracks (background plot, N_{LS}). The like sign distribution had to be normalized to the unlike sign one. Each like sign event was multiplied by the ratio N_b/N_{LS} in order to normalize background to signal, where N_b is the background number obtained from the mass distribution fit. This resultant distribution was then subtracted from the $N_\pm$ distribution, giving the true p_t distribution.

Figure 8.20 is the $\overline{\Lambda^\circ}$ true p_t distribution, shown three times for three different fitting functions to the curve in order to extract the $< p_t >$ value. The three functions used are

$$dN/dp_t = P1 \cdot p_t \cdot exp(-p_t \cdot P2), \tag{8.18}$$

$$dN/dp_t = P1 \cdot p_t \cdot exp(-\sqrt{p_t^2 + m^2}/P2), \tag{8.19}$$

$$dN/dp_t = (P1 \cdot p_t)/(p_t + P2)^{P3}. \tag{8.20}$$

$P1$, $P2$, and $P3$ are the fitted parameter values obtained from each of the individual fits. (a) is the $\overline{\Lambda^\circ}$ p_t distribution using Equation (8.18) as the fit to the distribution,

where $P1$ and $P2$ are the fitted parameters for this exponential function. (b) is the same distribution using Equation (8.19) as the fit to the distribution, where $P1$ and $P2$ are the fitted parameters for this function using the thermal exponential fit. (c) is the same distribution using Equation (8.20) as the fit to the distribution, where $P1$, $P2$, and $P3$ are the fitted parameters for this function.

Each of the three different fitting functions yielded similar values for the $< p_t >$, where 0.287 GeV/c was the greatest discrepancy between the results of the three fits. Taking the average of the three fitted results yielded a value of

$$< p_t > = 0.54 \pm 0.13 \text{ GeV/c},$$

where the systematic error was the rms deviation of the three different fits. The two exponential function fits were in close agreement, but the power law fit proved on average to give a lower $< p_t >$.

The three different fits used to get the average p_t values were model dependent and did not look at the low p_t region. This was explained by the fact that the low p_t particles were lost when simulated to traverse E771's spectrometer region. An alternative for getting the average p_t was to average directly the p_t values for the whole distribution as the final p_t distribution was corrected for the spectrometer acceptance. The procedure was the same as that used for getting the three model dependent $< p_t >$ values. That is, one had to normalize the background p_t distribution to the signal p_t distribution in order to perform the proper subtraction to get the correct p_t distribution. The distribution had to be overlay corrected for losses at small p_t. Then the simple average of the corrected p_t distribution was formed without performing any fitting procedures. The $< p_t >$ value obtained for

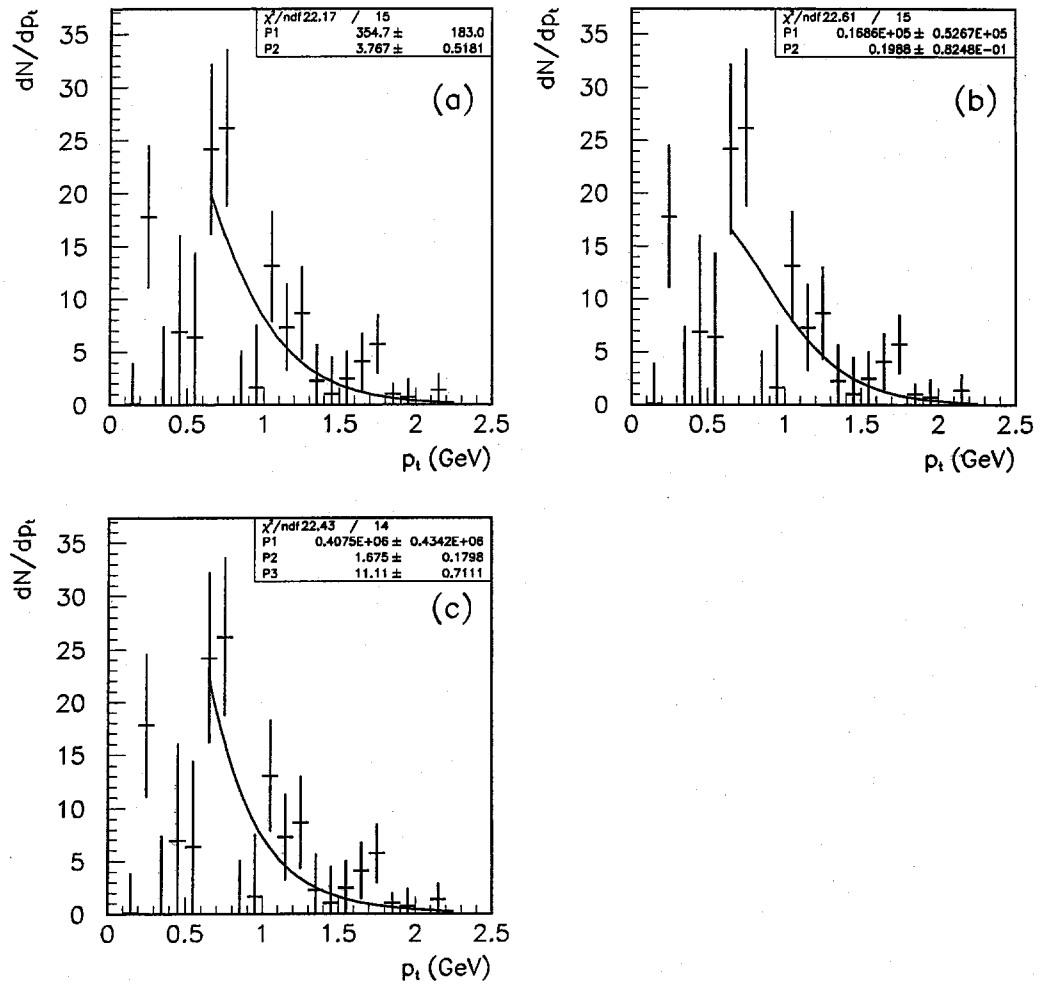

Figure 8.20: The $\overline{\Lambda^\circ}$ p_t distribution from single muon triggered events. The same plot is shown three times for each of three different fitting functions. (a) uses Equation (8.18) as the fit, (b) uses Equation (8.19) as the fit, and (c) uses Equation (8.20) as the fit.

the $\overline{\Lambda^o}$'s using this method was

$$< p_t >=0.82\pm0.30\ GeV/c.$$

It is noted that the latter procedure used to fit the $< p_t >$ yielded a higher value than that obtained from the three different fits. This is explainable by the fact that the power law fit described above generally gave a lower value than did the other two fits.

The multiplicity, rapidity, and Feynman-x distributions were all obtained the same way the p_t distribution was. That is, those events that were within $\pm$ 10 MeV of the $\overline{\Lambda^o}$ mass peak were retained and their respective distributions plotted.

As the main hadronic tracking program calculated its variables with respect to the laboratory frame, the y_{cm} and x_f distributions were transformed from the lab frame to the center of mass frame. With rapidity defined in the lab as

$$y_{lab} = \frac{1}{2}ln(\frac{E+P_l}{E-P_l}), \tag{8.21}$$

it was defined in the center of mass system as

$$y_{cm} = y_{lab} + y_{tx}, \tag{8.22}$$

where the transformation, y_{tx}, is defined as

$$y_{tx} = \frac{1}{2}ln(\frac{1-\beta_{cm}}{1+\beta_{cm}}). \tag{8.23}$$

E is the particle's energy and P_l its longitudinal momentum.

$$\beta_{cm} = P_{beam}/(\sqrt{P_{beam}^2 + m_p^2} + m_p),$$

where P_{beam} is the beam momentum and m_p the proton mass.

The Feynman-x distribution (in the center of mass system) is

$$x_f = \frac{2 \cdot p_{z(cm)}}{\sqrt{s}}, \tag{8.24}$$

where $p_{z(cm)} = \gamma_{cm} \cdot (P_z - \beta_{cm} \cdot E)$.

Figure 8.21 shows the $\overline{\Lambda^\circ}$ N_c, y_{cm}, and x_f distributions for the single muon triggered events. Plot (a) is the charged particle multiplicity distribution with $< N_c >$=11.8±7.4. The large error in the multiplicity is due to low statistics. (b) is the center of mass rapidity distribution. It is more pronounced in the forward region than the backward region due to the limited spectrometer acceptance. (c) is the center of mass x_f distribution. This distribution generally follows the same qualitative shape of the rapidity distribution.

8.6.2 Minimum Bias PYTHIA

In order to simulate a single muon trigger for a PYTHIA event, an event that is PYTHIA generated looks for muons. Once a muon is tagged, the program determines whether it had enough energy to penetrate the steel shielding and produce a triple coincidence in the RPC chambers. If so, it is counted as a single muon trigger. Once this step is complete, we continue with the event by looking for the V°'s. The V° particle is simulated to pass through the spectrometer region. It encounters the magnet where it experiences a p_t kick and deflected to traverse the rear chambers. The program checks to see that each track of the event hits at least three chamber planes upstream of the analysis magnet and three chamber planes downstream of the magnet. If two tracks of a generated V° pass the front and rear chamber hit criteria, the event is accepted and its relevant information plotted or put in counters for later use. The relevant information used from PYTHIA for comparison purposes consists of obtaining the average multiplicity for those events

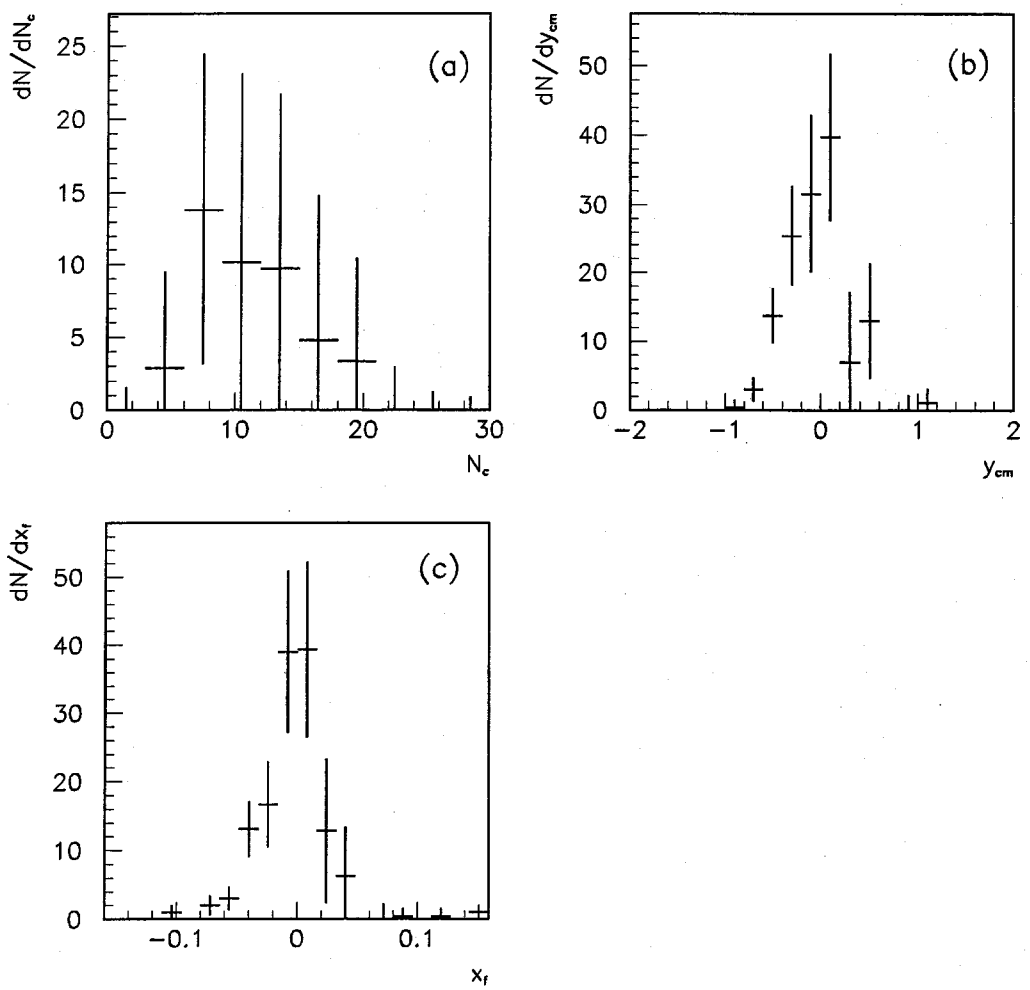

Figure 8.21: (a) N_c, (b) y_{cm}, and (c) center of mass x_f distributions for the $\overline{\Lambda^\circ}$ single muon triggered events. These distributions are not corrected for full spectrometer acceptance.

that have $\overline{\Lambda^\circ}$'s in them, obtaining the average multiplicity value for all events, irrespective of whether the event contained a $\overline{\Lambda^\circ}$, the number of $\overline{\Lambda^\circ}$'s generated (meaning, the particle is PYTHIA produced but may not necessarily pass the spectrometer acceptance criteria), the number of $\overline{\Lambda^\circ}$'s generated per event, and the average p_t value.

8.6.3 Comparison of Data to PYTHIA

Table 8.3 is a comparison of PYTHIA events to real data events for the study of $\overline{\Lambda^\circ}$ produced particles for a minimum bias run with the condition that the analyzed events contain single muon triggered events. The first column is the average multiplicity for an event that contained a $\overline{\Lambda^\circ}$. Once again, PYTHIA predicts a much smaller value from what was observed experimentally. This difference is about two times higher in multiplicity value for data events than for PYTHIA. The second column is the average multiplicity for all events, not taking into account whether or not a $\overline{\Lambda^\circ}$ was present. There is also a difference for what PYTHIA predicts and what is observed experimentally. The third column is the average number of $\overline{\Lambda^\circ}$'s generated ("generated" for data events meaning corrected up for 4π acceptance) per raw charged multiplicity. PYTHIA and data are in good agreement. The fourth column is the average number of $\overline{\Lambda^\circ}$'s generated per event. PYTHIA predicts a smaller value than what is experimentally observed. The last column is the $< p_t >$ for the $\overline{\Lambda^\circ}$. PYTHIA's value is about 0.1 GeV/c less than what is obtained via data.

As in the minimum bias events for no trigger criterion, PYTHIA and data were

	$< N >_{\overline{\Lambda^\circ}}$	$< N >_{evt}$	$< \frac{\overline{\Lambda^\circ}(gen)}{N_{all}} >$	$< \frac{\overline{\Lambda^\circ}(gen)}{evt} >$	$< p_t >_{\overline{\Lambda^\circ}}$ (GeV)
PYTHIA	4.1 ± 0.4	2.820 ± 0.005	0.00860 ± 0.00003	0.025 ± 0.002	0.41 ± 0.02
DATA	8.0 ± 3.0	9.451 ± 0.004	0.010 ± .001	0.0923 ± 0.0136	0.531 ± 0.073

Table 8.3: Comparison of minimum bias single muon triggered PYTHIA generated events and data events for $\overline{\Lambda^\circ}$ produced particles.

in agreement for some values, while they had big disagreements in others. The usual discrepancies revolved around PYTHIA's continual under-counting of the charged multiplicity.

8.7 Signal/Background Ratios

A good sampling of the V° mass distributions was obtained by applying various z-decay and $|\Delta z|$ cuts. From these variances, a range of signal/background ratios was obtained out of a sample of 1,569,455 tracked single muon triggered events.

The signal/background ratios for the K° mass distributions ranged from as low as 0.10 to as high as 0.20 when all track pairs were taken into consideration, that is, the mass distributions contained both non-coplanar and coplanar tracks. The signal/background ratios for the K° mass distributions ranged from as low as 0.84 to as high as 1.76 when only coplanar tracks were considered. It is apparent how the ratio increased significantly, showing how the coplanarity cut had a great influence in getting rid of the background combinatorics.

The signal/background ratios for the Λ° mass distributions ranged from as low as 0.18 to as high as 0.31 when all track pairs were taken into consideration, that

is, for the mass distributions containing both non-coplanar tracks and coplanar tracks. The signal/background ratios for the Λ° mass distributions ranged from a low of 0.50 to a high of 1.15, again showing how the coplanar cut increased the signal peak and decreasing the background region.

The signal/background ratios for the $\overline{\Lambda^\circ}$ mass distributions ranged from as low as 0.09 to as high as 0.17 when all track pairs were taken into consideration, that is, for the mass distributions containing both non-coplanar tracks and coplanar tracks. The signal/background ratios for the $\overline{\Lambda^\circ}$ mass distributions ranged from a low of 0.40 to as high as 0.70 when only coplanar track pairs were accepted.

8.8 Data Sets Analyzed for Single Muon Triggered Events

Out of 138 tapesets of data accumulation, where a tapeset consisted of twelve 2.239 GByte tapes, slightly more than two tapesets were analyzed for the single muon triggered events. Roughly 1.6 million single muon triggered events were tracked and studied for this analysis. Table 8.4 lists the tapesets and their respective JM sequence numbers used in this analysis. The last column is the total number of tracked events. The statistics include both single muon triggered events and double muon triggered events.

Tapeset Number	JM Sequence Numbers	Total 1μ and 2μ Tracked Events
TS20340	JM2859 $\rightarrow$ JM2870	1,607,791
TS20341	JM2871 $\rightarrow$ JM2882	1,636,468
TS20342	JM2883 $\rightarrow$ JM2884	104,922

Table 8.4: Run statistics for tracked single muon triggered events and double muon triggered events.

Chapter 9

Double-μ Triggered Events

The double muon triggered events contained tracks where two muons had satisfied the triple RPC coincidence requirement (see Section 3.1.3). Approximately 120 million di-μ triggered events were accumulated during the five week period of running. Of those 120 million di-μ triggered events, approximately 1.8 million di-μ tracked events were used for this analysis.

9.1 Raw K° Events, Overlay Efficiency, Corrected K° Acceptance

The procedures that will be described for fitting the K° events, for calculating the overlay efficiency, and for obtaining the corrected K° acceptances are the same as those employed for the single muon triggered events.

A comparison of the single muon triggered events to the double muon triggered events yields mass spectra of common characteristics, although the total number of entries for any one histogram plot yields more statistics for the di-μ triggered events due to the slightly higher number of events tracked. Figure 9.1 shows such a sampling of the K° mass distribution with different z-decay and $|\Delta z|$ cuts. These

plots do not require that the tracks be coplanar, where a coplanar track is defined as

$$cos(\theta) = \frac{(\vec{V} \times \vec{a}) \cdot (\vec{b} \times \vec{V})}{|\vec{V} \times \vec{a}||\vec{b} \times \vec{V}|} \geq 0.95. \tag{9.1}$$

$\vec{V}$ is the parent particle vector, and $\vec{a}$ and $\vec{b}$ are the first and second decay product vectors. The first row is the mass distribution for a fixed z-decay length greater than 5 *cm* from the main interaction vertex, while the progression of columns is for tighter cuts imposed on the $|\Delta z|$. The second row is the mass distribution for a fixed z-decay length greater than 10 *cm* from the main interaction vertex, while the columns are for $|\Delta z|$ cuts $\leq$ 20 *cm*, $\leq$ 15 *cm*, $\leq$ 10 *cm*, and $\leq$ 5 *cm*, respectively. The third row is the mass distribution for a fixed z-decay length greater than 30 *cm* from the main interaction vertex, while the columns are for $|\Delta z|$ cuts $\leq$ 20 *cm*, $\leq$ 15 *cm*, $\leq$ 10 *cm*, and $\leq$ 5 *cm*, respectively. The last row is the mass distribution for a fixed z-decay length greater than 50 *cm* from the main interaction vertex, while the columns are for $|\Delta z|$ cuts $\leq$ 20 *cm*, $\leq$ 15 *cm*, $\leq$ 10 *cm*, and $\leq$ 5 *cm*, respectively. As can be seen, the combination of tighter cuts increases the signal to noise ratio.

Figure 9.2 follows the same convention as that described for Figure 9.1 with the added condition that the tracks be coplanar. A comparison of the two figures shows a significant improvement of the signal to noise ratio, which enables good fitting procedures to be performed.

Figure 9.3 is an example of the information extracted from the mass plots. It shows the raw number of K°'s as a function of the $|\Delta z|$ cuts. The lines drawn through sets of different symbols refer to the different z-decay values. The looser

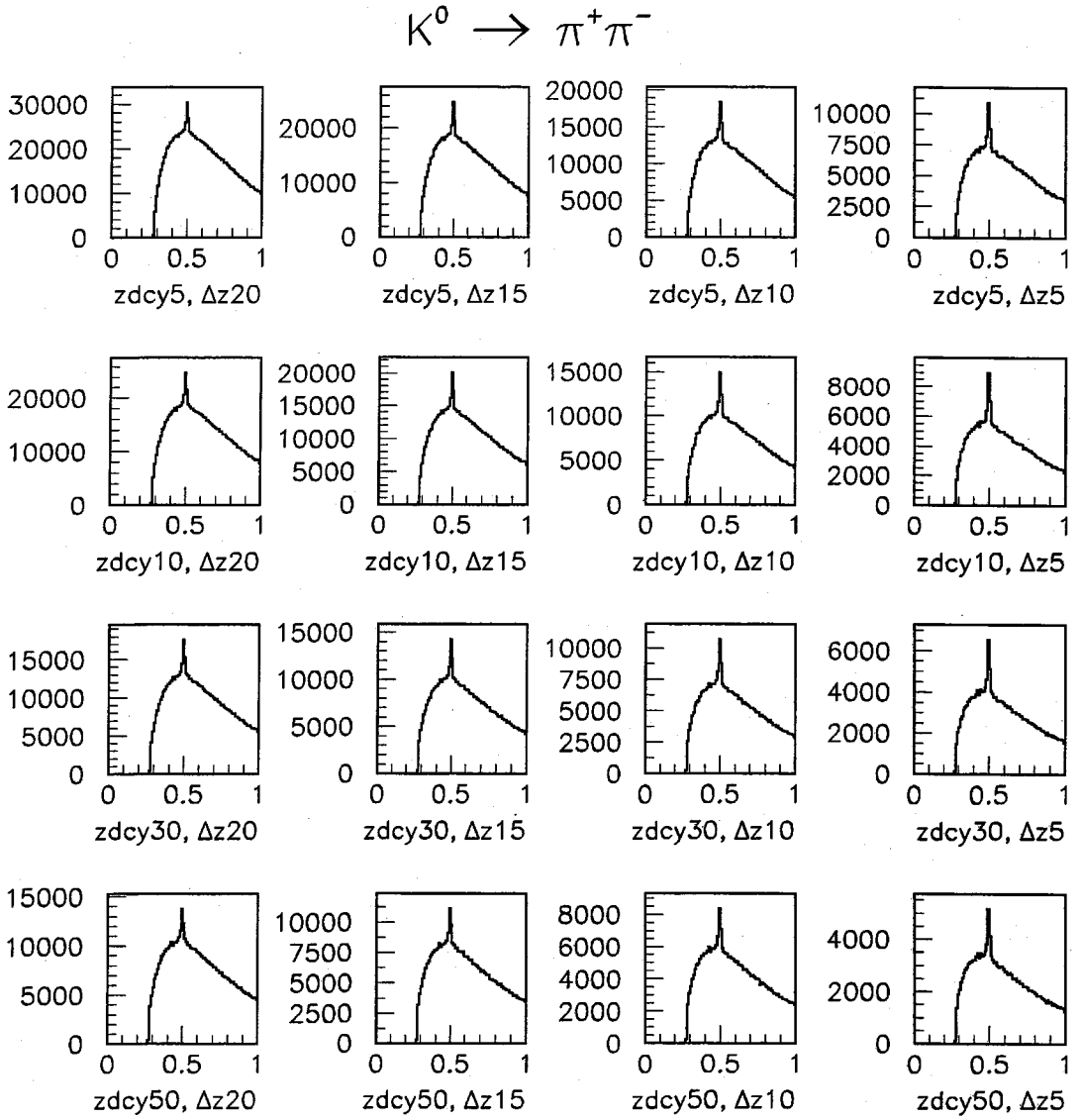

Figure 9.1: K° mass distributions from double muon triggered events for different z-decay and $|\Delta z|$ cuts, with no coplanarity criterion imposed. Each horizontal scale is the mass value in GeV/c^2, and each vertical scale is the number of pairs per 10 MeV/c^2.

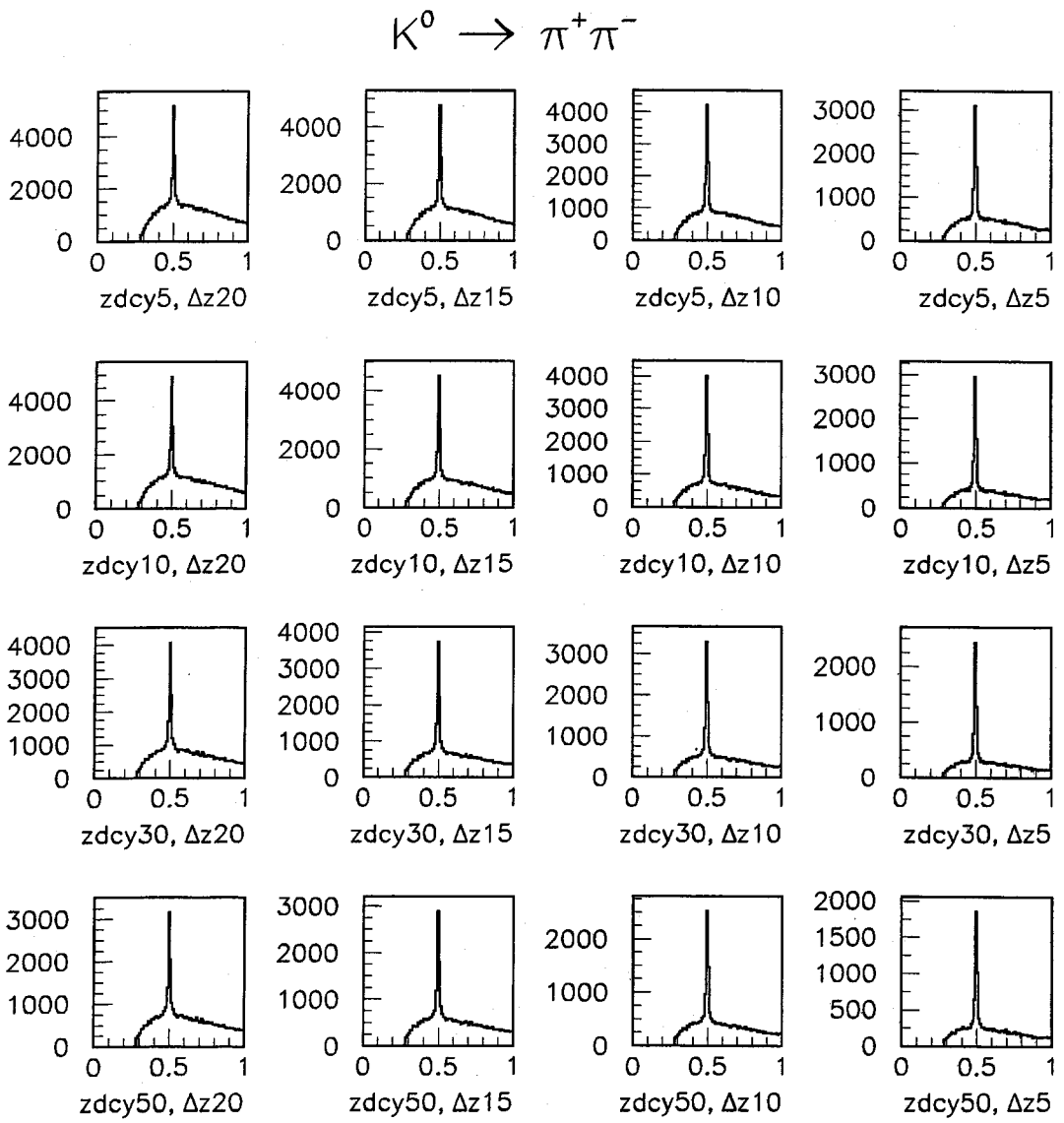

Figure 9.2: K° mass distributions from double muon triggered events for different z-decay and $|\Delta z|$ cuts, with a coplanarity criterion imposed. Each horizontal scale is the mass value in GeV/c^2, and each vertical scale is the number of pairs per 10 MeV/c^2.

the $|\Delta z|$ cut is, e.g. 20 cm, and the closer the K° is to the main interaction vertex, the more K°'s are produced. This plot shows a set of lines for those plots where the coplanarity cut was not implemented and another set of lines for those plots where a coplanarity cut was implemented. It is interesting to observe the overlap in the raw number of events observed for those K°'s where coplanarity was required and for those K°'s where none was.

The efficiency for tracking an event within a cut interval, defined as the overlay efficiency, is shown in Figure 9.4. It is plotted as a function of $|\Delta z|$, where the lines, dashes, dots, and dot-dashes joining their respective symbols are the different z-decay cuts from the main interaction vertex. The overlay tracking efficiency for K° detection using the double muon triggered events ranged from a low of 0.4% to a high of 1.85%.

Figure 9.5 is a plot of the ratio of the raw number of K°'s to the overlay efficiency, defined as the corrected number of K°'s (N_{K°/ϵ), versus the $|\Delta z|$ cuts. The symbols are for different z-decay cuts from the main interaction vertex. This plot shows a close agreement (some overlaps) between the values obtained for those events that had coplanar tracks and those events that did not require the tracks to be coplanar. This is indicative of the reliability for the overlay tracking program to correct for losses.

9.2 K° p_t, Multiplicity, Rapidity, and x_f Distributions

Important K° characteristics from double muon triggered events, such as the p_t, N_c, y_{cm}, and x_f distributions, will be discussed, and their relevant extracted in-

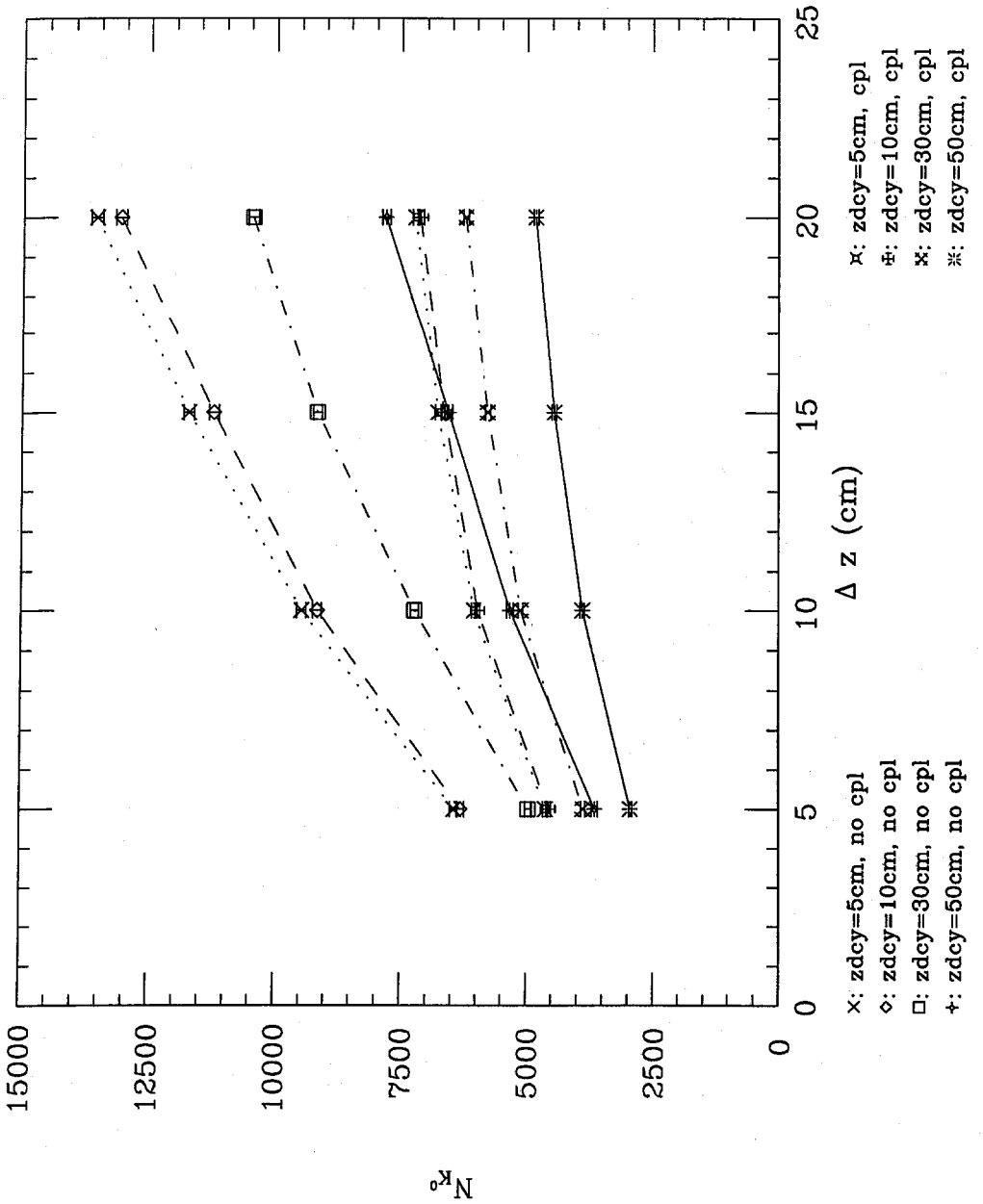

Figure 9.3: Total number of K°'s, $N_{K^{\circ}}$, as a function of $|\Delta z|$ and z-decay cuts. Shown are curves for coplanar tracks and curves for non-coplanar tracks.

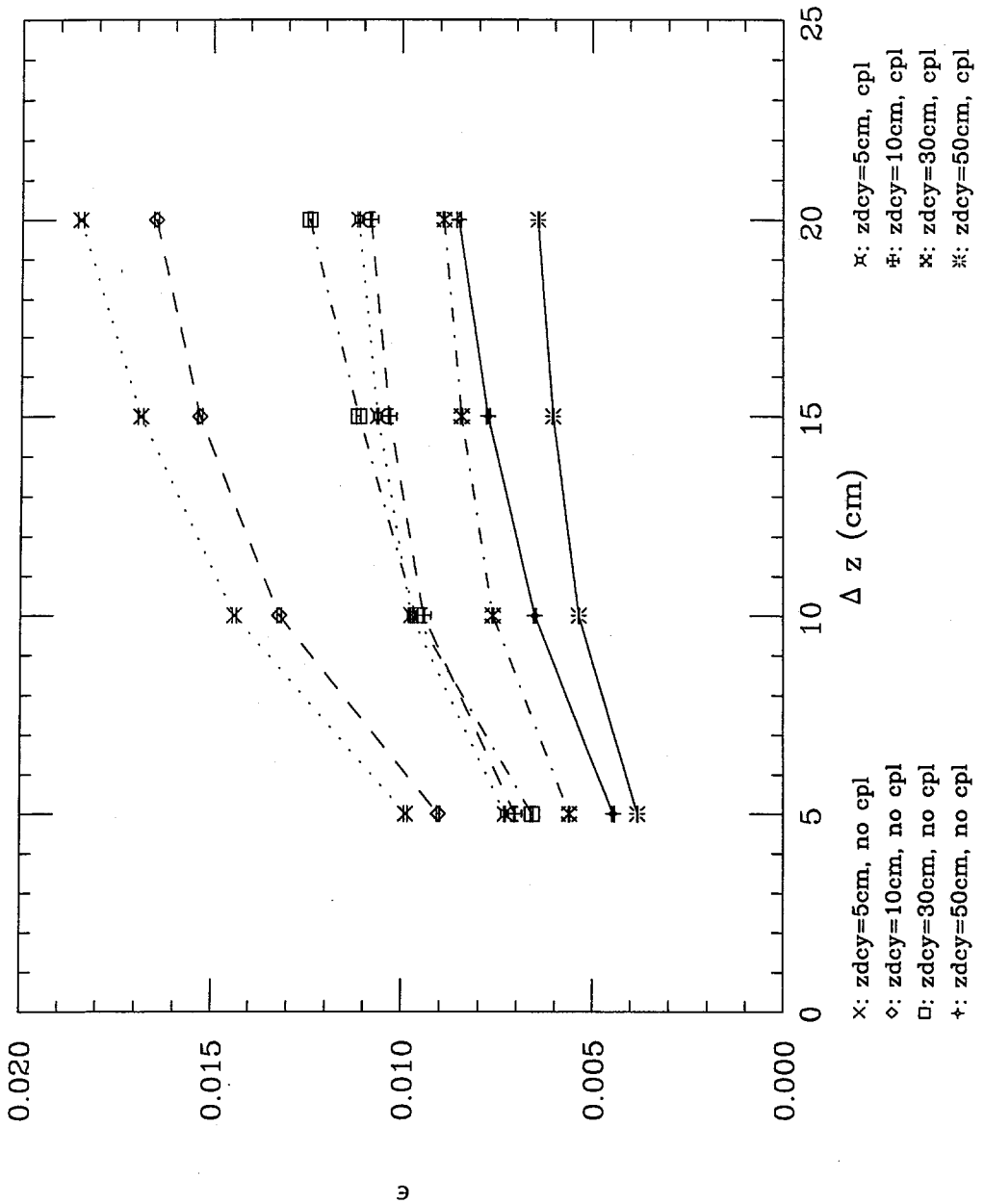

Figure 9.4: Overlay efficiency, ϵ, for tracking a K° as a function of $|\Delta z|$ and z-decay cuts. Shown are curves for coplanar tracks and curves for non-coplanar tracks.

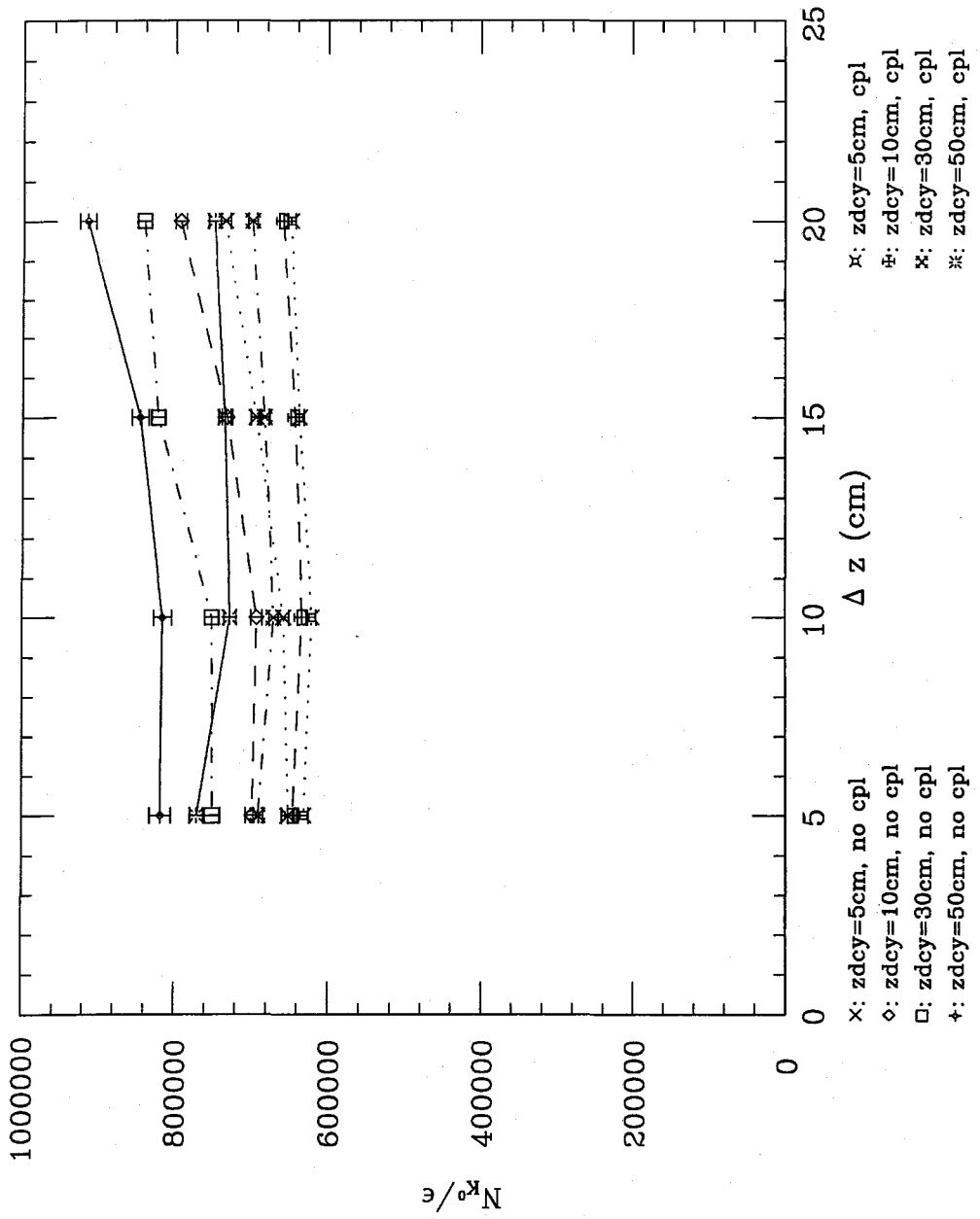

Figure 9.5: Corrected number of K°'s, $N_{K^{\circ}}/\epsilon$, as a function of $|\Delta z|$ and z-decay cuts. Shown are curves for coplanar tracks and curves for non-coplanar tracks.

formation will be compared to PYTHIA.

9.2.1 Data

The K° p_t distribution was obtained by restricting the acceptance of only those events whose mass values were within $\pm$ 30 MeV of the K° mass value. If they met this criterion, the p_t distribution was plotted. As shown in Figures 9.1 and 9.2, a background distribution existed beneath the mass peak which had to be accounted for and subtracted from the final p_t distribution This was taken care of by fitting the mass peak with a Gaussian (N_s) and a polynomial to fit the background (N_b). The p_t distribution was plotted for those events that had unlike sign tracks (signal plot, $N_\pm$), and it was also plotted for those events that had like sign tracks (background plot, N_{LS}). The like sign distribution had to be normalized to the unlike sign distribution. Each like sign event was multiplied by the ratio N_b/N_{LS} in order to normalize background to signal. This resultant distribution was subtracted from the $N_\pm$ distribution, giving the true p_t distribution curve.

Figure 9.6 is the K° true p_t distribution, shown three times for three independent functions used to fit the same distribution. These three functions were used to extract an average value for the p_t distribution. They are

$$dN/dp_t = P1 \cdot p_t \cdot exp(-p_t \cdot P2), \tag{9.2}$$

$$dN/dp_t = P1 \cdot p_t \cdot exp(-\sqrt{p_t^2 + m^2}/P2), \tag{9.3}$$

$$dN/dp_t = (P1 \cdot p_t)/(p_t + P2)^{P3}. \tag{9.4}$$

$P1$, $P2$, and $P3$ are the fitted parameters obtained from each of the individual fits. (a) is the K° p_t distribution using Equation (9.2) as a fit, where $P1$ and $P2$ are

the fitted parameters for this exponential function. (b) is the K° p_t distribution using Equation (9.3) as a fit, where $P1$ and $P2$ are the fitted parameters for this thermal exponential fit. (c) is the K° p_t distribution using Equation (9.4) as a fit, where $P1$, $P2$, and $P3$ are the fitted parameters for this function.

Each of the three functions yields similar values for the $< p_t >$, and the greatest discrepancy between the values is 0.163 GeV/c. The K° $< p_t >$ value, averaging all three fitting algorithms gives a value of

$$< p_t > = 0.51 \pm 0.10 \text{ GeV/c},$$

where the systematic error is the *rms* deviation in the three fits.

The three different fits used to get the average p_t values were model dependent and did not look at the low p_t region. This was explained by the fact that the low p_t particles were lost when simulated to traverse E771's spectrometer region. An alternative for getting the average p_t was to average directly the p_t values for the whole distribution as the final p_t distribution was corrected for the spectrometer acceptance. The procedure was the same as that used for getting the three model dependent $< p_t >$ values. That is, one had to normalize the background p_t distribution to the signal p_t distribution in order to perform the proper subtraction to get the correct p_t distribution. The distribution had to be overlay corrected for losses at small p_t. Then the simple average of the corrected p_t distribution was formed without performing any fitting procedures. The $< p_t >$ value obtained for the K°'s using this method was

$$< p_t >=0.75\pm0.06 \; GeV/c.$$

It is noted that the latter procedure used to fit the $< p_t >$ yielded a higher

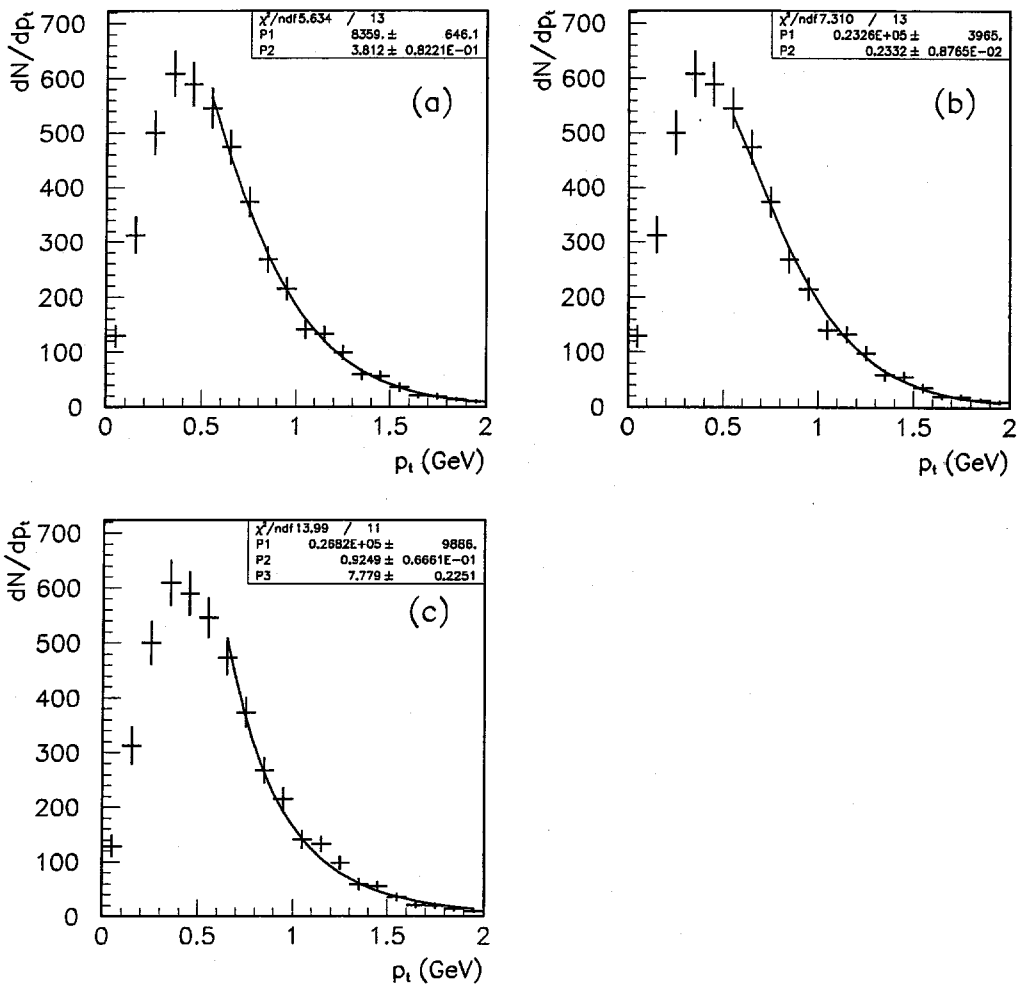

Figure 9.6: K° p_t distribution from double muon triggered events shown three times for each of three different fitting functions. (a) uses Equation (9.2) as the fit, (b) uses Equation (9.3) as the fit, and (c) uses Equation (9.4) as the fit.

value than that obtained from the three different fits. This is explainable by the fact that the power law fit described above generally gave a lower value than did the other two fits.

The multiplicity (N_c), rapidity (y_{cm}), and Feynman-x (x_f) distributions were all obtained the same way the p_t distribution was. That is, the background events had to be normalized to the signal events and subtracted from the signal events in order to get their true distributions.

The rapidity distribution, plotted in the center of mass system, is obtained from

$$y_{lab} = \frac{1}{2} ln(\frac{E + P_l}{E - P_l}), \tag{9.5}$$

so its center of mass value is

$$y_{cm} = y_{lab} + y_{tx}, \tag{9.6}$$

where the transformation from the lab to the center of mass frame is achieved by

$$y_{tx} = \frac{1}{2} ln(\frac{1 - \beta_{cm}}{1 + \beta_{cm}}). \tag{9.7}$$

E is the V°'s energy and P_l its longitudinal momentum.

$$\beta_{cm} = P_{beam}/(\sqrt{P_{beam}^2 + m_p^2} + m_p),$$

where P_{beam} is the beam momentum and m_p the proton mass.

Feynman's x variable, x_f, in the center of mass system, is defined as

$$x_f = \frac{2 \cdot p_{z(cm)}}{\sqrt{s}}, \tag{9.8}$$

where $p_{z(cm)} = \gamma_{cm} \cdot (P_z - \beta_{cm} \cdot E)$.

Figure 9.7 shows the K° N_c, y_{cm}, and x_f distributions for the double muon triggered events. (a) is the charged particle multiplicity distribution with $< N_c >$ $= 11.5 \pm 0.3$. (b) is the center of mass rapidity distribution. The distribution is more pronounced in the forward direction. This shows a definite trend in rejecting those particles produced in the backward region due to the spectrometer's limited acceptance region. (c) is the x_f distribution plotted in the center of mass system. This distribution generally follows the same qualitative behavior of (b).

9.2.2 Minimum Bias PYTHIA

A Monte Carlo PYTHIA program was run in order to determine how well PYTHIA predicts actual experimentally observed physics processes. As previously discussed in Chapter 5, PYTHIA may be manipulated to simulate different types of events, such as minimum bias events, charm enhanced events, or beauty enhanced events. A minimum bias program, designed to run only on those events that contained at least two muons as the trigger mechanism, was written in order to incorporate the Monte Carlo's random generation process with specially imposed restrictions.

A PYTHIA generated event steps through a process of muon identification. Once a muon is tagged, the program determines whether it had enough energy to penetrate the iron and concrete shieldings in order to form a triple coincidence in the three RPC chambers. The event searches for another muon and determines if that one also made it past the RPC hit criteria. If there are two muons that meet these criteria, the event is accepted as a double muon triggered event, and we continue with the event by looking for the V° particles. The V° particle is

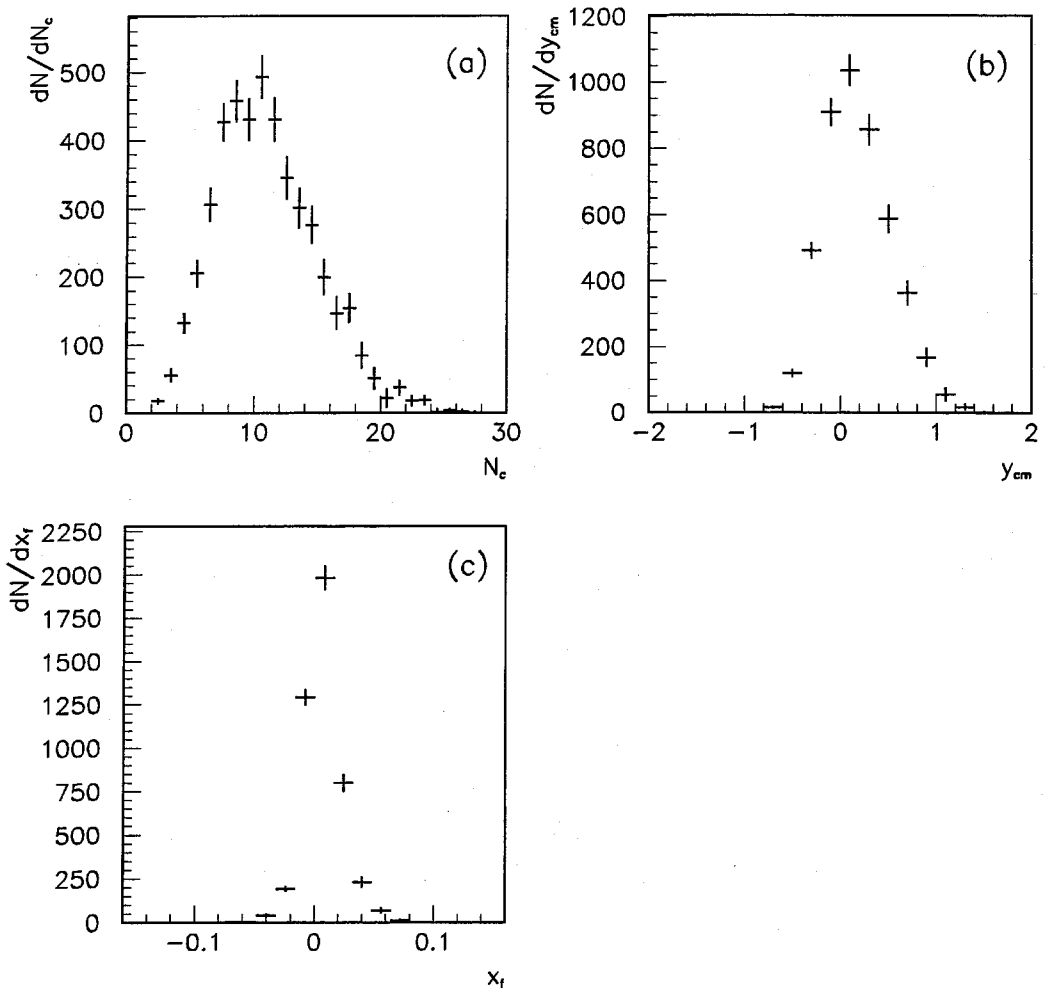

Figure 9.7: (a) N_c, (b) y_{cm}, and (c) center of mass x_f distributions for the K° from double muon triggered events. The distributions are not corrected for full spectrometer acceptance.

simulated to pass through the spectrometer region. It encounters the magnet where it experiences a p_t kick sending it along its new trajectory to traverse the rear chambers. The program checks to see that each track of the event hits at least three chamber planes upstream of the analysis magnet and at least three chamber planes downstream of the analysis magnet. If two tracks of a generated V° pass the front and rear chamber hit criteria, the event is accepted and its relevant information plotted or put in counters for later use. The information used from PYTHIA for data comparison purposes consisted of calculating the average multiplicity value for all events irrespective of whether or not the event contained a K°, the number of K°'s generated (i.e., the particle was PYTHIA produced but may not have necessarily passed through the spectrometer acceptance region), the number of K°'s generated per event, and the average p_t.

9.2.3 Comparison of Data to PYTHIA

Table 9.1 shows a comparison of PYTHIA events to real data events for the study of K° produced particles for a double muon triggered minimum bias run. The first column is the average multiplicity for an event that contained a K°. Due to the fact that PYTHIA consistently under predicts the multiplicity value, the requirement that a minimum bias run contain two muons as the trigger for an event has no influence on the final outcome, hence the big discrepancy between data and Monte Carlo. The second column is the average raw charged multiplicity for all events, and it does not take into account whether a K° was present. The third column is the average number of K°'s generated ("generated" in the experimental data's

viewpoint is overlay corrected for 4π acceptance) per raw charged multiplicity. PYTHIA predicts approximately twice that of what is observed experimentally. The fourth column is the average number of K°'s generated per event. PYTHIA predicts a value slightly smaller than what was experimentally observed. The last column is the $< p_t >$ for the K°. PYTHIA agrees with data's value.

	$< N >_{K^\circ}$	$< N >_{evt}$	$< \frac{K_s^\circ(gen)}{N_{all}} >$	$< \frac{K_s^\circ(gen)}{evt} >$	$< p_t >_{K_s^\circ}$ (GeV)
PYTHIA	4.6 ± 0.1	3.72 ± 0.04	0.07990 ± 0.00001	0.29 ± 0.06	0.54 ± 0.04
DATA	11.5 ± 0.3	9.536 ± 0.004	0.042 ± .004	0.399 ± 0.038	0.525 ± 0.011

Table 9.1: Comparison of minimum bias double muon triggered PYTHIA generated events and data events for K° produced particles.

Following the same convention as the single muon triggered events, PYTHIA and data are in relatively good agreement for some values, while they have big deviations for others. PYTHIA is good at predicting the $< p_t >$ and (N_{V°/evt), but it consistently under counts the charged particle multiplicity.

9.3 Raw Λ° Events, Overlay Efficiency, Corrected Λ° Acceptance

The procedures that will be described for fitting the Λ° events, for calculating the overlay efficiency, and for obtaining the corrected Λ° acceptances are the same as those employed for the single muon triggered events.

A comparison of the single muon triggered events and the double muon trig-

gered events produces relatively approximate mass distributions with more statistics in the Λ° mass distribution for the double muon triggered events. Shown in Figure 9.8 is a sample of the Λ° mass distribution plots for various z-decay and $|\Delta z|$ cuts. The Λ° mass distribution is for all track pairs, irrespective of whether or not they were coplanar, where a coplanar event satisfied

$$cos(\theta) = \frac{(\vec{V} \times \vec{a}) \cdot (\vec{b} \times \vec{V})}{|\vec{V} \times \vec{a}||\vec{b} \times \vec{V}|} \geq 0.95. \tag{9.9}$$

$\vec{V}$ is the parent particle vector, and $\vec{a}$ and $\vec{b}$ are the first and second decay product vectors.

The first row of plots is the mass distribution for a fixed z-decay length greater than 5 *cm* from the main interaction vertex, while the progression of columns is for tighter cuts on the $|\Delta z|$. The second row is the mass distribution for a fixed z-decay length greater than 10 *cm* from the main interaction vertex, and the columns are for $|\Delta z|$ cuts $\leq$ 40 *cm*, $\leq$ 30 *cm*, $\leq$ 20 *cm*, and $\leq$ 10 *cm*, respectively. The third and fourth rows are the mass distributions for fixed z-decay lengths greater than 30 *cm* and 50 *cm*, respectively, from the main interaction, and the columns are for the same $|\Delta z|$ cuts at those described for the second row of plots. The combination of tighter cuts increases the signal peak, thus increasing the signal to noise ratio which leads to a better fit for the mass distribution.

Figure 9.9 follows the same convention as that described for Figure 9.8 with the added condition that the tracks be coplanar. A comparison of the two figures shows a significant improvement of the signal to noise ratio.

Figure 9.10 is the raw number of Λ°'s plotted as a function of the $|\Delta z|$ cuts, where the numbers were extracted by fitting the various mass distributions. The

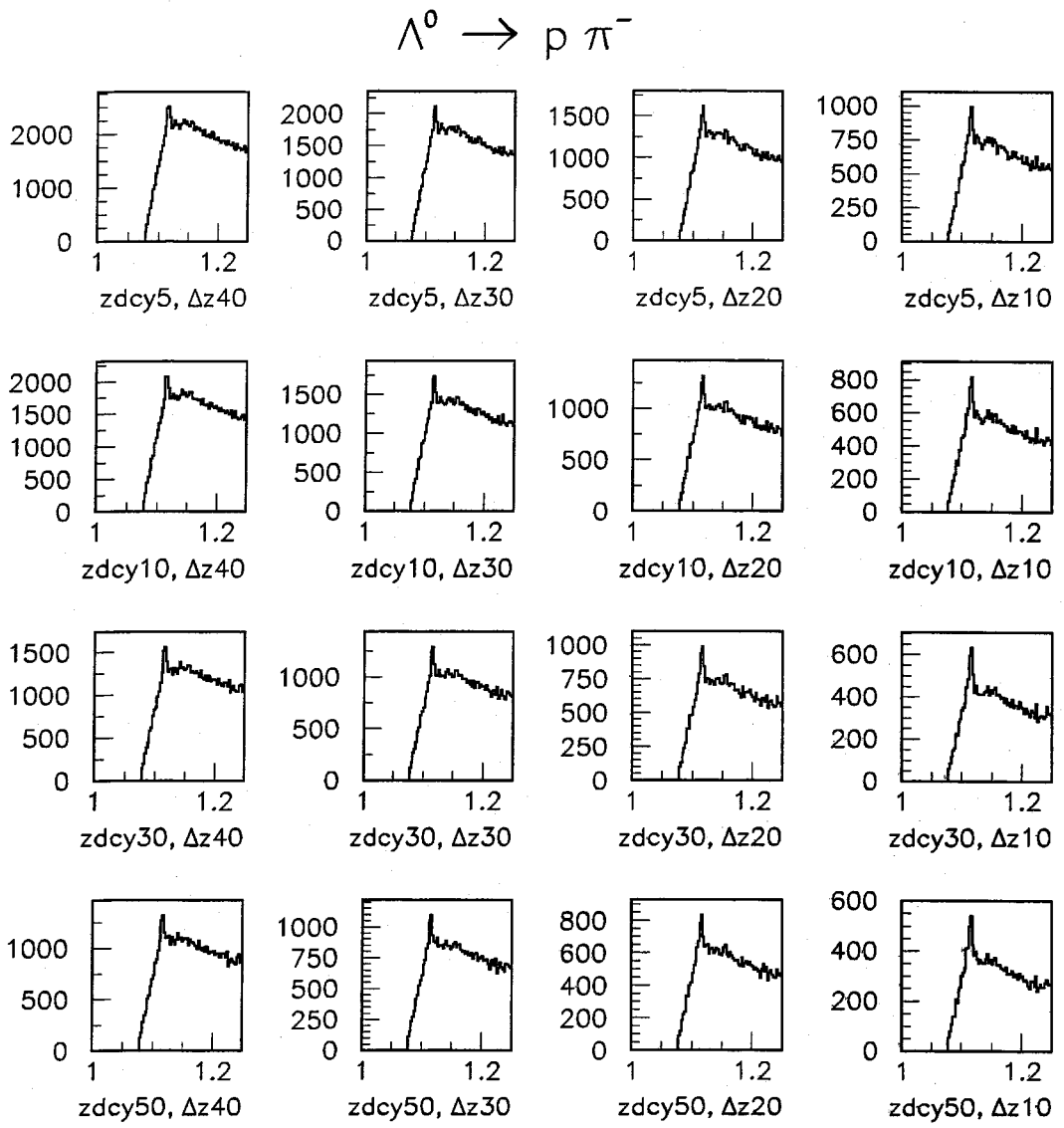

Figure 9.8: Λ° mass distributions from double muon triggered events for different z-decay and $|\Delta z|$ cuts, with no coplanarity cut imposed. Each horizontal scale is the mass value in GeV/c^2, and each vertical scale is the number of pairs per 2.5 MeV/c^2.

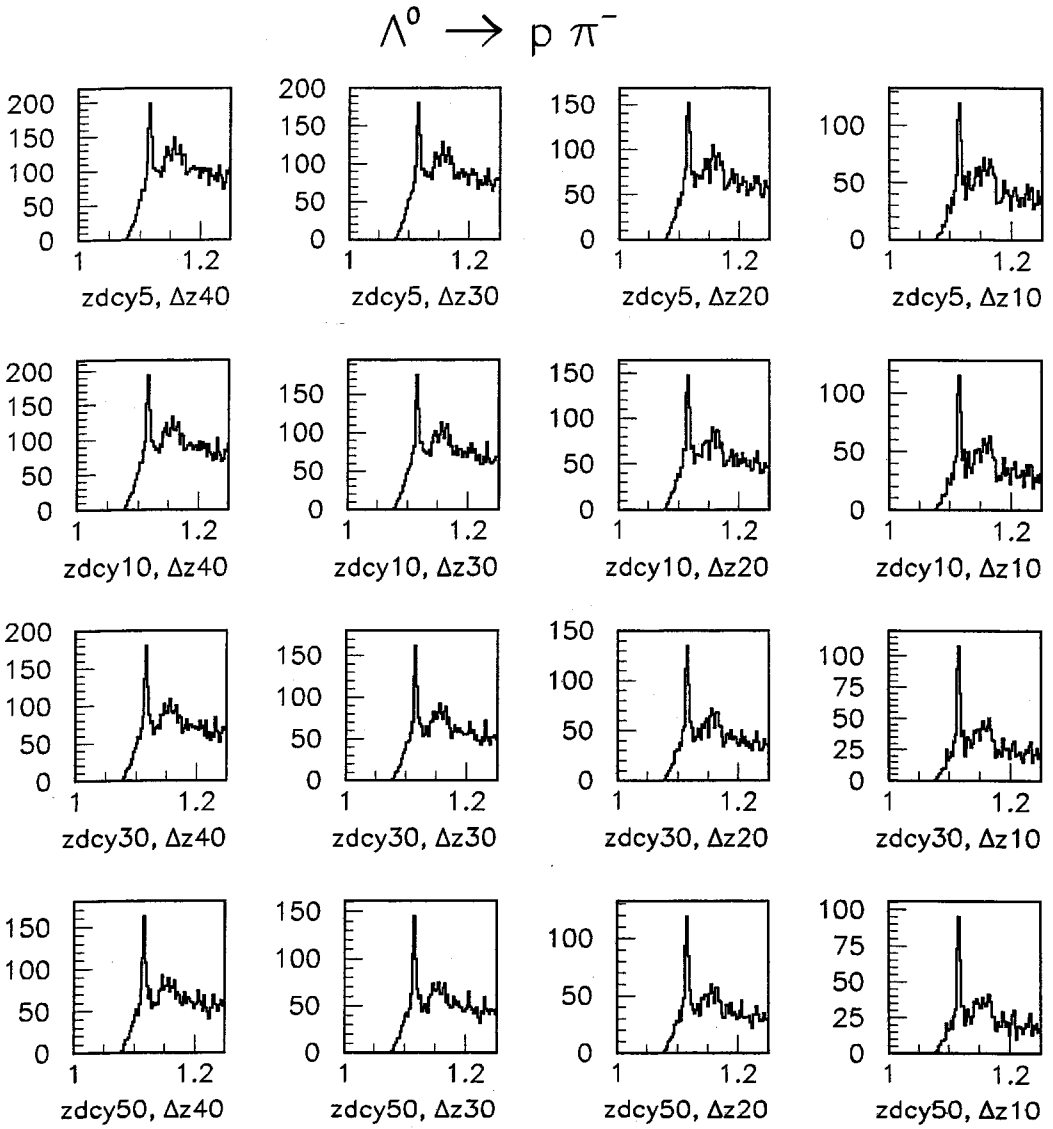

Figure 9.9: Λ° mass distributions from double muon triggered events for different z-decay and $|\Delta z|$ cuts, with a coplanarity cut imposed. Each horizontal scale is the mass value in GeV/c^2, and each vertical scale is the number of pairs per 2.5 MeV/c^2.

lines drawn through the sets of different symbols refer to the different z-decay values. The looser the $|\Delta z|$ cut is, e.g., $\leq 40\ cm$, and the closer the decay vertex of the Λ° is to the main interaction vertex, the more Λ°'s are produced, but there is also the increased background. This plot includes a set of lines for those tracks where a coplanarity cut was implemented and another shows those tracks where it was not implemented. There is a greater fluctuation in the raw number of Λ°'s counted for those tracks where no coplanarity cut was required, whereas those tracks that were required to be coplanar show a much smaller perturbation.

Figure 9.11 is the overlay efficiency for tracking an event within a specific cut interval as a function of $|\Delta z|$, where the lines, dashes, dots, and dot-dashes joining their respective symbols are the different z-decay cuts from the main interaction vertex. The overlay efficiency for tracking Λ° events is much smaller than that for the K°'s, ranging from a minimum of 0.24% to a maximum of 0.70%, and the K° overlay efficiency ranges from 0.4% to 1.85%. This is indicative of the tremendous difficulty in tracking and reconstructing Λ°'s.

Figure 9.12 is a plot of the corrected number of Λ°'s, the ratio of the number of raw Λ° events to the overlay efficiency ($N_{\Lambda^\circ}/\epsilon$), versus the $|\Delta z|$ cuts. The symbols indicate the different z-decay cuts from the main interaction vertex. A definite discrepancy exists between those tracks that were required to meet the coplanarity criterion and those that were not. The coplanar track lines, although tending to have a lower systematic fluctuation than the non-coplanar track lines, ended up with a lower corrected number of Λ°'s. This may be attributed to the fact that the coplanar tracks originally contained a small amount of statistics, the

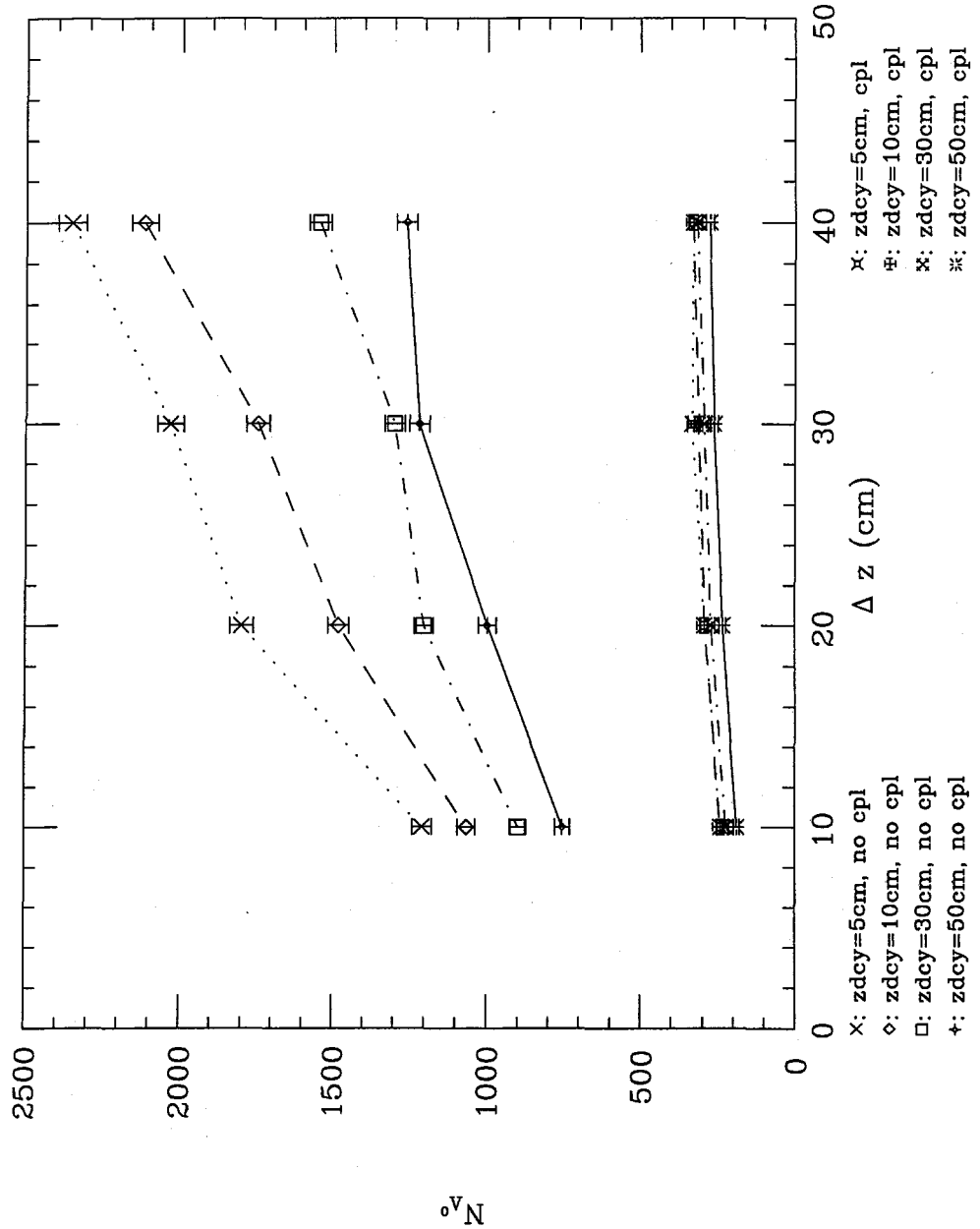

Figure 9.10: Total number of Λ^0's, N_{Λ^0}, as a function of $|\Delta z|$ and z-decay cuts. Shown are curves for coplanar tracks and curves for non-coplanar tracks.

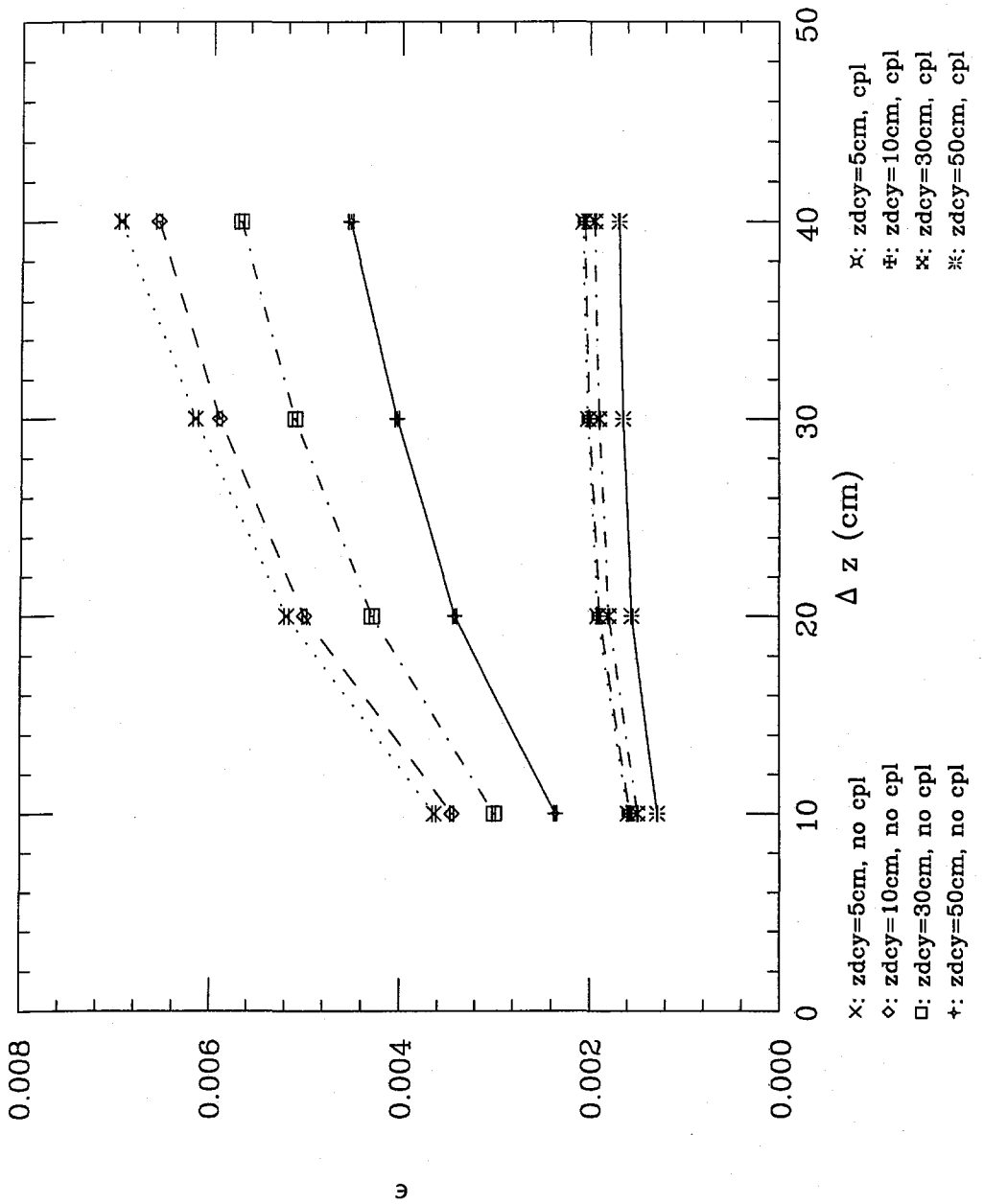

Figure 9.11: Overlay efficiency, ϵ, for tracking a Λ° as a function of $|\Delta z|$ and z-decay cuts. Shown are curves for coplanar tracks and curves for non-coplanar tracks.

overlay efficiency was too low, and the overlay tracking could not compensate for it. This could also mean that the coplanarity cut was too severe for the Λ°'s.

9.4 Λ° p_t, Multiplicity, Rapidity, and x_f Distributions

As one may be able to extract relevant Λ° characteristics from its $< p_t >$, N_c, y_{cm}, and x_f distributions, it is important to compare these to a theoretical model such as PYTHIA.

9.4.1 Data

As there was a different number of cuts applied to the mass spectrum in order to achieve the best signal/background ratio, a good p_t distribution was obtained. If the invariant mass of track pairs was within $\pm$ 10 MeV of the Λ° mass value, the p_t was plotted. As there existed a background distribution beneath the mass peak, a normalization and subtraction algorithm was implemented. The p_t distribution was plotted for events that had unlike sign tracks (signal plot, $N_\pm$) and like sign tracks (background plot, N_{LS}). The p_t distribution for the like sign tracks was normalized to the p_t distribution for the unlike sign tracks to obtain the proper background subtraction.

Figure 9.13 is the corrected p_t distribution. It is shown three times, each with a different fitted p_t function. The three different fitting functions are:

$$dN/dp_t = P1 \cdot p_t \cdot exp(-p_t \cdot P2), \tag{9.10}$$

$$dN/dp_t = P1 \cdot p_t \cdot exp(-\sqrt{p_t^2 + m^2}/P2), \tag{9.11}$$

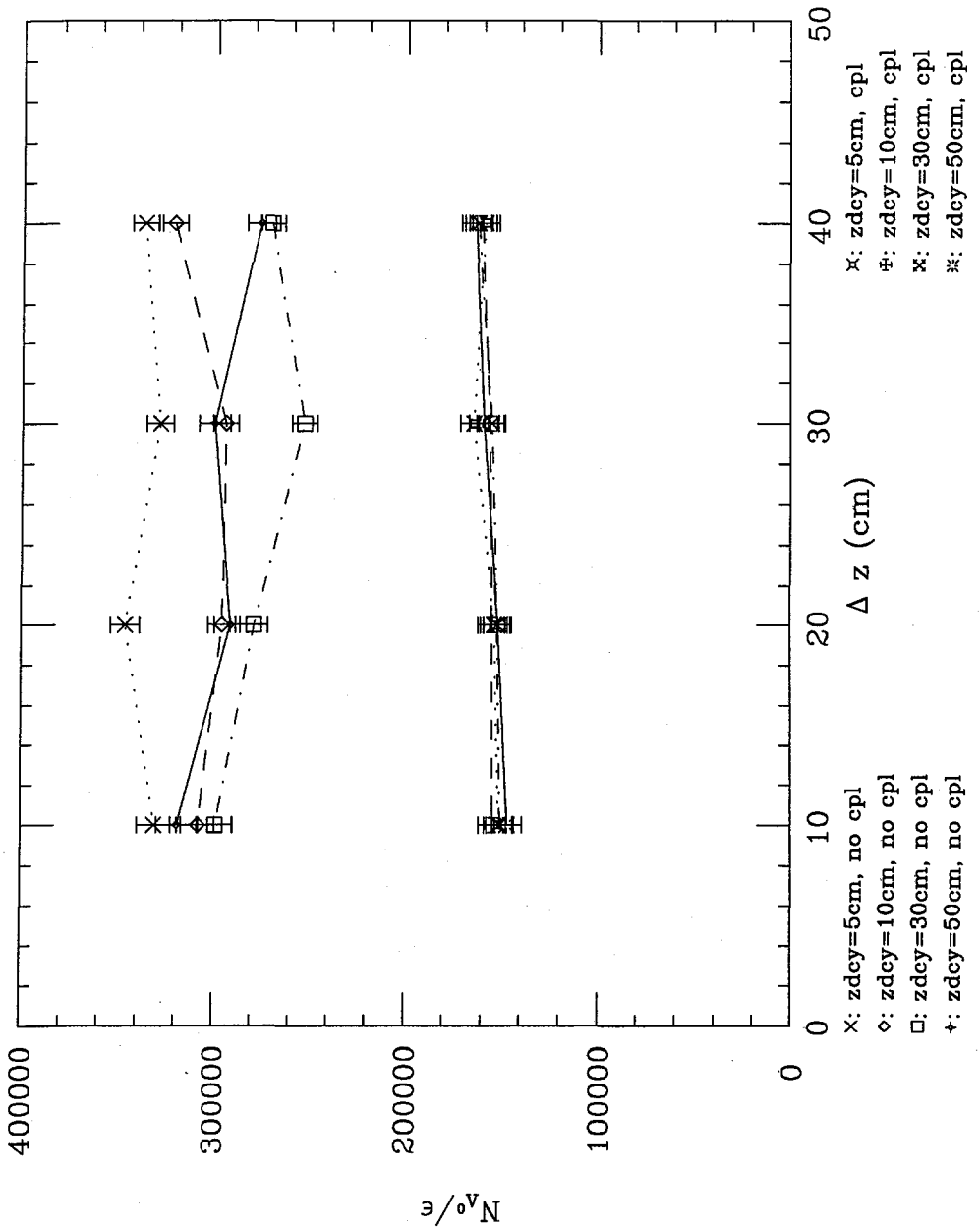

Figure 9.12: Corrected number of Λ^0's, N_{Λ^0}/ϵ, as a function of $|\Delta z|$ and z-decay cuts. Shown are curves for coplanar tracks and curves for non-coplanar tracks.

$$dN/dp_t = (P1 \cdot p_t)/(p_t + P2)^{P3}. \tag{9.12}$$

$P1$, $P2$, and $P3$ are the fitted parameter values obtained from each of the individual fits. (a) is the Λ° p_t distribution using Equation (9.10) as a fit, where $P1$ and $P2$ are the fitted parameters for this exponential function. (b) is the Λ° p_t distribution using Equation (9.11) as a fit, where $P1$ and $P2$ are the fitted parameters for this function involving the transverse energy (thermal exponential fit). (c) is the Λ° p_t distribution using Equation (9.12) as a fit, where $P1$, $P2$, and $P3$ are the fitted parameters for this function.

Each of the three different fitting functions yields similar values for the $< p_t >$, and the greatest discrepancy between the values is 0.251 GeV/c. The Λ° $< p_t >$ value, averaging for all three fitting algorithms is

$$< p_t > = 0.64 \pm 0.11 \text{ GeV/c},$$

where the systematic error is the *rms* deviation in the three fits. The power law fit to the p_t distribution gives a smaller $< p_t >$ value than does the two exponential function fits.

The three different fits used to get the average p_t values were model dependent and did not look at the low p_t region. This was explained by the fact that the low p_t particles were lost when simulated to traverse E771's spectrometer region. An alternative for getting the average p_t was to average directly the p_t values for the whole distribution as the final p_t distribution was corrected for the spectrometer acceptance. The procedure was the same as that used for getting the three model dependent $< p_t >$ values. That is, one had to normalize the background p_t distribution to the signal p_t distribution in order to perform the proper subtraction

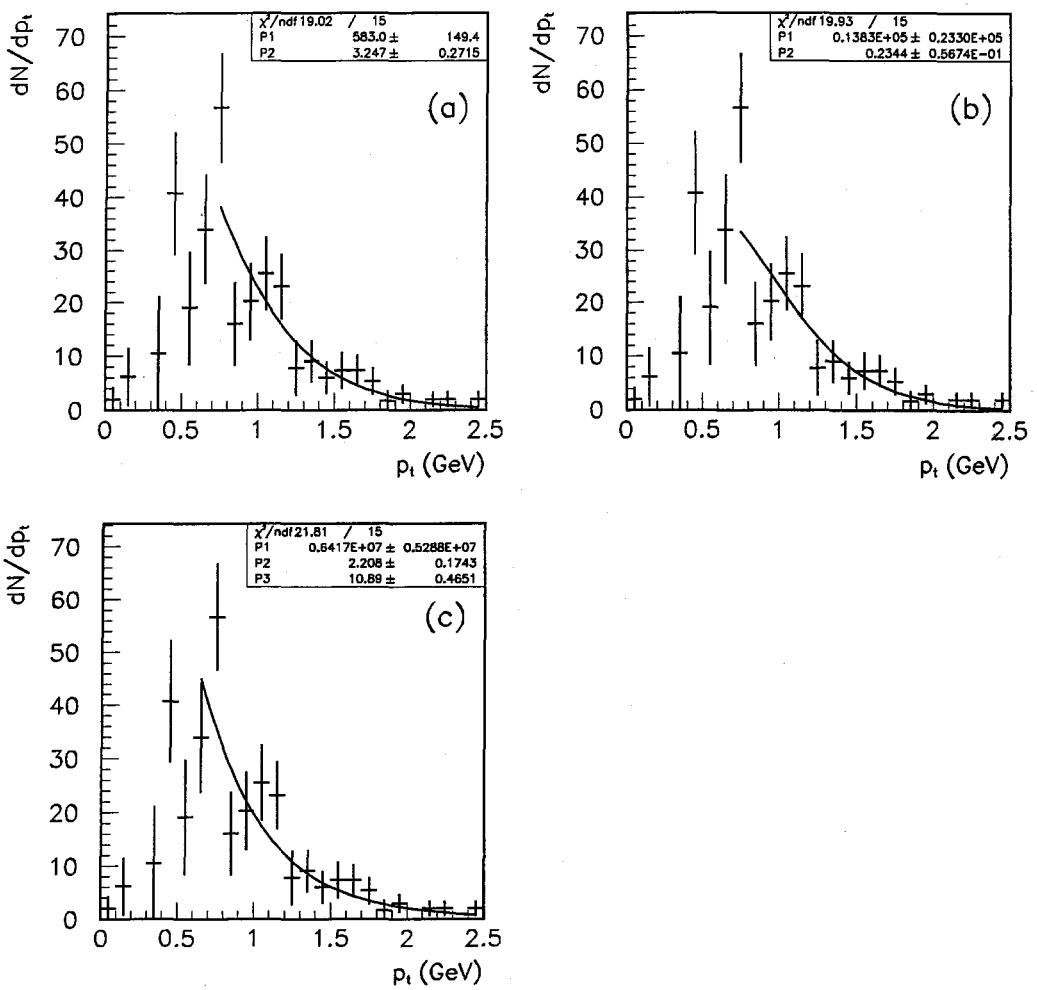

Figure 9.13: Λ° p_t distribution from double muon triggered events, same plot shown three times for each of three different fitting functions. (a) uses Equation (9.10) as the fit, (b) uses Equation (9.11) as the fit, and (c) uses Equation (9.12) as the fit.

to get the correct p_t distribution. The distribution had to be overlay corrected for losses at small p_t. Then the simple average of the corrected p_t distribution was formed without performing any fitting procedures. The $< p_t >$ value obtained for the Λ°'s using this method was

$$< p_t >=0.77\pm0.15\ GeV/c.$$

It is noted that the latter procedure used to fit the $< p_t >$ yielded a higher value than that obtained from the three different fits. This is explainable by the fact that the power law fit described above generally gave a lower value than did the other two fits.

The multiplicity, rapidity, and Feynman-x distributions were all obtained the same way the p_t distribution was. That is, those events that were within $\pm$ 10 MeV of the Λ° mass peak were retained and their respective distributions plotted, such as N_c, y_{cm}, and x_f. The true distribution was obtained by normalization and correcting for background.

The rapidity is defined in the laboratory frame to be

$$y_{lab} = \frac{1}{2}ln(\frac{E+P_l}{E-P_l}). \tag{9.13}$$

A transformation is performed to convert to the center of mass system,

$$y_{tx} = \frac{1}{2}ln(\frac{1-\beta_{cm}}{1+\beta_{cm}}), \tag{9.14}$$

so in the center of mass system

$$y_{cm} = y_{lab} + y_{tx}. \tag{9.15}$$

E is the particle energy and P_l its longitudinal momentum.

$$\beta_{cm} = P_{beam}/(\sqrt{P_{beam}^2 + m_p^2} + m_p),$$

where P_{beam} is the beam momentum and m_p the proton mass.

Feynman's x variable, x_f, in the center of mass system, is defined as

$$x_f = \frac{2 \cdot p_{z(cm)}}{\sqrt{s}}, \tag{9.16}$$

where $p_{z(cm)} = \gamma_{cm} \cdot (P_z - \beta_{cm} \cdot E)$.

Figure 9.14 shows the Λ° N_c, y_{cm}, and x_f distributions for the double muon triggered events. (a) is a distribution of the charged particle multiplicity, with $< N_c > = 12.1 \pm 1.3$. (b) is the rapidity distribution in the center of mass system. The rapidity distribution is more pronounced in the forward direction, indicative of the loss of events in the backward region due to the restricted spectrometer acceptance region. (c) is the center of mass x_f distribution. This distribution follows the same qualitative behavior as the rapidity distribution.

9.4.2 Minimum Bias PYTHIA

A Monte Carlo PYTHIA program was run in order to determine how well PYTHIA predicts actual experimentally observed physics processes. As previously discussed in Chapter 5, PYTHIA may be manipulated to simulate different types of events, such as minimum bias events, charm enhanced events, or beauty enhanced events. A minimum bias program, designed to run only on those events that contained at least two muons as the trigger mechanism, was written in order to incorporate the Monte Carlo's random generation process with specially imposed restrictions.

A PYTHIA generated event steps through a process of muon identification. Once a muon is tagged, the program determines whether it had enough energy to

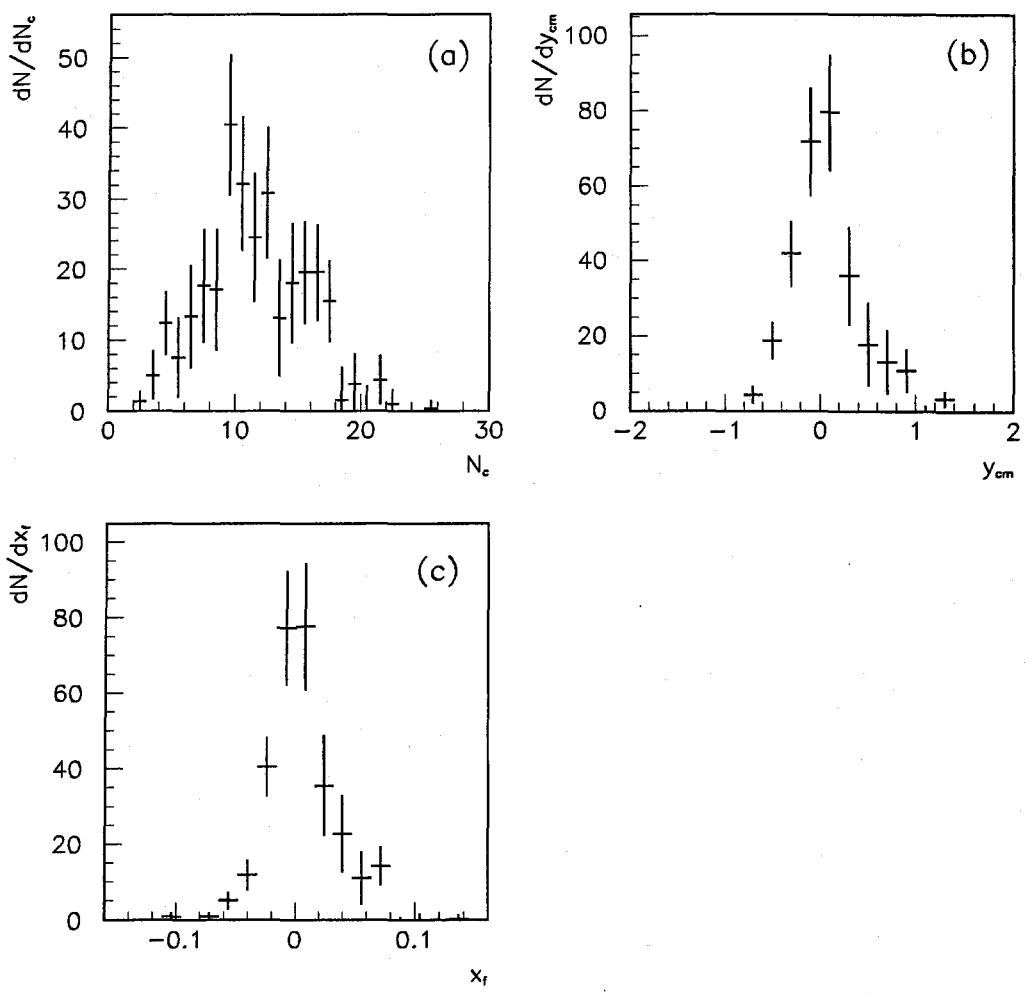

Figure 9.14: (a) N_c, (b) y_{cm}, and (c) center of mass x_f distributions for the Λ° double muon triggered events. These distributions are not corrected for full spectrometer acceptance.

penetrate the iron and concrete shieldings in order to form a triple coincidence in the three RPC chambers. The event searches for another muon and determines if that one also made it past the RPC hit criteria. If there are two muons that meet these criteria, the event is accepted as a double muon triggered event, and we continue with the event by looking for the Λ° particles. The Λ° particle is simulated to pass through the spectrometer region. It encounters the magnet where it experiences a p_t kick sending it along its new trajectory to traverse the rear chambers. The program checks to see that each track of the event hits at least three chamber planes upstream of the analysis magnet and at least three chamber planes downstream of the analysis magnet. If two tracks of a generated Λ° decay pass the front and rear chamber hit criteria, the event is accepted and its relevant information plotted or put in counters for later use. The information used from PYTHIA for data comparison purposes consisted of calculating the average multiplicity value for all events irrespective of whether or not the event contained a Λ°, the number of Λ°'s generated (i.e., the particle was PYTHIA produced but may not have necessarily passed through the spectrometer acceptance region), the number of Λ°'s generated per event, and the average p_t.

9.4.3 Comparison of Data to PYTHIA

Table 9.2 shows a comparison of PYTHIA events to real data events for the study of Λ° produced particles for a double muon triggered minimum bias run. The first column of the table is the average multiplicity for an event that contained a Λ°. Due to the fact that PYTHIA consistently under predicts the multiplicity

value, the requirement that a minimum bias run contain two muons as the trigger for an event has no influence on the final outcome, hence the big discrepancy between data and Monte Carlo. The second column is the average raw charged multiplicity for all events, and it does not take into account whether a Λ° was present. The third column is the average number of Λ°'s generated ("generated" in the experimental data's viewpoint is overlay corrected for 4π acceptance) per raw charged multiplicity. PYTHIA predicts approximately twice that of what is observed experimentally. The fourth column is the average number of Λ°'s generated per event. PYTHIA's prediction agrees quite well with data's result. The last column is the $< p_t >$ for the Λ°, and PYTHIA is within the error of the value obtained for data.

	$< N >_{\Lambda^\circ}$	$< N >_{evt}$	$< \frac{\Lambda^\circ(gen)}{N_{all}} >$	$< \frac{\Lambda^\circ(gen)}{evt} >$	$< p_t >_{\Lambda^\circ}$ (GeV)
PYTHIA	4.1 ± 0.5	3.72 ± 0.04	0.0382 ± 0.00001	0.14 ± 0.04	0.746 ± 0.323
DATA	12.1 ± 1.3	9.536 ± 0.004	0.01796 ± .00176	0.1712 ± 0.0167	0.616 ± 0.052

Table 9.2: Comparison of minimum bias double muon triggered PYTHIA generated events and data events for Λ° produced particles.

Excluding PYTHIA's predictions for the charged particle multiplicity, other values compared to data, such as p_t, are in agreement.

9.5 Raw $\overline{\Lambda^\circ}$ Events, Overlay Efficiency, Corrected $\overline{\Lambda^\circ}$ Acceptance

The procedures that will be described for fitting the $\overline{\Lambda^\circ}$ events, for calculating the overlay efficiency, and for obtaining the corrected $\overline{\Lambda^\circ}$ acceptances are the same as those employed for the single muon triggered events.

Compared to the single muon triggered events, the double muon triggered events accumulated slightly more statistics due to the higher number of double muon triggered events tracked, and so the distribution plots are of the same qualitative behavior as those for the single muon triggered events. Figure 9.15 shows the $\overline{\Lambda^\circ}$ mass distribution for different z-decay and $|\Delta z|$ cuts. The first through fourth rows show the mass distribution for z-decay cuts greater than 5 cm, 10 cm, 30 cm, and 50 cm, respectively, while the first through fourth columns show the mass distribution for $|\Delta z|$ cuts $\leq$ 40 cm, $\leq$ 30 cm, $\leq$ 20 cm, and $\leq$ 10 cm, respectively. Thus, the first row first column plot, for z-decay greater than 5 cm and $|\Delta z|$ less than 40 cm is the one with the loosest cuts. The mass peak is difficult to observe in this case, but becomes a bit more visible as the cuts are made tighter. The plots contained all tracks, irrespective of whether they were coplanar, coplanarity being

$$cos(\theta)\frac{(\vec{V}\times\vec{a})\cdot(\vec{b}\times\vec{V})}{|\vec{V}\times\vec{a}||\vec{b}\times\vec{V}|} \geq 0.95. \tag{9.17}$$

$\vec{V}$ is the parent particle vector, and $\vec{a}$ and $\vec{b}$ are the first and second decay product vectors.

Figure 9.16 follows the same convention as that described for Figure 9.15 with

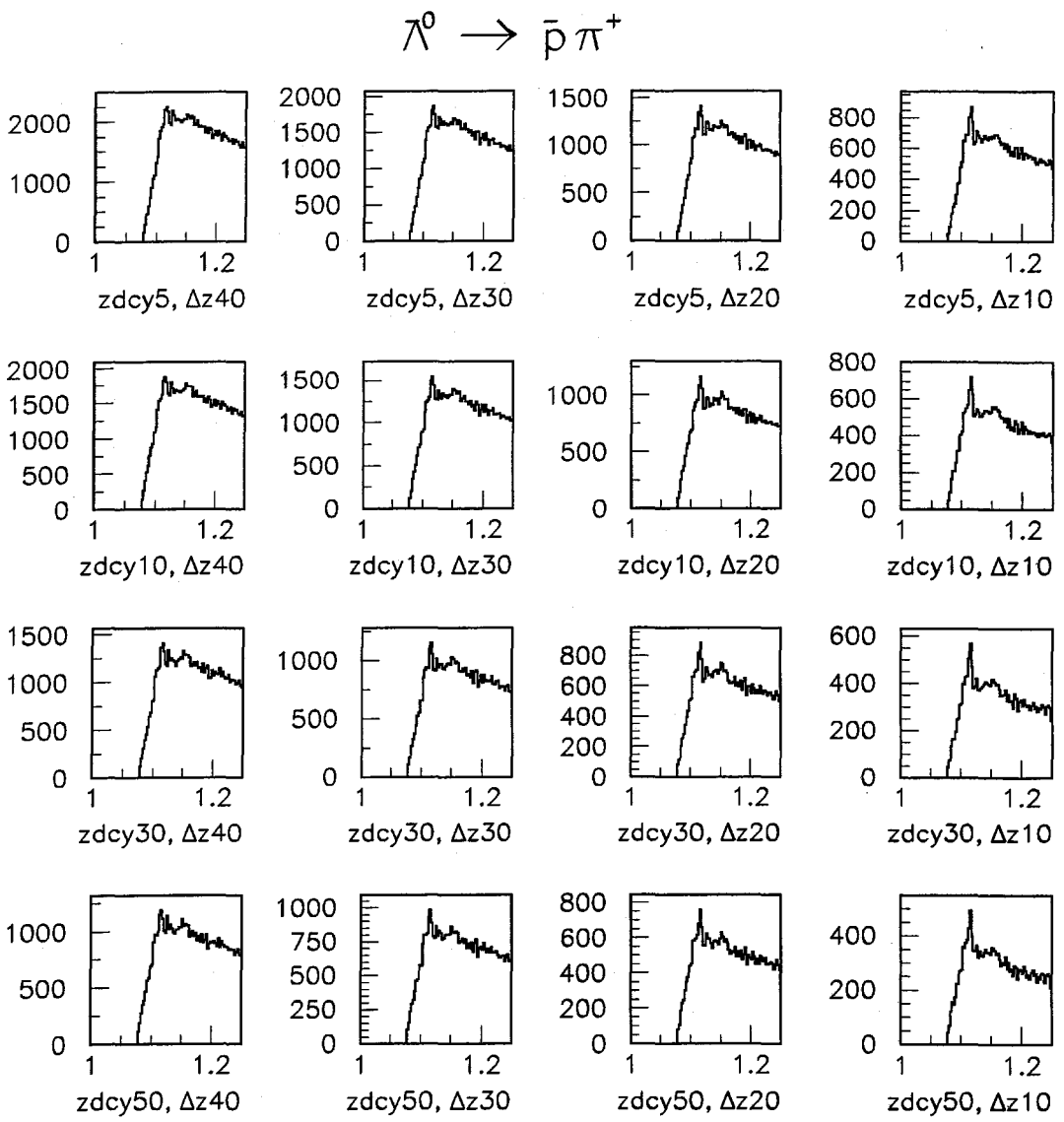

Figure 9.15: $\overline{\Lambda^\circ}$ mass distributions from double muon triggered events for different z-decay and $|\Delta z|$ cuts, with no coplanarity criterion imposed. Each horizontal scale is the mass value in GeV/c^2, and each vertical scale is the number of pairs per 2.5 MeV/c^2.

the added condition that the tracks be coplanar. A comparison of the two figures shows a more pronounced signal peak, therefore increasing the signal to noise ratio.

The significance of Figures 9.15 and 9.16 is brought out by observing the number of $\overline{\Lambda^\circ}$'s produced, by calculating the overlay tracking efficiency for $\overline{\Lambda^\circ}$ acceptance, and by calculating the corrected number of $\overline{\Lambda^\circ}$'s using the overlay efficiency number. In this context, Figure 9.17 is the raw number of $\overline{\Lambda^\circ}$ as a function of $|\Delta z|$ cuts. The lines drawn through sets of different symbols refer to the different z-decay values. The looser the $|\Delta z|$ cut is, and the closer to the main interaction vertex the decay of the $\overline{\Lambda^\circ}$, the more $\overline{\Lambda^\circ}$'s are produced, yet the background is also great. Contained in this plot are sets of lines pertaining to different classes of z-decay cuts for both coplanar and non-coplanar tracked events. Examination of the plot shows the coplanar tracks yielding small variations in numbers for the number of $\overline{\Lambda^\circ}$'s seen, whereas those tracks that did not require coplanarity had high deviations.

The overlay efficiency for tracking an event within a specified cut interval is shown in Figure 9.18. The overlay efficiency is plotted as a function of $|\Delta z|$, where the lines, dashes, dots, and dot-dashes joining the different symbols are the different z-decay cuts from the main interaction vertex. The overlay efficiency for tracking $\overline{\Lambda^\circ}$ events is quite small, ranging from a minimum of 0.24% to a maximum of 0.72%, comparable to those extracted for the Λ°'s. The quoted efficiency values were for tracks where no coplanarity criterion was imposed.

Figure 9.19 is the corrected number of $\overline{\Lambda^\circ}$'s, where the corrected number of $\overline{\Lambda^\circ}$'s

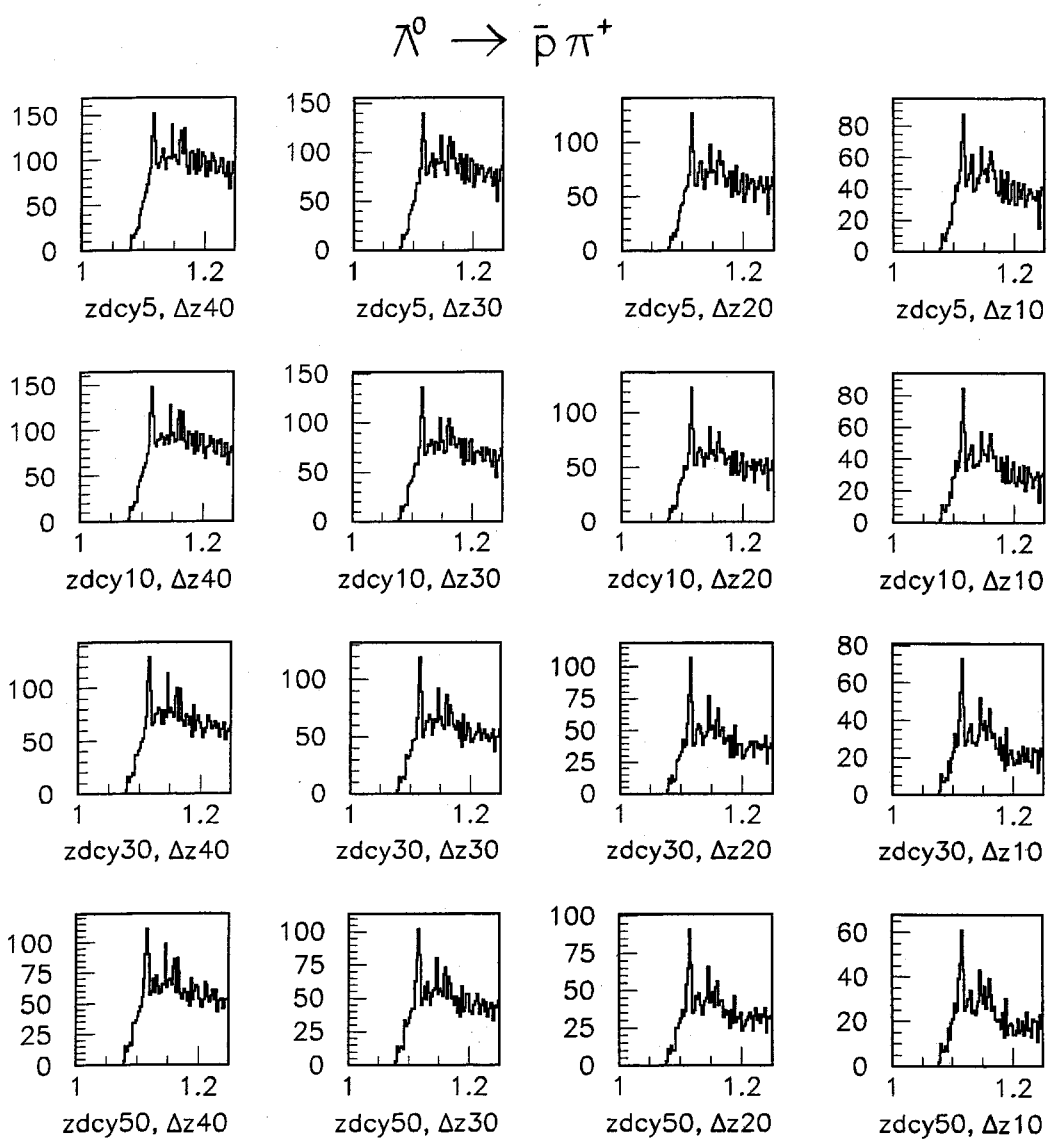

Figure 9.16: $\overline{\Lambda^\circ}$ mass distributions from double muon triggered events for different z-decay and $|\Delta z|$ cuts, with a coplanarity criterion imposed. Each horizontal scale is the mass value in GeV/c^2, and each vertical scale is the number of pairs per 2.5 MeV/c^2.

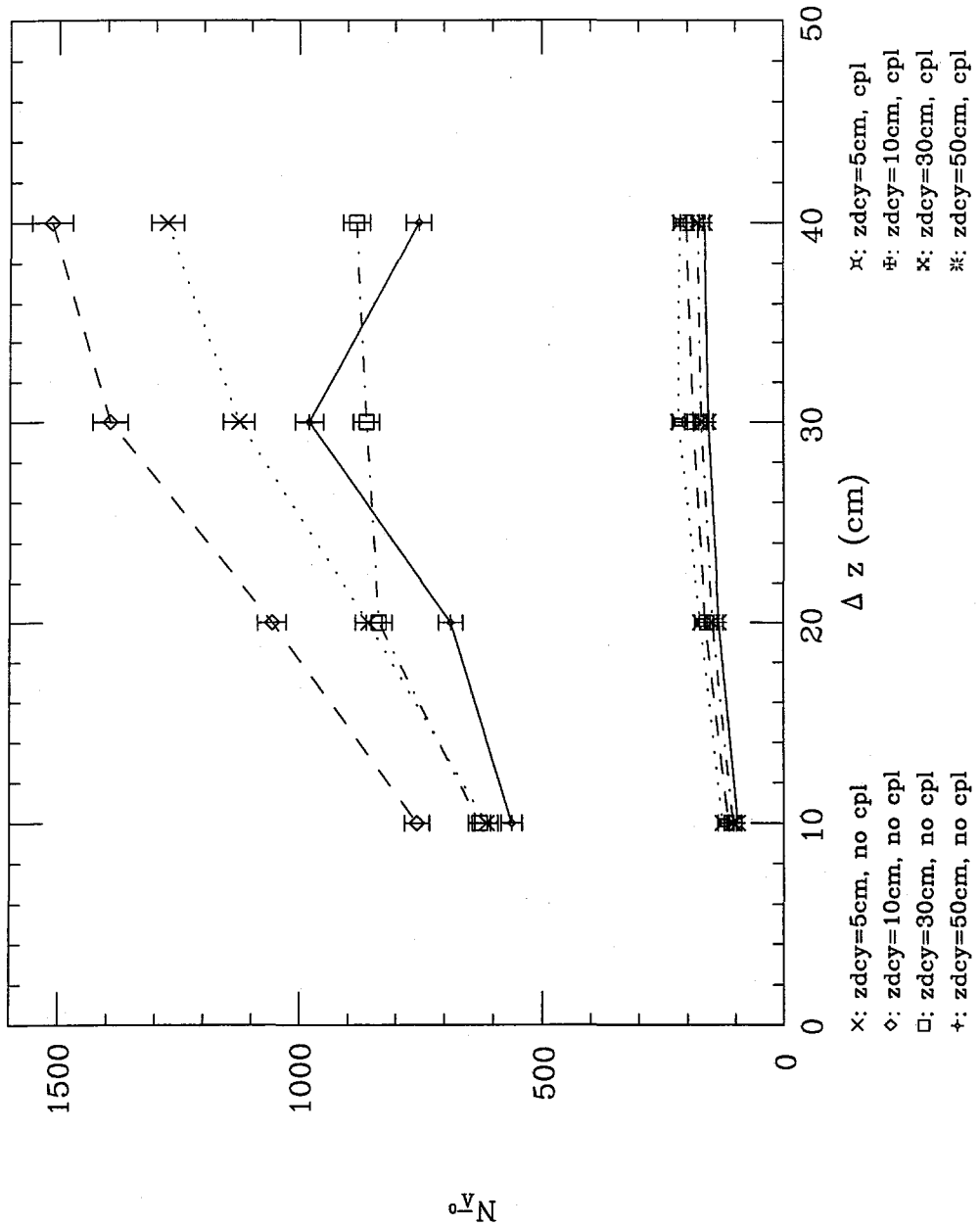

Figure 9.17: Total number of $\overline{\Lambda^o}$, $N_{\overline{\Lambda^o}}$, as a function of $|\Delta z|$ and z-decay cuts. Shown are curves for coplanar tracks and curves for non-coplanar tracks.

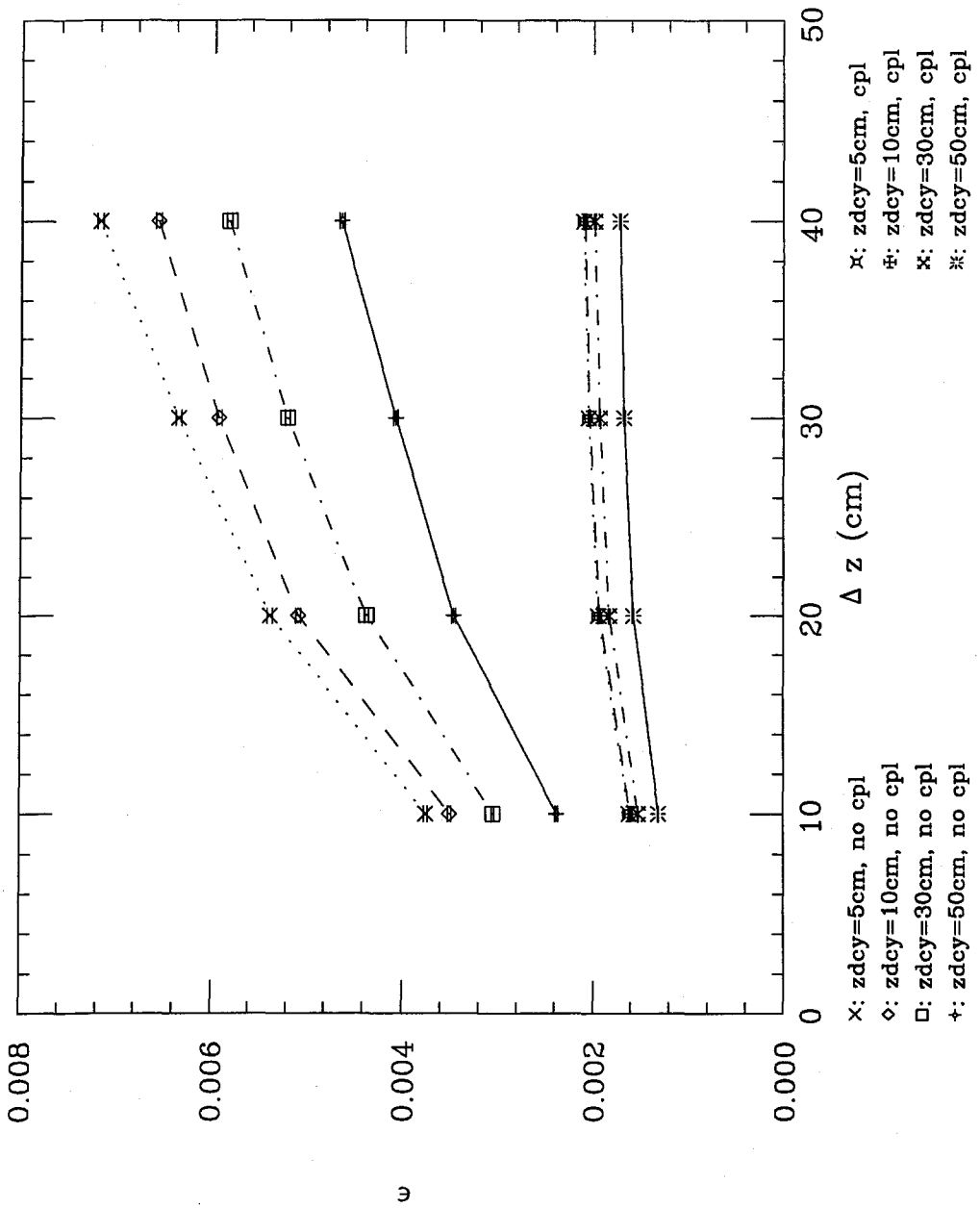

Figure 9.18: Overlay efficiency, ϵ, for tracking a $\overline{\Lambda^\circ}$ as a function of $|\Delta z|$ and z-decay cuts. Shown are curves for coplanar tracks and curves for non-coplanar tracks.

is achieved by taking the ratio of the raw number of $\overline{\Lambda^\circ}$'s to the overlay efficiency, versus the $|\Delta z|$ cuts. The individual plotted symbols are for different z-decay cuts from the main interaction vertex. A much larger fluctuation occurs for those tracks where no coplanarity was required, whereas those tracks that were required to be coplanar yielded much better agreements, thus confirming that performing fits on distributions where the signal to noise ratio is large produces less erroneous results.

9.6 $\overline{\Lambda^\circ}$ p_t, Multiplicity, Rapidity, and x_f Distributions

Important $\overline{\Lambda^\circ}$ characteristics from double muon triggered events, such as the p_t, N_c, y_{cm}, and x_f distributions, will be discussed, and their relevant extracted information will be compared to PYTHIA.

9.6.1 Data

As there was a different number of cuts applied to the mass spectrum in order to achieve the best signal/background ratio, a good p_t distribution was obtained. If the invariant mass of track pairs was within $\pm$ 10 MeV of the $\overline{\Lambda^\circ}$ mass value, the p_t was plotted. A background region existed beneath the mass peak, so a normalization and subtraction algorithm was implemented. The p_t distribution was plotted for events that had unlike sign tracks (signal plot, $N_\pm$) and like sign tracks (background plot, N_{LS}). The p_t distribution for the like sign tracks was normalized to the p_t distribution for the unlike sign tracks to obtain the proper background subtraction.

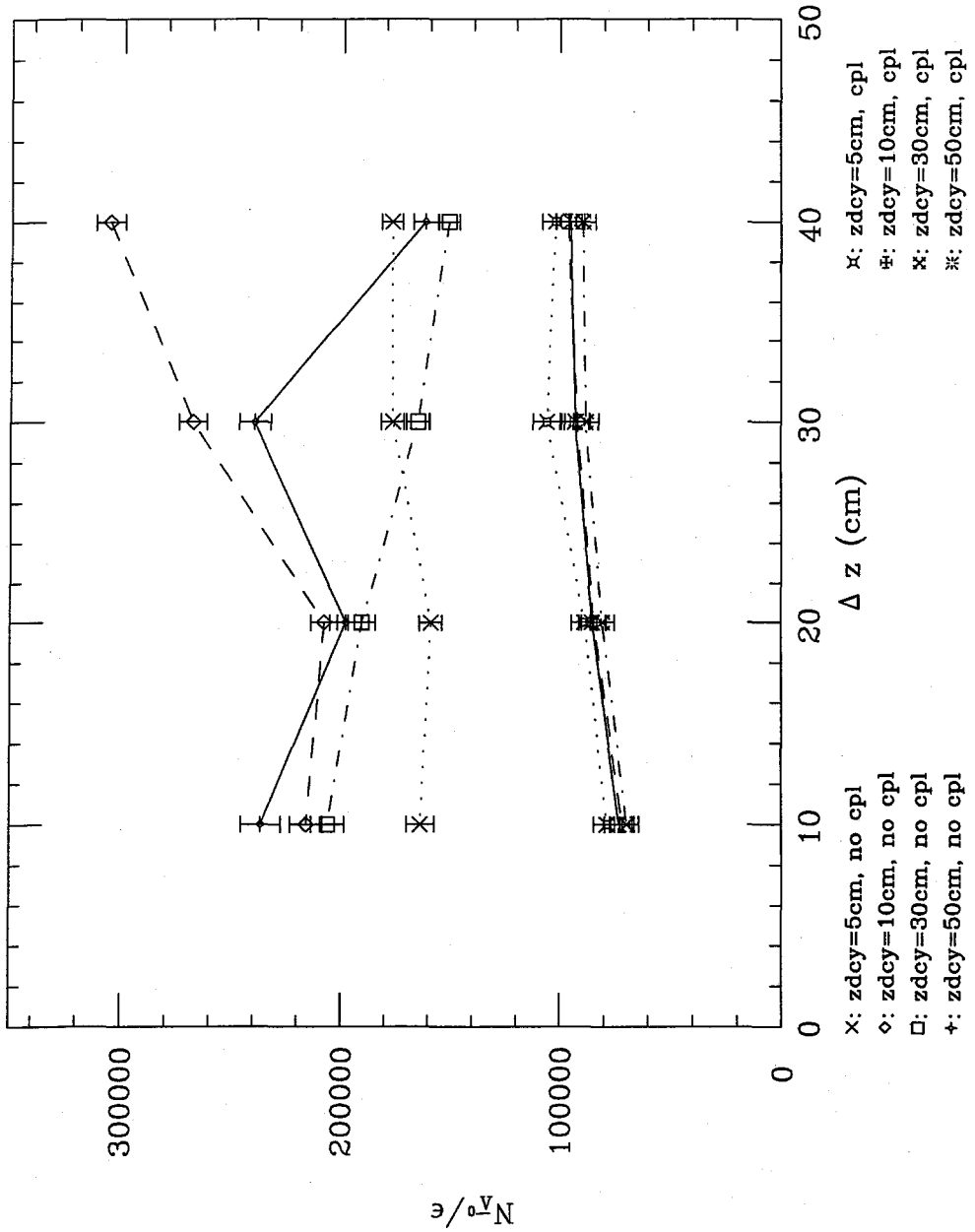

Figure 9.19: Corrected number of $\overline{\Lambda^0}$'s, $N_{\overline{\Lambda^0}}/\epsilon$, as a function of $|\Delta z|$ and z-decay cuts. Shown are curves for coplanar tracks and curves for non-coplanar tracks.

Figure 9.20 is the corrected p_t distribution. It is shown three times, each with a different fitted p_t function. The three different fitting functions are:

$$dN/dp_t = P1 \cdot p_t \cdot exp(-p_t \cdot P2), \tag{9.18}$$

$$dN/dp_t = P1 \cdot p_t \cdot exp(-\sqrt{p_t^2 + m^2}/P2), \tag{9.19}$$

$$dN/dp_t = (P1 \cdot p_t)/(p_t + P2)^{P3}. \tag{9.20}$$

$P1$, $P2$, and $P3$ are the fitted parameter values obtained from each of the individual fits. (a) is the $\overline{\Lambda^\circ}$ p_t distribution using Equation (9.18) as a fit, where $P1$ and $P2$ are the fitted parameters for this exponential function. (b) is the $\overline{\Lambda^\circ}$ p_t distribution using Equation (9.19) as a fit, where $P1$ and $P2$ are the fitted parameters for this function involving the transverse energy (thermal exponential fit). (c) is the $\overline{\Lambda^\circ}$ p_t distribution using Equation (9.20) as a fit, where $P1$, $P2$, and $P3$ are the fitted parameters for this function.

Each of the three different fitting functions yielded similar values for the $< p_t >$, and the greatest discrepancy between the values was 0.25 GeV/c. The $\overline{\Lambda^\circ}$ $< p_t >$ value, averaged for all three fitting algorithms was

$$< p_t > = 0.65 \pm 0.11 \text{ GeV/c},$$

where the systematic error was the *rms* deviation in the three fits. The two exponential fitting functions gave close $< p_t >$ values, but the power low fit proved on average to yield a lower $< p_t >$.

The three different fits used to get the average p_t values were model dependent and did not look at the low p_t region. This was explained by the fact that the low p_t particles were lost when simulated to traverse E771's spectrometer region. An

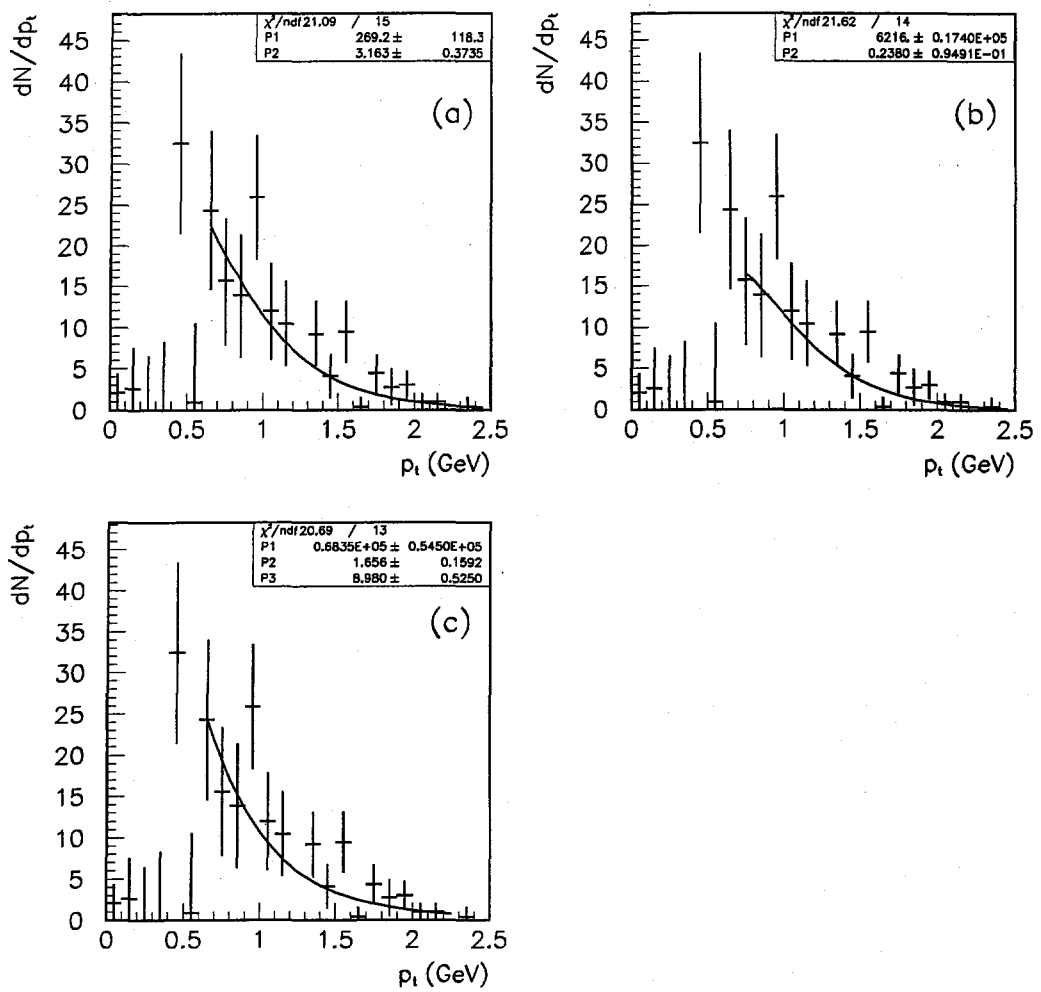

Figure 9.20: The $\overline{\Lambda^\circ}$ p_t distribution from double muon triggered events, same distribution shown three times for each of three different fitting functions. (a) uses Equation (9.18) as the fit, (b) uses Equation (9.19) as the fit, and (c) uses Equation (9.20) as the fit.

alternative for getting the average p_t was to average directly the p_t values for the whole distribution as the final p_t distribution was corrected for the spectrometer acceptance. The procedure was the same as that used for getting the three model dependent $< p_t >$ values. That is, one had to normalize the background p_t distribution to the signal p_t distribution in order to perform the proper subtraction to get the correct p_t distribution. The distribution had to be overlay corrected for losses at small p_t. Then the simple average of the corrected p_t distribution was formed without performing any fitting procedures. The $< p_t >$ value obtained for the $\overline{\Lambda^\circ}$'s using this method was

$$< p_t >=0.86\pm0.26\ GeV/c.$$

It is noted that the latter procedure used to fit the $< p_t >$ yielded a higher value than that obtained from the three different fits. This is explainable by the fact that the power law fit described above generally gave a lower value than did the other two fits.

The multiplicity, rapidity, and Feynman-x distributions were all obtained the same way the p_t distribution was. That is, those events that were within $\pm$ 10 MeV of the $\overline{\Lambda^\circ}$ mass peak were retained and their respective distributions plotted. The $\overline{\Lambda^\circ}$'s mass peak was fit with a Gaussian to the signal and a polynomial to the background. The ratio of signal to background was used as the normalization factor for the like sign tracked events for the "background" distribution. The normalized background distribution was then subtracted from the signal distribution in order to get the "true" distribution.

To obtain the center of mass rapidity distribution, we perform a transformation

on the laboratory rapidity distribution, where

$$y_{lab} = \frac{1}{2} ln(\frac{E + P_l}{E - P_l}), \tag{9.21}$$

and

$$y_{tx} = \frac{1}{2} ln(\frac{1 - \beta_{cm}}{1 + \beta_{cm}}). \tag{9.22}$$

In the center of mass system

$$y_{cm} = y_{lab} + y_{tx}. \tag{9.23}$$

E is the particle's energy and P_l its longitudinal momentum.

$$\beta_{cm} = P_{beam}/(\sqrt{P_{beam}^2 + m_p^2} + m_p),$$

where P_{beam} is the beam momentum and m_p the proton mass.

Feynman's x variable, x_f, in the center of mass system, is defined as

$$x_f = \frac{2 \cdot p_{z(cm)}}{\sqrt{s}}, \tag{9.24}$$

where $p_{z(cm)} = \gamma_{cm} \cdot (P_z - \beta_{cm} \cdot E)$.

Figure 9.21 is the $\overline{\Lambda^o}$ N_c, y_{cm}, and x_f distributions for the double muon triggered events. (a) is a distribution of the charged particle multiplicity, with a mean multiplicity of $< N_c >$=8.0 $\pm$ 3.0. The big error in the calculation of the multiplicity comes from that fact that so few statistics were accumulated for the $\overline{\Lambda^o}$'s. (b) is the rapidity distribution in the center of mass system. The rapidity distribution is more pronounced in the forward direction. This is due to the fact that the backward produced particles are not accepted due to the limited geometrical region. (c) is the center of mass x_f distribution in the center of mass system. This distribution follows the same qualitative curve as the y_{cm} distribution.

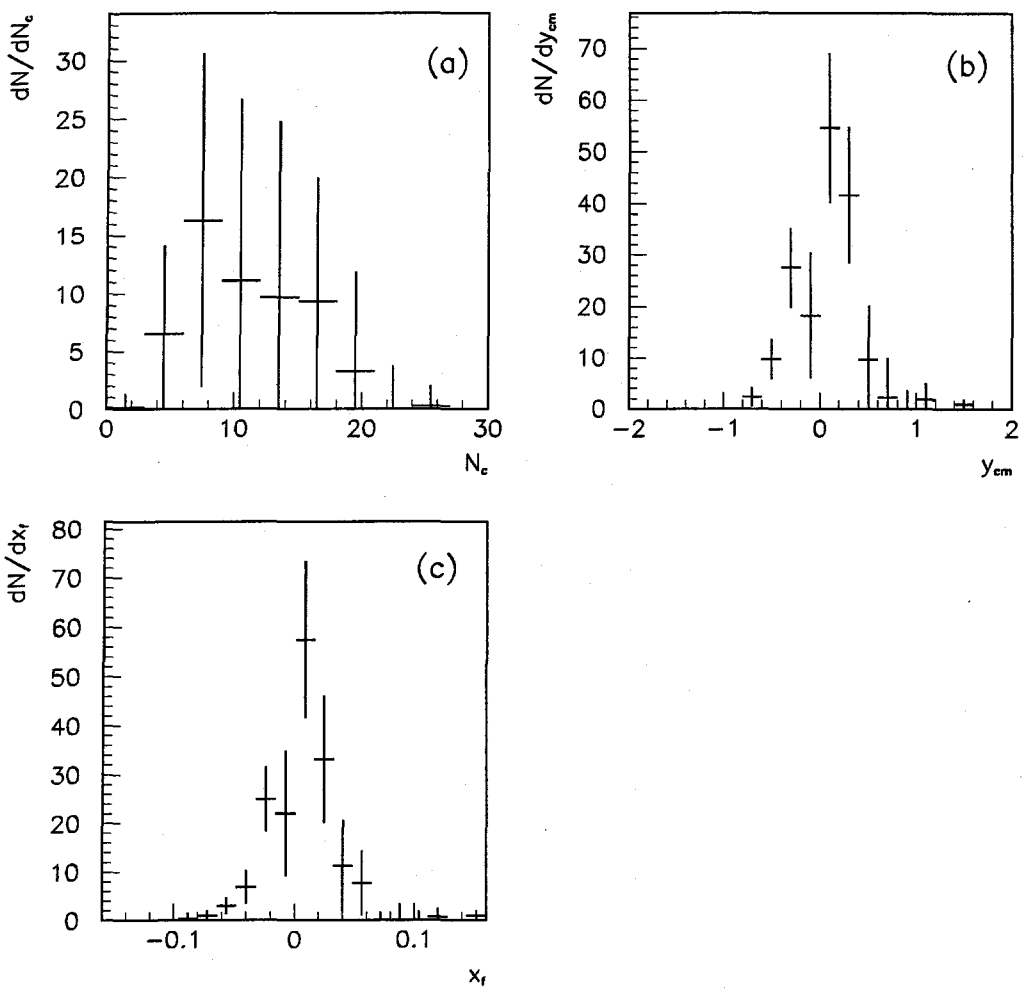

Figure 9.21: (a) N_c, (b) y_{cm}, and (c) center of mass x_f distributions for the $\overline{\Lambda^\circ}$ from double muon triggered events. These distributions are not corrected for full spectrometer acceptance.

9.6.2 Minimum Bias PYTHIA

A Monte Carlo PYTHIA program was run in order to determine how well PYTHIA predicts actual experimentally observed physics processes. As previously discussed in Chapter 5, PYTHIA may be manipulated to simulate different types of events, such as minimum bias events, charm enhanced events, or beauty enhanced events. A minimum bias program, designed to run only on those events that contained at least two muons as the trigger mechanism, was written in order to incorporate the Monte Carlo's random generation process with specially imposed restrictions.

A PYTHIA generated event steps through a process of muon identification. Once a muon is tagged, the program determines whether it had enough energy to penetrate the iron and concrete shieldings in order to form a triple coincidence in the three RPC chambers. The event searches for another muon and determines if that one also made it past the RPC hit criteria. If there are two muons that meet these criteria, the event is accepted as a double muon triggered event, and we continue with the event by looking for the V° particles. The V° particle is simulated to pass through the spectrometer region. It encounters the magnet where it experiences a p_t kick sending it along its new trajectory to traverse the rear chambers. The program checks to see that each track of the event hits at least three chamber planes upstream of the analysis magnet and at least three chamber planes downstream of the analysis magnet. If two tracks of a generated V° pass the front and rear chamber hit criteria, the event is accepted and its relevant information plotted or put in counters for later use. The information used from PYTHIA for data comparison purposes consisted of calculating the average

multiplicity value for all events irrespective of whether or not the event contained a $\overline{\Lambda^\circ}$, the number of $\overline{\Lambda^\circ}$'s generated (i.e., the particle was PYTHIA produced but may not have necessarily passed through the spectrometer acceptance region), the number of $\overline{\Lambda^\circ}$'s generated per event, and the average p_t.

9.6.3 Comparison of Data to PYTHIA

Table 9.3 is a comparison of PYTHIA events to real data events for the study of $\overline{\Lambda^\circ}$ produced particles for a minimum bias run with the condition that the analyzed events contained double muon triggered events. The first column is the average multiplicity for an event that contained a $\overline{\Lambda^\circ}$. PYTHIA predicted a slightly greater value for the double muon triggered events than it did for the single muon triggered events, although a big difference exists between PYTHIA'S and data's values. The second column is the average multiplicity for all events, not taking into account whether a $\overline{\Lambda^\circ}$ was present. There is a difference in values for what PYTHIA predicted and what was observed experimentally. PYTHIA's value was much less than what was obtained via data. As explained earlier, PYTHIA is not a good predictor of the charged particle multiplicity. The third column is the average number of $\overline{\Lambda^\circ}$'s generated ("generated" for a data event meaning that it was overlay corrected for full 4π acceptance) per charged multiplicity. The fourth column is the average number of $\overline{\Lambda^\circ}$'s generated per event. PYTHIA's value was much less than was was observed experimentally, about an order of magnitude smaller. The last column is the mean p_t for the $\overline{\Lambda^\circ}$. PYTHIA's value was about 0.2 GeV/c less than what was experimentally observed.

	$< N >_{\overline{\Lambda^\circ}}$	$< N >_{evt}$	$< \frac{\overline{\Lambda^\circ}(gen)}{N_{all}} >$	$< \frac{\overline{\Lambda^\circ}(gen)}{evt} >$	$< p_t >_{\overline{\Lambda^\circ}}$ (GeV)
PYTHIA	5.7 ± 0.9	3.72 ± 0.04	0.0035 ± 0.000003	0.013 ± 0.001	0.41 ± 0.03
DATA	8.0 ± 3.0	9.536 ± 0.004	0.0112 ± .0013	0.107 ± 0.012	0.632 ± 0.075

Table 9.3: Comparison of minimum bias double muon triggered PYTHIA generated events and data events for $\overline{\Lambda^\circ}$ produced particles.

PYTHIA and data tend to agree for some calculated values, but with PYTHIA's low charged particle multiplicity values, natural discrepancies will occur. The general trend of this theoretical model is that it tends to do a relatively good job of predicting what will occur, but caution must be used when performing some analyses.

9.7 Signal/Background Ratios

A good sampling of the V° mass distributions was obtained by applying various z-decay and $|\Delta z|$ cuts. From these variances, a range of signal/background ratios was obtained out of a sample of 1,770,583 tracked double muon triggered events.

The signal/background ratios for the K° mass distributions ranged from as low as 0.09 to as high as 0.19 when all track pairs were taken into consideration, that is, the mass distributions contained both non-coplanar and coplanar tracks. The signal/background ratios for the K° mass distributions ranged from as low as 0.85 to as high as 1.83 when only coplanar tracks were considered. It is apparent how the ratio increased significantly, showing how the coplanarity cut had a great influence in getting rid of the background combinatorics.

The signal/background ratios for the Λ° mass distributions ranged from as low as 0.20 to as high as 0.31 when all track pairs were taken into consideration, that is, for the mass distributions containing both non-coplanar tracks and coplanar tracks. The signal/background ratios for the Λ° mass distributions ranged from a low of 0.50 to a high of 1.03, again showing how the coplanar cut increased the signal peak and decreasing the background region.

The signal/background ratios for the $\overline{\Lambda^\circ}$ mass distributions ranged from as low as 0.16 to as high as 0.22 when all track pairs were taken into consideration, that is, for the mass distributions containing both non-coplanar tracks and coplanar tracks. The signal/background ratios for the $\overline{\Lambda^\circ}$ mass distributions ranged from 0.33 to a high of 0.50 when only coplanar tracks were accepted.

9.8 Data Sets Analyzed for Double Muon Triggered Events

Out of 138 tapesets of data accumulation, where a tapeset consisted of twelve 2.239 GByte tapes, slightly more than two tapesets were analyzed for the double muon triggered events. Roughly 1.8 million double muon triggered events were tracked and studied for this thesis. Table 9.4 lists the tapesets and their respective JM sequence numbers used in this analysis. The last column shows the total number of tracked events. This column includes both single and double muon triggered events.

Tapeset Number	JM Sequence Numbers	Total 1μ and 2μ Tracked Events
TS20340	JM2859 $\rightarrow$ JM2870	1,607,791
TS20341	JM2871 $\rightarrow$ JM2882	1,636,468
TS20342	JM2883 $\rightarrow$ JM2884	104,922

Table 9.4: Run statistics for tracked single muon triggered events and double muon triggered events.

Chapter 10

Charm and Beauty

This chapter will address the issue of neutral strange particle production using a sample of "charm enhanced" events and a sample of "beauty enhanced" events. We will describe the particular methods used in obtaining the enhanced events, and the relevant physics results will be presented.

10.1 Charm Enhanced Events

The total number of single muon triggered events accumulated in E771's run was about 60 million. Out of those 60 million triggered events, the tracking program gave an output of about 8 million tracked single muon triggered events. The charm enhanced tracking dealt with another form of tracking the 8 million tracked single muon triggered events.

In order to make a selection on events in the hopes of increasing the charm production, two passes were used in the tracking process. Pass I dealt with tracking those events that contained a single muon triggered event whose p_t value was greater than 0.8 GeV/c. Pass II retracked those events that survived Pass I's criteria with the added criteria:

- Accept an event if its muon track was detached from the primary vertex by greater than 70 μm, i.e., an impact parameter greater than 70 μm.
- Accept an event only if the front and rear tracks were matched. No pseudo tracks were accepted. A pseudo track was defined as a front track segment that was taken from the center of the magnet's coordinate position and extrapolated back to the main interaction target. A good track was one that met the front chamber hit criteria and matched the rear track segment.
- The number of silicon tracking planes hit in order to constitute a muon tracked event had to be greater than 8.
- The number of front chamber plane hits for the muon track segment had to be greater than 16.
- The p_t of the muon track segment had to be greater than 0.9 GeV/c.

Out of the 8 million events, approximately 60,000 events were accepted after the above described cuts were applied. The most important cuts in Pass II were the p_t cut and the detached muon cut, the impact parameter cut. Of the 60,000 events accepted as candidates for charm studies, approximately 45,000 were studied for this analysis.

10.1.1 K°, Λ°, and $\overline{\Lambda^\circ}$ Results

Due to the small amount of statistics analyzed for these charm enhanced events, thorough analyses similar to the ones performed in Chapters 7-9 were unable to be accomplished. Nevertheless, some results were obtainable, such as the $< p_t >$ value

for the K° particles, the average charged multiplicity per K° event, the average raw charged multiplicity, the average K° produced per charged multiplicity, and the average K° produced per event. Since the $\Lambda^\circ/\overline{\Lambda^\circ}$ production rate was much smaller than the K° production rate, and due to poor statistics, analyses like those performed on the K° were unable to be executed.

The following figures will contain mass distribution plots from the "charm enhanced" events for K°, Λ°, and $\overline{\Lambda^\circ}$ production. The importance of the fits to get various values, such as a particle's $< p_t >$, depends critically on how well the mass peak can be fit. Poor statistics can lead to spurious and unreliable results.

Figure 10.1 shows the K° mass distribution for a variety of z-decay and $|\Delta z|$ cuts from the sample of "charm enhanced" events. Each horizontal scale shows the mass value in GeV/c^2, and each vertical scale is the number of pairs per 10 MeV/c^2. The first row shows the K° mass plots for a fixed z-decay length greater than 5 cm from the main interaction vertex and with increasingly tighter cuts imposed on the $|\Delta z|$ of the two daughter tracks. As the $|\Delta z|$ cuts are made tighter, the peak appears more defined. The second row shows the K° mass plots for a fixed z-decay length greater than 10 cm downstream of the main interaction vertex and with tighter cuts imposed on the $|\Delta z|$ of the two daughter tracks in each column. The third and fourth rows show the K° mass plots for fixed z-decay lengths greater than 30 cm and 50 cm, respectively, downstream of the main interaction vertex and with increasingly tighter cuts imposed on the $|\Delta z|$ of the two daughter tracks in each column. All mass spectra in this figure were plotted irrespective of whether they were coplanar tracks.

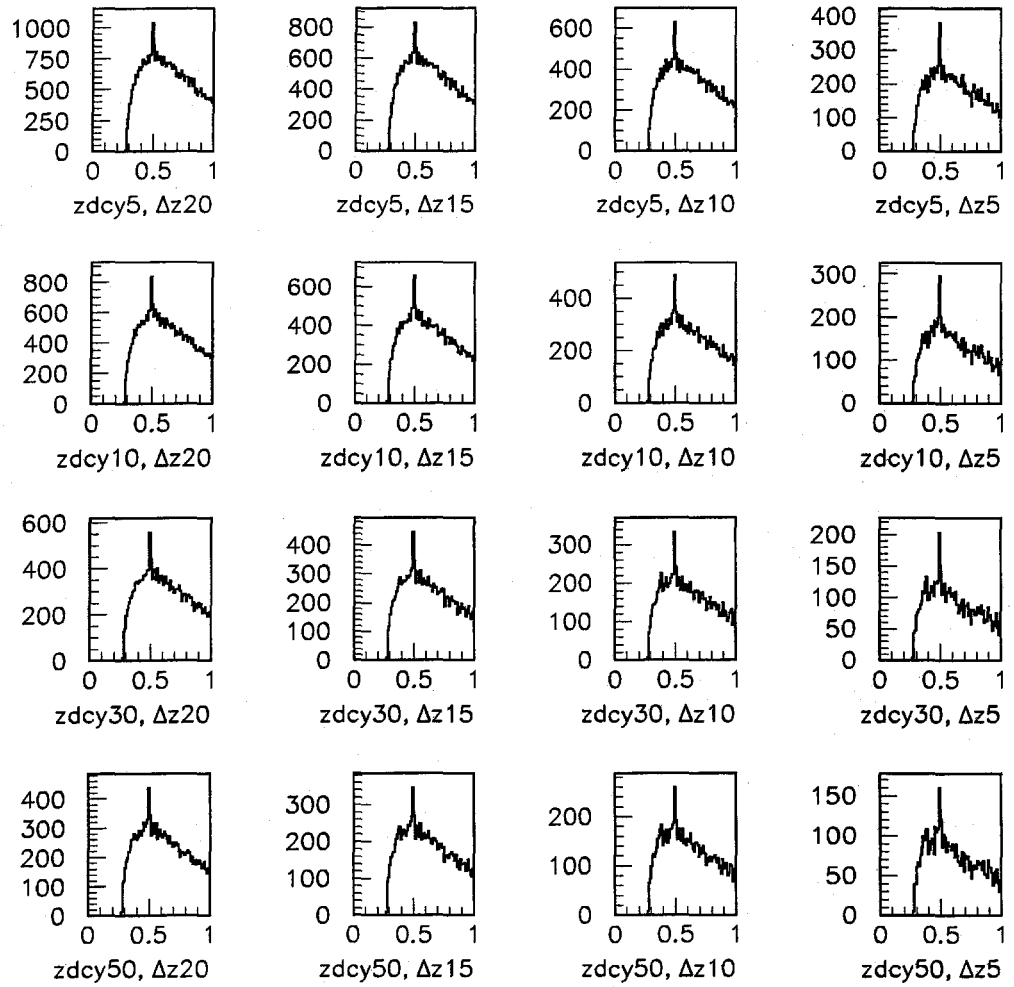

Figure 10.1: K° mass distributions from a charm enhanced sample for various z-decay and $|\Delta z|$ cuts, with no coplanarity criterion imposed. Each horizontal scale is the mass value in GeV/c^2, and each vertical scale is the number of pairs per 10 MeV/c^2.

Figure 10.2 shows the K° mass distribution for a variety of z-decay and $|\Delta z|$ cuts from the sample of "charm enhanced" events. These plots are for the requirement that the tracks be coplanar. Each horizontal scale shows the mass value in GeV/c^2, and each vertical scale is the number of pairs per 10 MeV/c^2. The first row shows the K° mass plots for a fixed z-decay length greater than 5 cm from the main interaction vertex and with increasingly tighter cuts imposed on the $|\Delta z|$ of the two daughter tracks. As the $|\Delta z|$ cuts are made tighter, the peak appears more defined. The second row shows the K° mass plots for a fixed z-decay length greater than 10 cm downstream of the main interaction vertex and with tighter cuts imposed on the $|\Delta z|$ of the two daughter tracks in each column. The third and fourth rows show the K° mass plots for fixed z-decay lengths greater than 30 cm and 50 cm, respectively, downstream of the main interaction vertex and with increasingly tighter cuts imposed on the $|\Delta z|$ of the two daughter tracks in each column.

Figure 10.3 shows the Λ° mass distribution for a variety of z-decay and $|\Delta z|$ cuts from the sample of "charm enhanced" events. Each horizontal scale shows the mass value in GeV/c^2, and each vertical scale is the number of pairs per 2.5 MeV/c^2. The first row shows the Λ° mass plots for a fixed z-decay length greater than 5 cm from the main interaction vertex and with increasingly tighter cuts imposed on the $|\Delta z|$ of the two daughter tracks. As the $|\Delta z|$ cuts are made tighter, the peak appears more defined. The second row shows the Λ° mass plots for a fixed z-decay length greater than 10 cm downstream of the main interaction vertex and with tighter cuts imposed on the $|\Delta z|$ of the two daughter tracks in each column.

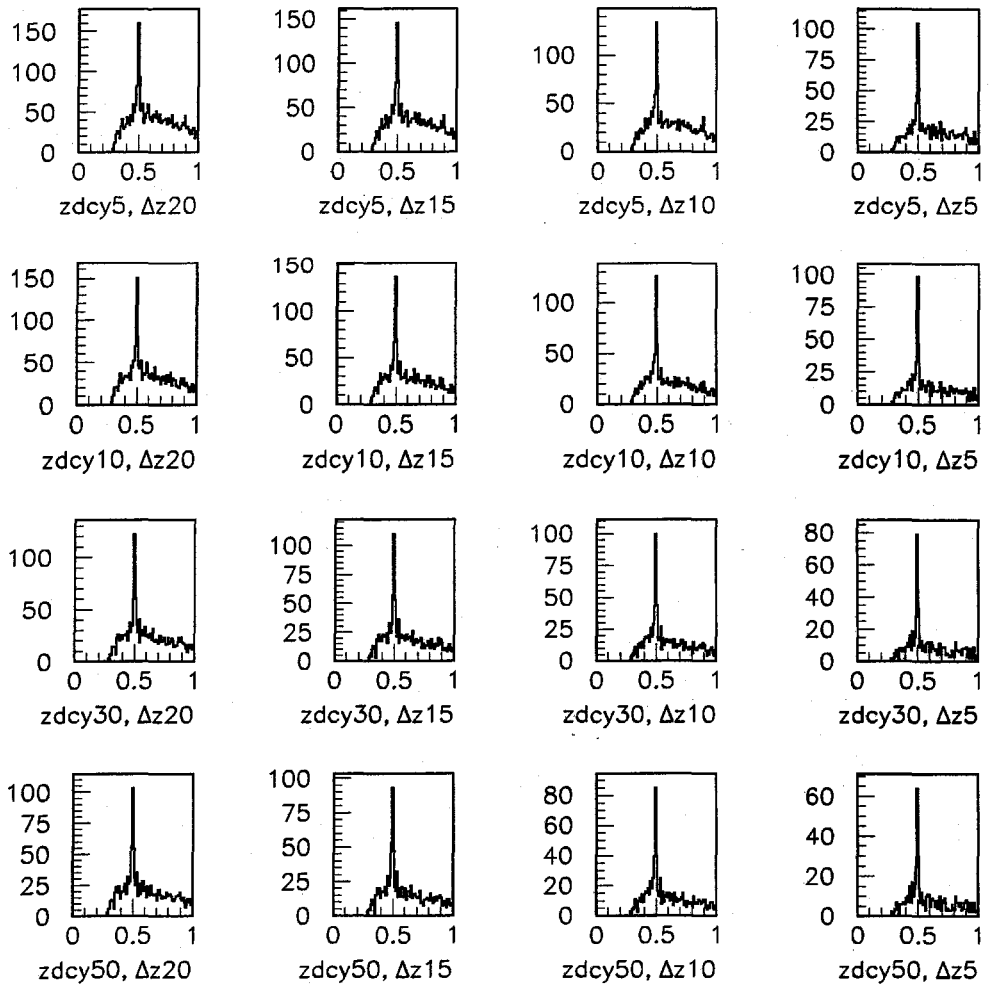

Figure 10.2: K° mass distributions from a charm enhanced sample for various z-decay and $|\Delta z|$ cuts, with a coplanarity criterion imposed. Each horizontal scale is the mass value in GeV/c^2, and each vertical scale is the number of pairs per 10 MeV/c^2.

The third and fourth rows show the Λ° mass plots for fixed z-decay lengths greater than 30 cm and 50 cm, respectively, downstream of the main interaction vertex and with increasingly tighter cuts imposed on the $|\Delta z|$ of the two daughter tracks in each column. These plots were made irrespective of whether the tracks were coplanar.

Figure 10.4 shows the Λ° mass distribution for a variety of z-decay and $|\Delta z|$ cuts from the sample of "charm enhanced" events. Each horizontal scale shows the mass value in GeV/c^2, and each vertical scale is the number of pairs per 2.5 MeV/c^2. The first row shows the Λ° mass plots for a fixed z-decay length greater than 5 cm from the main interaction vertex and with increasingly tighter cuts imposed on the $|\Delta z|$ of the two daughter tracks. As the $|\Delta z|$ cuts are made tighter, the peak appears more defined. The second row shows the Λ° mass plots for a fixed z-decay length greater than 10 cm downstream of the main interaction vertex and with tighter cuts imposed on the $|\Delta z|$ of the two daughter tracks in each column. The third and fourth rows show the Λ° mass plots for fixed z-decay lengths greater than 30 cm and 50 cm, respectively, downstream of the main interaction vertex and with increasingly tighter cuts imposed on the $|\Delta z|$ of the two daughter tracks in each column. These plots were made with the requirement that the tracks be coplanar.

Figure 10.5 shows the $\overline{\Lambda^\circ}$ mass distribution for a variety of z-decay and $|\Delta z|$ cuts from the sample of "charm enhanced" events. Each horizontal scale shows the mass value in GeV/c^2, and each vertical scale is the number of pairs per 2.5 MeV/c^2. All criteria are the same as those discussed for Figure 10.3

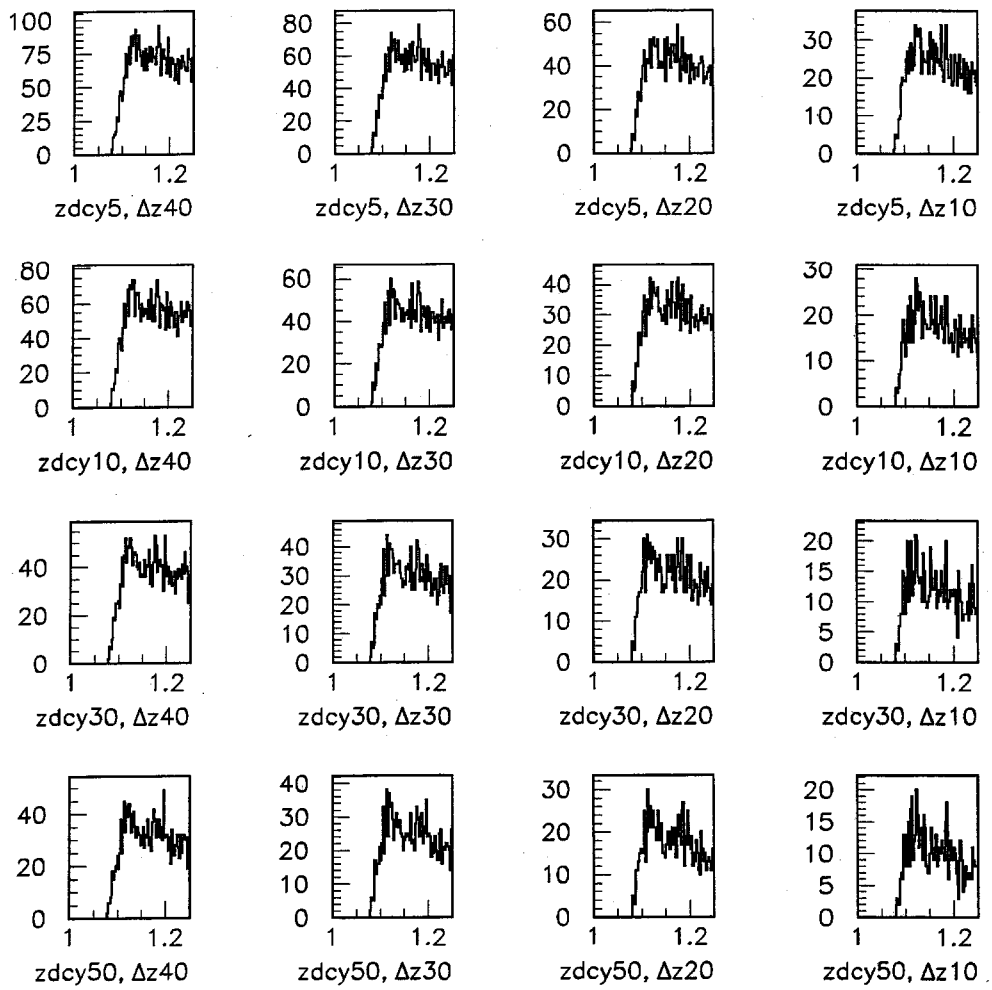

Figure 10.3: Λ° mass distributions from a charm enhanced sample for various z-decay and $|\Delta z|$ cuts, with no coplanarity criterion imposed. Each horizontal scale is the mass value in GeV/c^2, and each vertical scale is the number of pairs per 2.5 MeV/c^2.

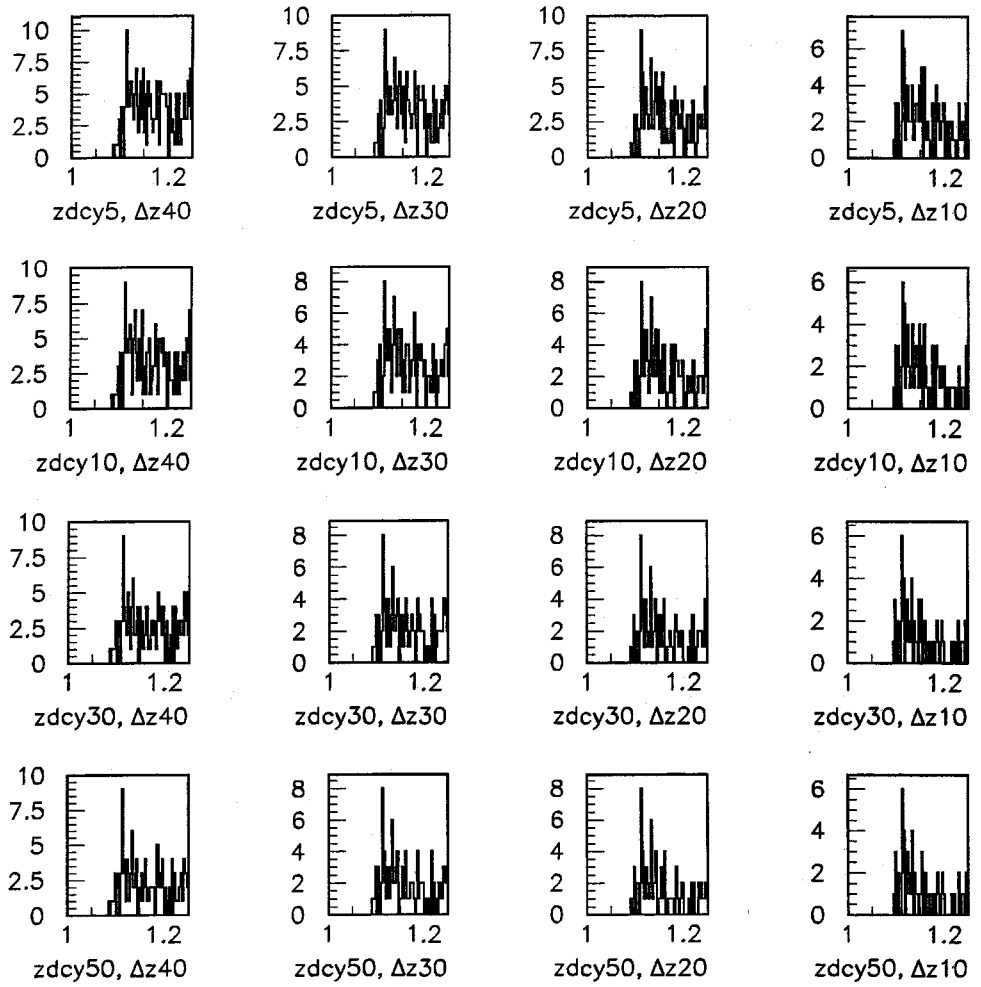

Figure 10.4: Λ° mass distributions from a charm enhanced sample for various z-decay and $|\Delta z|$ cuts, with a coplanarity criterion imposed. Each horizontal scale is the mass value in GeV/c^2, and each vertical scale is the number of pairs per 2.5 MeV/c^2.

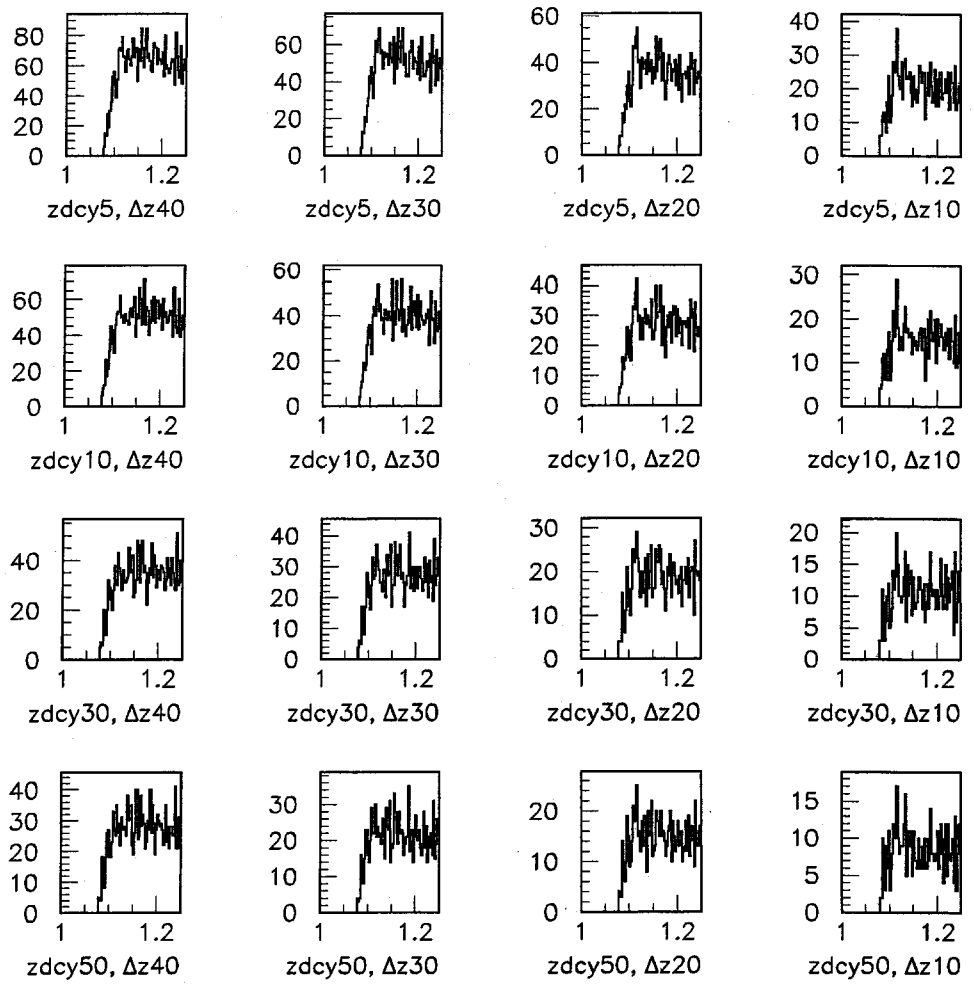

Figure 10.5: $\overline{\Lambda^\circ}$ mass distributions from a charm enhanced sample for various z-decay and $|\Delta z|$ cuts, with no coplanarity criterion imposed. Each horizontal scale is the mass value in GeV/c^2, and each vertical scale is the number of pairs per 2.5 MeV/c^2.

Figure 10.6 shows the $\overline{\Lambda^\circ}$ mass distribution for a variety of z-decay and $|\Delta z|$ cuts from the sample of "charm enhanced" events. Each horizontal scale shows the mass value in GeV/c^2, and each vertical scale is the number of pairs per 2.5 MeV/c^2. All criteria are the same as those discussed for Figure 10.4

One important measurement made using the charm enhanced events was the calculation of the $< p_t >$ value for the K°. In order to obtain a correct value, a set of criteria had to be met. These criteria involved plotting the K° p_t spectrum for those events that were within $\pm$ 30 MeV of the K° mass value. Due to the fact that a background existed underneath the signal peak in the mass distribution, the background region had to be subtracted from the p_t distribution plot. In order to achieve this, a fit was performed on the K° mass plot, where a Gaussian function was used to fit the signal peak, and a second degree polynomial was used to fit the background. Out of the total number of events, $N_{tot} = N_s + N_b$, within $\pm$ 30 MeV of the K° mass window, a ratio of N_s/N_b was calculated in order to be used in the p_t distribution subtraction algorithm. The p_t distribution was plotted for unlike sign pairs, *signal*, and it was plotted for the like sign pairs, *background*. N_{tot} for the unlike sign pairs was calculated from the mass distribution plot. N_{LS}, defined as the number of like sign pairs, had to be normalized to the true number of pairs in the background distribution for the unlike sign pairs. The ratio of N_b/N_{LS} was the normalization factor used for the like sign pairs plot. With this normalized to the proper number of background pairs, the background distribution was subtracted from the signal distribution yielding the correct p_t distribution. This distribution had to be overlay corrected for losses at small p_t. Then the simple average of the

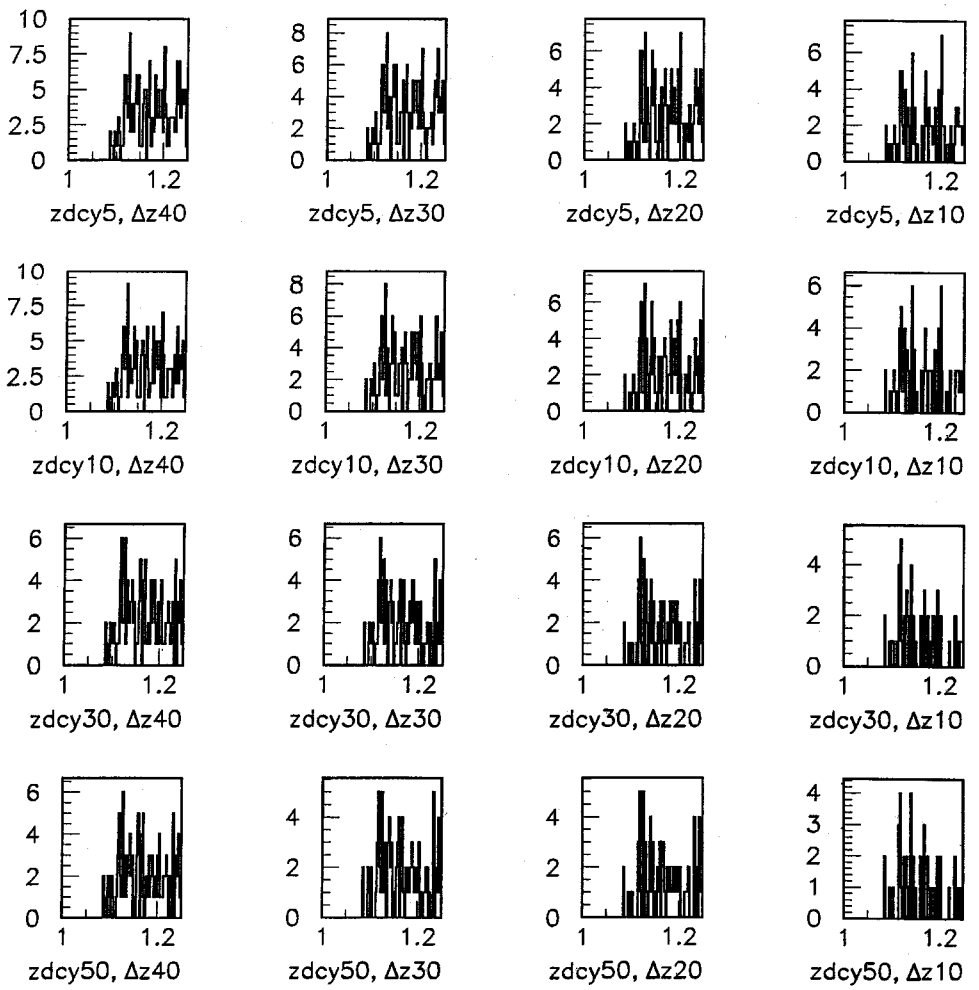

Figure 10.6: $\overline{\Lambda^{\circ}}$ mass distributions from a charm enhanced sample for various z-decay and $|\Delta z|$ cuts, with a coplanarity criterion imposed. Each horizontal scale is the mass value in GeV/c^2, and each vertical scale is the number of pairs per 2.5 MeV/c^2.

corrected p_t's was formed without benefit of any fitting procedure. The $< p_t >$ value obtained for the K°'s from the charm enhanced events was

$$< p_t >= 0.75 \pm 0.24\ GeV/c.$$

The raw multiplicity of all events, the multiplicity of events that contained a K°, the ratio of the number of K°'s produced per charged particle multiplicity, and the number of K°'s produced per event will be shown in tabulated form and compared to PYTHIA results.

The attempt to observe Λ° and $\overline{\Lambda^\circ}$ production for this small sample of charm enhanced events did not produce concrete results, and therefore a comparison procedure was not performed.

10.1.2 Charm PYTHIA

A Monte Carlo PYTHIA program, written especially for the generation of charm enhanced events ($c\bar{c}$), was run in order to use as a comparison to the results obtained from data. To simulate the experiment's run conditions most closely, the Monte Carlo PYTHIA was written to include the spectrometer acceptance region, and it was directed to produce charm enhanced events. Not only did the events have to be of charm characteristics, they also had to contain a high p_t single muon trigger.

The PYTHIA generated event looks to see if any muons came from decays of hadrons. Once a muon is found, the program determines whether its p_t value was great enough to pass the triple coincidence requirement for the three RPC

planes. If it is accepted, the program continues by looking for the neutral strange particles. The V° particle is simulated to pass through the spectrometer region. It encounters the magnet where it experiences a p_t kick and is deflected to traverse the rear chambers. The program checks to see that each track of the event hits at least three chamber planes upstream of the analysis magnet and three chamber planes downstream of the analysis magnet. If two tracks of a generated V° pass the front and rear chamber hit criteria, the event is accepted and its relevant information is plotted or put in counters for later use. The relevant information used from PYTHIA for comparison purposes consisted of the average multiplicity value for those events that had K°'s in them, the average multiplicity value for all events, irrespective of whether the event contained a K°, the number of K°'s generated (i.e., the particle was PYTHIA produced but may not have necessarily passed through the spectrometer acceptance region), the number of K°'s generated per event, and the average p_t value.

10.1.3 Comparison of Data to PYTHIA

Table 10.1 shows a comparison of PYTHIA charm enhanced ($c\bar{c}$) events to real data events for the study of K° produced particles. The first column is the average multiplicity for an event that contained a K°. PYTHIA's value differs from data's result by about a factor of three, and the same phenomenon is observable in the second column for the raw multiplicity. In general PYTHIA tends to underestimate the underlying multiplicity of interactions. The third column is the average number of K°'s generated ("generated" for data means that the event was overlay corrected

for 4π acceptance) per raw charged multiplicity (where a multiplicity event passed the spectrometer acceptance criteria). PYTHIA predicts more K°'s generated than what was observed experimentally and this is due to the fact that PYTHIA's prediction of N_c is consistently too low. The fourth column is the average number of K°'s generated per event. PYTHIA and data are in agreement within errors. The last column is the $K^{\circ} < p_t >$. Its value in the charm sample events is greater than PYTHIA's prediction. The PYTHIA prediction is within the range one would observe for Minimum bias generated events. PYTHIA is following the same trend it did when run for Minimum Bias events, getting a lower value than what is observed experimentally.

Mode (Trig)	$\langle N \rangle_{K_s^o\ evt}$	$\langle N \rangle_c$	$K_s^o(corr)/N_c$	$K_s^o(corr)/evt$	$\langle P_t \rangle_{K_s^o}$ (GeV)
DATA $c\bar{c}$ (1μ)	12.9±2.0	11.29±0.02	0.05±0.01	0.57±0.06	0.75±0.24
PYTHIA $c\bar{c}$ (1 μ)	4.3±0.1	3.43±0.02	0.1390±0.0002	0.48±0.01	0.443±0.005

Table 10.1: Comparison of charm enhanced PYTHIA generated events and data events for K° produced particles.

10.2 Beauty Enhanced Events

E771's main objective was the observation of beauty particles using a dimuon trigger. Approximately 130 million dimuon triggers were written to tape during the five week period of data accumulation.

The double muon candidates were identified in the the muon detector, and their trajectories were reconstructed by using the Resistive Plate Counter (RPC)

pads and scintillators. Track segments downstream of the analysis magnet were reconstructed using the downstream chamber hits within a search window defined by the RPC muon tracks. Track segments upstream of the analysis magnet were reconstructed and matched to the downstream muon segments to form momentum-assigned muon tracks. Opposite sign dimuon pairs were required to have originated from a common vertex determined by the silicon tracking. In a given event only the dimuon pair forming the best common vertex was kept for resonance studies.

Of the 130 million dimuon triggered events, a sample of 50,000 tracked dimuon events yielded about 12,000 to 17,000 $J/\Psi \rightarrow \mu^+\mu^-$ events, with the range depending on the various analysis cuts. This sample was classified as the beauty enhanced events in which to study neutral strange particle production. These events were re-tracked using the full hadron tracking program, and approximately 46,000 events were used for the analysis of neutral strange particle production.

10.2.1 K°, Λ°, and $\overline{\Lambda^\circ}$ Results

Just as for the charm enhanced events, the small sample of beauty enhanced events did not provide good statistics. As a result, limited analyses were performed. More physics results were obtained from the K° production than the Λ° due to the K° production rate being higher than the Λ° production rate. The relevant physics results obtained were the $< p_t >$ value for the K°, the average charged multiplicity per K° event, the average charged multiplicity, the average K° produced per charged multiplicity, and the average K° produced per event. Due to poor statistics for Λ° and $\overline{\Lambda^\circ}$ production, no analyses were performed in order to determine

V° enrichment for these particles.

The following figures will contain mass distribution plots from the "beauty enhanced" events for K°, Λ°, and $\overline{\Lambda^\circ}$ production. The importance of the fits to get various values, such as a particle's $< p_t >$, depends critically on how well the mass peak can be fit. Poor statistics can lead to spurious and unreliable results.

Figure 10.7 shows the K° mass distribution for a variety of z-decay and $|\Delta z|$ cuts from the sample of "beauty enhanced" events. Each horizontal scale shows the mass value in GeV/c^2, and each vertical scale is the number of pairs per 10 MeV/c^2. The first row shows the K° mass plots for a fixed z-decay length greater than 5 cm from the main interaction vertex and with increasingly tighter cuts imposed on the $|\Delta z|$ of the two daughter tracks. As the $|\Delta z|$ cuts are made tighter, the peak appears more defined. The second row shows the K° mass plots for a fixed z-decay length greater than 10 cm downstream of the main interaction vertex and with tighter cuts imposed on the $|\Delta z|$ of the two daughter tracks in each column. The third and fourth rows show the K° mass plots for fixed z-decay lengths greater than 30 cm and 50 cm, respectively, downstream of the main interaction vertex and with increasingly tighter cuts imposed on the $|\Delta z|$ of the two daughter tracks in each column. All mass spectra in this figure were plotted irrespective of whether they were coplanar tracks.

Figure 10.8 shows the K° mass distribution for a variety of z-decay and $|\Delta z|$ cuts from the sample of "beauty enhanced" events. These plots are for the requirement that the tracks be coplanar. Each horizontal scale shows the mass value in GeV/c^2, and each vertical scale is the number of pairs per 10 MeV/c^2. The first

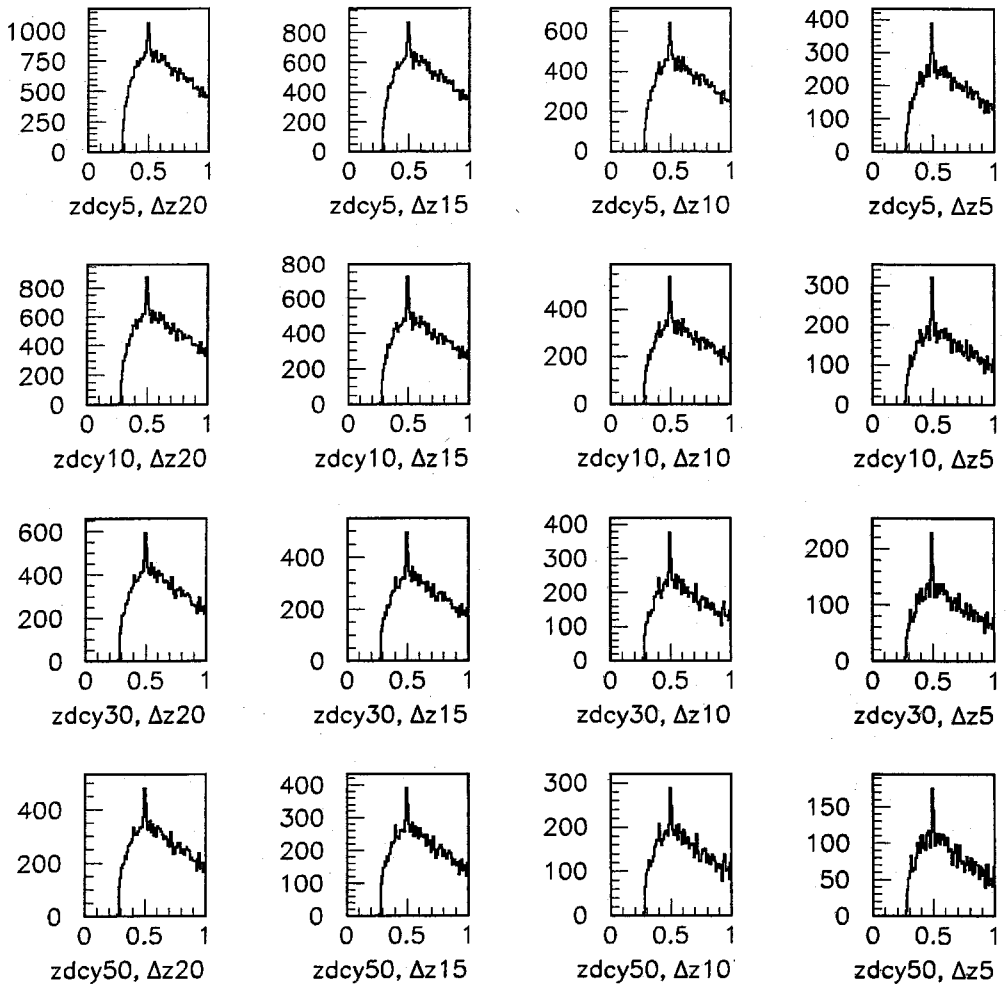

Figure 10.7: K° mass distributions from a beauty enhanced sample for various z-decay and $|\Delta z|$ cuts, with no coplanarity criterion imposed. Each horizontal scale is the mass value in GeV/c^2, and each vertical scale is the number of pairs per 10 MeV/c^2.

row shows the K° mass plots for a fixed z-decay length greater than 5 cm from the main interaction vertex and with increasingly tighter cuts imposed on the $|\Delta z|$ of the two daughter tracks. As the $|\Delta z|$ cuts are made tighter, the peak appears more defined. The second row shows the K° mass plots for a fixed z-decay length greater than 10 cm downstream of the main interaction vertex and with tighter cuts imposed on the $|\Delta z|$ of the two daughter tracks in each column. The third and fourth rows show the K° mass plots for fixed z-decay lengths greater than 30 cm and 50 cm, respectively, downstream of the main interaction vertex and with increasingly tighter cuts imposed on the $|\Delta z|$ of the two daughter tracks in each column.

Figure 10.9 shows the Λ° mass distribution for a variety of z-decay and $|\Delta z|$ cuts from the sample of "beauty enhanced" events. Each horizontal scale shows the mass value in GeV/c^2, and each vertical scale is the number of pairs per 2.5 MeV/c^2. The first row shows the Λ° mass plots for a fixed z-decay length greater than 5 cm from the main interaction vertex and with increasingly tighter cuts imposed on the $|\Delta z|$ of the two daughter tracks. As the $|\Delta z|$ cuts are made tighter, the peak appears more defined. The second row shows the Λ° mass plots for a fixed z-decay length greater than 10 cm downstream of the main interaction vertex and with tighter cuts imposed on the $|\Delta z|$ of the two daughter tracks in each column. The third and fourth rows show the Λ° mass plots for fixed z-decay lengths greater than 30 cm and 50 cm, respectively, downstream of the main interaction vertex and with increasingly tighter cuts imposed on the $|\Delta z|$ of the two daughter tracks in each column. These plots were made irrespective of whether the tracks were

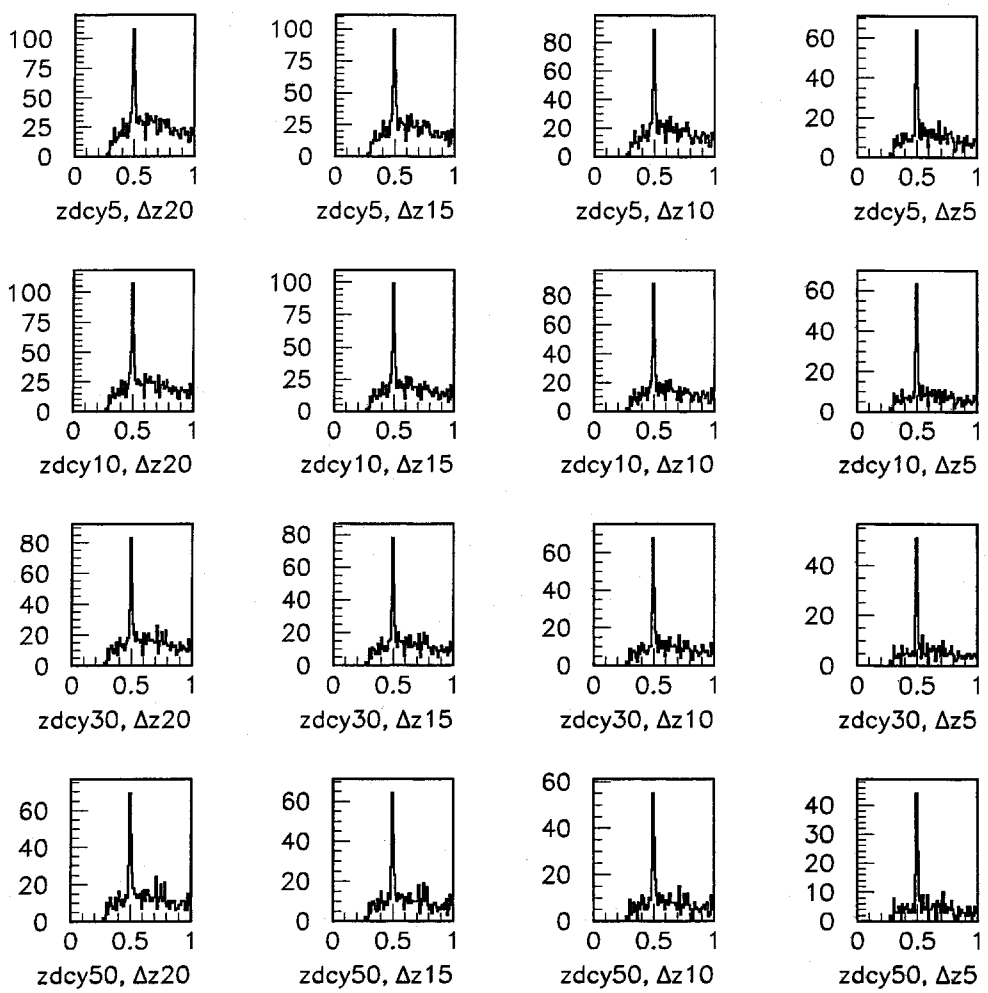

Figure 10.8: K° mass distributions from a beauty enhanced sample for various z-decay and $|\Delta z|$ cuts, with a coplanarity criterion imposed. Each horizontal scale is the mass value in GeV/c^2, and each vertical scale is the number of pairs per 10 MeV/c^2.

coplanar.

Figure 10.10 shows the Λ° mass distribution for a variety of z-decay and $|\Delta z|$ cuts from the sample of "beauty enhanced" events. Each horizontal scale shows the mass value in GeV/c^2, and each vertical scale is the number of pairs per 2.5 MeV/c^2. The first row shows the Λ° mass plots for a fixed z-decay length greater than 5 cm from the main interaction vertex and with increasingly tighter cuts imposed on the $|\Delta z|$ of the two daughter tracks. As the $|\Delta z|$ cuts are made tighter, the peak appears more defined. The second row shows the Λ° mass plots for a fixed z-decay length greater than 10 cm downstream of the main interaction vertex and with tighter cuts imposed on the $|\Delta z|$ of the two daughter tracks in each column. The third and fourth rows show the Λ° mass plots for fixed z-decay lengths greater than 30 cm and 50 cm, respectively, downstream of the main interaction vertex and with increasingly tighter cuts imposed on the $|\Delta z|$ of the two daughter tracks in each column. These plots were made with the requirement that the tracks be coplanar.

Figure 10.11 shows the $\overline{\Lambda^\circ}$ mass distribution for a variety of z-decay and $|\Delta z|$ cuts from the sample of "beauty enhanced" events. Each horizontal scale shows the mass value in GeV/c^2, and each vertical scale is the number of pairs per 2.5 MeV/c^2. All criteria are the same as those discussed for Figure 10.9

Figure 10.12 shows the $\overline{\Lambda^\circ}$ mass distribution for a variety of z-decay and $|\Delta z|$ cuts from the sample of "beauty enhanced" events. Each horizontal scale shows the mass value in GeV/c^2, and each vertical scale is the number of pairs per 2.5 MeV/c^2. All criteria are the same as those discussed for Figure 10.10

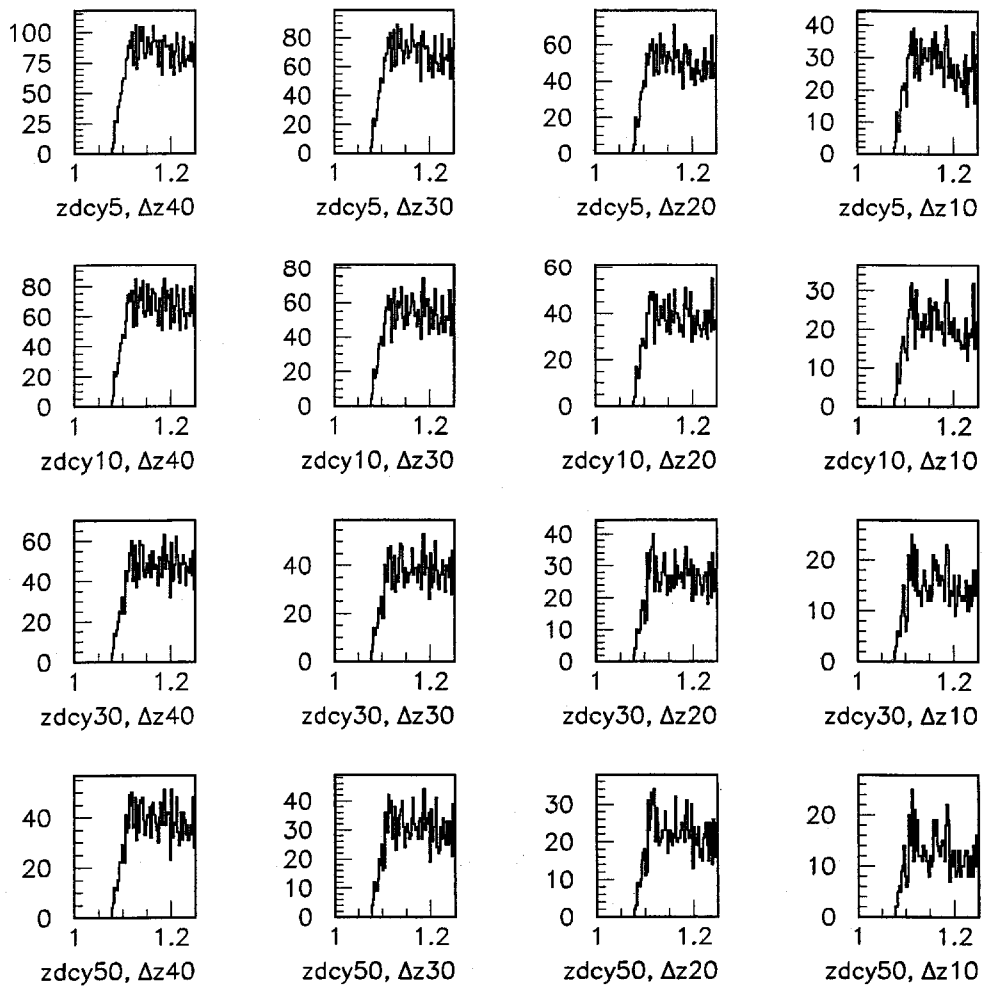

Figure 10.9: Λ° mass distributions from a beauty enhanced sample for various z-decay and $|\Delta z|$ cuts, with no coplanarity criterion imposed. Each horizontal scale is the mass value in GeV/c^2, and each vertical scale is the number of pairs per 2.5 MeV/c^2.

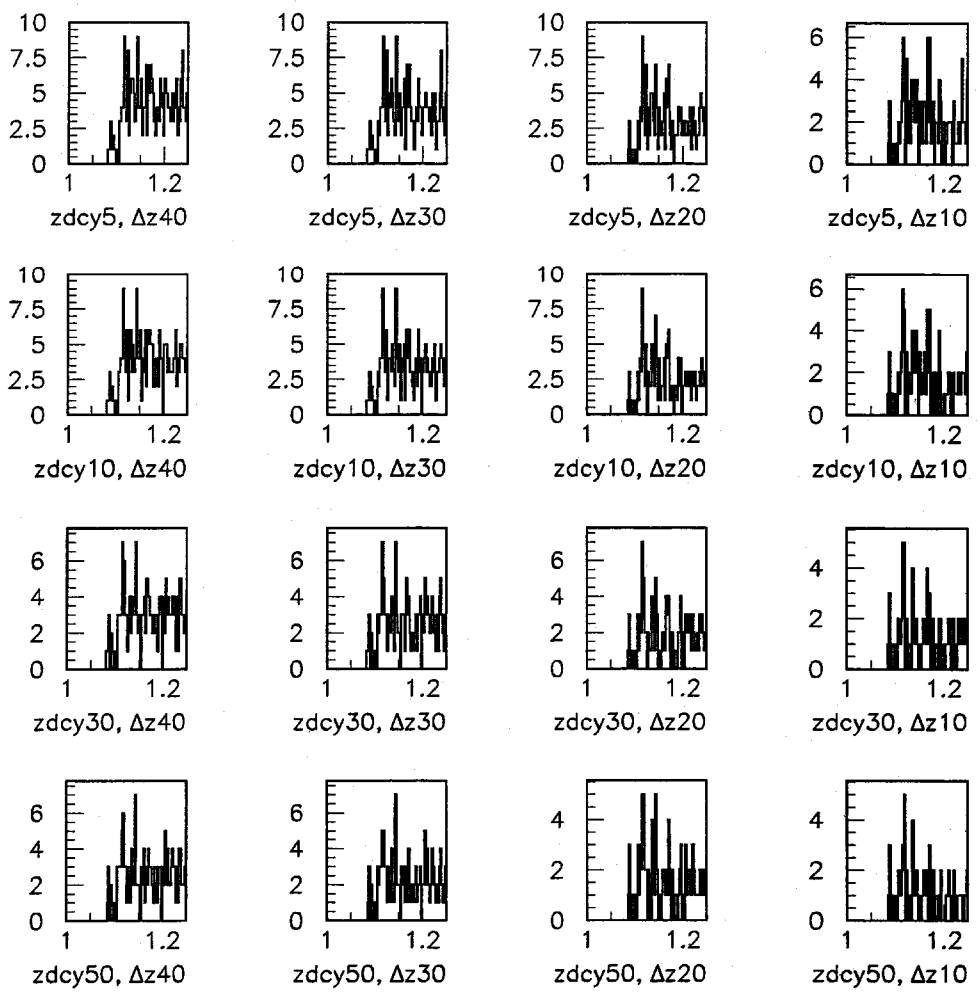

Figure 10.10: Λ° mass distributions from a beauty enhanced sample for various z-decay and $|\Delta z|$ cuts, with a coplanarity criterion imposed. Each horizontal scale is the mass value in GeV/c^2, and each vertical scale is the number of pairs per 2.5 MeV/c^2.

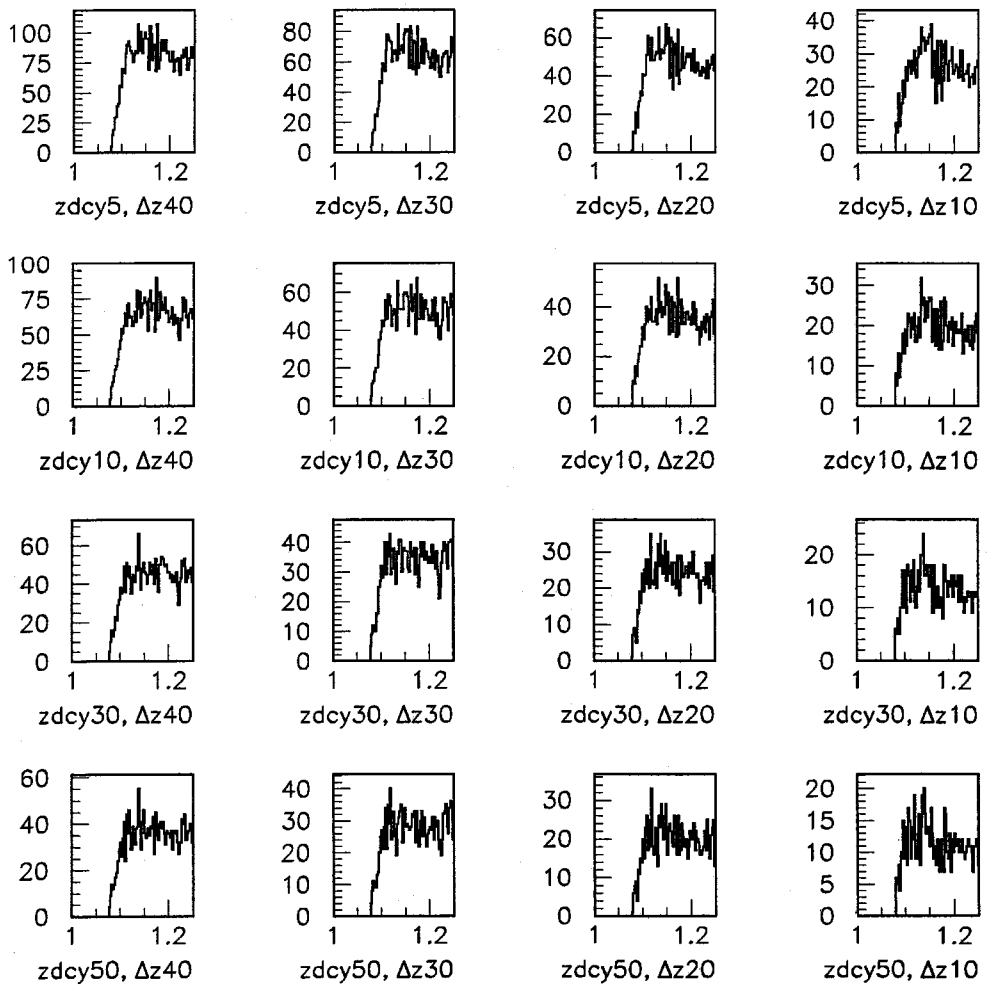

Figure 10.11: $\overline{\Lambda^{\circ}}$ mass distributions from a beauty enhanced sample for various z-decay and $|\Delta z|$ cuts, with no coplanarity criterion imposed. Each horizontal scale is the mass value in GeV/c^2, and each vertical scale is the number of pairs per 2.5 MeV/c^2.

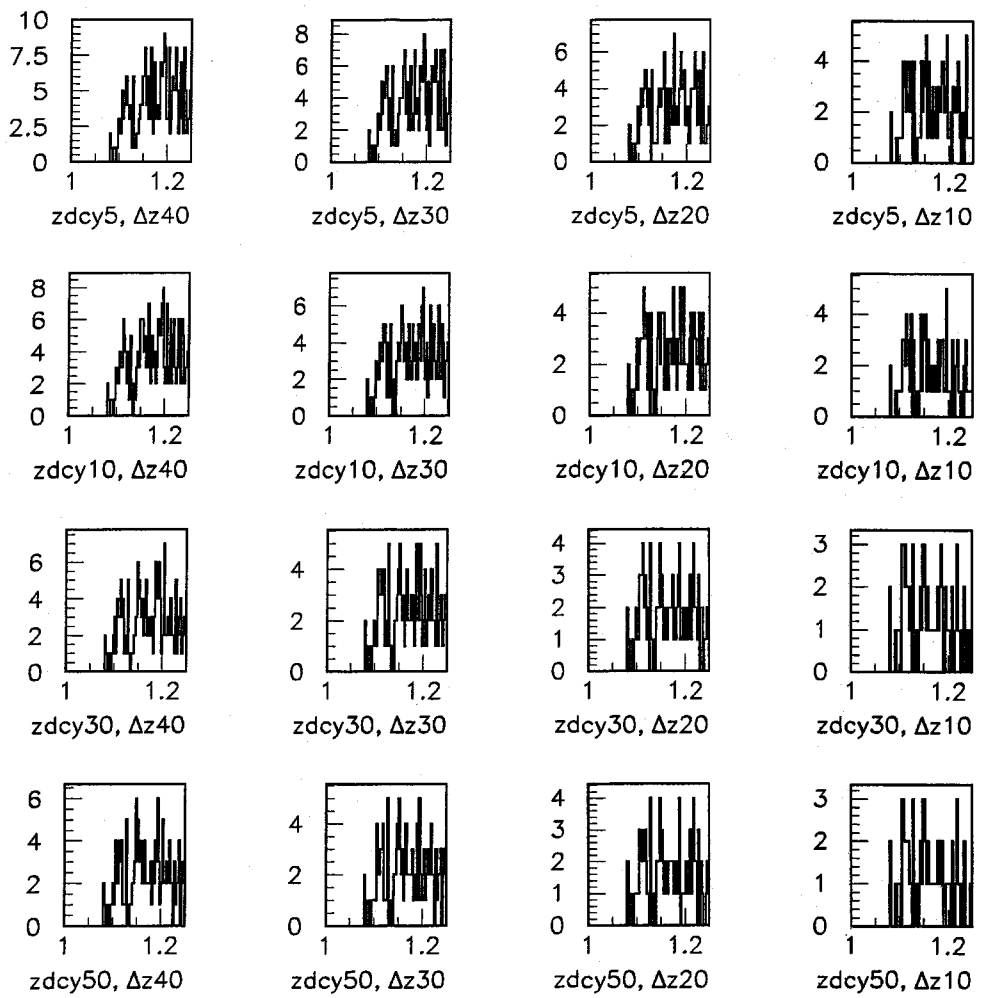

Figure 10.12: $\overline{\Lambda^{\circ}}$ mass distributions from a beauty enhanced sample for various z-decay and $|\Delta z|$ cuts, with a coplanarity criterion imposed. Each horizontal scale is the mass value in GeV/c^2, and each vertical scale is the number of pairs per 2.5 MeV/c^2.

Following the same outline discussed for the charm enhanced events, the $< p_t >$ value was calculated for the K° particle. Briefly, the $< p_t >$ was obtained by getting a true p_t distribution when the background was subtracted from the signal plot. The $< p_t >$ value calculated for the K° from the beauty enhanced sample was $0.69 \pm 0.19\ GeV/c$.

10.2.2 Beauty PYTHIA

A Monte Carlo PYTHIA program was used to generate beauty enhanced ($b\bar{b}$) events. The generation of these enhanced events required a switch set to turn on the beauty production for each event. PYTHIA performed the main task of generating the particles, and the rest of the Monte Carlo program took a particular particle and simulated its traversal through the spectrometer region.

As the real data beauty enhanced events came from dimuon triggers only, the PYTHIA Monte Carlo was written such that only events containing dimuon triggers were accepted and analyzed. If a dimuon trigger was produced, the Monte Carlo looked for a V°. Once one was found, its passage through the spectrometer was simulated, and its properties were recorded as a V° that passed through the spectrometer's region.

As the $< p_t >$ values, the average multiplicity value for those events that had a V° in them, the average multiplicity for all events, the average number of V°'s produced per multiplicity, and the average number of V°'s produced per event were obtained for data, so too was the same procedure performed on the PYTHIA generated events. This was done for comparison purposes, to determine how close

PYTHIA was able to predict what actually occurred in experiment.

10.2.3 Comparison of Data to PYTHIA

Table 10.2 shows a comparison of PYTHIA beauty enhanced events to real data for the study of K° produced particles. The first column is the average multiplicity for an event that contained a K°. The second column is the charged multiplicity for all events. The third column is the average number of K°'s produced (produced here means the number of Kaons seen after correcting up using the overlay efficiency) per charged multiplicity, The fourth column is the average number of K°'s produced per event, and the fifth column contains the $K^\circ < p_t >$.

Mode (Trig)	$\langle N \rangle_{K_s^\circ\ evt}$	$\langle N \rangle_c$	$K_s^\circ(corr)/N_c$	$K_s^\circ(corr)/evt$	$\langle P_t \rangle_{K_s^\circ}$ (GeV)
DATA $b\bar{b}$ (2μ)	13.5±2.1	12.17±0.022	0.038±0.009	0.462±0.106	0.693±0.194
PYTHIA $b\bar{b}$ (2 μ)	6.9±0.1	6.6±0.1	0.0827±0.00007	0.55±0.01	0.54±0.04

Table 10.2: Comparison of beauty enhanced PYTHIA generated events and data events for K° production.

Examination of Table 10.2 shows a discrepancy between PYTHIA and experiment. PYTHIA has systematically predicted smaller multiplicities than observed experimentally. It predicted a greater number of K°'s produced per charged multiplicity and per event, yet its prediction of the $< p_t >$ was less than experimentally observed. Inclusion of the error bars, however, allows PYTHIA and data to be in agreement for the average number of K°'s produced per event and for the $< p_t >$.

As can be seen by the charm and beauty analyses, these "enhanced" events have enriched the K° production per event, per charged multiplicity, and the

$< p_t >$ values have increased as well relative to the minimum bias sample studied in Chapter 7. Chapter 11 will coalesce the results for the experimentally calculated values for the K°'s, Λ°'s, and $\overline{\Lambda^{\circ}}$'s, for minimum bias events, single muon and double muon triggered events, and the charm and beauty enhanced events.

Chapter 11

Results and Conclusions

11.1 Cross Sections

From the outset, the main thrust of this dissertation was to determine the total cross sections for K°, Λ°, and $\overline{\Lambda^\circ}$ production and the differential cross sections for these particles at zero rapidity. Their values were calculated from minimum bias events.

The estimated total cross sections were obtained from the minimum bias events using the overlay tracking efficiency in order to get the corrected number of V°'s used in the calculations. Table 11.1 shows the K°, Λ°, and $\overline{\Lambda^\circ}$ total cross sections and the cross sections at zero rapidity.

A comparison at other energies of σ_{tot} for K° production shows a value that is increasing with increasing beam energy. A comparison of σ_{tot} for Λ° production also follows the trend of increasing cross section for increasing beam energy. A comparison of σ_{tot} for the $\overline{\Lambda^\circ}$ particles is indicative of a plateauing effect with increasing beam energy, or a much slower increase in the cross section.

Figure 11.1 shows the estimated total cross section plots for the K°'s, the Λ°'s, and the $\overline{\Lambda^\circ}$'s compared to world data as a function of energy.

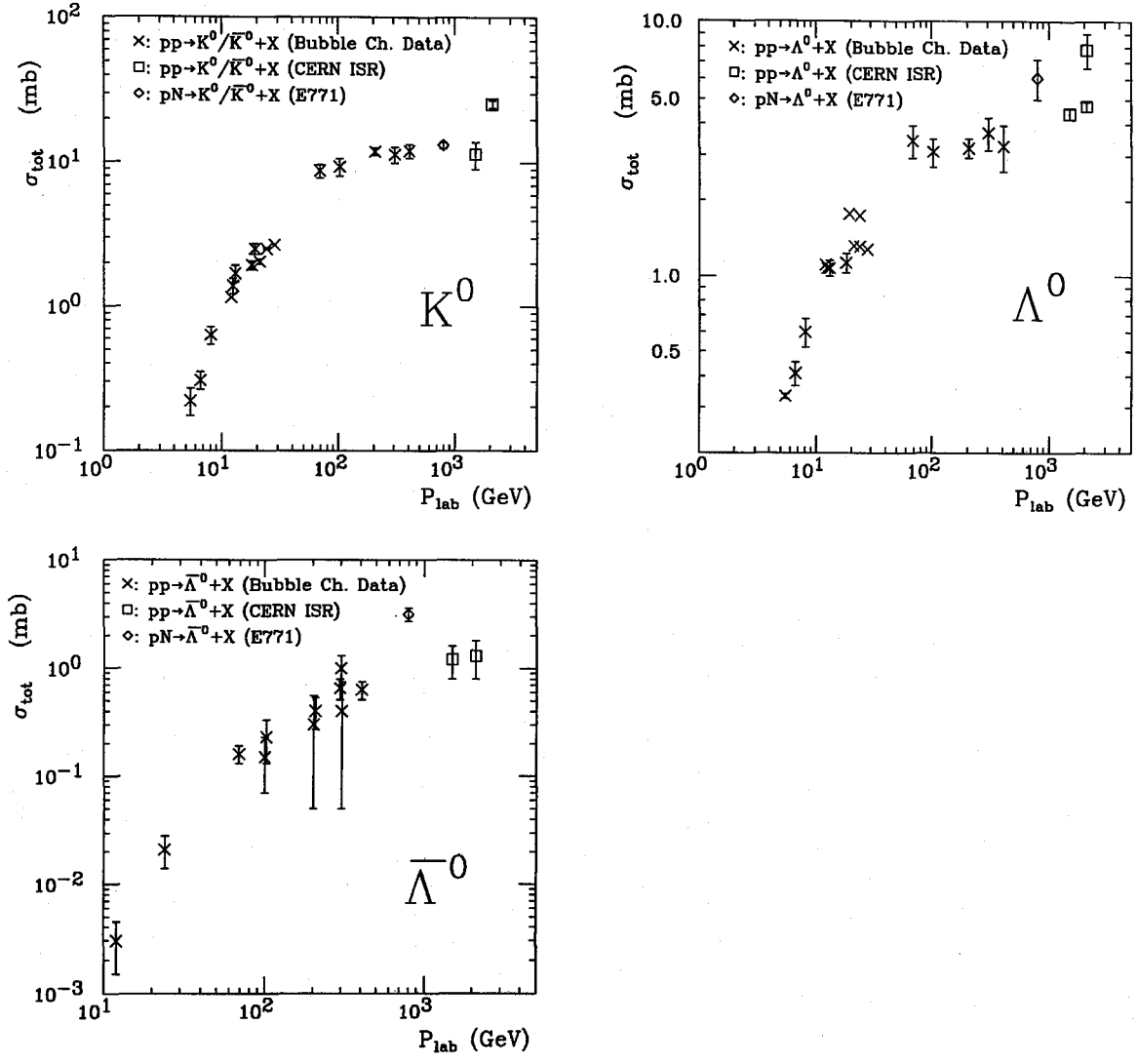

Figure 11.1: Estimated total cross section values for K°, Λ°, and $\overline{\Lambda^\circ}$ production for E771 data and compared to world data.

Particle ID	σ_{tot} (mb)	$(d\sigma/dy)_{y=0}$ (mb)
K°	13.31 ± 0.65	1.46 ± 0.06
Λ°	6.06 ± 1.09	0.40 ± 0.08
$\overline{\Lambda^\circ}$	3.15 ± 0.45	0.32 ± 0.09

Table 11.1: σ_{tot} and $(d\sigma/dy)_{y=0}$ for K°, Λ°, and $\overline{\Lambda^\circ}$ production from minimum bias triggered events.

Figure 11.2 shows the differential cross section plots at zero rapidity for the K°'s, the Λ°'s, and the $\overline{\Lambda^\circ}$'s versus world data.

The conclusions that may be drawn here in relation to cross sections are the following:

- All three cross section values increase with increasing energy. The total cross section for K° production has a plateauing effect, yet its σ_{tot} is still on an increasing trend, albeit a slower one. The total cross sections for Λ° and $\overline{\Lambda^\circ}$ production are also increasing, but they too tend to plateau as a function of increasing energy.

- The differential cross section at zero rapidity for Λ° production seems constant (forward produced mostly), and it is slowly increasing for K° and $\overline{\Lambda^\circ}$ production (centrally produced).

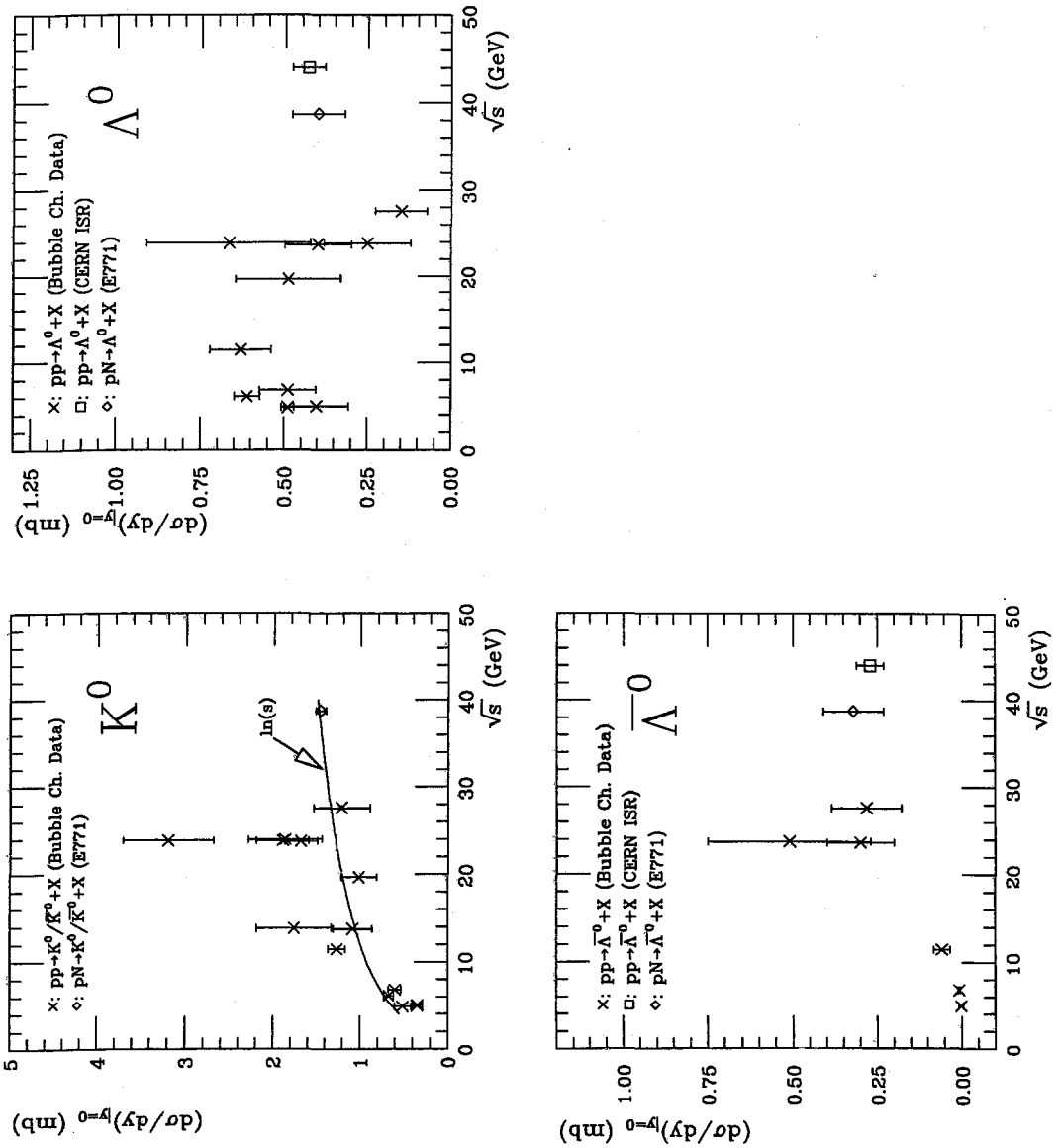

Figure 11.2: Differential cross section plots at zero rapidity for K°, Λ°, and $\overline{\Lambda^\circ}$ production for E771 data and compared to world data.

11.2 Enriched V° Production

Another goal achieved in this thesis was the observation that different types of triggers enriched V° production as compared to minimum bias events. What follows will be various tables describing values obtained for physical quantities which were thought to be sensitive to various hardware and software triggers used in the experiment.

Table 11.2 shows the final tally of the different triggered events for the production of K° particles. This table is for all triggers analyzed in this thesis such as the minimum bias events, the single muon triggered events, the double muon triggered events, the charm enhanced events, and the beauty enhanced events. The first column lists the particular trigger that was analyzed. The second column is the average multiplicity for those events that contained a K°, and the third column is the average spectrometer multiplicity of all events (the raw multiplicity). The fourth column is the average number of K°'s produced (where a produced K° was the actual number obtained from the overlay efficiency had the detector been 100% efficient) per spectrometer charged multiplicity, and the fifth column is the average number of K°'s produced per event. Finally, the sixth column is the K° $< p_t >$.

Figure 11.3 shows the tabulated K° values plotted for comparison purposes as a function of increasing trigger complexity.

Table 11.3 shows the final tally of the different triggered events for the production of the Λ° particles. This table is for three trigger types analyzed in this thesis such as the minimum bias events, the single muon triggered events, and the

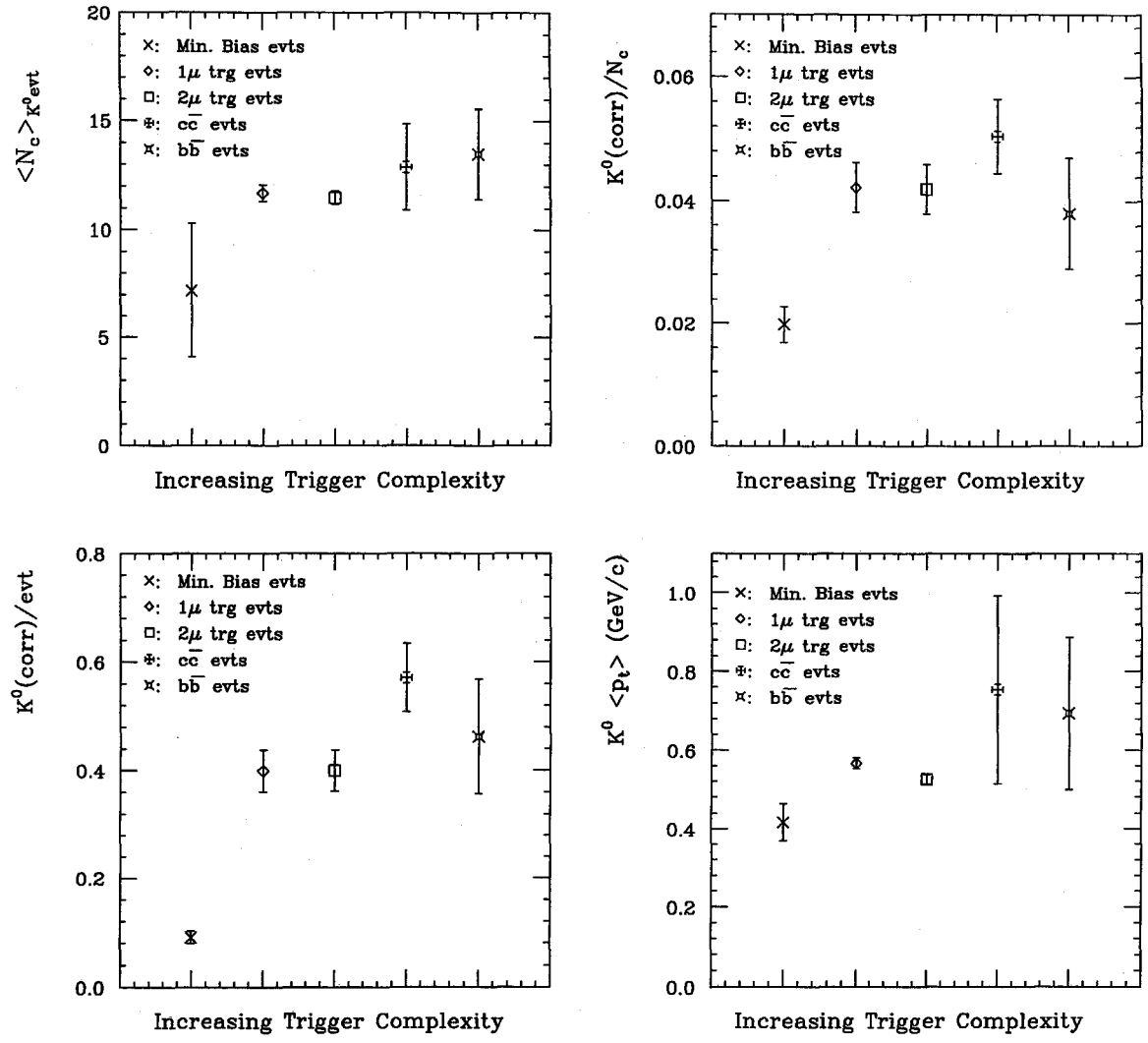

Figure 11.3: Plots of the various quantities measured for K° production as a function of increasing trigger complexity.

Mode (Trig)	$\langle N \rangle_{K_s^\circ\ evt}$	$\langle N \rangle_c$	$K_s^\circ(corr)/N_c$	$K_s^\circ(corr)/evt$	$\langle P_t \rangle_{K_s^\circ}$ (GeV)
Min Bias (No Trig)	7.2±3.1	4.547±0.008	0.020±0.003	0.09±0.01	0.42±0.05
(1μ)	11.7±0.4	9.451±0.004	0.0422±0.004	0.40±0.04	0.57±0.01
(2μ)	11.5±0.3	9.536±0.004	0.0419±0.004	0.40±0.04	0.53±0.01
$c\bar{c}$ (1μ)	12.9±2.0	11.29±0.02	0.05±0.01	0.57±0.06	0.75±0.24
$b\bar{b}$ (2μ)	13.5±2.1	12.17±0.02	0.04±0.01	0.46±0.11	0.69±0.19

Table 11.2: Various data measurements for $K^\circ \rightarrow \pi^+\pi^-$ from minimum bias events, single muon and double muon triggered events, and $c\bar{c}$ and $b\bar{b}$ enhanced events.

double muon triggered events.

Mode (Trig)	$\langle N \rangle_{\Lambda^\circ\ evt}$	$\langle N \rangle_c$	$\Lambda^\circ(corr)/N_c$	$\Lambda^\circ(corr)/evt$	$\langle P_t \rangle_{\Lambda^\circ}$ (GeV)
Min Bias (No Trig)	5.3±2.6	4.55±0.01	0.020±0.003	0.09±0.01	0.51±0.06
(1μ)	11.8±1.5	9.451±0.004	0.018±0.001	0.17±0.01	0.47±0.05
(2μ)	12.1±1.3	9.536±0.004	0.018±0.002	0.17±0.02	0.62±0.05

Table 11.3: Various data measurements for $\Lambda^\circ \rightarrow p\pi^-$ from minimum bias events, single muon triggered events, and double muon triggered events.

Figure 11.4 shows the tabulated Λ° values plotted for comparison purposes as a function of increasing trigger complexity.

Table 11.4 shows the final tally of the different triggered events for the production of the $\overline{\Lambda^\circ}$ particles. This table is for three different triggers analyzed in this thesis such as the minimum bias events, the single muon triggered events, and the double muon triggered events. As discussed for the K° and Λ° tables, this one follows the same convention.

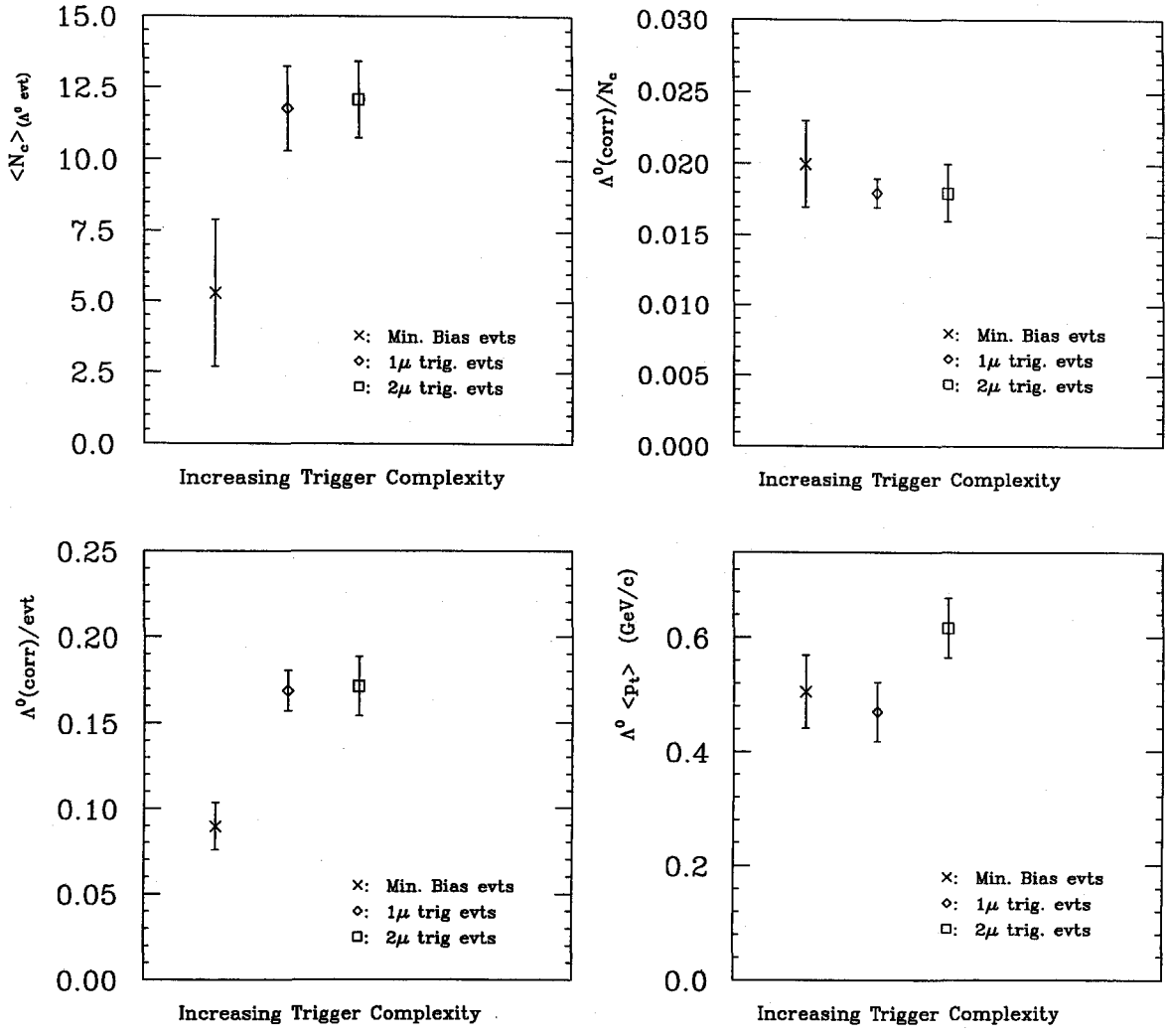

Figure 11.4: Plots of the various quantities measured for Λ° production as a function of increasing trigger complexity.

Mode (Trig)	$\langle N \rangle_{\overline{\Lambda^\circ}\ evt}$	$\langle N \rangle_c$	$\overline{\Lambda^\circ}(corr)/N_c$	$\overline{\Lambda^\circ}(corr)/evt$	$\langle P_t \rangle_{\overline{\Lambda^\circ}}$ (GeV)
Min Bias (No Trig)	7.5±3.0	4.55±0.01	0.012±0.002	0.053±0.005	0.41±0.09
(1μ)	8.0±3.0	9.451±0.004	0.010±0.001	0.092±0.014	0.53±0.07
(2μ)	8.0±3.0	9.536±0.004	0.011±0.001	0.107±0.012	0.63±0.08

Table 11.4: Various data measurements for $\overline{\Lambda^\circ} \rightarrow \overline{p}\pi^+$ from minimum bias events, single muon triggered events, and double muon triggered events.

Figure 11.5 shows the tabulated $\overline{\Lambda^\circ}$ values plotted for comparison purposes as a function of increasing trigger complexity.

Although a small amount of data was accumulated for the charm and beauty enhanced events, it was observed that increasing the $c\overline{c}$ and $b\overline{b}$ production enriches V° production, as well observed for K° production. Better statistics would have yielded similar results for the Λ°'s and $\overline{\Lambda^\circ}$'s as well.

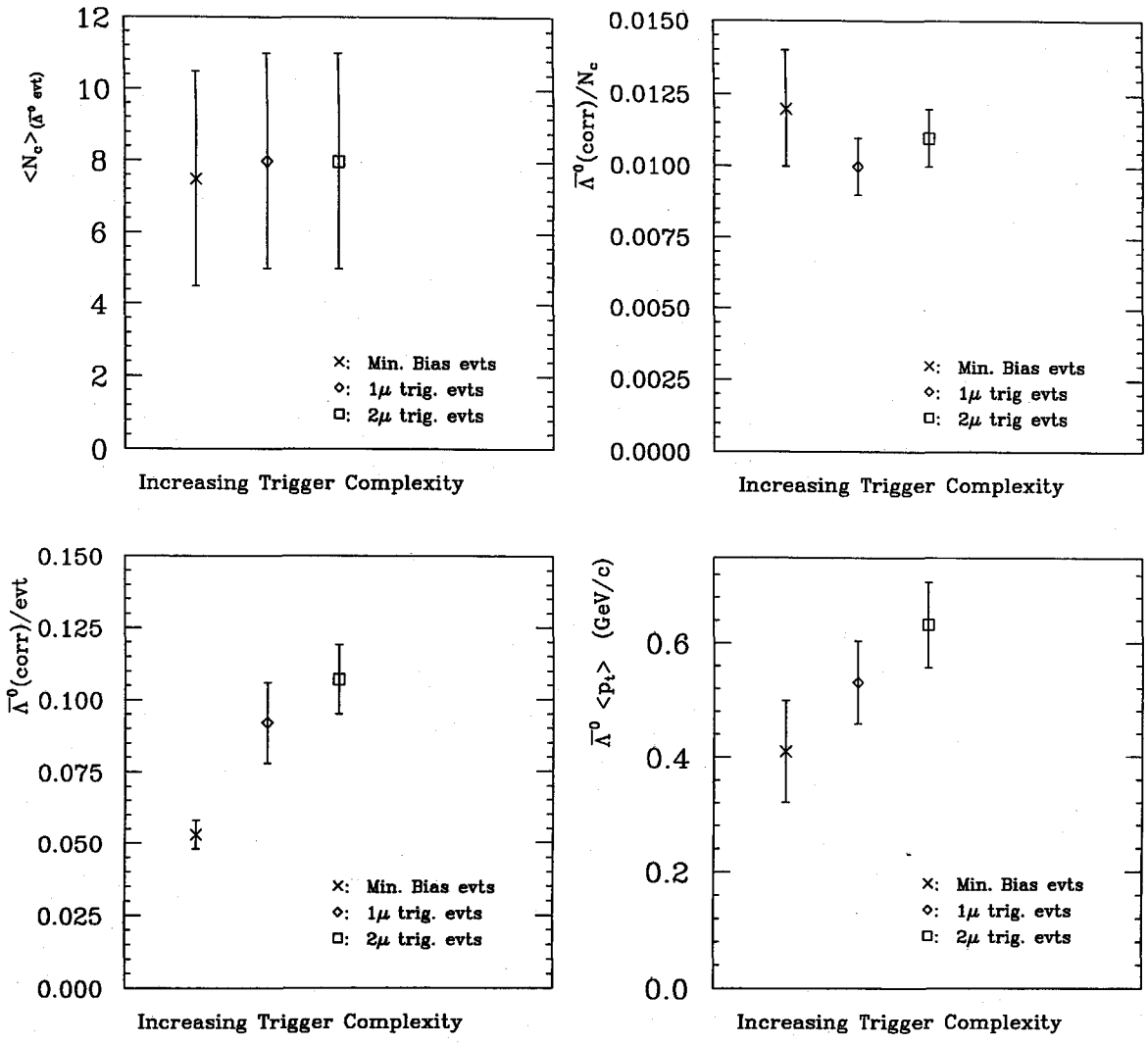

Figure 11.5: Plots of the various quantities measured for $\overline{\Lambda^0}$ production as a function of increasing trigger complexity.

Bibliography

[1] S. Weinberg, Phys. Rev. Lett. **19**, 1264 (1967).

[2] A. Pais, Phys. Rev. **86**, 663 (1952).

[3] D. Griffiths, "Introduction to Elementary Particles", Wiley and Sons, 1987.

[4] M. Kobayashi and T. Maskawa, Prog. Theor. Phys. **49**, 652 (1973).

[5] N. Cabibbo, Phys. Rev. Lett. **10**, 531 (1963).

[6] "Review of Particle Properties", Phys. Rev. **D50**, 1315 (1994).

[7] J. Augustin *et al.*, SPEAR Collaboration, Phys. Rev. Lett. **33**, 1406 (1974).

[8] J. Aubert *et al.*, AGS Collaboration, Phys. Rev. Lett. **33**, 1404 (1974).

[9] S.L. Glashow, J. Iliopoulos, and L. Maiani, Phys. Rev. **D2**, 1285 (1970).

[10] UA1 Collaboration, Phys. Lett. **B273**, 540 (1991).

[11] 12.4 GeV/c: K. Jaeger *et al.*, Phys. Rev. **D11**, 1756 (1975).
12 and 24 GeV/c: V. Blobel *et al.*, Nucl. Phys. **B69**, 454 (1974).
69 GeV/c: V.V. Ammosov *et al.*, Nucl. Phys. **B115**, 269 (1976).
100 GeV/c: M. Alston-Garnjost *et al.*, Phys. Rev. Lett. **35**, 142 (1975).
102 GeV/c: J. Chapman *et al.*, Phys. Lett. **47B**, 465 (1973).
205 GeV/c: K. Jaeger *et al.*, Phys. Rev. **D11**, 2405 (1975).
300 GeV/c: A. Sheng *et al.*, Phys. Rev. **D11**, 1733 (1975).
400 GeV/c: R.D. Kass *et al.*, Phys. Rev. **D20**, 605 (1979).
405 GeV/c: H. Kichimi *et al.*, Phys. Rev. **D20**, 37 (1979).

[12] B. Andersson *et al.*, Nucl. Phys. **B281**, 289 (1987).
B. Nilsson-Almqvist *et al.*, Comput. Phys. Commun. **43**, 387 (1987).

[13] C. Wei and G. Mo, "E771 Halo Veto Logic", E771 Internal Note, January 1992.

[14] "Review of Particle Properties", Phys. Rev. **D50**, 1241 (1994).

[15] A. McManus *et al.*, IEEE Transactions on Nuclear Science **39**, 1249 (1992).

[16] L. Spiegel *et al.*, "A Combination Drift Chamber/Pad Chamber for Very High Readout Rates", 1991 IEEE Nuclear Science Symposium (Santa Fe, New Mexico, 1991), Vol. 1, 381 (1991).

[17] C. Swoboda *et al.*, "A high-Rate Fastbus Silicon Strip Readout System", IEEE Transactions on Nuclear Science, Vol. 37 (1990).

[18] R.K. Bock, H. Grote, D. Notz, and M. Regler, "Data Analysis techniques for High-Energy Physics Experiments", Cambridge University Press, 1990.

[19] B. Cox *et al.*, Nucl. Instr. and Meth. **A219**, 487 (1984).
D. Wagoner *et al.*, Nucl. Instr. and Meth. **A238**, 315 (1985).
B. Cox *et al.*, Nucl. Instr. and Meth. **A238**, 321 (1985).
R. Rameika *et al.*, Nucl Instr. and Meth. **A242**, 215 (1986).
L. Spiegel *et al.*, IEEE Trans. Nucl. Sci. **36**, 86 (1989).
C.M. Jenkins *et al.*, IEEE Trans. Nucl. Sci. **36**, 117 (1989).

[20] L. Antoniazzi, *et al.*, "Resistive Plate Counters Readout System", Nuclear Instruments and Methods in Physics Research **A307**, 312 (1991).
L. Antoniazzi, *et al.*, "The E771 RPC Muon Detector", Nuclear Instruments and Methods in Physics Research **A315**, 92 (1992).

[21] M. Boussicut *et al.*, IEEE Transactions on Nuclear Science **NS25**, 144 (1978).

[22] G. Mo and C. Wei, "E771 Scintillator Beam Trigger", E771 Internal Note, January 1992.

[23] C. Durandet, "E771 Silicon Interaction Trigger", E771 Internal Note, January 1992.

[24] G. Corti, "The 1A Trigger", E771 Internal Note, January 1992.
G. Introzzi *et al.*, "FNAL E771 RPC Muon Trigger", Frontier Detectors for Frontier Physics, 6th Pisa Meeting on Advanced Detectors, La Biodola, Italy, 1994.

[25] P. Hanlet, "The E771 Data Acquisition System", E771 Internal Note, January 1992.

[26] D.H. Brick *et al.*, Phys. Rev. **D41**, 765 (1990).

[27] DeMarzo *et al.*, Phys. Rev. **D26**, 1019 (1982).

[28] "Review of Particle Properties", Phys. Rev. **D50**, 1336 (1994).

[29] H.-U. Bengtsson and T. Sjöstrand, Computer Physics Commun. **46**, 43 (1987).

[30] T. Sjöstrand, Computer Physics Commun. **39**, 347 (1986).
T. Sjöstrand and M. Bengtsson, Computer Physics Commun. **43**, 367 (1987).

[31] N. Metropolis, Journal of Chemical Physics **21**, 1087 (1953).

[32] R. Hagedorn, in *Cargèse Lectures in Physics*, (Gordon and Breach, New York, 1973), Vol. 6, pg. 643.

[33] R.P. Feynman *et al.*, Phys. Rev. **D18**, 3320 (1978).
S.M. Berman *et al.*, Phys. Rev. **D4**, 3388 (1971).

[34] H. Kichimi *et al.*, Phys. Rev. **D20**, 37 (1979).

[35] GEANT3 User's Guide, CERN Program Library, DD/EE/84-1.

[36] J. Podolanski and R. Armenteros, Phil. Magazine **45**, 13 (1954).

[37] P. Hanlet, "The LED and Random Triggers", E771 Internal Note, February 1992.

[38] 5.45, 6.6, 8.0 GeV/c: K. Jaeger *et al.*, Phys. Rev. **D11**, 2405 (1975).
12, 24 GeV/c: V. Blobel *et al.*, Nucl. Phys. **B69**, 454 (1974).
12.4 GeV/c: K. Jaeger *et al.*, Phys. Rev. **D11**, 1756 (1975).
19 GeV/c: H. Bøggild *et al.*, Nucl. Phys. **B57**, 77 (1973).
13.0, 18.0, 21.0, 24.0, 28.0 GeV/c: B.Y. Oh *et al.*, Nucl. Phys. **B49**, 14 (1972).
69 GeV/c: H. Blumenfeld *et al.*, Phys. Lett. **45B**, 525 (1973); *ibid.* **45B** 528 (1973).
102 GeV/c: J. Chapman *et al.*, Phys. Lett. **47B**, 465 (1973).
303 GeV/c: F. T. Dao *et al.*, Phys. Rev. Lett. **30**, 1151 (1973).
405 GeV/c: A. A. Seidl *et al.*, report given at the Meeting of the American Physical Society, Washington, D.C., 1974 (unpublished). See also K. Jaeger *et al.*, Phys. Rev. **D11**, 2405 (1975).
1500 GeV/c: (K°'s only.) D. Drijard *et al.*, Z. Phys. **C9**, 293 (1981).
1500 and 2100 GeV/c: (Λ°'s only.) S. Erhan *et al.*, Phys. Lett. **85B**, 447 (1979).
2115 GeV/c: D. Drijard *et al.*, Z. Phys. **C12**, 217 (1982).

[39] 12 and 24 GeV/c: V. Blobel *et al.*, Nucl. Phys. **B69**, 454 (1974).
12.4 GeV/c: K. Jaeger *et al.*, Phys. Rev. **D11**, 1756 (1975).
19 GeV/c: H. Bøggild *et al.*, Nucl. Phys. **B57**, 77 (1973).
69 GeV/c: V.V. Ammosov *et al.*, Nucl. Phys. **B115**, 269 (1976).
100 GeV/c: M. Alston-Garnjost *et al.*, Phys. Rev. Lett. **35**, 142 (1975).
102 GeV/c: J. Chapman *et al.*, Phys. Lett. **47B**, 465 (1973).

205 GeV/c: K. Jaeger *et al.*, Phys. Rev. **D11**, 2405 (1975).
300 GeV/c: F. LoPinto *et al.*, Phys. Rev. **D22**, 573 (1980).
300 GeV/c: A. Sheng *et al.*, Phys. Rev. **D11**, 1733 (1975).
300 GeV/c: B.S. Yuldashev *et al.*, Phys. Rev. **D43**, 2792 (1991).
303 GeV/c: F.T. Dao *et al.*, Phys. Rev. Lett. **30**, 574 (1973).
405 GeV/c: H. Kichimi *et al.*, Phys. Rev. **D20**, 37 (1979).
1500 and 2100 GeV/c: S. Erhan *et al.*, Phys. Lett. **85B**, 447 (1979).

[40] 12 and 24 GeV/c: V. Blobel *et al.*, Nucl. Phys. **B69**, 454 (1974).
12.4 GeV/c: K. Jaeger *et al.*, Phys. Rev. **D11**, 1756 (1975).
19 GeV/c: H. Bøggild *et al.*, Nucl. Phys. **B57**, 77 (1973).
69 GeV/c: V.V. Ammosov *et al.*, Nucl. Phys. **B115**, 269 (1976).
205 GeV/c: K. Jaeger *et al.*, Phys. Rev. **D11**, 2405 (1975).
300 GeV/c: F. LoPinto *et al.*, Phys. Rev. **D22**, 573 (1980).
300 GeV/c: A. Sheng *et al.*, Phys. Rev. **D11**, 1733 (1975).
300 GeV/c: B.S. Yuldashev *et al.*, Phys. Rev. **D43**, 2792 (1991).
405 GeV/c: H. Kichimi *et al.*, Phys. Rev. **D20**, 37 (1979).

[41] 12 and 24 GeV/c: V. Blobel *et al.*, Nucl. Phys. **B69**, 454 (1974).
69 GeV/c: V.V. Ammosov *et al.*, Nucl. Phys. **B115**, 269 (1976).
100 GeV/c: M. Alston-Garnjost *et al.*, Phys. Rev. Lett. **35**, 142 (1975).
102 GeV/c: J. Chapman *et al.*, Phys. Lett. **47B**, 465 (1973).
205 GeV/c: G. Charlton *et al.* Phys. Rev. Lett. **30**, 574 (1973).
205 GeV/c: K. Jaeger *et al.*, Phys. Rev. **D11**, 2405 (1975).
300 GeV/c: F. LoPinto *et al.*, Phys. Rev. **D22**, 573 (1980).
300 GeV/c: A. Sheng *et al.*, Phys. Rev. **D11**, 1733 (1975).
303 GeV/c: F.T. Dao *et al.*, Phys. REv. Lett. **30**, 574 (1973).
405 GeV/c: H. Kichimi *et al.*, Phys. Rev. **D20**, 37 (1979).
1100 GeV/c: F.W. Büsser *et al.*, Phys. Lett. **61B**, 309 (1976).

[42] 12 and 24 GeV/c: V. Blobel *et al.*, Nucl. Phys. **B69**, 454 (1974).
69 GeV/c: V.V. Ammosov *et al.*, Nucl. Phys. **B115**, 269 (1976).
300 GeV/c: F. LoPinto *et al.*, Phys. Rev. **D22**, 573 (1980).
300 GeV/c: A. Sheng *et al.*, Phys. Rev. **D11**, 1733 (1975).
405 GeV/c: H. Kichimi *et al.*, Phys. Rev. **D20**, 37 (1979).
1100 GeV/c: F.W. Büsser *et al.*, Phys. Lett. **61B**, 309 (1976).